8-25-2009

Photoionization of the Be Isoelectronic Sequence: Relativistic and Nonrelativistic R-Matrix Calculations

Wei-Chun Chu
Georgia State University

PHOTOIONIZATION OF THE Be ISOELECTRONIC SEQUENCE:

RELATIVISTIC AND NONRELATIVISTIC *R*-MATRIX CALCULATIONS

by

WEI-CHUN CHU

Under the Direction of Steven Manson

ABSTRACT

The photoionization of the beryllium-like isoelectronic series has been studied. The bound state wave functions of the target ions were built with CIV3 program. The relativistic Breit-Pauli *R*-matrix method was used to calculate the cross sections in the photon energy range between the ionization threshold and $1s^2 4f_{7/2}$ threshold for each ion. For the total cross sections of Be, B^+, C^{+2}, N^{+3}, and O^{+4}, our results match experiment well. The comparison between the present work and other theoretical works are also discussed. We show the comparison with our *LS* results as it indicates the importance of relativistic effects on different ions. In the analysis, the resonances converging to $1s^2 2l_j$ and $1s^2 3l_j$ were identified and characterized with quantum defects, energies and widths using the eigenphase sum methodology. We summarize the general appearance of resonances along the resonance series and along the isoelectronic sequence. Partial cross sections are also reported systematically along the sequence. All calculations were performed on the NERSC system.

INDEX WORDS: Photoionization, *R*-matrix, Cross section, Beryllium-like ion, Resonance

PHOTOIONIZATION OF THE Be ISOELECTRONIC SEQUENCE: RELATIVISTIC AND NONRELATIVISTIC *R*-MATRIX CALCULATIONS

by

WEI-CHUN CHU

A Dissertation Submitted in Partial Fulfillment of the Requirements for the Degree of

Doctor of Philosophy

in the College of Arts and Sciences

Georgia State University

2009

PHOTOIONIZATION OF THE Be ISOELECTRONIC SEQUENCE:

RELATIVISTIC AND NONRELATIVISTIC *R*-MATRIX CALCULATIONS

by

WEI-CHUN CHU

Committee Chair:	Steven Manson
Committee:	Vadym Apalkov
	William Nelson
	Brian Thoms
	Paul Wiita

Electronic Version Approved:

Office of Graduate Studies
College of Arts and Sciences
Georgia State University
December 2009

ACKNOWLEDGEMENTS

I am grateful to my advisor, Dr. Steven Manson, who patiently taught me, throughout the whole program, not only the physics on my research field but also the general idea of doing scientific research. His knowledge of the history of science and his particular humor have also greatly encouraged me in my path of the study in physics. I also thank Dr. Hsiao-Ling Zhou's guidance on dealing with many difficulties that we met in the research, and her significant help on computer programming issues. Dr. Alan Hibbert of Queen's University at Belfast is appreciated for his instruction and comments on using his numerical package, and for kindly providing the related data. Alfred Müller, Stefan Schippers, Ron Phaneuf, Ralf Wehlitz and S. B. Whitfield supplied the numerical tables of their published data, enriching the whole presentation of our research. I also thank Dr. Unil Perera's advice on general academic and research issues, as well as the personal issues during the years of study. The discussions on research and course works with my group members, Mr. Ayao Mamert Sossah and Ms. Prahba Padukka, and our former group member, Mr. Chieh-Jen Yang, were precious and helpful in my study. I deeply appreciate the graduate committee members, Dr. Vadym Apalkov, Dr. William Nelson, Dr. Brian Thoms, and Dr. Paul Wiita, for their suggestions and comments.

TABLE OF CONTENTS

LIST OF TABLES

LIST OF FIGURES

1. INTRODUCTION

1.1. Photoionization

The study of atomic processes in ionized matter is of great importance since ions compose not only the biggest part of the universe, but also occur in many laboratory settings. Since the early years of quantum mechanics, theory and experiment in atomic collisions and spectroscopy form a very critical part of the examination of the properties of matter. Being the core process of many physical and chemical reactions, photoionization and its reverse process, electron-ion recombination, occur in numerous astronomical objects, and other physical systems. Owing to improvement in experimental techniques and computational power, a lot of experimental and theoretical data have been generated in the past ten years.

For experiment, the merged-beam method broadens the choice of target ions and increases the accuracy of absolute cross section measurements. It is used for absolute cross section measurements in most major laboratories in the world today. Also, in synchrotron development, third-generation light sources have improved the measurements by raising the light intensity and the photon energy range since the early 90s. On the calculational side, different approaches are continuously being tested with the rapid growth of computational speed in the modern day computers. With the parallel development of experiments and calculations, a comprehensive comparison and analysis can be carried out. More details of these experiments and calculations will be reviewed in the next sections.

1.2. Developments in Experiment

The most important advance in cross section measurements is the use of synchrotron radiation. Its development and theory were reviewed in a recent article by Bilderback [1]. Today

more than 50 synchrotron facilities over the world are in operation for research in chemistry, physics, materials science, biology and other fields. These continuous and polarized light sources have energies ranging from the IR to the X-ray region.

Synchrotrons use magnetic fields to accelerate the charges to generate radiation. After World War II, the first generation machines were used in fundamental particle physics studies, and the theory and design of synchrotron was well understood. Third-generation synchrotron light sources came into operation nearly twenty years ago. They were designed to provide reliable light sources with a wide range of photon energy, high intensity, and continuous operation. The most important features of modern synchrotrons are the storage ring and the undulator. A storage ring is a closed track for the electron beam to run as many times as possible in order to greatly reduce the power required. With a high quality vacuum chamber in the storage ring, the lifetime of the beam is from 5 to 100 hours. An undulator is a magnetic device that generates sinusoidal magnetic field along the trajectory of the electron beam. The spatial period of the field is determined relativistically to relate the electron speed to the radiation frequency. The third generation machines have significantly increased the brilliance (number of photons emitted per unit time, per unit photon energy, per unit solid angle, per unit source size) from the previous ones. Among these modern facilities, the Advanced Light Source (ALS) in USA, ASTRID in Denmark, the Photon Factory and SPring-8 in Japan, and SuperACO in France have been the sites of large scale cross section measurements.

To measure the absolute photoionization cross section, other than the issue of insufficient light intensity, the difficulty has long been the calibration process of the target atomic systems for any accurate measurement. The merged-beam method, for which Kjeldsen gave a thorough review recently [2], was first employed by Peart *et al* [3] in ionization of ions electron-impact

cross section measurements. The application on photoionization, which was first used by Lyon *et al* [4], aligns the target ion beam and the photon beam for some distance as the interaction region. This effectively compensates for the usually low density of ions and the limited light intensity which are common in absolute cross section measurements. Thus, this method can be applied to many more charge-states than other methods in almost all elements, and the absolute cross section measurement can be made since the ion density can be determined. West discussed the impact and improvement that this technique has brought to absolute cross section measurements in a review paper [5]. Lyon's measurement, described above, along with his following works at Daresbury in 1986-1987 [6][7], were the first applications of this method in ions. Later Koizumi *et al* [8] at Photon Factory in Japan and ASTRID storage ring at University of Aarhus in Denmark also did the measurements using merged-beam method and it is generally used now.

1.3. Developments in Calculations

To calculate atomic processes, an accurate description of the wave functions of the system is required. For the discrete atomic wave functions, calculation methods such as the Hartree-Fock (HF) method [9][10] have been developed, and many computational packages are available. For atomic processes involving continuum states, like electron-atom collision or ionization, there are various methods with different advantages and disadvantages.

Random phase approximation (RPA) was first applied to photoionization by Altick and Glassgold [11]. It describes the photoionization process as an atomic system with the nonrelativistic Hamiltonian perturbed by a single-frequency oscillating external field. Wave functions are obtained using a time-dependent variational principle. This method exhibited considerable success in closed-shell atomic systems such as rare gases [12]. Relativistic random

phase approximation (RRPA) was developed by Johnson and Lin [13], with which the photoionization parameters in Ar, Kr and Xe were presented by Huang *et al* [14]. Multiconfigurational relativistic random phase approximation (MCRRPA) by Huang and Johnson [15] was carried out later along this track.

Similar to RPA, many body perturbation theory (MBPT) has the same radiation term in the Hamiltonian, but while the radiation contains only the first order, the specified electron correlation expands to all orders. Based on the fermionic many-body theory by Goldstone [16], the formalism of MBPT was done by Kelly [17][18][19], and various examples are shown in his review paper [20]. Double-photoionization was enabled based on this method in the work of Chang *et al* [21].

The central idea of *R*-matrix theory is the division of the configuration space into internal and external regions [22]. The standard *R*-matrix method was introduced by Lane and Robson in 1966 [23] for nuclear reaction calculations. The first computational *R*-matrix package was published by Berrington *et al* [24] in 1974 based on the theory by Burke and Seaton [25] for electron-atom scattering or photoionization. Later Scott and Taylor published the Breit-Pauli *R*-matrix (BPRM) code [26] to include the relativistic corrections. The full relativistic version based on Dirac equation was developed by Norrington in 2004 [27]. Among the theoretical efforts using *R*-matrix, Opacity Project [28] and Iron Project [29] contain the most complete data so far, covering energy levels, oscillator strengths, photoionization cross sections and more in a wide selection of atoms and ions. Being the core theory of our calculation, the details of *R*-matrix theory will be shown later in the dissertation.

1.4. Focus of Present Work

The present study focuses on the calculation of the photoionization cross sections of Be-like isoelectronic ions and the analysis of the data obtained. This isoelectronic sequence is chosen due to the simple ionic form and the importance in astrophysics. The theoretical energy levels of target ions and initial ions are compared with the NIST values to ensure the quality of the wave functions used. To estimate the accuracy of our total cross sections, our theoretical results are compared with the available experimental results which exist for Be, B^{+}, C^{+2}, N^{+3}, and O^{+4} ions. The ground state and metastable state partial cross sections are separately compared with other theoretical results and are analyzed.

The *R*-matrix theory that we base our calculations on was well presented by Burke *et al* [30] and by Berrington *et al* [31]. The *R*-matrix program we use in this work is a modified and extended program by Badnell in 2002 [27] from its ancestor package RMATRX1 developed by Berrington *et al* in 1995 [31]. It merges two older packages [26][32] to combine the *LS*-coupling and intermediate-coupling schemes. The code includes the Breit-Pauli term in the Hamiltonian as an option. We took advantage of this feature to obtain the results with and without the Breit-Pauli terms, as this indicated the effect of relativistic interactions on the results. The atomic orbital functions that are fed into the program were optimized by CIV3 program developed by Hibbert [33]. To analyze the photoionization resonances, the QB program by Quigley *et al* [34][35] was adopted to obtain the energies, quantum defects and widths of the resonances. With these parameters associated with each resonance, we observe the general behavior of the resonances in different channels and analyze how it evolves with *Z*. We then discuss the features of overlapping resonances. Some other conclusions are also drawn from the trend along the isoelectronic sequence.

The plan of this dissertation are as follows. Chapter 2 is the theory behind our calculations. The general idea along with the necessary mathematical formulation of photoionization are given, which are common in all calculational methods, followed by the basic concepts and derivations of *R*-matrix theory, the *R*-matrix quantities applied in photoionization, and the Breit-Pauli corrections and recoupling for relativistic calculations. The next chapter, Chapter 3, illustrates the procedures used in the computational programs. The inputs to and the products out from these steps are given. The main tasks and the important numerical adjustments of the programs are also described. Presented in Chapter 4 are the theoretical results, including the energy levels and the cross sections, as well as the available experimental and theoretical results for comparison. Chapter 5 is the analysis of our results. The first part focuses on the identification and characterization of the resonances. Their main features are also discussed. The second part focuses on how all the features evolve along with *Z* in this sequence. Chapter 6 presents the conclusions of the present work. The references are listed after the chapters. Appendix A derives quantum mechanically how we apply the perturbation theory on an atomic system in an electromagnetic field. Appendix B shows the radial functions of the atomic orbitals by the CIV3 calculation for all ions.

2. THEORY

2.1. Photoionization Theory

In this section we present the theoretical approach to the most measured quantity in photoionization, the cross section, by considering the atomic system quantum mechanically in the presence of the electromagnetic radiation. This is a common starting point for all numerical calculation methods. We also emphasize the role of resonances as important in the photoionization phenomenon. Some detailed mathematical derivations are relegated to Appendix A. We use Gaussian units in this section. The general theory of photoionization cross section is reviewed and discussed in details by Burke [36] and by Amusia [37]. Time-dependent perturbation theory in quantum mechanics is well described by Merzbacher [38] and by Sakurai [39].

2.1.1. Basic process

The single photoionization process, which involves one incident photon and one ejected electron, is described by

$$\mathrm{A}_i + h\nu \rightarrow \mathrm{A}_j^+ + e^- \tag{2.1}$$

where A_i is an atom or ion in state *i* and A_j^+ an positive ion in state *j*. In general both *i* and *j* can be a ground state or excited state, and the initial atomic system can be neutral or charged ion (if it is a negative ion, the process is called photodetachment). The photon *hv* is usually considered either linearly polarized or not polarized, which can be described by the combination of two independent polarization states.

In some photon energy ranges, the photoionization can proceed either directly to the continuum ionized state, or go through an intermediate excited state, a resonance, which is described by

$$\mathrm{A}_i + h\nu \rightarrow \mathrm{A}_k^* \rightarrow \mathrm{A}_j^+ + e^- \tag{2.2}$$

where A_k^* stands for the intermediate excited state. Figure 2.1 shows this process schematically. The delay process from the excited state, A_k^*, to the ionization is called autoionization. The interference of these two routes is characterized by a resonance profile in the photoionization cross section, which will be discussed in Subsection 2.1.3.

2.1.2. Cross section

The general definition of total cross section, σ, for scattering is given by

$$\sigma = \frac{\text{Number of events per unit time per scatterer}}{\text{Flux of incident particles}}. \tag{2.3}$$

In the single photoionization of an atom or molecule, which is our current focus, it is equivalent to write

$$\sigma = \frac{\text{Energy absorbed per unit time}}{\text{Energy flux of radiation field}}. \tag{2.4}$$

In the theoretical approach, the initial system of an atom or ion with N+1 electrons is in a specific eigenstate of the (N+1)-electron Hamiltonian, and the radiation field is described by a plane wave with frequency ω. The energy flux cU (U is energy density) of a plane electromagnetic wave is

$$cU = \frac{c}{2}\left(\frac{|E_0|^2}{2\pi} + \frac{|B_0|^2}{2\pi} \right) \tag{2.5}$$

where E_0 and B_0 are amplitudes of electric field $\vec{E}$ and magnetic field $\vec{B}$, respectively. In terms of the vector potential $\vec{A}$, with

$$\begin{aligned} \vec{E} &= -\frac{1}{c}\frac{\partial \vec{A}}{\partial t}, \\ \vec{B} &= \vec{\nabla} \times \vec{A} \end{aligned} \tag{2.6}$$

the energy flux is given by

$$cU = \frac{\omega^2}{2\pi c}\left|A_0\right|^2 \tag{2.7}$$

where the vector potential is

$$\vec{A}(\vec{r},t) = A_0 \hat{\varepsilon}\left(e^{i\vec{k}\cdot\vec{r}-i\omega t}\right), \tag{2.8}$$

where $\hat{\varepsilon}$ is the unit vector along the direction of the vector potential.

Now we assume that the initial state of the system is a discrete state $|i\rangle$ with total energy E_i, and after the absorption of photon energy $\hbar\omega$, the final state $|j\rangle$ is continuum with energy E_j. The normalization of $|i\rangle$ and $|j\rangle$ are $\langle i|i'\rangle = \delta_{ii'}$ and $\langle j|j'\rangle = \delta_{jj'}\delta(E_j - E_{j'})$, so the dimension of $|j\rangle$ has an extra factor of $\sqrt{1/\text{Energy}}$ to the dimension of $|i\rangle$. With the transition probability rate $W_{i\to j}$, Eq. (2.4) gives $\sigma = (\hbar\omega/cU)W_{i\to j}$, which in turn gives (see Appendix A for details)

$$\sigma_V = \frac{4\pi^2\hbar^2 e^2}{m^2 c\omega}\left|\langle j|\hat{\varepsilon}\cdot\vec{D}_V|i\rangle\right|^2 \tag{2.9}$$

in velocity form and

$$\sigma_L = \frac{4\pi^2 e^2\omega}{c}\left|\langle j|\hat{\varepsilon}\cdot\vec{D}_L|i\rangle\right|^2 \tag{2.10}$$

in length form, where *m* is electron mass. The dipole velocity operator $\vec{D}_V$ and the dipole length operator $\vec{D}_L$ are defined in Eq. (A.15) and Eq. (A.18) respectively in Appendix A. In atomic units, the Bohr radius is $a_0 = \hbar^2/me^2$, the fine structure constant is $\alpha = e^2/\hbar c$, and the energy is measured in the units of e^2/a_0; Eq. (2.9) and Eq. (2.10) are reduced to (remember $\vec{D}_V$, $\vec{D}_L$, and $|j\rangle$ need to be in atomic units)

$$\sigma_V = \frac{4\pi^2 \alpha a_0^2}{\omega} \left| \left\langle j \left| \hat{\varepsilon} \cdot \vec{D}_V \right| i \right\rangle \right|^2 \tag{2.11}$$

and

$$\sigma_L = 4\pi^2 \alpha a_0^2 \omega \left| \left\langle j \left| \hat{\varepsilon} \cdot \vec{D}_L \right| i \right\rangle \right|^2 \tag{2.12}$$

where ω is the photon energy in atomic units. For the exact wave functions, σ_V and σ_L are identical [40]. However, for many electron systems, exact wave functions are not possible. Thus, the initial state $|i\rangle$ and the final state $|j\rangle$ of the system are described by expansions of a basis set. In such a case, the comparison of σ_V and σ_L can indicate the quality of the approximate wave functions employed.

2.1.3. Resonances

For the radiative transition that we described above, if the final energy is higher than the first ionization threshold, the final state will be a mixture of the discrete states and at least one continuum state. The discrete and continuum states correspond to closed and open channels, which will be discussed in more detail when we introduce the *R*-matrix theory in Section 2.2. Also in the ionization region, the cross section features resonance structures, owing to the interference of direct and indirect ionization channels.

The analysis of resonances developed by Fano [41] shows that the shape of a resonance in the cross section can be expressed by

$$\sigma = \sigma_0 + A\frac{(q+\varepsilon)^2}{1+\varepsilon^2} \tag{2.13}$$

where

$$\varepsilon = \frac{E - E_r}{\Gamma/2}, \tag{2.14}$$

E_r is the resonance energy and Γ is the resonance width. Figure 2.3 shows the function $(q+\varepsilon)^2/(1+\varepsilon^2)$ with $q=0$, $q=1$, and $q=2$. When applying this picture to $\sigma(E)$, the parameter E_r defines the center of the peak, and Γ defines the scaling in E. The Fano profile is usually used in characterizing the resonance by fitting the function Eq. (2.13) to the data to get the parameters. It is also shown in Ref. [41] that under the condition where only one discrete (resonance) state φ_n and one continuum state ψ_E are presented, with the normalizations

$$\begin{aligned} \langle \varphi_n | H | \varphi_{n'} \rangle &= E_n \delta_{nn'} \\ \langle \varphi_n | H | \psi_E \rangle &= V_E \\ \langle \psi_E | H | \psi_{E'} \rangle &= E\delta(E - E') \end{aligned} \tag{2.15}$$

where H is the total Hamiltonian, Γ is determined by $\Gamma = \pi|V_E|^2$ calculated at the resonance energy E_r. Thus, Γ is considered a measure of the strength of the interaction between the discrete and the continuum at the resonance energy. If the system is prepared in the combination of the discrete (resonance) state φ_n and the continuum state ψ_E, the mean lifetime for autoionization will be $\hbar/(2\pi|V_E|^2)$.

2.2. Nonrelativistic *R*-Matrix Theory

This section is based on the theory described by Burke *et al* [42], Burke and Taylor [43], Scott and Burke [44], and Berrington *et al* [45]. We also follow the notations used in these papers here.

2.2.1. Equation of motion

Photoionization of an isolated (*N*+1)-electron atomic system can be written generally as

$$\mathrm{A}^{n+} + h\nu \rightarrow \mathrm{A}^{(n+1)+} + e^{-} \tag{2.16}$$

where the initial atomic system A^{n+} (*n*=0 for neutral atom) has *N*+1 electrons and the final atomic system includes an *N*-electron residual $\mathrm{A}^{(n+1)+}$ (also called target state) and a scattered electron (also called a photo-electron). The system can be described by a time-independent total wave function, which is the solution to the time-independent Schrödinger equation

$$H^{N+1}\Psi = E\Psi\,. \tag{2.17}$$

where *E* is the total energy. The nonrelativistic Hamiltonian H^{N+1} is written in cgs unit as

$$H^{N+1} = \sum_{i=1}^{N+1}\left(-\frac{\hbar^2}{2m}\nabla_i^2 - \frac{Ze^2}{r_i} + \sum_{j>i}^{N+1}\frac{e^2}{r_{ij}}\right), \tag{2.18}$$

in which the one-electron part includes the kinetic energy and the Coulomb potential, and the two-electron part is the electromagnetic interaction between any two electrons; r_i is the distance from nucleus to the *i*th electron and r_{ij} is the distance between the *i*th electron and the *j*th electron. The nucleus is considered infinitely heavy and has no structure at this level. For simplicity in the derivations, we use atomic unit (a.u. = $me^4/\hbar^2$ = 27.2114 eV = 4.35975 J) as

the unit of H^{N+1} and Bohr radius ($a_0 = \hbar^2/me^2 = 5.29177\times10^{-11}$ m) as the unit *r*, now and throughout the chapter, and rewrite Eq. (2.18) in the form of

$$H^{N+1} = \sum_{i=1}^{N+1}\left(-\frac{1}{2}\nabla_i^2 - \frac{Z}{r_i} + \sum_{j>i}^{N+1}\frac{1}{r_{ij}}\right). \tag{2.19}$$

Since the system is spherically symmetric, it is convenient to adopt spherical coordinate to describe it. In spherical coordinates, the two-electron term in the Hamiltonian is

$$\frac{1}{r_{ij}} = \sum_{lm}\left(\frac{4\pi}{2l+1}\right)Y_l^{m*}(\hat{r}_i)Y_l^m(\hat{r}_j)\frac{r_<^l}{r_>^{l+1}} \tag{2.20}$$

where $r_<$ and $r_>$ are smaller and larger ones of r_i and r_j, respectively.

2.2.2. N-electron states

Since only single-electron ionization is considered here, it is reasonable to focus on the first *N* electrons, which form the target states, before the scattered electron is included. The eigenstates of this *N*-electron system is characterized by (now *i* and *j* are the indices of different eigenstates instead of electron numbers)

$$\left\langle \Phi_i \middle| H^N \middle| \Phi_j \right\rangle = \delta_{ij}E_i^N \tag{2.21}$$

where the eigenstates Φ_i correspond to *N*-electron energies E_i^N. Any bound target state is a linear combination of the Φ_i. To construct these wave functions, we start by looking at the single-electron (bound) atomic orbitals as the functions of position $\vec{r}$ and spin state m_s:

$$o_{nlm}(\vec{r}, m_s) = \frac{1}{r}P_{nl}(r)Y_l^m(\hat{r})\chi(m_s). \tag{2.22}$$

The orbitals $o_{nlm}(\vec{r},m_s)$ are the hydrogenic eigenfunctions with *n* the principle quantum number, *l* the angular momentum quantum number with *m* the *z* component, respectively. The radial part $P_{nl}(r)$ is restricted by the orthogonality condition

$$\langle P_{nl}|P_{n'l}\rangle = \delta_{nn'} \tag{2.23}$$

which is required by the orthogonality of the basis set o_{nlm}

$$\langle o_{nlm}|o_{n'l'm'}\rangle = \delta_{nn'}\delta_{ll'}\delta_{mm'}. \tag{2.24}$$

The optimization of radial functions $P_{nl}(r)$ is done prior to utilization of *R*-matrix program and carried out by other programs such as CIV3 or SUPERSTRUCTURE. The details of the CIV3 results in the present work will be presented in Chapter 3. We shall call $P_{nl}(r)$ 'bound orbitals' as distinguished from 'continuum orbitals' that we will encounter later.

Now we define the *N*-electron configurations ϕ_k as

$$\phi_k(x_1\cdots x_N)=\frac{1}{\sqrt{N!}}\sum_P e^P o_1(x_1)\cdots o_N(x_N) \tag{2.25}$$

where the summation is over all interchanges of the electron indices with the correct permutation symbol e^P. The $\phi_k(x_1\ldots x_N)$ are totally antisymmetric with respect to interchange of particles. Each *k* in Eq. (2.25) indicates a different set of $\{o_1\ldots o_N\}$, where each o_ν is a member of the set $o_{nlm}(\vec{r},m_s)$ in Eq. (2.22), with *x* as the combined coordinate of position $\vec{r}$ and spin σ. Theoretically, *k* can be infinite since the number of hydrogenic orbitals is infinite, but practically we have to limit the number of configurations to make the calculation feasible. For example, in helium, $N=2$, $\{o_1,o_2\}$ can be $\{1s,1s\}$, $\{2s,2s\}$, $\{2p,2p\},\ldots$ in $^1S^e$ symmetry, and the number of terms in the expansion Eq. (2.25) depends on the accuracy required. It is trivial to see

that $\phi_k(x_1 \ldots x_N)$ are orthogonal since the orbitals o_ν are orthogonal, and with infinite *k* they form a complete basis set.

These configurations are suitable to be the basis set of the *N*-electron wave functions, and the configuration-interaction (CI) expansion of Φ_i is

$$\Phi_i(x_1, \cdots, x_N) = \sum_k b_{ik} \phi_k(x_1, \cdots, x_N). \tag{2.26}$$

With the same basis set, the *N*-electron Hamiltonian is

$$\left\langle \phi_k \middle| H^N \middle| \phi_{k'} \right\rangle = H^N_{kk'}, \tag{2.27}$$

and Eq. (2.21) is equivalent to the diagonalization of $H^N_{kk'}$.

2.2.3. The ejected electron

When the ejected electron is added to the target wave function to complete the wave function for the (*N*+1)-electron system, some requirements must be kept in mind. First, the total angular momentum must be conserved. To yield a specific total angular momentum, there might be a few different ways to couple the target angular momentum and the ejected electron angular momentum. These different pairs of the target states Φ_i and the ejected electron wave functions are called the scattering channels. For example, a 2*p* target state (*l*=1) and an *s*-wave ejected electron (*l*=0) are coupled an *L*=1 state, and a 2*s* target state and a *p*-wave ejected electron can also form a *L*=1 state, but they are different channels.

Second, the total energy of the system must be conserved. The total energy *E*, which is the sum of the target state energy E_i^N and ejected electron energy $k_i^2/2$, is determined by the initial state energy E_0^{N+1} and the incident photon energy ω, in atomic units. This conservation is

$$E = E_i^N + \frac{k_i^2}{2} = E_0^{N+1} + \omega \tag{2.28}$$

or

$$\frac{k_i^2}{2} = \omega + \left(E_0^{N+1} - E_i^N\right) \tag{2.29}$$

to show the dependence of k_i on the photon energy. The channel is said to be "open" if $E - E_i^N > 0$ or "closed" if $E - E_i^N < 0$. $E - E_i^N = 0$ simply means the total energy is just the ionization threshold energy.

R-matrix theory is characterized by the partition of configuration space [22]. Figure 2.2 sketches this partitioning. Let there be a spherical shell with radius *a* centered at the nucleus of the atomic system. This shell is designed to largely enclose all the bound state wave functions. It assumes that outside the shell, the bound state wave functions vanish, and there exists solely the continuum ejected electron. With *a* chosen to meet this condition, the inner region and the outer region are described as follows:

1) For $r < a$, the system contains *N*+1 indistinguishable electrons. The exchange term between any two electrons in the Hamiltonian must be included as in Eq. (2.19). The target wave functions Φ_i and the scattered electron are coupled totally-antisymmetrically. The final state wave functions are expanded in terms of configurations in a manner similar to Eq. (2.26).

2) For $r > a$, the (*N*+1)-electron system is viewed as a two-body system. The *N*-electron system is replaced effectively by a central potential centered at $r = 0$. The ejected electron then is under a local potential and can be solved with an asymptotic expansion.

Other than the convergence at $r = 0$ and the asymptotic form at $r \to \infty$, the boundary conditions include the continuity of wave function at $r = a$. The details of formatting the wave

functions in these two regions will be discussed in the later sections. In practice, *a* is determined to be sufficiently large so as

$$\left|P_{nl}(r)\right| < \delta \qquad \text{if} \quad r > a \tag{2.30}$$

for all the bound orbitals $P_{nl}(r)$ in use.

2.2.4. Internal region

In the internal region, the system consists of *N*+1 indistinguishable electrons. The total wave function is an (*N*+1)-electron antisymmetric function with all the exchange terms. All the bound state wave functions are confined in the inner region, which means they drop to zero at the boundary $r = a$. In order to obtain the wave function in this region for any energy *E*, an energy-independent basis set $\psi_k(x_1 \ldots x_{N+1})$ are built as

$$\psi_k(x_1 \cdots x_{N+1}) = \mathcal{A} \sum_{ij} c_{ijk} \overline{\Phi}_i(x_1 \cdots x_N; \hat{r}_{N+1}\sigma_{N+1}) \frac{u_{ij}(r_{N+1})}{r_{N+1}} + \sum_j d_{jk} \phi_j(x_1 \cdots x_{N+1}), \tag{2.31}$$

in which we demand $\psi_k(x_1 \cdots x_{N+1})$ to be eigenfunctions of H^{N+1} with eigenvalues E_k in the defined region. For each channel *i*, the function $\overline{\Phi}_i(x_1 \ldots x_N; \hat{r}_{N+1}\sigma_{N+1})$ is the target state wave function $\Phi_i(x_1 \ldots x_N)$ coupled with its corresponding angular term and spin term of the scattered electron to form the specific total angular momentum and total spin. Notice that now *i* is the index of channels instead of the index of target states; the number of channels is generally more than the number of target states; the $u_{ij}(r_{N+1})$ are the continuum radial functions of the ejected electron, which are the only non-zero functions at $r = a$. We will talk about the determination of these radial functions later. The antisymmetry operator $\mathcal{A}$ indicates the inclusion of all the interchange terms between the target electrons and the scattered electron to have the total antisymmetry. In the last term, we include the (*N*+1)-electron configurations $\phi_j(x_1 \cdots x_{N+1})$ to

ensure the completeness of this basis set. Similar to $\phi_k(x_1 \cdots x_N)$ in Subsection 2.2.2, $\phi_j(x_1 \cdots x_{N+1})$ are formed with the single-electron orbitals.

To make it a more compact form, Eq. (2.31) can be written as

$$\psi_k = \sum_\lambda V_{k\lambda} \varphi_\lambda \tag{2.32}$$

where $V_{k\lambda}$ are the collection of the coefficients c_{ijk} and d_{jk}, and φ_λ are the collection of the basis functions in Eq. (2.31). The Hamiltonian H^{N+1} is written in the φ_λ basis as

$$\left(\varphi_\lambda \middle| H^{N+1} \middle| \varphi_{\lambda'}\right) = H^{N+1}_{\lambda\lambda'} \tag{2.33}$$

where the round brackets indicate that the range of integration is the inner region $0 \le r \le a$. The coefficients $V_{k\lambda}$ of ψ_k are determined by diagonalizing H^{N+1},

$$\left(\psi_k \middle| H^{N+1} \middle| \psi_{k'}\right) = E_k \delta_{kk'}. \tag{2.34}$$

The functions $\psi_k(x_1 \ldots x_{N+1})$ are then the eigenfunctions of H^{N+1} described by eigenvectors $V_{k\lambda}$ with eigenvalues E_k, and are suitable to be the basis set for the total wave function in the inner region.

2.2.5. Continuum orbitals

For the continuum functions $u_{ij}(r)$ in Eq. (2.31), *i* is the channel label, which is associated with angular momentum l_i, and for each *i, j* is the label of a discrete set of solutions. Theoretically, as long as $u_{ij}(r)$ form a complete set of basis that satisfies the boundary conditions at $r = 0$ and $r = a$, they are valid solutions in the previous section. Other than these requirements, the choice of $u_{ij}(r)$ focuses on making the convergence of Eq. (2.31) quick.

The appropriate continuum functions $u_{ij}(r)$ in channel *i* are usually determined by solving the equation

$$\left(\frac{\mathrm{d}^2}{\mathrm{d}r^2}-\frac{l_i(l_i+1)}{r^2}+V_0(r)+k_{ij}^2\right)u_{ij}(r)=\sum_n \Lambda_{ijn}P_{nl_i}(r) \tag{2.35}$$

with the boundary conditions

$$\begin{aligned} u_{ij}(0)&=0 \\ \frac{a}{u_{ij}(a)}\frac{\mathrm{d}u_{ij}(a)}{\mathrm{d}r}\bigg|_{r=a}&=b\,. \end{aligned} \tag{2.36}$$

In Eq. (2.35), the summation of indices *n* is over all atomic orbitals of angular momentum l_i in the bound state expansion. The Lagrange multipliers Λ_{ijn} are chosen to meet the orthogonality conditions

$$\left(u_{ij}\middle|P_{nl_i}\right)=0 \tag{2.37}$$

for all $\{n,l\}$. Notice here the range of integration is from $r=0$ to $r=a$, as indicated by the round bracket. Since the solutions $u_{ij}(r)$ also satisfy

$$\left(u_{ij}\middle|u_{ij'}\right)=\delta_{jj'}, \tag{2.38}$$

the atomic and continuum orbitals together

$$P_{n_{\min}l_i}(r),\cdots,P_{n_{\max}l_i}(r),u_{i1}(r),u_{i2}(r),\cdots \tag{2.39}$$

form a complete basis set in the region $0\le r\le a$. For the potential $V_0(r)$ in Eq. (2.35), in principle, the choice is arbitrary but will have an effect on how fast the expansion converges. In our case, we choose $V_0(r)$ to be the average static potential viewed by the ejected electron. However, the choice is not critical since Eq. (2.37) serves effectively as an pseudo attractive potential. The choice of *b* is also arbitrary in principle, and we set it to zero. Now from Eq. (2.35)

we see that $u_{ij}(r)$ are solutions to a eigenvalue equation with eigenvalues $k_{ij}^2/2$, and are totally independent of the total energy *E*.

2.2.6. R-matrix

Now it comes to the stage to build, associated with the given total energy *E*, the wave function Ψ in the internal region and the *R*-matrix to connect the wave function through the internal and external region. The wave function is described as

$$\Psi = \sum_k A_{Ek}\psi_k \tag{2.40}$$

in the ψ_k basis which is constructed by Eq. (2.35). In order to find A_{Ek}, we put Eq. (2.17), Eq. (2.34) and Eq. (2.40) together to form

$$\left(\psi_k\left|H^{N+1}\right|\Psi\right)-\left(\Psi\left|H^{N+1}\right|\psi_k\right)=(E-E_k)\left(\psi_k|\Psi\right)=(E-E_k)A_{Ek}\,. \tag{2.41}$$

Within H^{N+1}, since the potential energy operator commutes with the position operator $\vec{r}$ and operates equally from the right and from the left on any wave function of position, the potential energy part on the left hand side of Eq. (2.41) vanishes, and only the kinetic energy part stands out. Thus, this relation is rewritten as

$$-\frac{1}{2}(N+1)\left[\left(\psi_k\left|\nabla^2_{N+1}\right|\Psi\right)-\left(\Psi\left|\nabla^2_{N+1}\right|\psi_k\right)\right]=(E-E_k)A_{Ek}\,, \tag{2.42}$$

where ∇_{N+1} acts on $\vec{r}_{N+1}$. In Eq. (2.42), only the continuum orbitals contribute to the non-zero part on the left hand side, so using Eq. (2.31) to define

$$w_{ik}(r)=\sum_j c_{ijk}u_{ij}(r)=r\left(\overline{\Phi}_i|\psi_k\right), \tag{2.43}$$

we further simplify Eq. (2.42) to

$$-\frac{1}{2}\sum_{ijk'}A_{Ek'}\left[\left(\overline{\Phi}_i w_{ik}(r_{N+1})\left|\nabla^2_{N+1}\right|\overline{\Phi}_j w_{jk'}(r_{N+1})\right)-\left(\overline{\Phi}_j w_{jk'}(r_{N+1})\left|\nabla^2_{N+1}\right|\overline{\Phi}_i w_{ik}(r_{N+1})\right)\right]=(E-E_k)A_{Ek}\,. \tag{2.44}$$

Since Φ_i are orthogonal functions, only $i = j$ terms on the left hand side survive, and Eq. (2.44) becomes

$$-\frac{1}{2}\sum_i \left[\left(w_{ik}(r) \left| \frac{\mathrm{d}^2}{\mathrm{d}r^2} \right| F_i(r) \right) - \left(F_i(r) \left| \frac{\mathrm{d}^2}{\mathrm{d}r^2} \right| w_{ik}(r) \right) \right] = (E - E_k) A_{Ek} \tag{2.45}$$

where the dummy variable r_{N+1} is replaced by *r*, and $F_i(r)$, the reduced radial wave function of the ejected electron in channel *i* at energy *E* is defined by

$$F_i(r) = \sum_k A_{Ek} w_{ik}(r) = r\left(\overline{\Phi}_i \middle| \Psi\right). \tag{2.46}$$

With Green's second identity, which reads (for arbitrary second-order continuous functions $f_1(x)$ and $f_2(x)$)

$$\int_{x_1}^{x_2} (f_1 f_2'' - f_1'' f_2)\mathrm{d}x = (f_1 f_2' - f_1' f_2)\Big|_{x_1}^{x_2} \tag{2.47}$$

and the boundary conditions in Eq. (2.36), we convert Eq. (2.45) to

$$-\frac{1}{2}\sum_i w_{ik}(a)\left(F_i'(a) - \frac{b}{a} F_i(a) \right) = (E - E_k) A_{Ek}\,, \tag{2.48}$$

which gives the expression for the A_{Ek} where we have used $F'(a)$ as the abbreviation of $\mathrm{d}F(r)/\mathrm{d}r\big|_{r=a}$. Its expression is simply

$$A_{Ek} = \frac{1}{2a(E_k - E)} \sum_i w_{ik}(a)[aF_i'(a) - bF_i(a)]. \tag{2.49}$$

Plugging in these A_{Ek} back to Eq. (2.46), we get

$$F_i(a) = \sum_j R_{ij}(E)\left(aF_j'(a) - bF_j(a)\right) \tag{2.50}$$

where the *R*-matrix is defined by

$$R_{ij}(E) = \frac{1}{2a} \sum_k \frac{w_{ik}(a) w_{jk}(a)}{E_k - E} \tag{2.51}$$

where $w_{ik}(r)$ and E_k are determined by the solution of ψ_k in Eq. (2.34), and E is the total energy.

For each set of the conserved quantum numbers (total angular momentum L, total spin S, and parity π), the (N+1)-Hamiltonian is diagonalized once, and $R_{ij}(E)$ as a function of E is obtained. The set of scattered wave functions at $r=a$ are solved for using the coupled equations, Eq. (2.50). With these $F_i(a)$, we obtain A_{Ek} through Eq. (2.49), and the wave function in the internal region is done.

2.2.7. Buttle correction

In a practical calculation we only take finite terms in the expansion Eq. (2.32). For the omitted terms, even if each single term is small when E_k is far from E, they may add up coherently and make a considerable effect. This brings the main error to the wave function. Now consider the equation

$$\left(\frac{\mathrm{d}^2}{\mathrm{d}r^2}-\frac{l_i(l_i+1)}{r^2}+V_0(r)+k_i^2\right)u_i^0(r)=0\,, \tag{2.52}$$

which is similar to Eq. (2.35), but k_{ij}^2 is replaced by k_i^2 where the $k_i^2/2$ are the channel energies (defined in Sec. 2.2.3). Suppose we truncate the expansion of R-matrix after the first N terms, then the correction, according to the method described by Buttle [46], is

$$\begin{aligned} R_{ii}^c &\approx \frac{1}{a}\sum_{j=N+1}^{\infty}\frac{u_{ij}(a)^2}{k_{ij}^2-k_i^2} \\ &= \left(a\frac{u_i^{0\,\prime}(a)}{u_i^0(a)}-b\right)^{-1}-\frac{1}{a}\sum_{j=1}^{N}\frac{u_{ij}(a)^2}{k_{ij}^2-k_i^2} \end{aligned} \tag{2.53}$$

to the diagonal elements of *R*-matrix. Here $u_{ij}(r)$ and k_{ij} are the solutions to the eigenvalue equation Eq. (2.35) satisfying the boundary conditions Eq. (2.36). Adding this correction to *R*-matrix, Eq. (2.51) is rewritten as

$$R_{ij}(E)=\frac{1}{2a}\sum_{k}\frac{w_{ik}(a)w_{jk}(a)}{E_k-E}+R_{ii}^{c}\delta_{ij}\,. \tag{2.54}$$

R_{ii}^{c} is often a simple continuous function of k_i^2 when $k_i^2<k_{ij}^2$. Since the number of required terms in the correction is usually large, we can fit this function to a few k_i^2 to fix the form of the function and estimate all the terms. Seaton developed the fitting process that we use in *R*-matrix calculation [47].

2.2.8. External region

Here we turn to the wave function in the external region. In this region the scattered electron is distinguishable from the first *N* electrons that stay with the nucleus. The total wave function is expanded in the form of

$$\Psi(x_1\ldots x_{N+1})=\sum_{i}\overline{\Phi}_i(x_1\ldots x_N;\hat{r}_{N+1}\sigma_{N+1})\frac{F_i(r_{N+1})}{r_{N+1}} \tag{2.55}$$

where $\overline{\Phi}_i$ are the same channel functions in Eq. (2.31), and the $F_i(r_{N+1})$ are the corresponding reduced radial wave functions of the scattered electron. In this form we omit the antisymmetry operator $\mathcal{A}$ to exclude the exchange terms between scattered electron and any bound electron. Plugging in this total wave function into Schrödinger equation Eq. (2.17), we get the equation for the functions $F_i(r)$ as

$$\left(\frac{\mathrm{d}^2}{\mathrm{d}r^2}-\frac{l_i(l_i+1)}{r^2}+\frac{2z}{r}+k_i^2\right)F_i(r)=2\sum_{j}V_{ij}(r)F_j(r). \tag{2.56}$$

where the summation over *j* covers up to the number of channel functions $\overline{\Phi}_i$ in use, $k_i^2/2$ are the channel energies, $z \equiv Z - N$ is the effective charge of the target, $r \equiv r_{N+1}$ while the condition $r > r_m$ is valid in the whole external region, and with the expansion of Eq. (2.20), $V_{ij}(r)$ is given by

$$\begin{aligned} V_{ij}(r) &= \left\langle \overline{\Phi}_i \left| \sum_{n=1}^{N} \frac{1}{r_{n,N+1}} \right| \overline{\Phi}_j \right\rangle \\ &= \left\langle \overline{\Phi}_i \left| \sum_{n=1}^{N} \sum_{lm} \left(\frac{4\pi}{2l+1} \right) \frac{r_n^l}{r^{l+1}} Y_l^{m*}(\hat{r}_n) Y_l^m(\hat{r}_{N+1}) \right| \overline{\Phi}_j \right\rangle \\ &= \sum_l \frac{1}{r^{l+1}} \left\langle \overline{\Phi}_i \left| \sum_{n=1}^{N} r_n^l P_l(\cos\theta_{n,N+1}) \right| \overline{\Phi}_j \right\rangle \end{aligned} \tag{2.57}$$

Note that in theory the expansion contains infinite *l* terms, but here we include only up to some maximum *l* value specified by the program user to make the calculation feasible. Defining the long-range potential coefficient a_{ij}^l as

$$a_{ij}^l = \left\langle \overline{\Phi}_i \left| \sum_{n=1}^{N} r_n^l P_l(\cos\theta_{n,N+1}) \right| \overline{\Phi}_j \right\rangle, \tag{2.58}$$

Eq. (2.56) is reduced to

$$\left(\frac{\mathrm{d}^2}{\mathrm{d}r^2} - \frac{l_i(l_i+1)}{r^2} + \frac{2z}{r} + k_i^2 \right) F_i(r) = 2 \sum_l \sum_j \frac{a_{ij}^l}{r^{l+1}} F_j(r) \tag{2.59}$$

which can be integrated outward starting from $r = a$ and fitted to the asymptotic form at $r \to \infty$. Suppose we have *n* total channels and n_o open channels in the calculation, and we order n_o first in the *n* channels so that $k_1^2 \geq \cdots \geq k_{n_o}^2 \geq k_{n_o+1}^2 \geq \cdots \geq k_n^2$. Let us extend $F_i(r)$ to the double-index $F_{ij}(r)$ where the additional index *j* is for the n_o linearly independent solutions. The boundary conditions at $r \to \infty$ are

$$F_{ij}(r)\underset{r\to\infty}{=}\begin{cases}\dfrac{1}{\sqrt{k_i}}\left(\delta_{ij}\sin\theta_i+K_{ij}\cos\theta_i\right) & k_i^2>0 \quad \text{(open channels)}\\ \delta_{ij}\exp\left(-\phi_i\right) & k_i^2<0 \quad \text{(closed channels)}\end{cases} \tag{2.60}$$

where the $n_o\times n_o$ reactance matrix K_{ij} (K-matrix) is to be determined when we apply the connection between internal and external wave functions through R-matrix, and other parameters are defined by

$$\begin{aligned}\theta_i &= k_i r-\frac{1}{2}l_i\pi-\eta_i\ln(2k_i r)+\arg\Gamma(l_i+1+i\eta_i)\\ \eta_i &= -\frac{z}{k_i}\\ \phi_i &= |k_i|r-\frac{z}{|k_i|}\ln(2|k_i|r)\end{aligned} \tag{2.61}$$

Note that the parameters ϕ_i are not related to the configuration functions $\phi_k(x_1\ldots x_N)$ that we defined earlier. Now the wave function in the external region will be done by solving Eq. (2.59) and boundary conditions in Eq. (2.60) once we get K_{ij}.

2.2.9. Open channel solutions

In this section, we find the total wave function with the reduced radial functions $F_{ij}(r)$ satisfying the boundary conditions in both the internal and external region. If we change to matrix format and use a dot as the abbreviation of the derivative of r ($\mathrm{d}f/\mathrm{d}r=\dot{f}$), Eq. (2.50) is expressed in the form of

$$\boldsymbol{F}=a\boldsymbol{R}\cdot\dot{\boldsymbol{F}}-b\boldsymbol{R}\cdot\boldsymbol{F} \tag{2.62}$$

which gives the values of the reduced radial functions $\boldsymbol{F}$ at $r=a$, where $\boldsymbol{R}$ is an $n\times n$ matrix. We now introduce $n+n_o$ linearly independent solutions of F_{ij} in the external region satisfying the boundary conditions

$$
\begin{aligned}
s_{ij}(r)_{r\to\infty} &= \delta_{ij}\sin\theta_i \qquad\qquad i=1,n \quad j=1,n_o \\
c_{ij}(r)_{r\to\infty} &= \begin{cases} \delta_{ij}\cos\theta_i & i=1,n \quad j=1,n_o \\ \delta_{ij}\exp(-\phi_i) & i=1,n \quad j=n_o+1,n \end{cases}
\end{aligned}
\tag{2.63}
$$

in which θ_i and ϕ_i are defined in Subsection 2.2.8. The solutions $\boldsymbol{s}$ and $\boldsymbol{c}$ can be obtained straightforwardly, and there are a few available numerical packages for these solutions in the market. $\boldsymbol{F}$ is a linear combination of $\boldsymbol{s}$ and $\boldsymbol{c}$:

$$\boldsymbol{F} = \boldsymbol{s} + \boldsymbol{c}\boldsymbol{K} \tag{2.64}$$

and its first derivative is

$$\dot{\boldsymbol{F}} = \dot{\boldsymbol{s}} + \dot{\boldsymbol{c}}\boldsymbol{K}\,. \tag{2.65}$$

With these expressions, Eq. (2.62) becomes

$$\boldsymbol{s} + \boldsymbol{c}\boldsymbol{K} = a\boldsymbol{R}(\dot{\boldsymbol{s}} + \dot{\boldsymbol{c}}\boldsymbol{K}) - b\boldsymbol{R}(\boldsymbol{s} + \boldsymbol{c}\boldsymbol{K}), \tag{2.66}$$

and the solution for $\boldsymbol{K}$ is

$$\boldsymbol{K} = \boldsymbol{B}^{-1}\boldsymbol{A} \tag{2.67}$$

where the matrices $\boldsymbol{A}$ and $\boldsymbol{B}$ are

$$\boldsymbol{A} = -\boldsymbol{s} + a\boldsymbol{R}\left(\dot{\boldsymbol{s}} - \frac{b}{a}\boldsymbol{s}\right) \tag{2.68}$$

and

$$\boldsymbol{B} = +\boldsymbol{c} - a\boldsymbol{R}\left(\dot{\boldsymbol{c}} - \frac{b}{a}\boldsymbol{c}\right) \tag{2.69}$$

respectively. The *K*-matrix thus carries the information from the internal region through the *R*-matrix and determines the wave function in the external region. The *K*-matrix is real and symmetric.

2.3. Radiative Process

In this section, we consider the interaction between a photon with specified energy and an atomic system. The atomic system in this case is described by the (N+1)-electron wave function discussed above.

2.3.1. Closed channel solutions

When all channels are closed, the general form of the wave function in the internal and the external region, as shown in Subsection 2.2.6 and Subsection 2.2.8, stay the same, but the boundary conditions change, thus changing the matching of the solutions. The external wave function has to satisfy the boundary conditions for $c_{ij}(r)$ but not $s_{ij}(r)$ in Eq. (2.63), to satisfy the conditions

$$c_{ij}(r) \underset{r\to\infty}{=} \delta_{ij} \exp(-\phi_i) \qquad i = 1,n \quad j = 1,n \tag{2.70}$$

where ϕ_i holds the same definition. $\boldsymbol{F}$ is then given by the expansion of $\boldsymbol{c}$ as

$$\boldsymbol{F} = \boldsymbol{c}\boldsymbol{x} \tag{2.71}$$

where $\boldsymbol{x}$ replaces $\boldsymbol{K}$ as the coefficients of $\boldsymbol{F}$. Eq. (2.66) then gives

$$\boldsymbol{B}\boldsymbol{x} = 0 \tag{2.72}$$

when we plug in the form of Eq. (2.71) to solve for $\boldsymbol{x}$, where $\boldsymbol{B}$ is defined by Eq. (2.69). To obtain nontrivial solutions of $\boldsymbol{x}$, the condition $\det \boldsymbol{B} = 0$ must be met, which requires the energy eigenvalues to be negative.

2.3.2. Dipole matrices

In order to perform the dipole approximation calculation that was discussed in Section 2.1, we use the dipole matrix involving the initial and final state wave functions as the formalism to calculate the photoionization. We introduce the dipole length and velocity operators as

$$\vec{D}_L = \sum_n \vec{r}_n \tag{2.73}$$

and

$$\vec{D}_V = -\sum_n \vec{\nabla}_n \tag{2.74}$$

where the summation of *n* is over all electrons.

Using the convention of Fano and Racah [48], we introduce the reduced dipole matrix $D(a,b)$ between state *a* and state *b* as

$$D(a,b) = \left(L_a \left\| \vec{D}_l \right\| L_b\right) = \frac{\sqrt{2L_a+1}}{C(L_b l L_a; M_b \mu)} \left\langle L_a M_a \left| D_l^{\mu} \right| L_b M_b \right\rangle \tag{2.75}$$

The normalization of the bound states is

$$\left\langle \Psi_n \middle| \Psi_{n'} \right\rangle = \delta_{nn'}, \tag{2.76}$$

and the normalization of the free state is

$$\left\langle \Psi_E \middle| \Psi_{E'} \right\rangle = \delta(E - E'). \tag{2.77}$$

We divide $D(a,b)$ into two terms as

$$D(a,b) = D^{(\mathrm{I})}(a,b) + D^{(\mathrm{O})}(a,b) \tag{2.78}$$

where $D^{(\mathrm{I})}(a,b)$ is the contribution from the internal region and $D^{(\mathrm{O})}(a,b)$ from the external region. Now we discuss them separately.

a. $D^{(\mathrm{I})}$

Suppose there are two wave functions Ψ_α and Ψ_β defined in the internal region. With the expansion of Ψ_E of Eq. (2.40), the dipole matrix for the internal region is

$$\begin{aligned} D^{(\mathrm{I})}(\alpha,\beta) &= \left(\Psi_\alpha \middle\| D^{(I)} \middle\| \Psi_\beta\right) \\ &= \sum_{kk'} A_{\alpha k} A_{\beta k'} M_{kk'} \end{aligned} \tag{2.79}$$

where $M_{kk'}$ is defined by

$$M_{kk'} = \left(\psi_k \middle\| D^{(I)} \middle\| \psi_{k'}\right). \tag{2.80}$$

The coefficients A_{Ek} can be written in matrix form, which we will apply shortly, by

$$\boldsymbol{A}_E = \begin{bmatrix} A_{E1} & & & 0 \\ & \ddots & & \\ & & A_{Ek} & \\ 0 & & & \ddots \end{bmatrix} \tag{2.81}$$

where *k* is the element index and *E* is a parameter of the matrix. With expansion of ψ_k in Eq. (2.32), we can further write $M_{kk'}$ as

$$M_{kk'} = \sum_{\lambda\lambda'} V_{k\lambda} V_{k'\lambda'} D_{\lambda\lambda'} \tag{2.82}$$

where the elements of reduced matrix *D* are

$$D_{\lambda\lambda'} = \left(\varphi_\lambda \middle\| D^{(I)} \middle\| \varphi_{\lambda'}\right). \tag{2.83}$$

If the constant *b* introduced by the boundary condition Eq. (2.36) is set as 0 (which is a common setup in practice), the coefficients, A_{Ek}, are

$$\begin{aligned} A_{Ek} &= \frac{1}{2(E_k - E)} \sum_i w_{ik}(a) F_i'(a) \\ &= \frac{1}{2(E_k - E)} \left(\boldsymbol{w}_E^{\mathrm{T}} \boldsymbol{F}_E'\right)_k \\ &= \frac{1}{2a(E_k - E)} \left(\boldsymbol{w}_E^{\mathrm{T}} \boldsymbol{R}_E^{-1} \boldsymbol{F}_E\right)_k \end{aligned} \tag{2.84}$$

where the superscript “T” is transpose, and where we have plugged in

$$\boldsymbol{F}' = \frac{1}{a}\boldsymbol{R}^{-1}\boldsymbol{F} \tag{2.85}$$

as the matrix form of Eq. (2.50) (with $b = 0$), and the parameter E is labeled on each matrix to distinguish A_{Ek} at different energies. Now we introduce the diagonal matrix $\boldsymbol{G}_E$ with diagonal elements (with index k)

$$G_{Ek} = \frac{1}{2a(E_k - E)}, \tag{2.86}$$

Eq. (2.79) is in the final matrix form as

$$D^{(\mathrm{I})}(\alpha,\beta) = \boldsymbol{F}_\alpha^{*\mathrm{T}}\boldsymbol{R}_\alpha^{-1}\boldsymbol{w}_\alpha\boldsymbol{G}_\alpha\boldsymbol{M}\boldsymbol{G}_\beta\boldsymbol{w}_\beta^{\mathrm{T}}\boldsymbol{R}_\beta^{-1}\boldsymbol{F}_\beta \tag{2.87}$$

b. $D^{(\mathrm{O})}$

Now let us focus on the length operator. Since in the external region, the exchange terms between the photoelectron and the target electrons no longer exist, we divide the $\vec{D}$ operator as $\vec{D} = \vec{R} + \vec{r}$ where $\vec{R}$ is responsible for the target wave functions and $\vec{r}$ for the photoelectron. Its matrix elements between state α and state β are then

$$D^{(\mathrm{O})}(\alpha,\beta) = \sum_{ii'}\left[x_{ii'}\left(F_{ia}\middle|F_{i'b}\right) + y_{ii'}\left(F_{ia}\middle|r\middle|F_{i'b}\right)\right] \tag{2.88}$$

where

$$\begin{aligned} x_{ii'} &= \left(\overline{\Phi}_i\middle\|\vec{R}\middle\|\overline{\Phi}_{i'}\right) \\ y_{ii'} &= \left(\overline{\Phi}_i\middle\|\hat{r}\middle\|\overline{\Phi}_{i'}\right) \end{aligned}. \tag{2.89}$$

The coefficients $x_{ii'}$ are non-zero only when the transition between the target states is permitted by the optical selection rule, and when $l_i = l_{i'}$; the coefficients $y_{ii'}$ are non-zero only when the

two channels are built by the same target state, and when $l_i = l_{i'} \pm 1$. The evaluation of Eq. (2.88) is described by Seaton [49].

2.4. Breit-Pauli *R*-Matrix Theory

The fully relativistic Dirac equation of motion can be approximated by the Schrödinger equation with the relativistic correction terms. The Breit-Pauli Hamiltonian of the system is expressed as

$$H_{\mathrm{BP}} = H + H_{\mathrm{REL}} \tag{2.90}$$

where *H* has been fully discussed (as H^{N+1} for (*N*+1)-electron system) in Section 2.2. In the RMATRX1 code, H_{REL} contains the corrections up to the order of $\alpha^2 Z^4$, which makes

$$H_{\mathrm{REL}} = H_{\mathrm{mass}} + H_{\mathrm{D1}} + H_{\mathrm{SO}} \tag{2.91}$$

where

$$H_{\mathrm{mass}} = -\frac{\alpha^2}{8}\sum_n \nabla_n^4 \qquad \text{mass-correction term} \tag{2.92}$$

$$H_{\mathrm{D1}} = -\frac{\alpha^2 Z}{8}\sum_n \nabla_n^2\left(\frac{1}{r_n}\right) \qquad \text{one-body Darwin term} \tag{2.93}$$

$$H_{\mathrm{SO}} = \frac{\alpha^2 Z}{2}\sum_n \frac{\vec{l}_n \cdot \vec{s}_n}{r_n^3} \qquad \text{spin-orbit interaction} \tag{2.94}$$

in which the summation of *n* covers all the electrons in the system. Each one of the three terms can be switched on or off optionally in the program. In these terms, H_{mass} and H_{D1} commute with L^2, L_Z, S^2, S_Z, and π, while H_{SO} commutes with only J^2, J_Z, and π; thus, in the Breit-Pauli calculation including H_{SO}, the symmetry of the total wave function in Eq. (2.31) is

defined by J and π instead of L, S and π. That is to say, each $J\pi$-symmetry of the (N+1)-electron system goes through an independent run in the program.

In the Breit-Pauli R-matrix (BPRM) program, the Hamiltonian in Eq. (2.33), the long-range potential coefficients in Eq. (2.58), and the dipole matrix in Eq. (2.83) all need to be transformed into the pair-coupling scheme, which is defined by

$$\begin{aligned} \vec{J}_i + \vec{l} &= \vec{K} \\ \vec{K} + \vec{s} &= \vec{J} \end{aligned} \tag{2.95}$$

where $\vec{J}_i$ is the total angular momentum of the target state in the ith channel, $\vec{l}$ and $\vec{s}$ are the orbital and spin angular momentums of the photoelectron, and $\vec{J}$ is the total angular momentum of the final state. The whole procedure starts with the calculation of these matrices in LS-coupling first, as what we have shown in Section 2.2; then, using an unitary transformation, they are converted to the pair-coupling expressions. Note that in BPRM, only the $J\pi$ symmetry in the initial (N+1)-electron system is specified in each calculation, and the contributions from all the LS terms are taken into account.

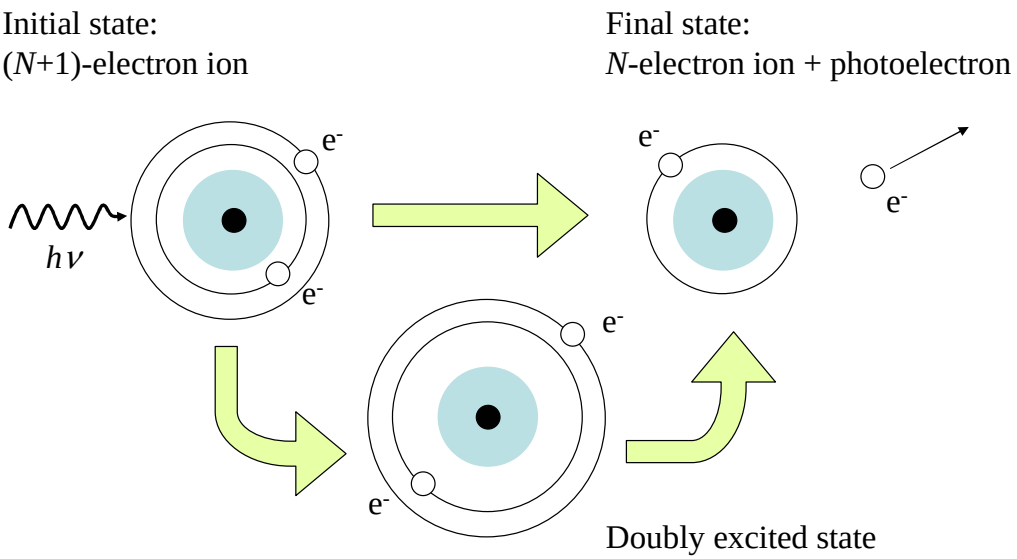

Figure 2.1. The photoionization process. It goes either straight to the final ionized state or passes an intermediate excited state.

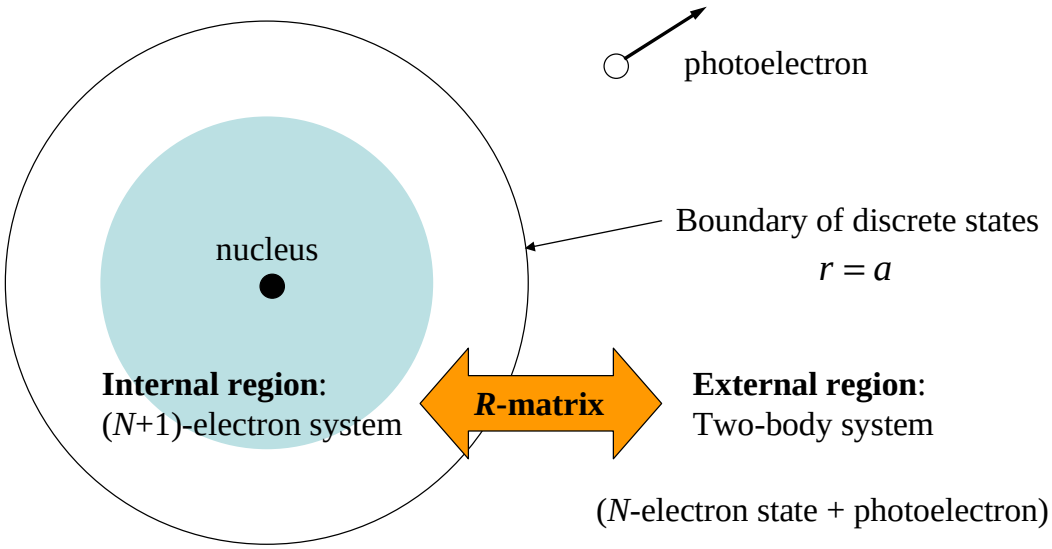

Figure 2.2. The *R*-matrix theory divides the configuration space into the internal region where all exchange terms of the N+1 electrons are included, and the external region where the system is simplified as a two-body system.

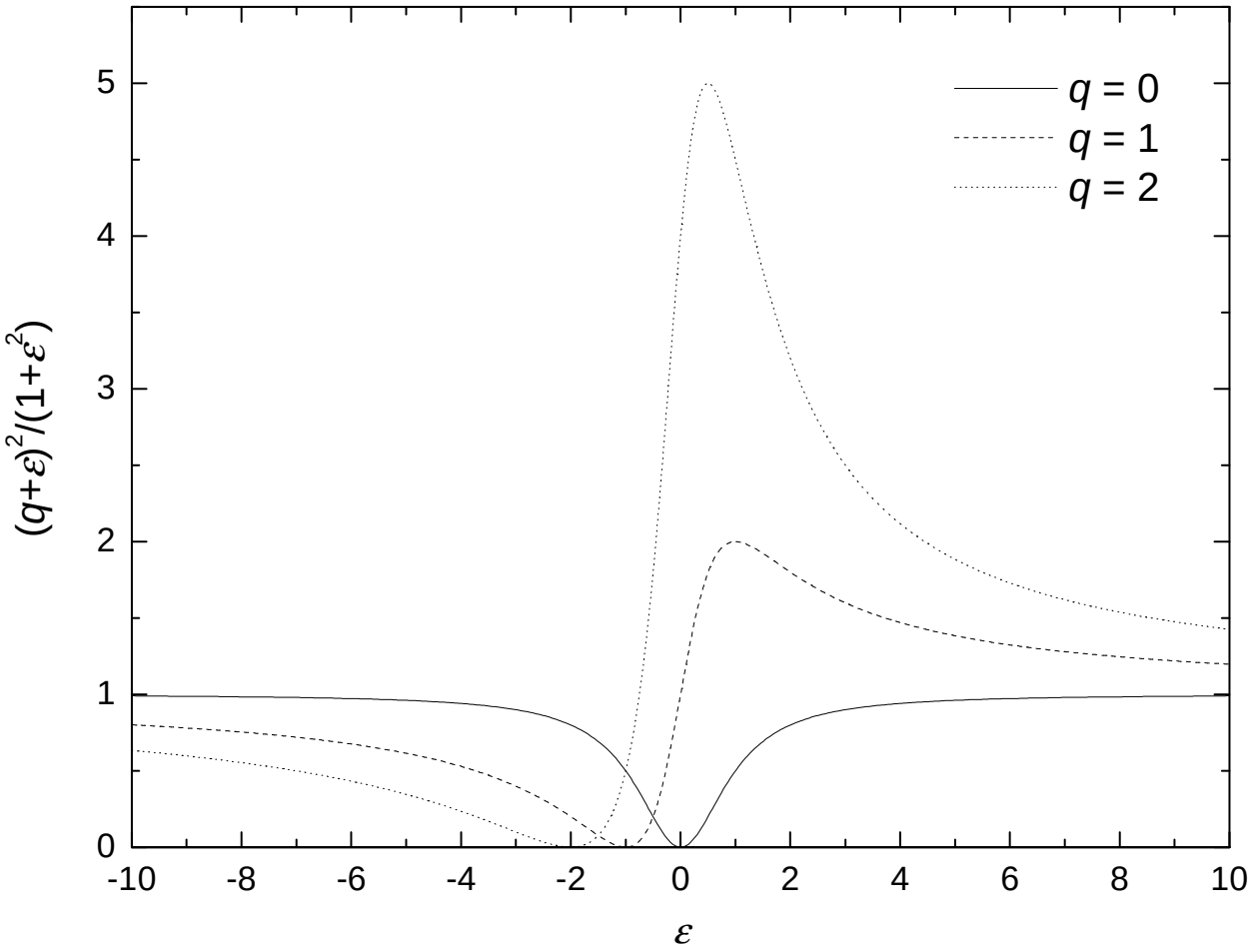

Figure 2.3. The Fano profile with different q values. The $q = 0$ (solid) curve shows a symmetric (downward) peak, and the $q = 1$ (dashed) curve shows an asymmetric peak.

3. METHOD OF CALCULATIONS

The main computational tools in this work are the CIV3 code [33] to generate the discrete wave functions and energy levels, the modified RMATRX1 code [27] (including the *LS* and BP calculations) to calculate the cross sections, and the QB program [35] to characterize the resonances using the eigenphase sum. Figure 3.1 shows the programs that we used in the present work and the workflow through them. In separate sections, we discuss in detail the use of these programs and how we optimized the calculations to maintain both the accuracy of results and the efficiency of the processes.

3.1. CIV3 Program

3.1.1. Introduction

The CIV3 program, developed by Hibbert [33], is a package to construct configuration interaction (CI) wave functions and energies, and to calculate electric-dipole oscillator strengths. The job of CIV3 in our present work is to generate the radial functions of the single-electron orbitals of the *N*-electron target states for us to feed into the *R*-matrix program.

As introduced in Chapter 2, the CI expansion of the total wave function is

$$\Psi^{LS} = \sum_{i=1}^{M} b_i \phi_i^{LS} \tag{3.1}$$

where ϕ_i^{LS} are the configurations constructed by coupling the single-electron orbitals in a way to keep the total $\boldsymbol{L}$ and total $\boldsymbol{S}$ common to all configurations, as indicated by *LS* on both sides of the equation. We choose *M* to be large enough to cover all the non-negligible configurations contributing to Ψ^{LS}. Each orbital $o_{nlm}(\vec{r}, m_s)$ is a product of a radial function $P_{nl}(r)$, a

spherical harmonic $Y_l^m(\hat{r})$, and a spin function $\chi(m_s)$, as described in Section 2.2.2. The coefficients b_i in Eq. (3.1) are determined by the diagonalization of the *N*-electron Hamiltonian whose elements are

$$H_{ij} = \left\langle \phi_i^{LS} \middle| H \middle| \phi_j^{LS} \right\rangle, \qquad i, j = 1, \ldots, M \tag{3.2}$$

and we can write the *j*th eigenvector as

$$\Psi^{(j)LS} = \sum_{i=1}^{M} b_i^{(j)} \phi_i^{LS} \tag{3.3}$$

where *j* goes up to *M*. The respective eigenvalues $E^{(j)}$ are

$$\left\langle \Psi^{(j)} \middle| H \middle| \Psi^{(k)} \right\rangle = E^{(j)} \delta_{jk} . \tag{3.4}$$

The condition

$$E^{(j)} \geq E_{\text{exact}}^{(j)} \tag{3.5}$$

must be true since in general the truncated set ϕ_i^{LS} does not form a complete basis set.

The condition Eq. (3.5) allows us to find an approach to optimize the orbitals as we choose the best set of $P_{nl}(r)$ to minimize $E^{(j)}$, where the $E^{(j)}$ now are viewed as the variational functionals of $\{P_{nl}(r)\}$.

The radial functions are represented in Slater-type format as

$$P_{nl}(r) = \sum_{j=1}^{k} C_{jnl} r^{I_{jnl}} \exp(-\zeta_{jnl} r), \qquad n \geq l+1 \tag{3.6}$$

with the orthonormality condition

$$\int_0^\infty P_{nl}(r) P_{n'l}(r) \mathrm{d}r = \delta_{nn'}, \tag{3.7}$$

where C_{jnl} are real numbers, ζ_{jnl} are positive real numbers, and I_{jnl} are integers. If $k = n-1$, for a fixed set of $\{I_{jnl}, \zeta_{jnl}\}$, the coefficients C_{jnl} are uniquely determined by Eq. (3.7). If $k > n-1$, we can choose some or all of the parameters to be variational parameters. The case of $k < n-1$ is simply forbidden by Eq. (3.7).

3.1.2. The computational setup

In the present work to construct the 3-electron target state wave functions, 9 configurations were considered. They are $1s^2 2s\ ^2S^e$, $1s^2 2p\ ^2P^o$, $1s^2 3s\ ^2S^e$, $1s^2 3p\ ^2P^o$, $1s^2 3d\ ^2D^e$, $1s^2 4s\ ^2S^e$, $1s^2 4p\ ^2P^o$, $1s^2 4d\ ^2D^e$, and $1s^2 4f\ ^2F^o$. A fixed core of $1s^2$ effectively portrays the common part of the configurations because the present consideration of ion selection and energy range allows only negligible inner shell excitation or ionization.

As a general rule in our work, each *nl* orbital is optimized by varying its parameters to minimize the corresponding state energy. For example, to optimize 3*s* orbital, we take two configurations, $1s^2 2s\ ^2S^e$ and $1s^2 3s\ ^2S^e$, as basis, where 1*s* and 2*s* are known functions (they are better fixed before 3*s* to reduce the chance of divergent outcome, although the program offers the option to vary more than one orbital at a time), and only 3*s* is to be determined. Then we calculate the radial integrals of Eq. (3.2) and diagonalize the 2×2 Hamiltonian to obtain the eigenvalues $E^{(1)}$ and $E^{(2)}$ (with $E^{(1)} < E^{(2)}$). $E^{(2)}$ is the quantity that we try to minimize when varying the parameters of 3*s* because $1s^2 3s\ ^2S^e$ corresponds to, although not exactly, the higher energy state. For another example, to optimize 4*p* orbital, we just take $1s^2 2p\ ^2P^o$, $1s^2 3p\ ^2P^o$, and $1s^2 4p\ ^2P^o$ as basis and repeat the procedure until $E^{(3)}$ is minimized. Note here that only the configurations of the same *L* have to be included as basis since the radial integral is zero between states of different *L*.

In each ion, we took the 1*s* and 2*s* radial functions from the HF calculations by Clementi and Roetti [50] or Weiss [51] depending on the availability. For other orbitals, the orbitals of each l value were optimized sequentially from low n to high n. Taking p orbitals ($l=1$) for example, P_{2p} was given initially by

$$P_{2p} = C^0_{2p,1} r e^{-\zeta^0_{2p,1} r}, \tag{3.8}$$

where we have applied $k = n - l$ condition to the form in Eq. (3.6). The program generated the iterations from $\left(C^0_{2p,1}; \zeta^0_{2p,1}\right)$ and updated the coefficients until they converged to the (uniquely) optimized values $\left(C_{2p,1}; \zeta_{2p,1}\right)$. Thus P_{2p} was determined. Then for

$$P_{3p} = C^0_{3p,1} r e^{-\zeta^0_{3p,1} r} + C^0_{3p,2} r^2 e^{-\zeta^0_{3p,2} r}, \tag{3.9}$$

we set the starting coefficients $\left(C^0_{3p,1}, C^0_{3p,2}; \zeta^0_{3p,1}, \zeta^0_{3p,2}\right) = \left(C_{2p,1}, 0; \zeta_{2p,1}, \zeta_{2p,1}\right)$ (where $C_{2p,1}$ is 1 since 2*p* had only one term) and went through the iteration process to get the final coefficients $\left(C_{3p,1}, C_{3p,2}, \zeta_{3p,1}, \zeta_{3p,2}\right)$. Then again for 4*p*, the coefficients of the first two terms were taken from the resultant 3*p* orbital, leaving $C^0_{4p,3} = 0$ and $\zeta^0_{3p,3} = \zeta^0_{3p,2}$. In our case, 4*p* was the highest *p* orbital in this procedure; if it was not, we would have repeated it up to the desired highest *np*. If the calculation did not converge for some orbital, which rarely happened, we raised k by 1 (adding one more term in Eq. (3.6)) and tried the whole process again, and so on and so forth until it converged.

In Appendix B, we present the wave function data from the CIV3 calculations, along with the HF data of 1*s* and 2*s* orbitals, for all the ions in this study. These wave functions are what we fed into the *R*-matrix calculation.

3.2. RMATRX Program

3.2.1. Module STG1

The whole RMATRX package in use in the present work was the modified version by Badnell in 2002 [27] based on Berrington's package [31].

The main tasks in the first stage of *R*-matrix program (RMATRX STG1) are to calculate the continuum functions, defined in Eq. (2.35), and to calculate the radial integrals as preparation for constructing the Hamiltonian matrix in the next stage. Three different types of radial integrals are done here: the one-electron, two-electron, and multipole radial integrals. The one-electron radial integral is to evaluate the single variable integral of the one-electron operator

$$h = -\frac{\mathrm{d}^2}{\mathrm{d}r^2} + \frac{l(l+1)}{r^2} - \frac{2Z}{r} \tag{3.10}$$

between any two radial functions, which can be either or both bound or continuum. The two-electron radial integral is written as

$$R^k(n_1l_1, n_2l_2, n_3l_3, n_4l_4) = \int_0^{r_a} \mathrm{d}r_1 \int_0^{r_a} \mathrm{d}r_2 \; P_{n_1l_1}(r_1) P_{n_2l_2}(r_2) \frac{r_<^k}{r_>^{k+1}} P_{n_3l_3}(r_1) P_{n_4l_4}(r_2) \tag{3.11}$$

where $r_>$ and $r_<$ are the larger and the smaller ones of r_1 and r_2 respectively. For the multipole radial integrals, the velocity form and the length form are processed in separate subroutines. In the velocity form, only dipole term is included:

$$I_V(i, j) = \int_0^{r_a} U_i(r) \left(\frac{\mathrm{d}}{\mathrm{d}r} + \frac{\alpha}{r} \right) U_j(r) \mathrm{d}r \tag{3.12}$$

with

$$\alpha = \begin{cases} l_j & \text{if } l_j = l_i + 1 \\ -l_i - 1 & \text{if } l_j = l_i - 1 \end{cases}, \tag{3.13}$$

while in the length form, the integral of order k is given by

$$I_L^k(i,j) = \int_0^{r_a} U_i(r) r^k U_j(r) \mathrm{d}r \,, \tag{3.14}$$

where the order k taken into account is up to some maximum value defined by the input parameter.

In the present calculation, all the bound orbitals were provided in the input as Slater-type functions, which we optimized using CIV3 program. This data is given in Appendix B.

3.2.2. Module STG2

In the second stage (RMATRX STG2), first, the target state Hamiltonian matrix in Eq. (2.27) is diagonalized, which means the target (bound) state wave functions are obtained. Then the Hamiltonian matrix elements (Eq. (2.33)) and the dipole matrix elements (Eq. (2.83)) for the (N+1)-electron states in the internal region are constructed, and the long-range potential coefficients (Eq. (2.58)) are evaluated.

In the input to STG2, all the configurations needed to build the target states and the (N+1)-electron states are listed separately as the complete basis for the system, and all the target states and (N+1)-electron states are specified in $LS\pi$ terms here. In our case, the 9 configurations in Section 3.1.2 were used in the target states, and there were 81 4-electron configurations for initial and final states, which were established by assigning the photoelectron an arbitrary orbital ranging from 2*s* to 4*f*, and attaching it onto the 9 target configurations. In brief, we considered 14 $LS\pi$ terms, ${}^{(1,3)}(S,P,D,F)^{\mathrm{e}}$ and ${}^{(1,3)}(P,D,F)^{\mathrm{o}}$, for ($N$+1)-electron states whether being used in the initial or the final states.

If the calculation is nonrelativistic, each of the 14 $LS\pi$ terms constitutes a specific Hamiltonian matrix and a specific dipole matrix, and it will go on to the next stage to carry out an independent calculation for the initial and final states, and obtain the cross section for a given

photon energy. On the other hand, if the calculation is relativistic (Breit-Pauli), it will first go through the recoupling process from *LS*-coupling to pair-coupling as described in Section 2.4, in the optional stage RMATRX RECUPD (also called RMATRX STGJK). The Hamiltonian matrices, the long-range potential coefficients, and the dipole matrices that are defined in STG2 are transformed into the new coupling scheme where the matrices are cut into the blocks of different $J\pi$ terms. Each Hamiltonian block, which is specified by a $J\pi$ now, is further diagonalized where the relativistic corrections in Eq. (2.91) for the Hamiltonian also come in. We will call the nonrelativistic *R*-matrix calculation "*LS* calculation" as an abbreviation.

3.2.3. Module STGH

The main tasks in RMATRX STGH are to diagonalize the (N+1)-electron Hamiltonian in the continuum basis, and to process the dipole matrices in the new form where the Hamiltonian is diagonal. The program receives the matrices created in either *LS*-coupling in the nonrelativistic calculation or pair-coupling in BPRM. The transformation of the dipole matrices is shown in Eq. (2.82). The $\boldsymbol{D}$ matrix and the $\boldsymbol{M}$ matrix can be in length form or velocity form.

3.2.4. Module STG4

This stage deals with the external region wave functions. Eq. (2.59) is solved here where the *R*-matrix is matched on the $r=a$ boundary, and all the photoionization and collision observables are calculated. Subprograms used include STGB, STGF, and STGBF; STGB and STGF consider the total wave functions with bound state and continuum state boundary conditions, respectively, and STGBF calculates the photoionization (or collision) data.

In the present work, for the nonrelativistic calculation, we picked the $^1S^e$ ground state and the $^3P^o$ metastable state as our initial bound states. Thus, the photoionization transitions allowed by the selection rules were

$$1s^2 2s^2\left(^1S^e\right)+h\nu \rightarrow \left[1s^2 nl+\mathrm{e}^-(kl')\right]\left(^1P^o\right) \tag{3.15}$$

for the ground state and

$$1s^2 2s2p\left(^3P^o\right)+h\nu \rightarrow \left[1s^2 nl+\mathrm{e}^-(kl')\right]\left(^3S^e,^3P^e,^3D^e\right) \tag{3.16}$$

for the metastable state. In BPRM, the corresponding transitions, in *LSJ* terms, were

$$1s^2 2s^2\left(^1S_0^e\right)+h\nu \rightarrow \left[1s^2 nl+\mathrm{e}^-(kl')\right]\left(^1P_1^o\right) \tag{3.17}$$

for the ground state and

$$1s^2 2s2p\left(^3P_{0,1,2}^o\right)+h\nu \rightarrow \left[1s^2 nl+\mathrm{e}^-(kl')\right]\left(^3S_{0,1}^e,^3P_{0,1,2}^e,^3D_{1,2,3}^e\right) \tag{3.18}$$

for the metastable state. The $^3P^o$ metastable state in *LS* case splits to three $^3P_J^o$ states in BPRM. Notice that in BPRM, the transitions are only specified by $J\pi$ terms, which means that only $0^e \rightarrow 1^o$ was defined in the ground state transition, and only $0^o \rightarrow 1^e$, $1^o \rightarrow \left(0^e,1^e,2^e\right)$, and $2^o \rightarrow \left(1^e,2^e,3^e\right)$ were defined in the metastable state transitions; in each $J\pi$ term, the contributions from the full range of the *LS* terms were considered. Each of the four transitions generated an individual cross section as a function of photon energy.

3.3. QB Program

The QB program [35] is the tool for the analysis of resonances in photoionization and collision theory, which is based on QB method [34] of Quigley and Berrington. The resonance energies (position) E_r, the widths Γ, and the effective quantum numbers ν are calculated in this program.

Let us look at the $n_o \times n_o$ *K*-matrix defined in Eq. (2.60). Diagonalization of $\boldsymbol{K}$ gives n_o eigenvalues λ_i. This can be easily written as

$$\boldsymbol{KX} = \boldsymbol{X\lambda}, \tag{3.19}$$

where $\boldsymbol{\lambda}$ is the diagonal matrix with diagonal elements λ_i. The eigenphase of each i is then defined as

$$\delta_i = \tan^{-1}\lambda_i, \qquad i = 1, \cdots, n_o, \tag{3.20}$$

and the eigenphase sum δ is defined as the sum of δ_i over all open channels. Theoretically, δ will increase by π radians at the energy of a resonance (remember $\boldsymbol{K}$ is a function of total energy E, as well as δ_i and δ). In practice, since the width of a resonance cannot be infinitesimal, the finite width smooths out $\delta(E)$ around the resonance; thus, the resonance position is determined to be where $\delta(E)$ changes most rapidly as a function of E. Once we find $\delta' \equiv \mathrm{d}\delta/\mathrm{d}E$ (where we use a prime ($'$) to denote the derivative with respect to E), the local maxima of it are the resonance positions.

The Breit-Wigner form [52] of $\delta(E)$ is described by

$$\delta(E) = \bar{\delta}(E) + \tan^{-1}\frac{\Gamma/2}{E_r - E}, \tag{3.21}$$

where $\bar{\delta}$ is the background, and Γ and E_r are the width and the energy of the resonance. Assuming the background varies slowly enough with E ($\bar{\delta}' << 1/\Gamma$), the differentiation of Eq. (3.21) gives

$$\Gamma = \left.\frac{2}{\delta'(E)}\right|_{E=E_r}, \tag{3.22}$$

which relates the resonance width to the derivative of eigenphase sum. In order to get $\delta'(E)$, first we notice the differentiation of Eq. (3.19) gives

$$\boldsymbol{\lambda}' = \boldsymbol{X}^T \boldsymbol{K}' \boldsymbol{X} \ . \tag{3.23}$$

Defining the *Q*-matrix as

$$\boldsymbol{Q} = \left(-\boldsymbol{s}' + a\boldsymbol{R}'\dot{\boldsymbol{s}} + a\boldsymbol{R}\dot{\boldsymbol{s}}'\right) + \left(-\boldsymbol{c}' + a\boldsymbol{R}'\dot{\boldsymbol{c}} + a\boldsymbol{R}\dot{\boldsymbol{c}}'\right)\boldsymbol{K} \ , \tag{3.24}$$

and following Eq. (2.67), $\boldsymbol{K}'$ is given by

$$\boldsymbol{K}' = \boldsymbol{B}^{-1}\boldsymbol{Q} \ . \tag{3.25}$$

Combining Eq. (3.23), Eq. (3.25), and the differentiation of Eq. (3.20), we obtain $\delta'(E)$.

Since *K*-matrix is determined by the boundary condition on the final state wave function at any specific final energy *E*, in the QB program, the user specifies the symmetry only of the final state but not the initial state. Each resonance represents the interaction strength between a bound (excited) state and the continuum state in the final state total wave function. In the present calculation, only the 1^o final state is populated from the ground 0^e state, i.e., the $0^e \rightarrow 1^o$ transition. For the metastable state calculation, the transitions $0^o \rightarrow 1^e$, $1^o \rightarrow \left(0^e, 1^e, 2^e\right)$, and $2^o \rightarrow \left(1^e, 2^e, 3^e\right)$ are all allowed. Since the differences among the various final *J*-states are small, we analyze the resonances of the 1^e final state, which can be reached from each of the metastable state. Also note that in the present study, the bound state energy of the 0^o state was taken as the reference energy for the conversion between ν and E_r of the resonances for all the metastable states.

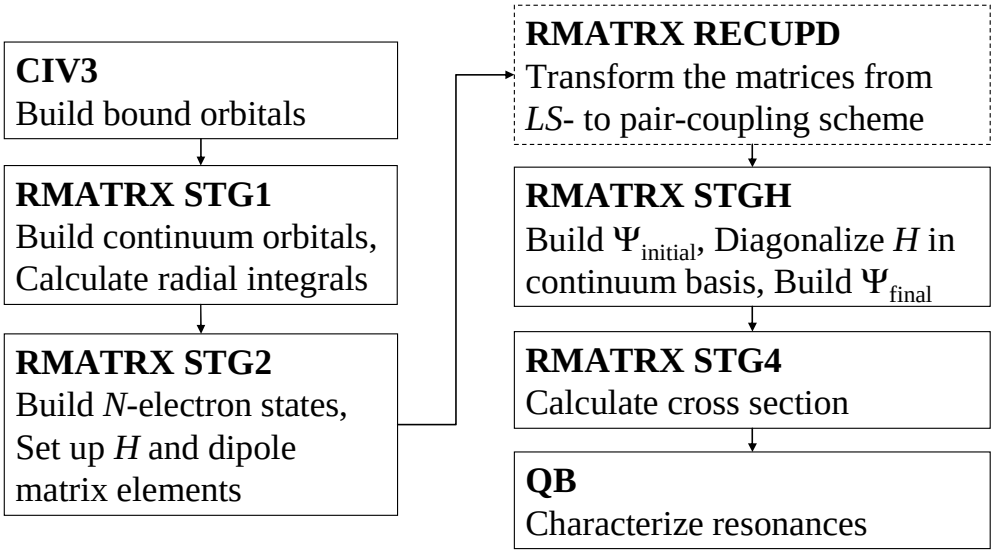

Figure 3.1. The flowchart of the calculations. The stage RMATRX RECUPD, enclosed by the dashed-lined box, is used only for BPRM but not for nonrelativistic calculations.

4. RESULTS

4.1. Energy Levels

The comparison between our theoretical and the experimental energy levels, including target state and initial state energies, is a good indication of the quality of our wave functions. We show the target state energies (relative to the $1s^2 2s_{1/2}$ ground state energy) from $1s^2 2p_{1/2}$ to $1s^2 2f_{7/2}$ of all 14 ions in Table 4.1, where the experimental data is from the database of National Institute of Standards and Technology (NIST) [53]. Very good agreement between our values and the experiments can be seen throughout the table. The higher percentage errors usually occur in low n states such as $2p$ state, but among the same n states, higher l states have bigger errors. The average error of all levels in one ion is highest in Be as 0.56%, and the error goes down generally as the ion becomes heavier, where it shows the lowest error in Ti^{+18} as 0.05%. Seven out of the totally of 14 ions have the error less than 0.1%. From this estimate, it appears that the target state wave functions are built very precisely.

To check the quality of our (N+1)-electron initial state wave function, we compare our ionization energies from the initial state of each set of $J\pi$. In Table 4.2 and Table 4.3, we list the ionization energies of all ions from $^1S_0^e$ ground state and from $^3P_0^o$ metastable state respectively. The differences among $^3P_0^o$, $^3P_1^o$, and $^3P_2^o$ are usually less then one-thousandth of their values. The largest splitting of the ionization energies of these $^3P_J^o$ metastable states, in Fe^{+22}, is 1.15 Ryd, which is less than 1% of its $^3P_0^o$ state ionization energy at 140.411 Ryd. For this reason, the list of the ionization energy of the $^3P_1^o$ and $^3P_2^o$ metastable states are omitted. Similar to the target state case, the percentage error here also shows a pattern that starts highest

in Be and drops down for heavier ions like Mg^{+8} or Si^{+10}, but differently from target state case, it now rises when *Z* goes still higher. The error of the ground state ionization energy is 0.44% in Be as the highest and 0.01% in Si^{+10} as the lowest. The error of the metastable state ionization energy is 0.62% in Be as the highest and 0.01% in Mg^{+8} as the lowest. The possible reason for the descending error along *Z* is that the orbitals are asymptotically hydrogenic when *Z* is large, and in the CIV3 program, the hydrogenic orbital is perfectly described by the Slater form. That the error rises again toward higher *Z* might be because of the size of the nucleus. In the calculation, we take the nucleus as a point charge in the Coulomb potential; in reality, the nucleus spreads out in space and affects the distribution of the electrons. As *Z* increases, the electrons are drawn near to the nucleus, and the overlap between the nucleus and the electrons distorts the wave functions more significantly. Another reason of the rising error with *Z* might be relativistic effects. Although in BPRM the Hamiltonian includes the relativistic terms, the orbitals that we created in CIV3 and fed into *R*-matrix were not relativistic, as they would be if we started with Dirac equation.

To sum up the comparison between our energy levels and the NIST values, we have demonstrated that our calculation is in very good agreement with experiment. The average error of the target state energies is 0.18%, and the average error of the ionization energies of ground and metastable initial states are 0.13% and 0.17%, respectively, over all 14 ions. These evince the high quality of our total wave functions in both target states and initial state.

4.2. Ground and Metastable State Cross Sections

The cross sections of the $^1S_0^e$ ground state and the $^3P_0^o$, $^3P_1^o$, and $^3P_2^o$ metastable states of the 14 ions were calculated separately, in the energy range from the ionization threshold to the $1s^2 4f_{7/2}$ threshold using the BPRM program. A constant photon energy interval was set for

each case to make an even distribution of a total of 10^5 energy points over the range; except a few ions for which we increased the energy points to match the other results with which we compared our results, which will be discussed in the next two sections. Figure 4.1 and Figure 4.2 are respectively the ground and the metastable state cross sections. The length and velocity gauge agree very well in the cross sections; the percentage difference between them is at most a few percent, which further suggests the wave functions are quite accurate. With this agreement between the two gauges, only the results in the length form are presented in our report. For the metastable state, since the three $^3P_J^o$ cross sections are almost identical, we show the statistical average (1:3:5) of the $^3P_0^o$, $^3P_1^o$, and $^3P_2^o$ cross sections in the picture. For each ion, the cross sections of ground and metastable states are shown on the same scale so that we can easily compare the results. Some general features of the evolution of the cross sections with Z are reported here.

Just above the ionization threshold, the 2*pns* and 2*pnd* resonances dominate. These resonances are wide enough to hide at least a large portion of the background cross sections. At the middle energy range of each picture the resonances converge to n=3 thresholds. Here the resonances are significantly narrower, but the resonance profiles at the beginning of each series are clearly seen, as they provide rich information for us to investigate the structure of the system and the properties of the process. At still higher energy range, where the resonances converge to n=4 thresholds, the resonances are very narrow and short, whose characteristics will not be seen without a considerable enlargement of the cross section profile. The interesting fact is that the overall ground and metastable state cross sections are alike, especially for high-Z ions. Quantitative similarity of them implies that there is a connection between these continua with opposite parities and with different spin-multiplicities.

When we take a closer look at the evolution of the cross sections of both states along the sequence, some general comments on the background cross section, the thresholds, and the resonances can be drawn. We will report this analysis in Chapter 5.

4.3. Cross Sections Compared with Experiments

In this section we show the total cross sections of the first five ions, Be, B^{+1}, C^{+2}, N^{+3}, and O^{+4}, for which the measured data is available. Each experiment measured the absolute cross section of the designated ion in a mixture of states. Each experimental group reported the fractions of each of these states in the mixture. We followed the information provided for the fractions and obtained the total cross section as the linear summation over the cross sections of the individual states.

4.3.1. Be

For the neutral Be atom two experiments in separate energy ranges have been reported, both performed at the University of Wisconsin Synchrotron Radiation Center (SRC). Wehlitz *et al* [54] measured the ground state cross section from the ionization threshold at 9.3227 eV to the 2*p* threshold at 13.277 eV with energy step (ΔE) 20 meV below, 5 meV beyond, 12.60 eV and monochomator bandpass of 12 meV, which we take as the full width at half maximum (FWHM) when convoluting our theoretical cross section calculated with energy step ΔE = 68 μeV. Figure 4.3 shows the present BPRM and nonrelativistic *LS R*-matrix cross sections along with the experimental results from 9.2 eV to 13.3 eV. From the comparison of the BPRM and *LS* results it is clear that relativistic effects in the photoionization of neutral beryllium are negligible. The present theoretical results show excellent agreement with experiment below about 12.5 eV, but the experimental peaks seem to be truncated, compared to theory, at higher energy. It is evident,

however, that the positions of the resonances are in excellent agreement over the whole range. We can think of no explanation for the lower resonances in the series being more accurate than the higher members, so this could be an experimental problem.

In the higher energy range, near the 3*s* and 3*p* thresholds, SRC measurements were made by Olalde-Velasco *et al* [55] with energy step 15 meV from 16 eV to 19.5 eV and 5 meV beyond 19.5 eV. With our energy step ΔE = 68 μeV, we convolute our result with FWHM = 27.5 meV and FWHM = 7.5 meV, below and beyond 19.5 eV respectively to compare with experiment. BPRM and nonrelativistic cross sections as well as the measurement are shown in Figure 4.4. Just as in the lower energy range, the difference between BPRM and nonrelativistic results is negligible. The overall background cross section in the calculation is about 0.6 Mb higher than the measurement, and there is a 0.1 eV energy shift between calculation and measurement.

4.3.2. B^+

The B^+ calculation is compared with the measurement by Schippers *et al* [56] at Advanced Light Source (ALS) at Lawrence Berkeley National Laboratory (LBNL). The measurement was done with ΔE = 4 meV from 22.50 eV to 31.26 eV, whereas our calculation was performed with ΔE = 13.6 μeV. In the calculation, we assume that the initial beam has 71% $^1S^e_0$ ground state ions and 29% $^3P^o_1$ metastable state ions [56]. The calculations and the measurement are shown in Figure 4.5. Both calculations are convoluted with FWHM = 25 meV. Below the ground state ionization threshold at 25.091 eV (calculated result), the cross section is purely metastable photoionization. The theoretical threshold for metastable state is 20.44 eV in the present calculation, which the experiment could not identify because the photon flux was too low. The difference between the BPRM result and the nonrelativistic result is clearly the splitting of the resonances in this region. BPRM clearly shows the peaks that are missing in

nonrelativistic cross section. The BPRM result matches the measurement well except for an overall energy shift of about 0.05 eV.

4.3.3. C^{+2}

In the C^{+2} ion, the experiment was conducted by Müller *et al* [57] at ALS. It was done with ΔE = 4 meV from 40.84 eV to 56.98 eV. We assume that 60% of the ions were in the $^1S_0^e$ ground state and 40% in the $^3P^o$ metastable state in the initial ion beam; specifically 30% $^3P_0^o$ and 5% each of $^3P_1^o$ and $^3P_2^o$ [57]. The calculations used an energy step size ΔE = 12.2 μeV and are convoluted with FWHM = 30 meV. As shown in Figure 4.6, similar to the B^+ case, the splitting is the biggest difference between the two calculations. Compared with the experiment, the experimental threshold energies 41.39 eV and 47.89 eV are higher than the present values 41.28 eV and 47.81 eV for metastable state and ground state respectively. The theoretical background cross section is a bit higher than experimental cross section near the $2p_{3/2}$ threshold of $^1S_0^e$ ground state at 55.8987 eV. Other than that, our BPRM result matches the experiment well in all resonance positions and widths.

4.3.4. N^{+3}

Experimental work on N^{+3} ions was performed by Bizau *et al* [58] at ASTRID at the University of Aarhus. They obtained the cross section with ΔE = 100 meV in the range 63.00 eV to 90.00 eV. In our calculation, we used ΔE = 13.6 μeV and convoluted the result with FWHM = 230 meV. The fractions of $^1S_0^e$ ground state and $^3P^o$ metastable state are assumed to be 65% and 35% respectively [58]; in the absence of any more detailed information on the excited intital states, we assumed that the three metastable states were populated statistically. In Figure 4.7, it is

seen that the difference between BPRM and the nonrelativistic results is that the peak heights and strengths in the metastable region below 79 eV are larger in the BPRM case. This is likely because the inclusion of relativistic effects in the BPRM calculation opens photoionization channels that are forbidden in the nonrelativistic *LS* case, thereby increasing the resonance oscillator strengths. Comparing our BPRM calculation with experiment, we find that in the low energy range where only the metastable state contributes, the background agrees well but the resonances are slightly weaker than experiment, but much closer than the nonrelativistic results. In the higher energy range where ground state photoionization dominates, the experimental cross section is very noisy and it is difficult to pick out the higher resonances, but the first few show reasonable agreement. The nonresonant background cross sections are in good agreement in the lower energy region where only the metastables contribute, but theory is a bit higher than experiment at the higher energies where ground state photoionization dominates.

In addition, there has been some recent high-resolution experimental work in very narrow energy ranges reported [59]; the region of the metastable thresholds, and the region of the 2*p*5*p* resonances. Apart from a small energy shift, our calculations, convoluted with the experimental resolution (not shown), show excellent agreement.

4.3.5. O^{+4}

The measured cross section was obtained by Champeaux *et al* [60] at SuperACO at LURE in France with ΔE = 56.4 meV in the range from 99.60 eV to 129.75 eV. In the calculation, we had an energy step size ΔE = 13.6 μeV and it was convoluted with the experimental FWHM = 250 meV. The experiment reported fractions of 50% $^1S_0^e$ ground state ions and 50% $^3P^o$ metastable state ions in the beam; since no breakdown of the metastable part of the beam was reported, we assumed a statistical distribution as in the N^{+3} case, discussed

above. Similar to N^{+3} ions, in Figure 4.8 the BPRM cross section shows stronger resonances than those in the nonrelativistic one in the region of the spectrum due to metastable photoionization only. The reason is presumably the same as that in the N^{+3} case. The comparison between our calculation and the experiment is also similar to the N^{+3} case. The background and resonance positions match well with experiment in the metastable region, but it is much harder to read the resonance information in the ground state region in the experiment.

4.4. Cross Sections Compared with Other Calculations

The details of Opacity Project (OP) are described by Seaton [28]; the photoionization of Be-like ions was studied by Tully *et al* [61]. OP includes atomic data of 15 isoelectronic ions up to Fe^{+22} based on the nonrelativistic *R*-matrix calculation. To give the flavor of the comparison of the OP results with the present BPRM data, and how it changes along the isoelectronic sequence, the comparison for Be, Ne^{+6}, Ar^{+14} and Fe^{+22} are shown in Figure 4.9 to Figure 4.12 respectively for both ground and metastable states; our BPRM results are the statistical average of the three $^3P^o$ metastable states. For Be, in Figure 4.9, the ground state comparison shows that the OP ground state threshold energy is a bit lower than the BPRM result and, thus, lower than the experimental (NIST) value, by about 0.1 eV. For the metastable state, the OP threshold is too low by considerably more than that. Consequently, the OP metastable cross section at threshold is about 10% too high. In addition, careful comparison reveals that the OP resonances are at somewhat different energies than the present BPRM results. Since the latter are in good agreement with experiment, as detailed above, it is evident that the OP calculation is lacking in this respect as well. Most importantly, however, is that the energy mesh used in the OP calculation is seen to be much too coarse to correctly reproduce the resonances in both ground

and metastable states. This results in much of the resonance oscillator strength being absent from the OP cross sections, as seen in Figure 4.9.

For Ne^{+6}, shown in Figure 4.10, the comparison is qualitatively similar, but the discrepancies are quantitatively greater, owing to the fact that relativistic interactions are more important in Ne^{+6} than in neutral Be; for Ne^{+6}, the OP thresholds are too low by several eV and the 2p thresholds are seen to be even worse, especially for the ground state. Further, owing to the energy step size, the higher 2*pnl* resonances are absent from the OP results.

Going up to Ar^{+14}, Figure 4.11, the comparison is seen to be dramatically worse. The OP thresholds are off by of the order of 20 eV. In addition, the resonances are almost unobservable; and those that are seen are at rather incorrect energies. Only the OP background, nonresonant cross section is reasonably good in this case. However, we note that the OP background cross section is not significantly better than the results of a central-field Hartree-Slater (HS) calculation which give a threshold value of the ground state cross section of about 0.11 Mb [62], in good agreement with these results.

For Fe^{+22}, Figure 4.12, the comparison is similar to the Ar^{+14} case, but even further apart. The OP thresholds are so far off that the whole OP resonance region converging to 2*p* ranges from 137 Ryd to 142 Ryd, but it ranges from 143 Ryd to 148 Ryd in the present work, and there no overlap between these regions between the two calculations. The OP thresholds are off by ~ 100 eV! Again, the OP background cross section is reasonably accurate, but so is the simple HS result of the compilation of Ref. [62].

Several photoionization calculation of lower members of the isoelectronic sequence, Be [63][64], B^{+} [65][66], and C^{+2} [67][68], have been calculated for both ground and metastable states using a variational *R*-matrix method (VRM) [69]. In these calculations, the $1s^2$ core is

replaced by an effective potential which is optimized by comparison of binding energies with experiment, and the wave functions of the two outer electrons are solved by the Schrödinger equation. The basic differences between this method and the present calculation are: the variational *R*-matrix calculations are nonrelativistic while ours include relativistic effects; also, that method is semi-empirical, based on optimizing the potential due to inner-shell electrons to fit experimental energies, while ours is purely *ab initio*. In Figure 4.13 to Figure 4.15 a comparison of the present BPRM photoionization cross sections with the variational *R*-matrix results are shown for Be, B^+, and C^{+2} ions, respectively; all cross sections presented are in length gauge since the length and velocity results essentially coincide in both calculations. Our cross sections are generally in good agreement with the variational *R*-matrix results, but there are a few differences in all three cases. First, both our $^1S^e_0$ ground state and $^3P^o$ metastable state ionization thresholds are lower than the variational *R*-matrix values. Second, the inclusion of relativistic effects opens more ionization channels, which cause splitting of some of the resonances, as seen in the figures. Third, there are differences in the shapes of the resonances at the beginning of some Rydberg series. For example, in Figure 4.13, the thin resonance near 11.8 eV is seen to have a different shape in the two calculations which amounts to almost a vertical flip, and a similar flip occurs around 23.2 eV in B^+. This means in the analysis of Beutler-Fano profile of resonance, the *q* value has opposite sign in the two calculations, which implies either the discrete or the continuum final state at the corresponding energy has a phase difference between the calculations.

There have also been calculations of the photoionization of C^{+2} [70][71], N^{+3} [70] and O^{+4} [72] using orbitals obtained with the SUPERSTRUCTURE code [73] and nonrelativistic *R*-matrix to calculate the cross sections, except for C^{+2} where a relativistic calculation was also done. Figure

4.16 to Figure 4.18 show the comparison of our BPRM cross sections with the previous nonrelativistic results [70][72] for both ground and metastable states of C^{+2}, N^{+3}, and O^{+4} ions, respectively. The general features of the cross sections, such as the ionization thresholds, resonance positions and widths match pretty well. As seen in these figures, however, the main difference between their calculations and ours is the splitting of resonances due to relativistic effects. Note further, that the comparison of their results with our nonrelativistic cross sections (not shown) show excellent agreement, thereby indicating that these earlier calculations include the important physics, except for the relativistic effects. To emphasize this point, note that using the same methods for discrete states, but with a BPRM formulation for the continuum states, the relativistic photoionization calculation for C^{+2} was performed [72] and included both ground and metastable states [74]; the comparison with the present BPRM results are shown in Figure 4.19, where excellent overall agreement is seen, both as to resonance positions and background nonresonant cross sections. Some small differences are seen in the amplitudes and shapes of the very narrow resonances. Also, for the ground state cross section, the peaks of the Ref. [72] higher resonances of the major series are erratic, while our results are not. We attribute this to a lack of sufficient density of energy points in the neighborhood of these resonance peaks in Ref. [72]. A similar BPRM calculation [31] for O^{+4} has been performed (not shown) and the agreement with the present calculation is similar to that of the C^{+2} comparison exhibited in Figure 4.19.

BPRM calculations of the photoionization of B^{+} [56], C^{+2} [57], and N^{+3} [59] using the same discrete orbital methodology as used in the present paper have also been reported. For the B^{+} and C^{+2} cases, the results for the experimental admixture of ground and metastable states, suitably convoluted with the experimental width, are shown in Figure 4.5 and Figure 4.6

respectively. As can be seen, they are almost identical to the present BPRM results. This is hardly surprising since the two calculations used essentially the same target states, although somewhat different versions of the BPRM code [76]. The very slight differences in the results around some of the narrow resonances can be largely traced to not using enough energy points in the energy mesh to completely characterize the resonance [76]. For the case of N^{+3} [57], where many energy points are used in very narrow energy ranges, our calculated results match the previous result essentially exactly. In any case, the agreement strongly suggests that both calculations were done correctly.

Table 4.1. Energy levels (in Rydbergs) in the present work and in NIST data [53] for the Li-like target ions. All energies are relative to $1s^2 2s^2\ {}^2S^e_{1/2}$ ground state energy.

	Present	NIST	Present	NIST	Present	NIST	Present	NIST	Present	NIST
	Be Z=4		B^+ Z=5		C^{+2} Z=6		N^{+3} Z=7		O^{+4} Z=8	
$2p\ {}^2P^o_{1/2}$	0.293	0.291	0.445	0.441	0.594	0.588	0.740	0.733	0.886	0.878
$2p\ {}^2P^o_{3/2}$	0.293	0.291	0.445	0.441	0.594	0.589	0.742	0.736	0.891	0.883
$3s\ {}^2S^e_{1/2}$	0.799	0.804	1.637	1.642	2.754	2.760	4.150	4.157	5.826	5.832
$3p\ {}^2P^o_{1/2}$	0.876	0.879	1.754	1.758	2.912	2.917	4.349	4.354	6.066	6.070
$3p\ {}^2P^o_{3/2}$	0.876	0.879	1.754	1.758	2.912	2.917	4.350	4.354	6.067	6.071
$3d\ {}^2D^e_{3/2}$	0.888	0.894	1.780	1.787	2.953	2.961	4.407	4.414	6.141	6.148
$3d\ {}^2D^e_{5/2}$	0.888	0.894	1.780	1.787	2.954	2.961	4.407	4.414	6.141	6.148
$4s\ {}^2S^e_{1/2}$	1.047	1.052	2.160	2.166	3.650	3.657	5.518	5.525	7.763	7.770
$4p\ {}^2P^o_{1/2}$	1.077	1.082	2.207	2.213	3.714	3.721	5.599	5.606	7.861	7.867
$4p\ {}^2P^o_{3/2}$	1.077	1.082	2.207	2.213	3.715	3.721	5.599	5.606	7.861	7.868
$4d\ {}^2D^e_{3/2}$	1.082	1.088	2.218	2.225	3.732	3.739	5.625	5.631	7.892	7.900
$4d\ {}^2D^e_{5/2}$	1.082	1.088	2.218	2.225	3.732	3.739	5.625	5.631	7.892	7.900
$4f\ {}^2F^o_{5/2}$	1.083	1.088	2.218	2.225	3.732	3.740	5.624	5.632	7.893	7.901
$4f\ {}^2F^o_{7/2}$	1.083	1.088	2.218	2.225	3.732	3.740	5.624	5.632	7.893	7.901
	Ne^{+6} Z=10		Mg^{+8} Z=12		Si^{+10} Z=14		S^{+12} Z=16		Ar^{+14} Z=18	
$2p\ {}^2P^o_{1/2}$	1.176	1.168	1.467	1.458	1.759	1.750	2.053	2.045	2.350	2.342
$2p\ {}^2P^o_{3/2}$	1.191	1.183	1.503	1.494	1.833	1.825	2.189	2.182	2.581	2.575
$3s\ {}^2S^e_{1/2}$	10.018	10.023	15.331	15.334	21.771	21.769	29.345	29.344	38.060	38.055
$3p\ {}^2P^o_{1/2}$	10.338	10.341	15.733	15.733	22.255	22.253	29.911	29.908	38.709	38.697
$3p\ {}^2P^o_{3/2}$	10.342	10.346	15.743	15.745	22.276	22.274	29.951	29.949	38.776	38.766
$3d\ {}^2D^e_{3/2}$	10.450	10.457	15.885	15.888	22.453	22.452	30.163	30.156	39.024	39.013
$3d\ {}^2D^e_{5/2}$	10.451	10.455	15.888	15.892	22.460	22.458	30.175	30.169	39.045	39.035
$4s\ {}^2S^e_{1/2}$	13.386	13.392	20.524	20.527	29.181	29.180	39.368	39.364	51.093	51.083
$4p\ {}^2P^o_{1/2}$	13.517	13.522	20.688	20.687	29.379	29.374	39.599	39.594	51.358	51.348
$4p\ {}^2P^o_{3/2}$	13.519	13.524	20.692	20.687	29.388	29.384	39.616	39.612	51.387	51.377
$4d\ {}^2D^e_{3/2}$	13.563	13.570	20.756	20.753	29.461	29.459	39.703	39.700	51.488	51.478
$4d\ {}^2D^e_{5/2}$	13.564	13.570	20.758	20.756	29.464	29.461	39.708	39.706	51.497	51.487
$4f\ {}^2F^o_{5/2}$	13.565	13.573	20.754	20.759	29.467	29.467	39.713	39.710	51.502	x
$4f\ {}^2F^o_{7/2}$	13.566	13.573	20.755	20.760	29.468	29.469	39.715	39.712	51.507	x

	Ca^{+16} Z=20		Ti^{+18} Z=22		Cr^{+20} Z=24		Fe^{+22} Z=26	
$2p\ ^2P^o_{1/2}$	2.651	2.643	2.956	2.948	3.265	3.258	3.602	3.572
$2p\ ^2P^o_{3/2}$	3.019	3.016	3.515	3.514	4.082	4.086	4.745	4.745
$3s\ ^2S^e_{1/2}$	47.924	48.086	58.947	58.922	71.140	71.102	84.508	84.497
$3p\ ^2P^o_{1/2}$	48.657	48.648	59.764	59.739	72.043	72.005	85.515	85.460
$3p\ ^2P^o_{3/2}$	48.764	48.755	59.927	59.907	72.280	72.251	85.844	85.815
$3d\ ^2D^e_{3/2}$	49.048	49.037	60.247	60.218	72.637	72.594	86.234	86.197
$3d\ ^2D^e_{5/2}$	49.082	49.064	60.300	60.270	72.714	72.672	86.343	86.321
$4s\ ^2S^e_{1/2}$	64.368	x	79.205	79.162	95.618	95.557	113.627	113.584
$4p\ ^2P^o_{1/2}$	64.667	64.816	79.538	79.505	95.984	95.937	114.020	113.989
$4p\ ^2P^o_{3/2}$	64.711	64.865	79.604	79.576	96.080	96.040	114.156	114.135
$4d\ ^2D^e_{3/2}$	64.827	64.812	79.735	79.707	96.227	96.185	114.319	114.266
$4d\ ^2D^e_{5/2}$	64.842	64.847	79.757	79.729	96.259	96.217	114.365	114.320
$4f\ ^2F^o_{5/2}$	64.848	64.838	79.764	79.736	96.267	x	114.374	114.342
$4f\ ^2F^o_{7/2}$	64.855	64.838	79.775	79.745	96.283	x	114.397	114.379

Table 4.2. Binding energies (in Rydbergs) of all $1s^2 2s^2\ ^1S^e_0$ ground state initial ion, in the present work and in NIST data [53].

Ion	Present	NIST	Ion	Present	NIST
Be Z=4	0.682	0.685	Si^{+10} Z=14	35.008	35.012
B^+ Z=5	1.844	1.849	S^{+12} Z=16	47.942	47.930
C^{+2} Z=6	3.514	3.520	Ar^{+14} Z=18	62.920	62.897
N^{+3} Z=7	5.688	5.694	Ca^{+16} Z=20	79.957	79.900
O^{+4} Z=8	8.365	8.371	Ti^{+18} Z=22	99.069	98.960
Ne^{+6} Z=10	15.228	15.234	Cr^{+20} Z=24	120.276	120.100
Mg^{+8} Z=12	24.107	24.100	Fe^{+22} Z=26	143.601	143.953

Table 4.3. Binding energies (in Rydbergs) of all $1s^2 2s2p\ ^3P^o_0$ metastable state initial ion, in the present work and in NIST data [53].

Ion	Present	NIST	Ion	Present	NIST
Be Z=4	0.482	0.485	Si^{+10} Z=14	33.456	33.464
B^+ Z=5	1.502	1.509	S^{+12} Z=16	46.122	46.115
C^{+2} Z=6	3.034	3.042	Ar^{+14} Z=18	60.831	60.813
N^{+3} Z=7	5.072	5.082	Ca^{+16} Z=20	77.598	77.546
O^{+4} Z=8	7.614	7.625	Ti^{+18} Z=22	96.436	96.334
Ne^{+6} Z=10	14.209	14.220	Cr^{+20} Z=24	117.365	117.202
Mg^{+8} Z=12	22.821	22.820	Fe^{+22} Z=26	140.411	140.780

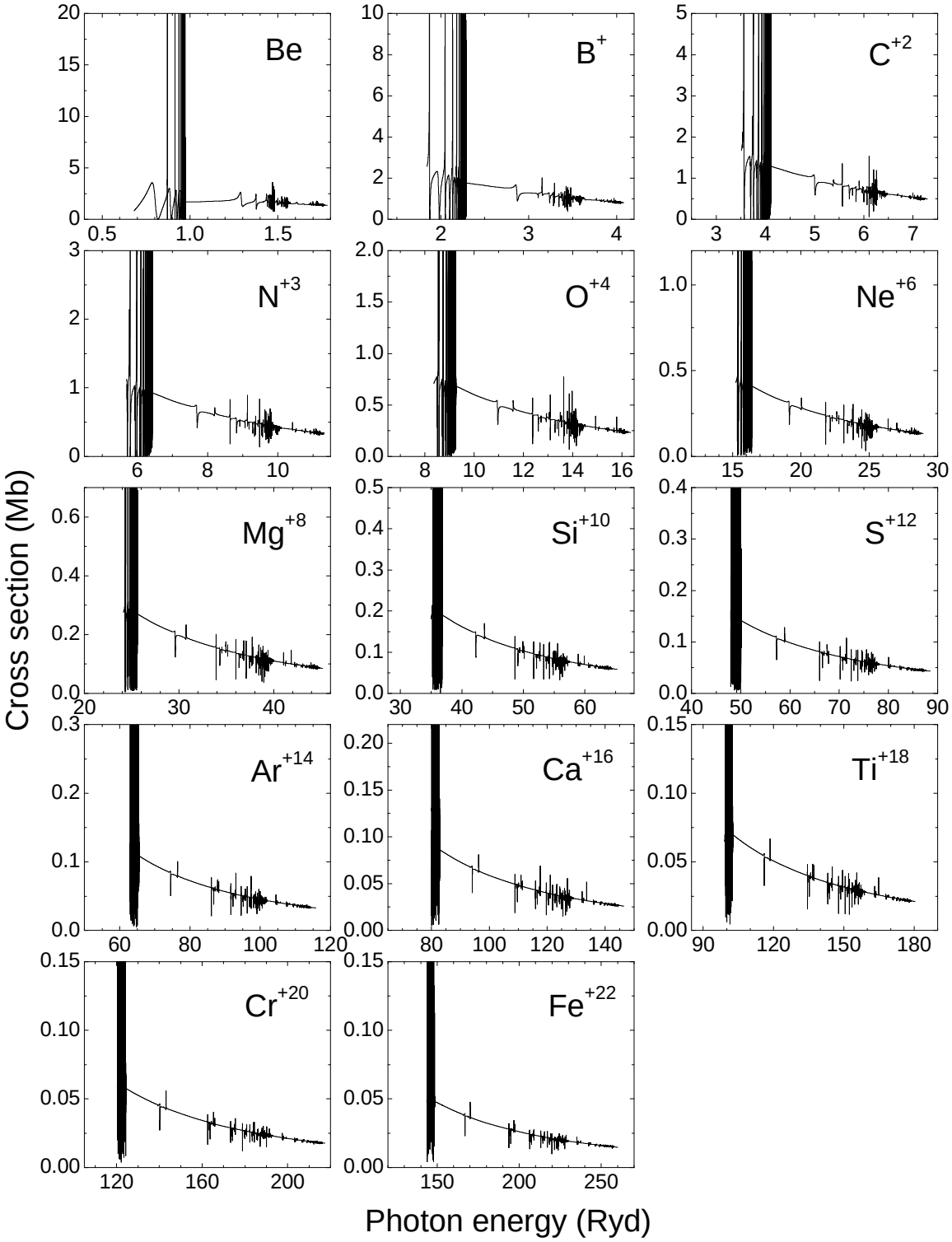

Figure 4.1. $1s^2 2s^2\ {}^1S_0^e$ ground state photoionization cross sections of Be, B^+, C^{+2}, N^{+3}, O^{+4}, Ne^{+6}, Mg^{+8}, Si^{+10}, S^{+12}, Ar^{+14}, Ca^{+16}, Ti^{+18}, Cr^{+20} and Fe^{+22} up to the $1s^2 4f$ thresholds of the three-electron final state ion calculated using BPRM methodology.

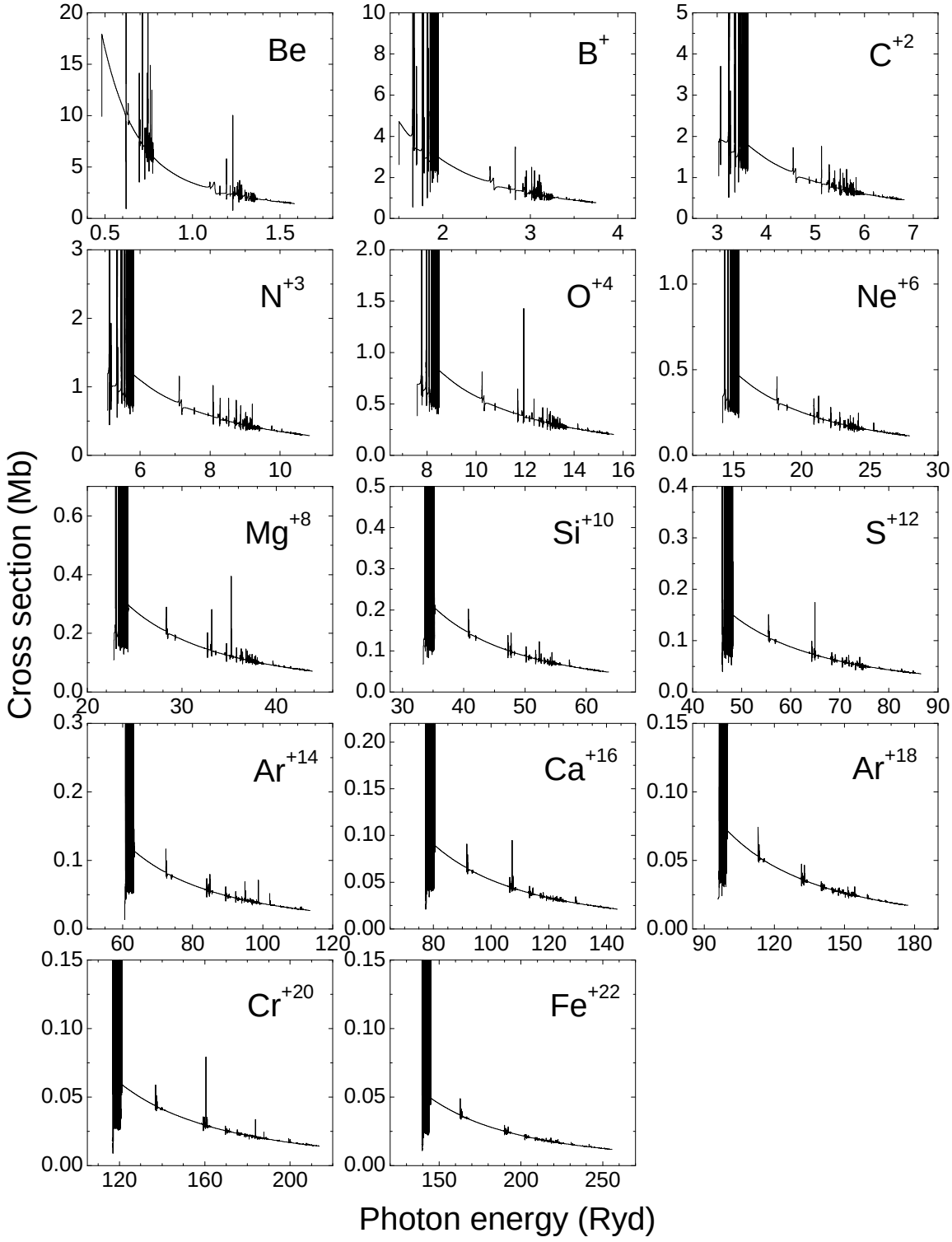

Figure 4.2. As Figure 4.1 but for the $1s^2 2s2p\ ^3P_0^o$ metastable state. The cross section shown is a statistical average of the three individual $^3P_J^o$ cross sections.

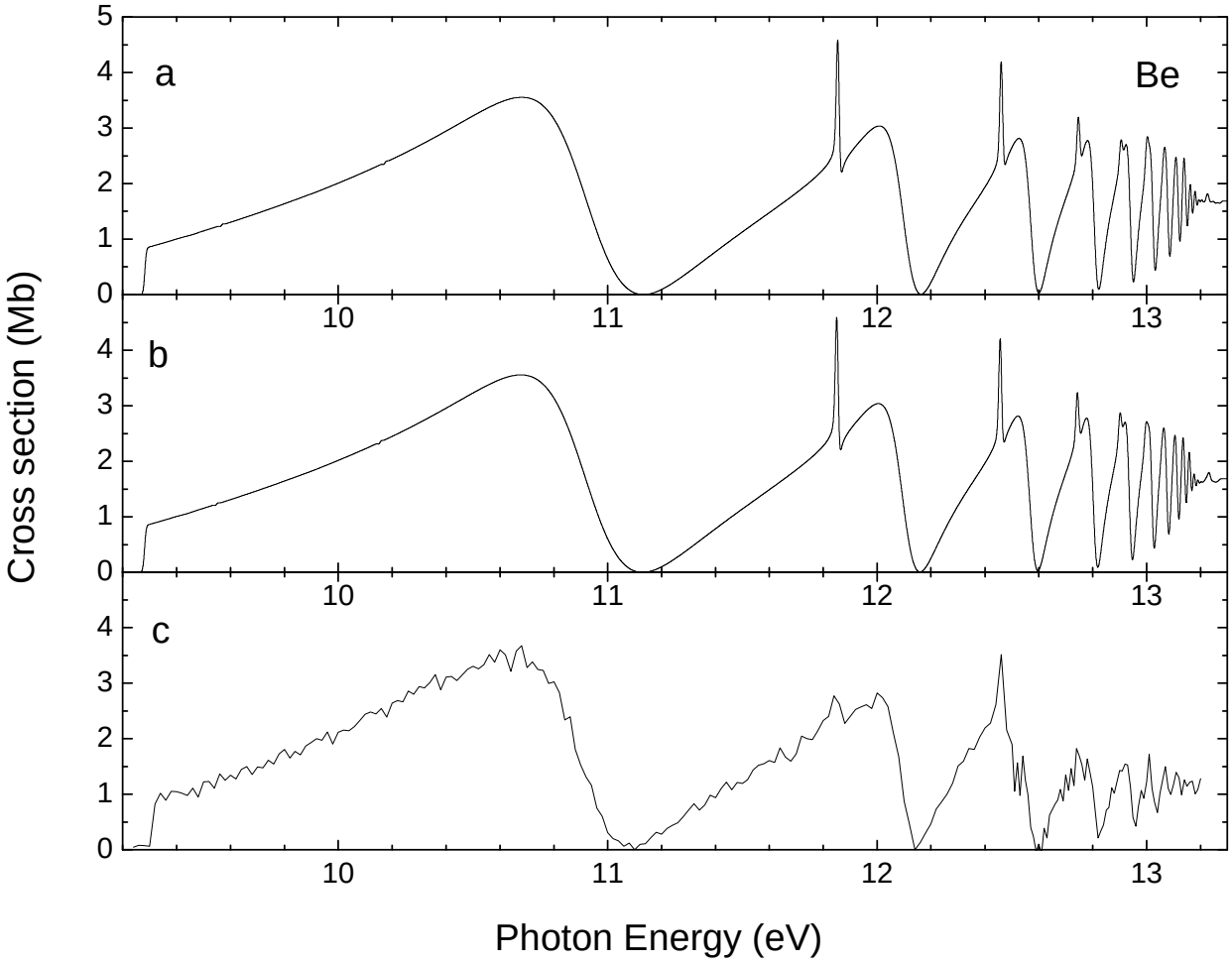

Figure 4.3. Photoionization cross section of ground state Be from 9.2 eV to 13.3 eV; (a) present BPRM result, (b) present nonrelativistic result, (c) experiment [54]. Both theoretical cross sections were calculated with energy step ΔE = 68 μeV, and convoluted with FWHM = 12 meV to match experiment.

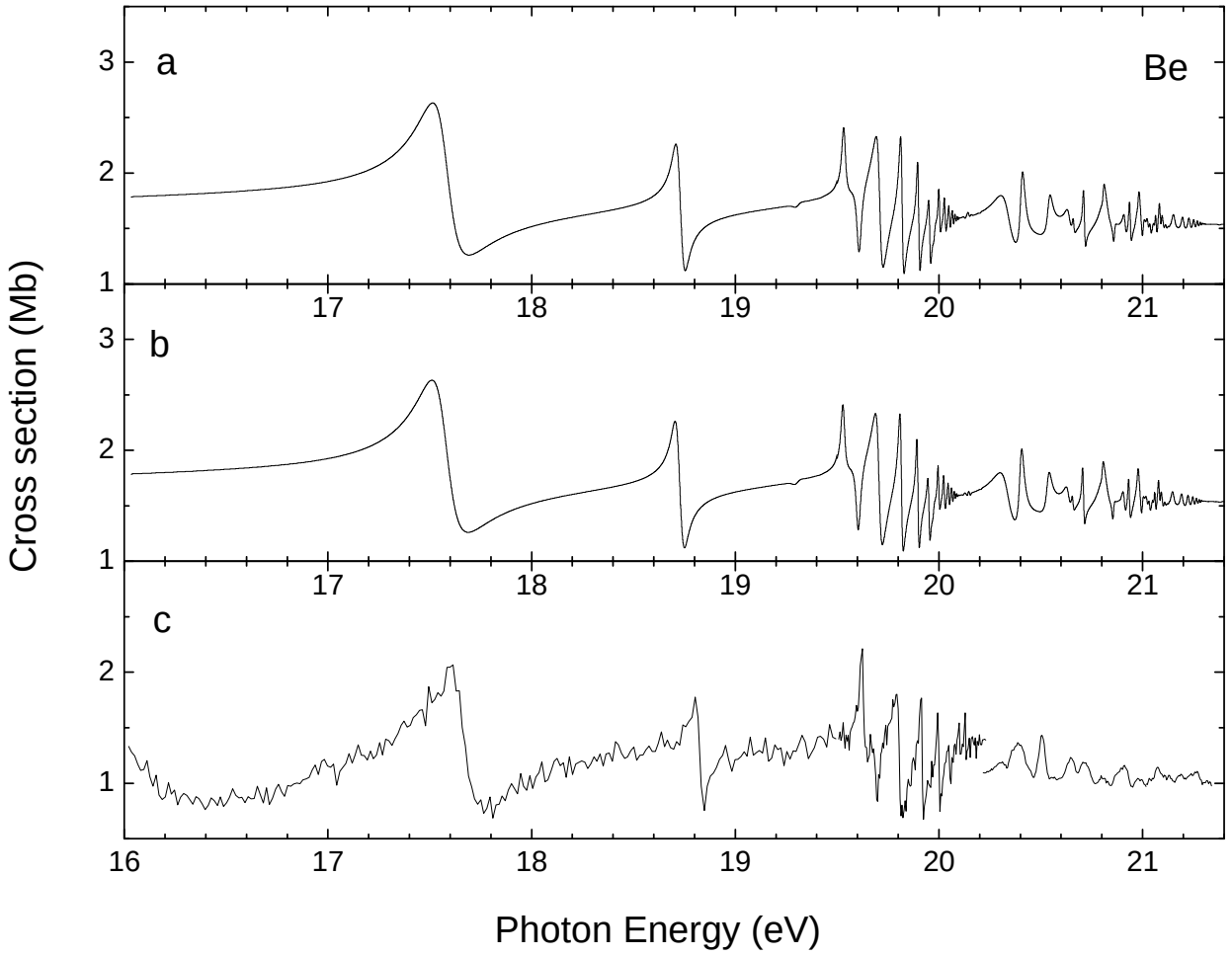

Figure 4.4. Photoionization cross section of ground state Be from 16 eV to 21.5 eV; (a) present BPRM result, (b) present nonrelativistic result, (c) experiment [55]. Both theoretical cross sections were calculated with energy step ΔE = 68 μeV, and convoluted with FWHM = 5 meV to match experiment.

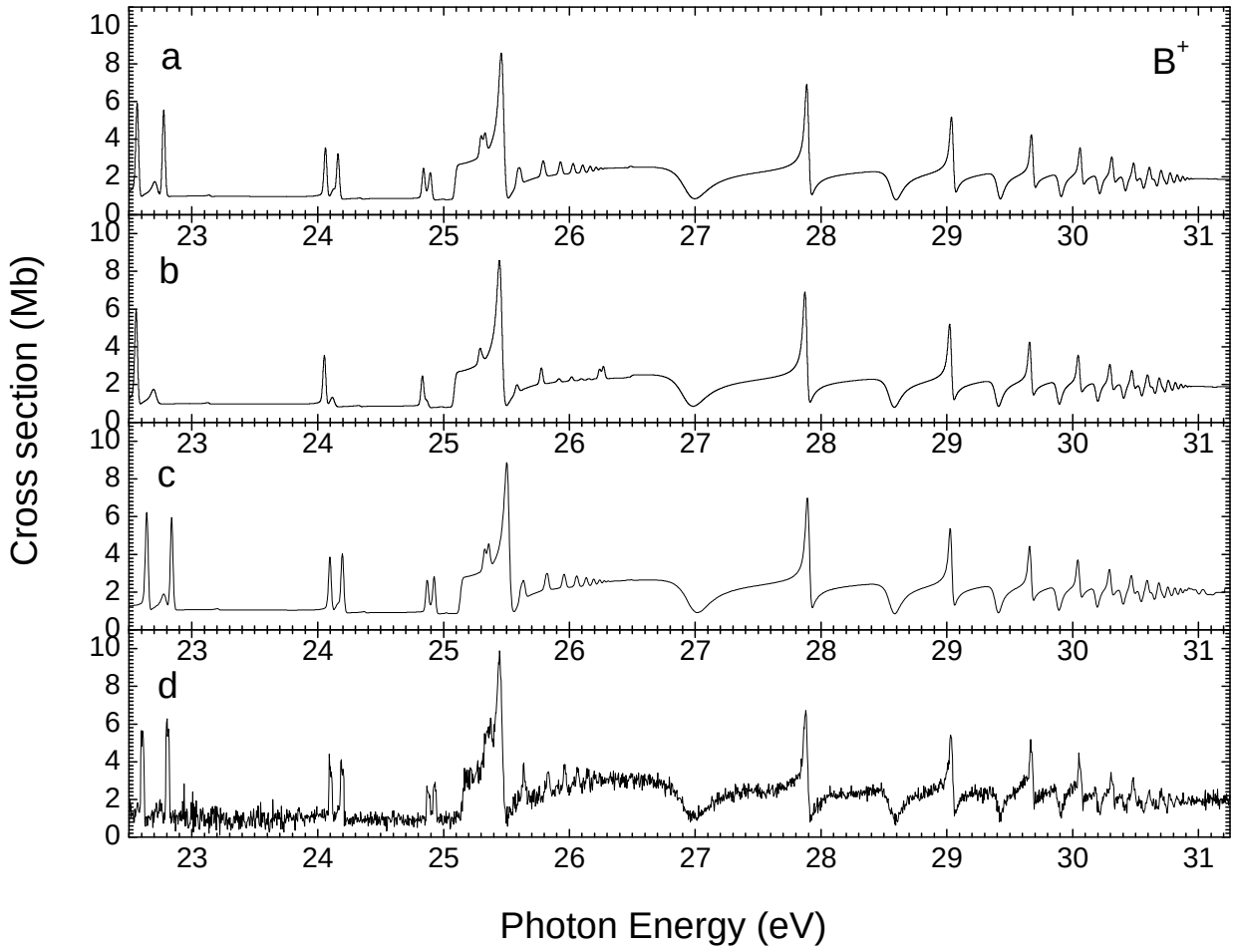

Figure 4.5. Photoionization cross section of B^+ from 22.5 eV to 31.25 eV. The theoretical results are a weighted sum of ground state (71%) and metastable $^3P_1^o$ state (29%) cross sections [56]; (a) present BPRM result, (b) present nonrelativistic result, (c) previous BPRM result [56] multiplied by 1.05, (d) experiment [56]. Both present results were calculated with energy step ΔE = 13.6 μeV and convoluted with FWHM = 25 meV to match experiment. The previous BPRM result was convoluted in the same manner, and the ground state and metastable state results were shifted by -22 meV and 4 meV, respectively, to match the measurement.

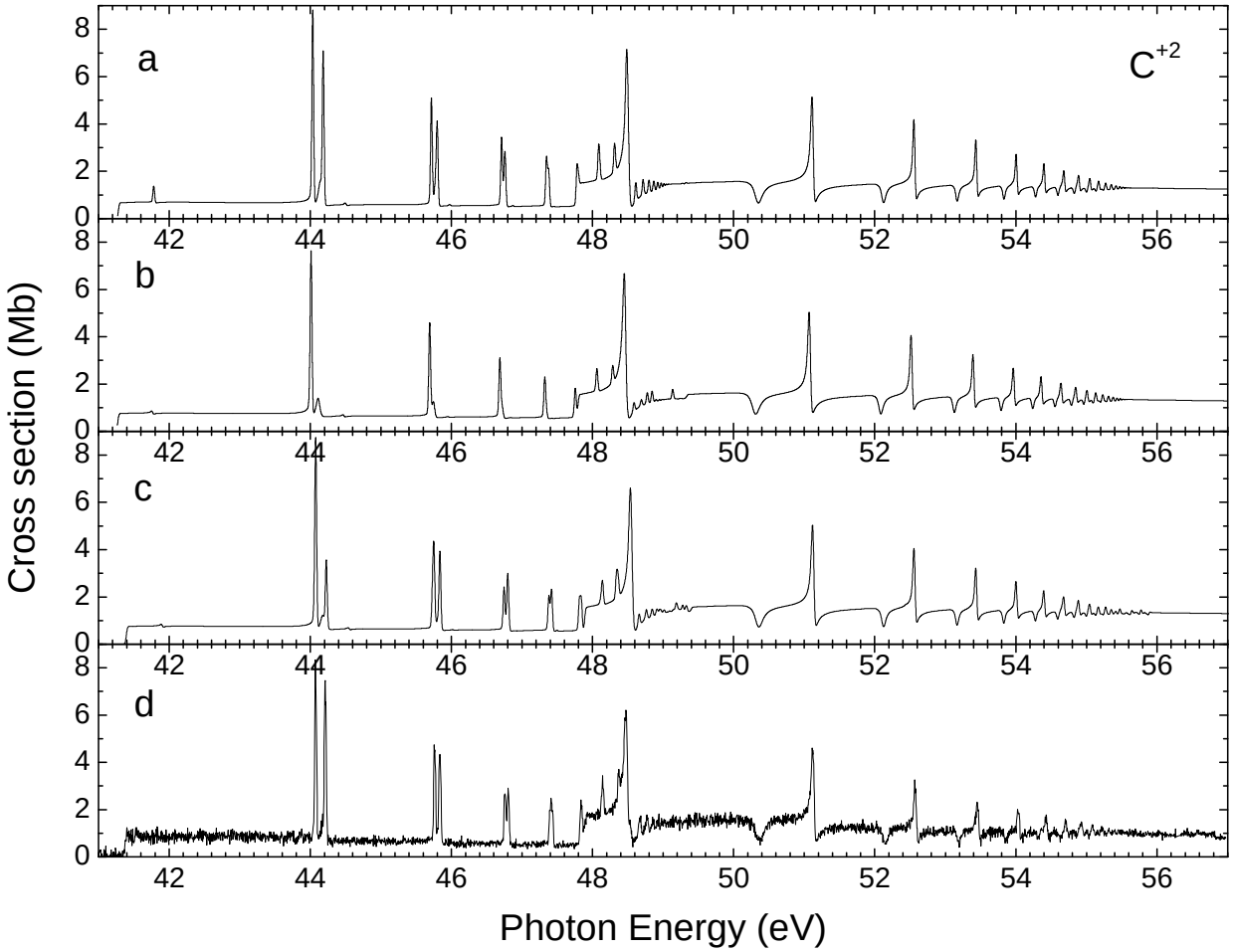

Figure 4.6. Photoionization cross section of C^{+2} from 41 eV to 57 eV. The theoretical results are a weighted sum of ground state (60%) and metastable $^3P_0^o$ state (30%), $^3P_1^o$ state (5%), and $^3P_2^o$ state (5%) cross sections [57]; (a) present BPRM result, (b) present nonrelativistic result, (c) previous BPRM result [57], (d) experiment [57]. All present results were calculated with energy step ΔE = 12.2 μeV and convoluted with FWHM = 30 meV to match experiment. The previous BPRM result was convoluted in the same manner.

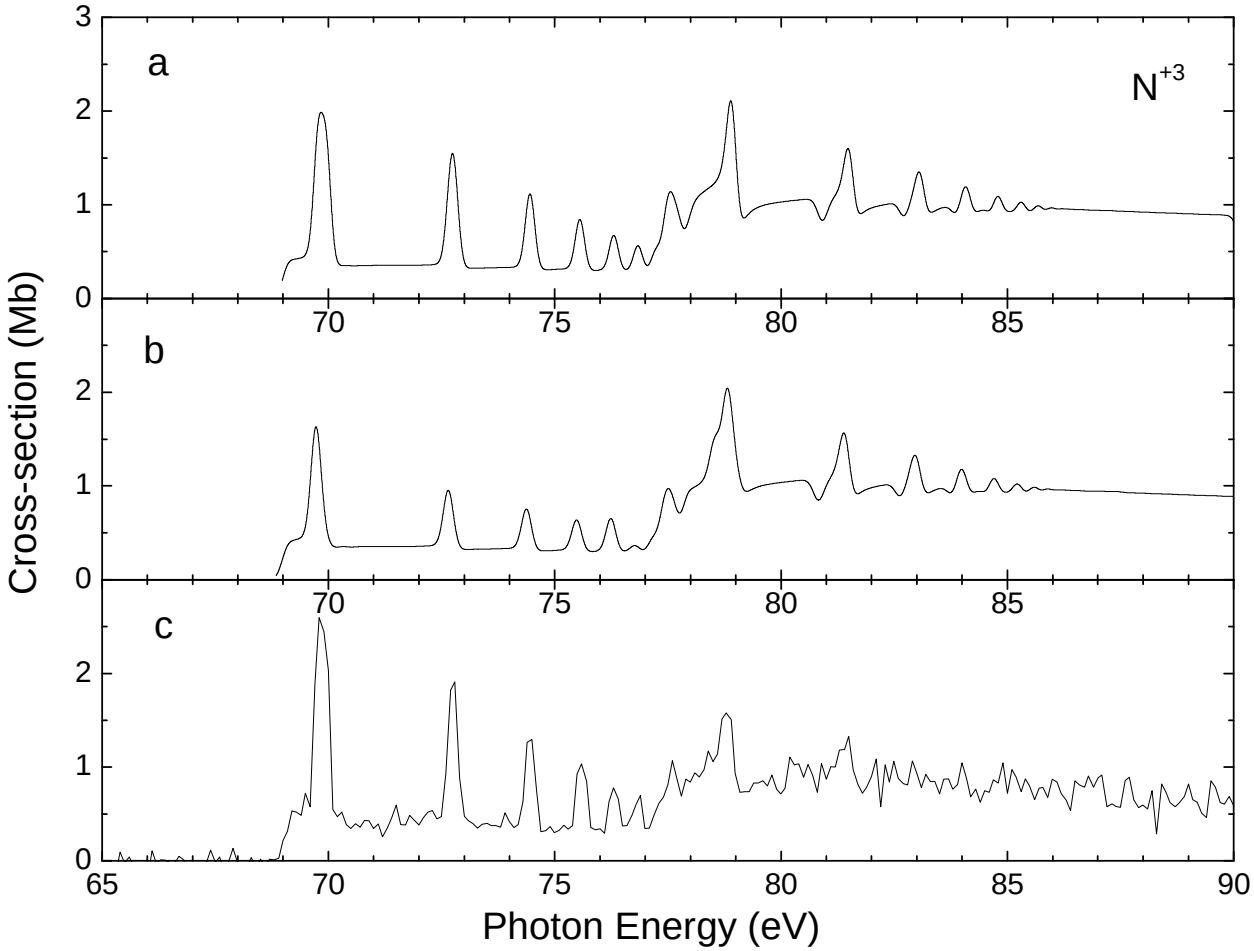

Figure 4.7. Photoionization cross section of N^{+3} from 65 eV to 90 eV. The theoretical results are a weighted sum of ground state (65%) and metastable state (35%) cross sections [58]; it was assumed that the metastable fractions were statistical. Shown are (a) present BPRM result, (b) present nonrelativistic result, (c) experiment [58]. Both present results were calculated with energy step ΔE = 13.6 μeV and convoluted with FWHM = 230 meV to match experiment.

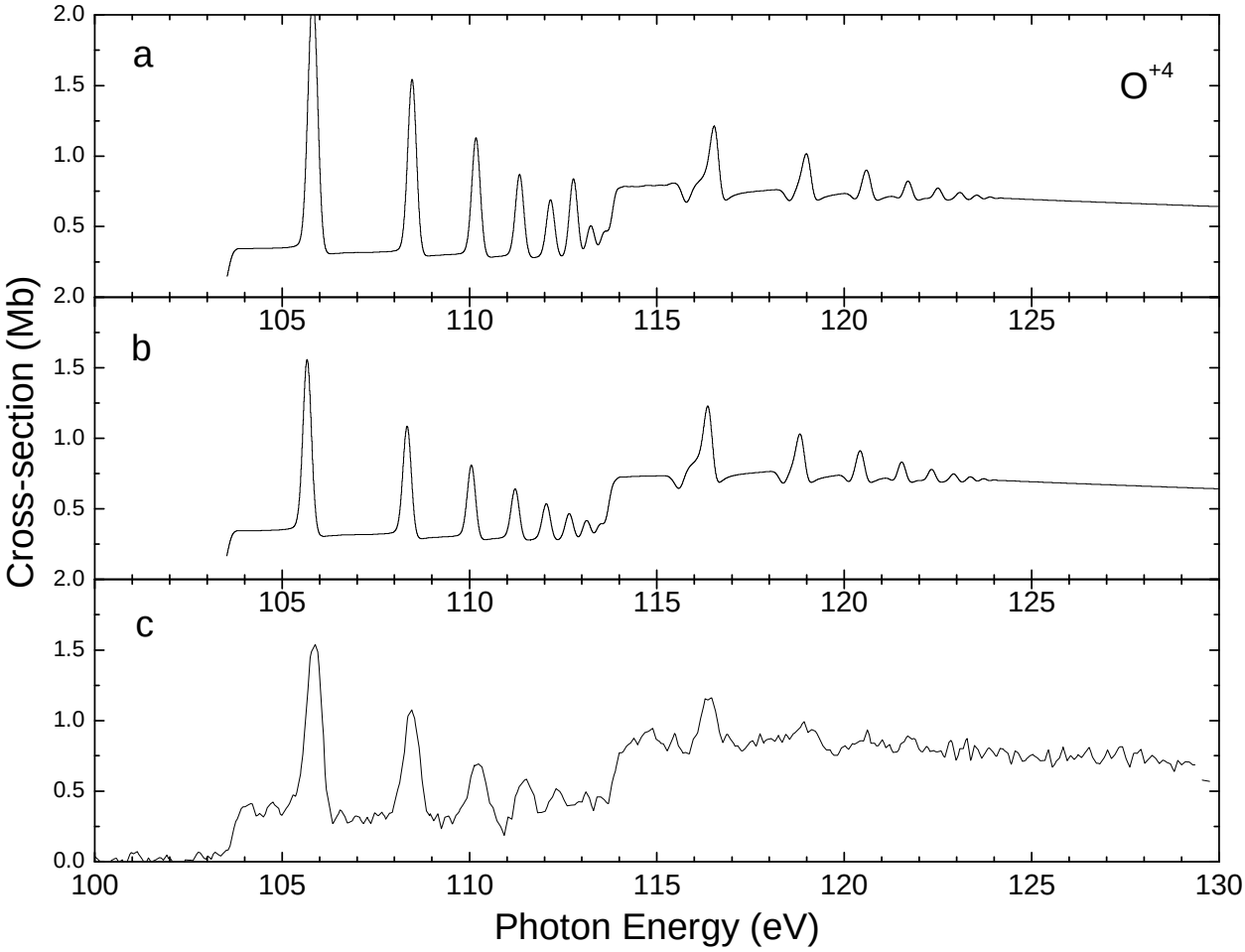

Figure 4.8. Photoionization cross section of O^{+4} from 95 eV to 130 eV. The theoretical results are a weighted sum of ground state (50%) and metastable state (50%) cross sections [60]; it was assumed that the metastable fractions were statistical. Shown are (a) present BPRM result, (b) present nonrelativistic result, (c) experiment [60]. Both present results were calculated with energy step ΔE = 13.6 μeV and convoluted with FWHM = 250 meV to match experiment.

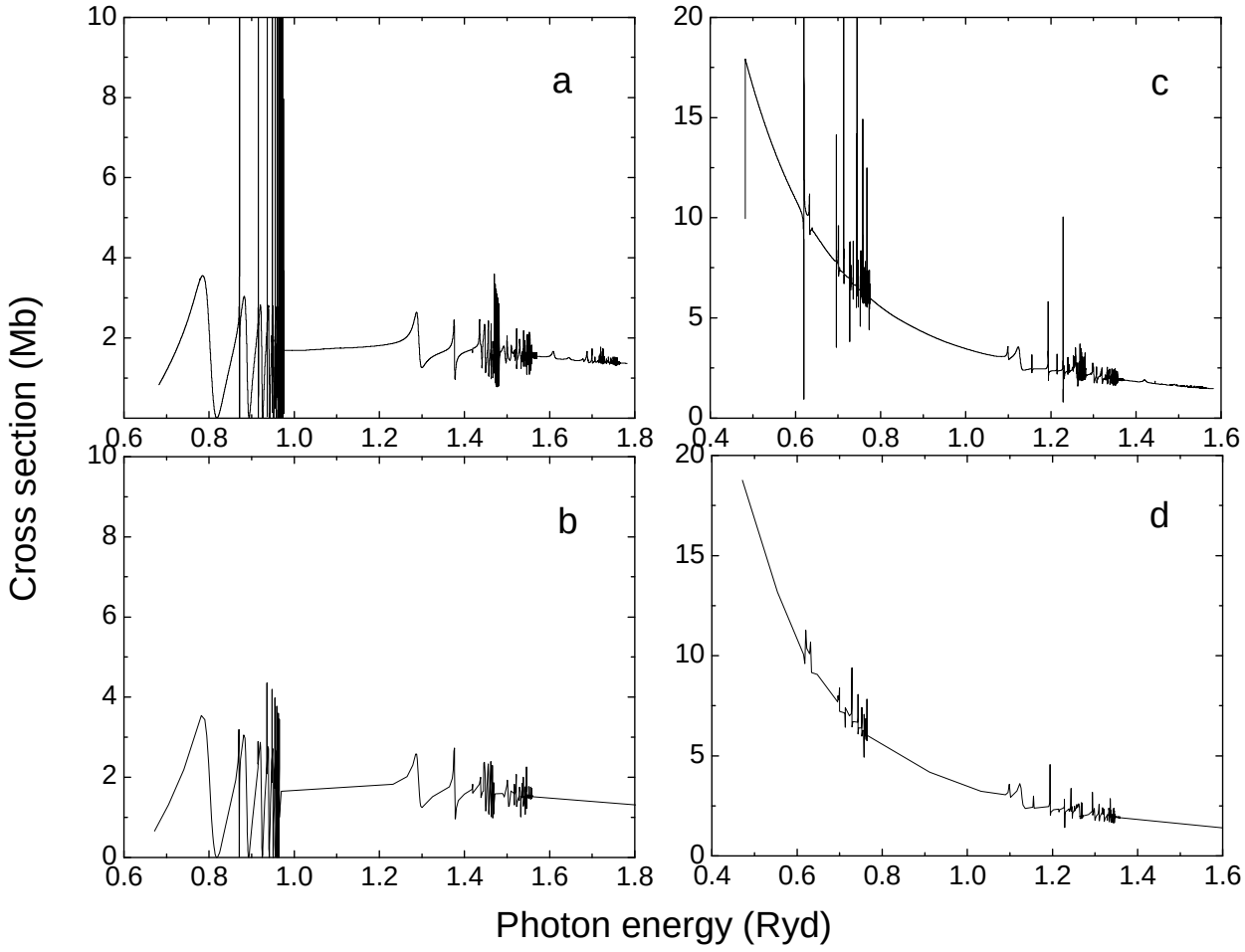

Figure 4.9. Comparison of the present BP photoionization cross sections, (a) ground state, (c) metastable state for Be with OP results, (b) ground state, (d) metastable state [61]. The metastable BP results shown are a statistical average of the three $^3P_j^o$ cross sections.

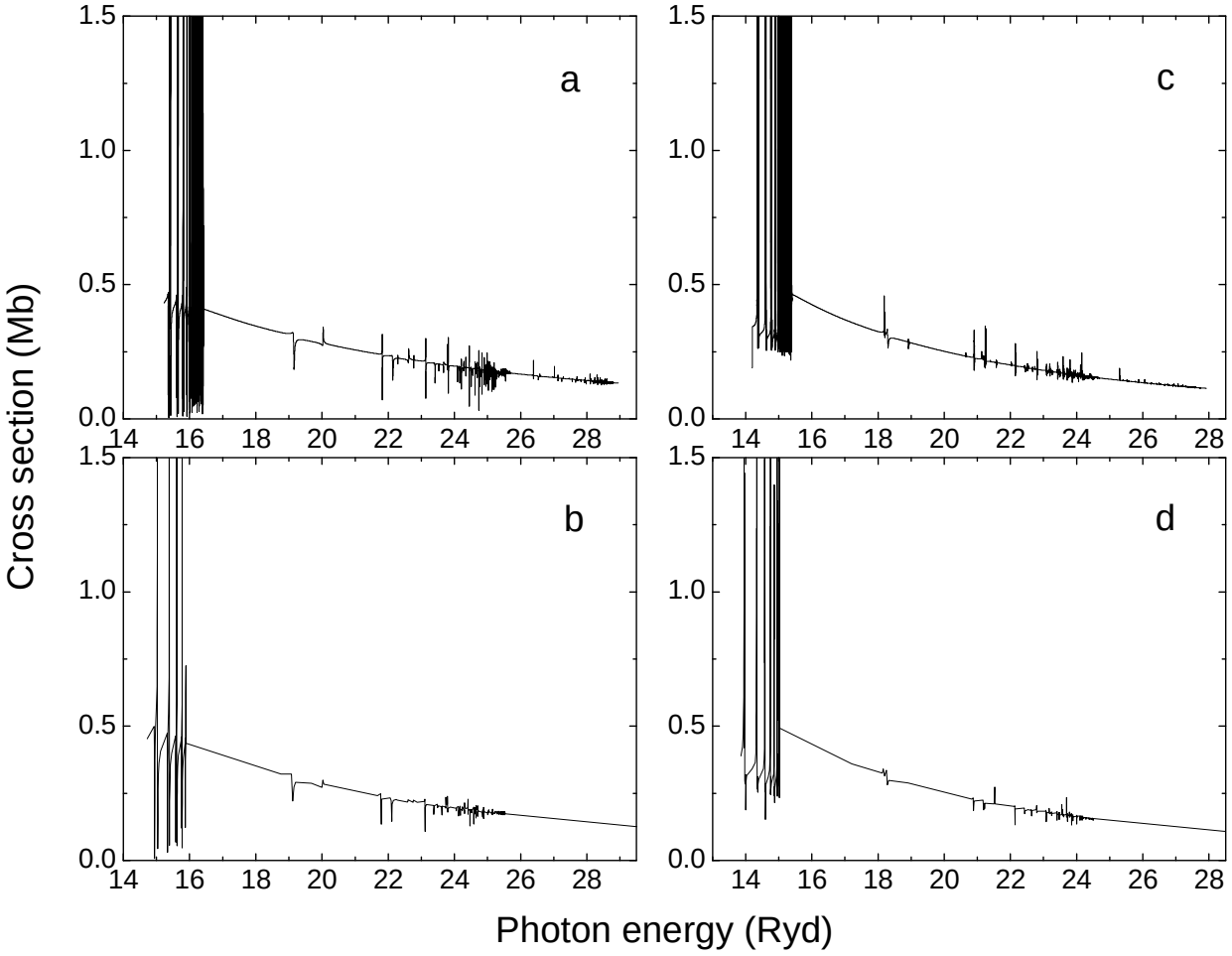

Figure 4.10. As Figure 4.9 for Ne^{+6}.

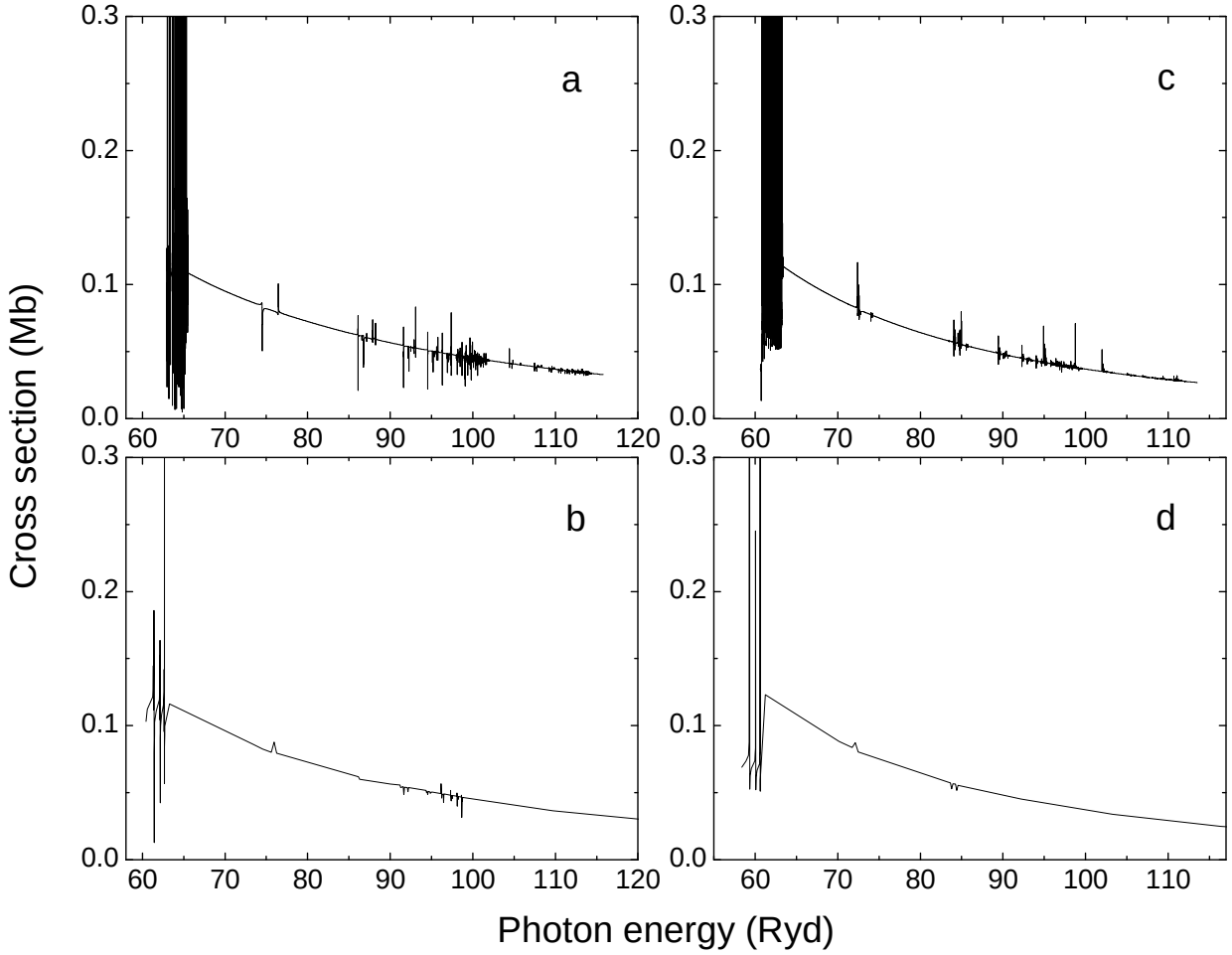

Figure 4.11. As Figure 4.9 for Ar^{+14}.

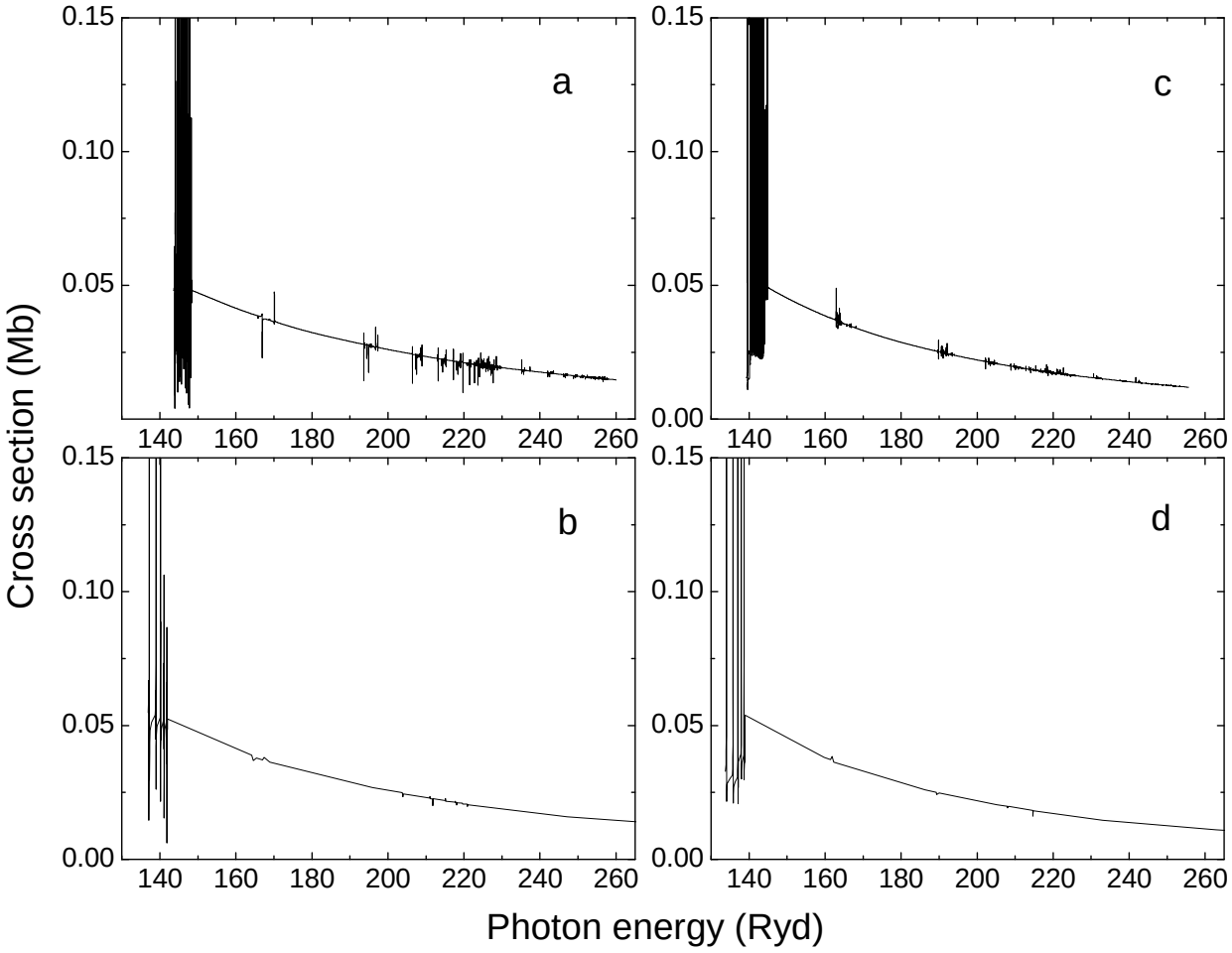

Figure 4.12. As Figure 4.9 for Fe^{+22}.

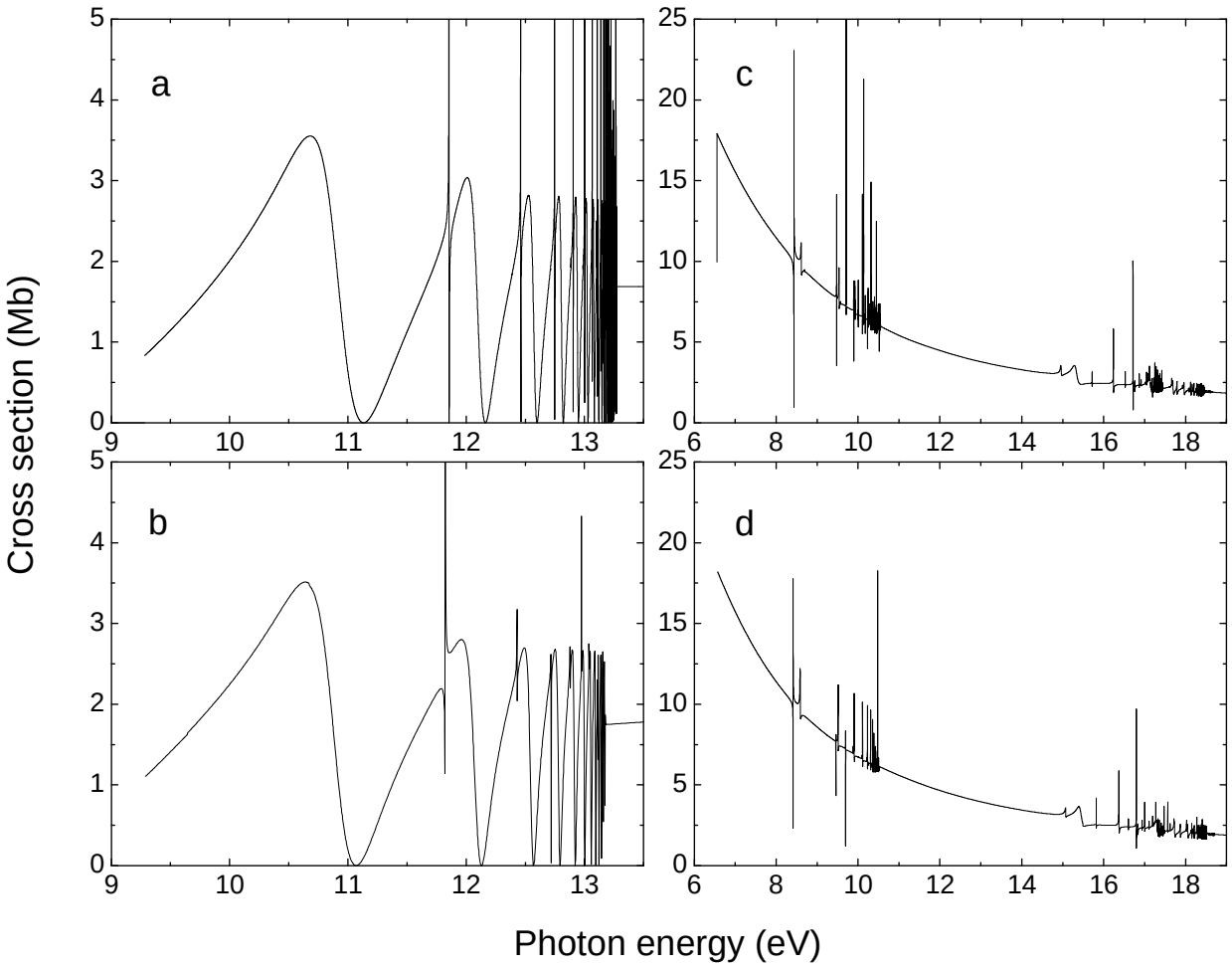

Figure 4.13. Total photoionization cross section of Be; (a) present BP ground state result, (b)VRM ground state result for [63], (c) present BP metastable state result, (d) VRM metastable state result [64]. The BP metastable state cross section is a statistical average of the three $^3P_j^o$ cross sections.

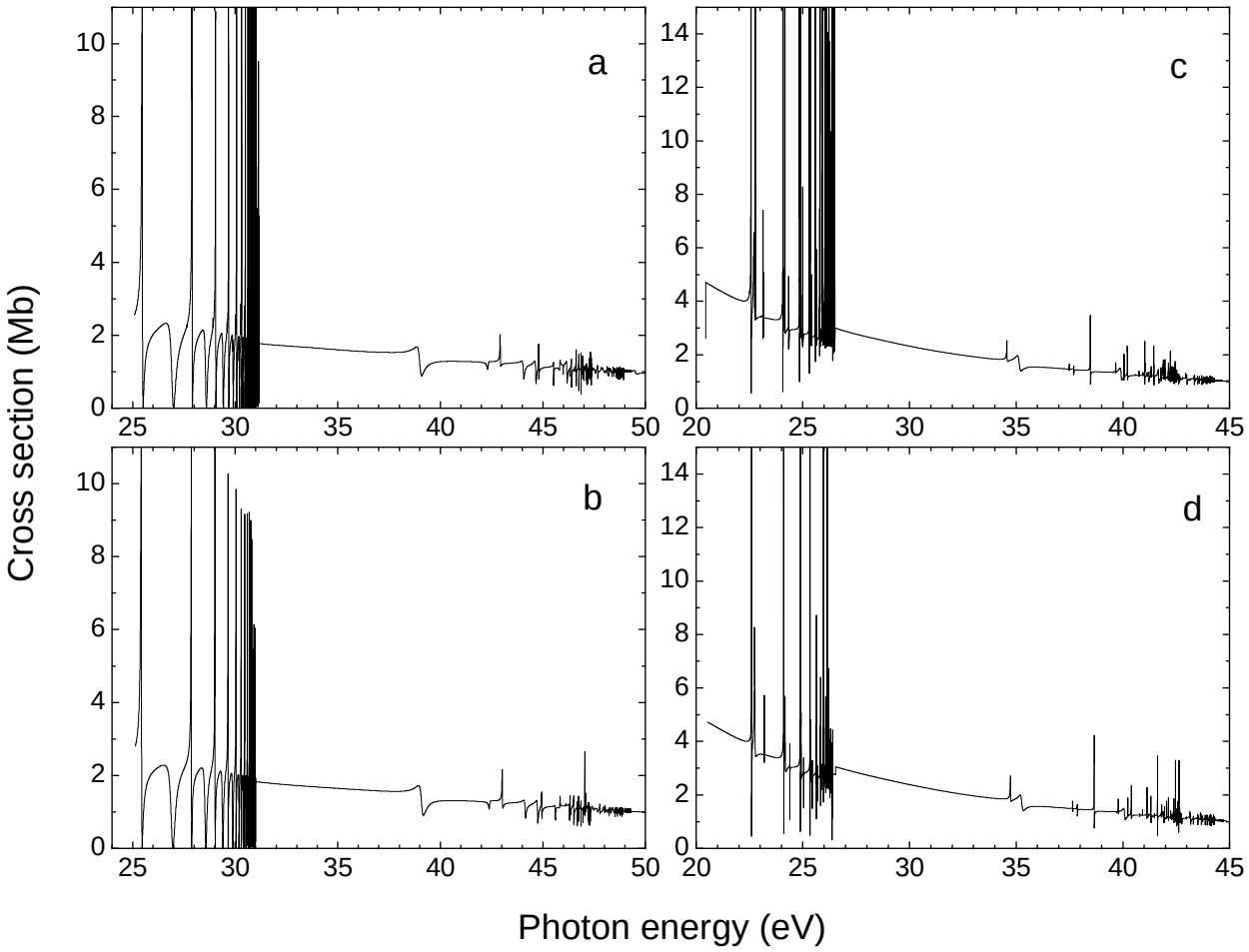

Figure 4.14. As Figure 4.13 for B^+; the VRM results are from Refs. [65] and [66] for ground and metastable states, respectively.

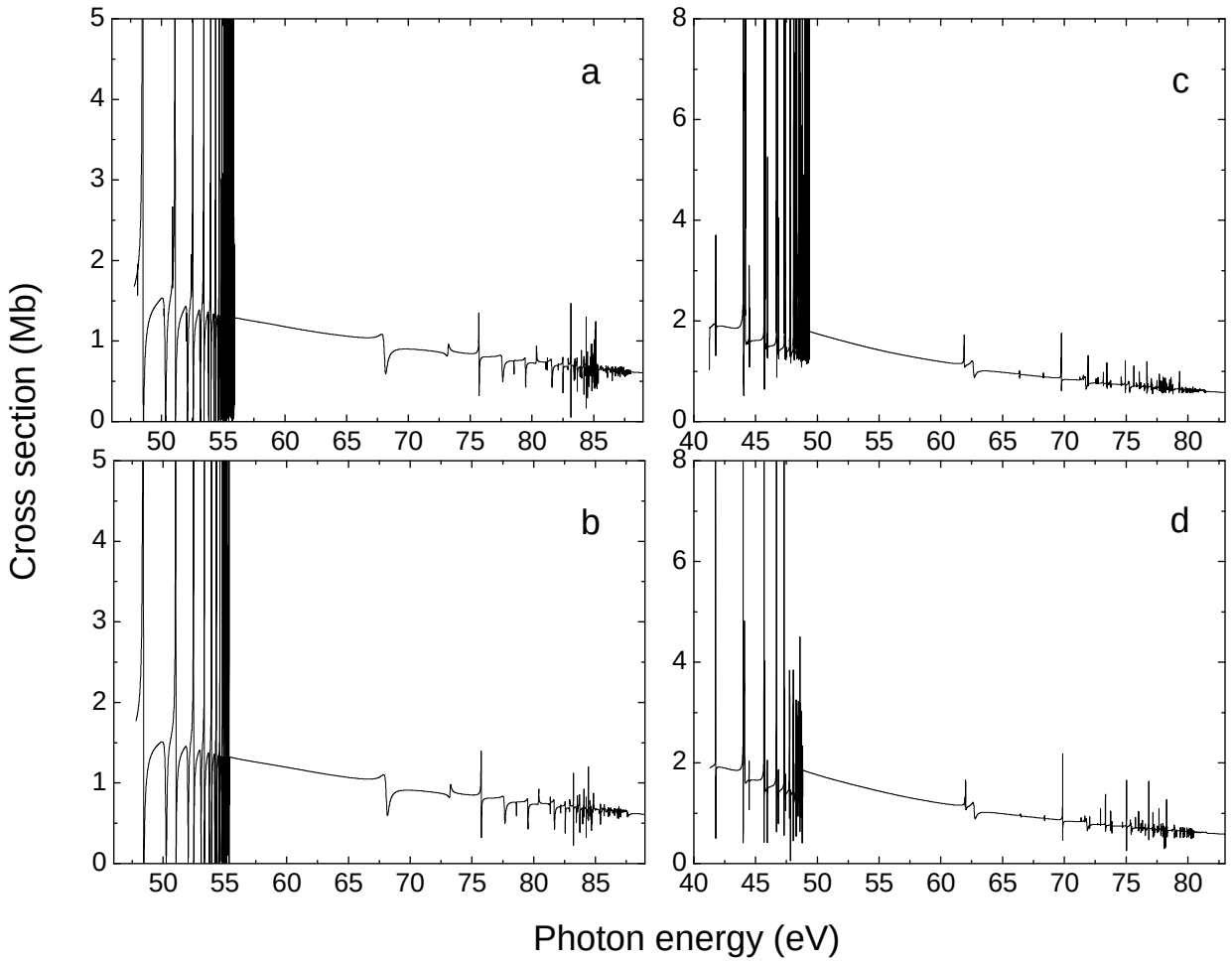

Figure 4.15. As Figure 4.13 for C^{+2}; the VRM results are from Refs. [67] and [68] for ground and metastable states, respectively.

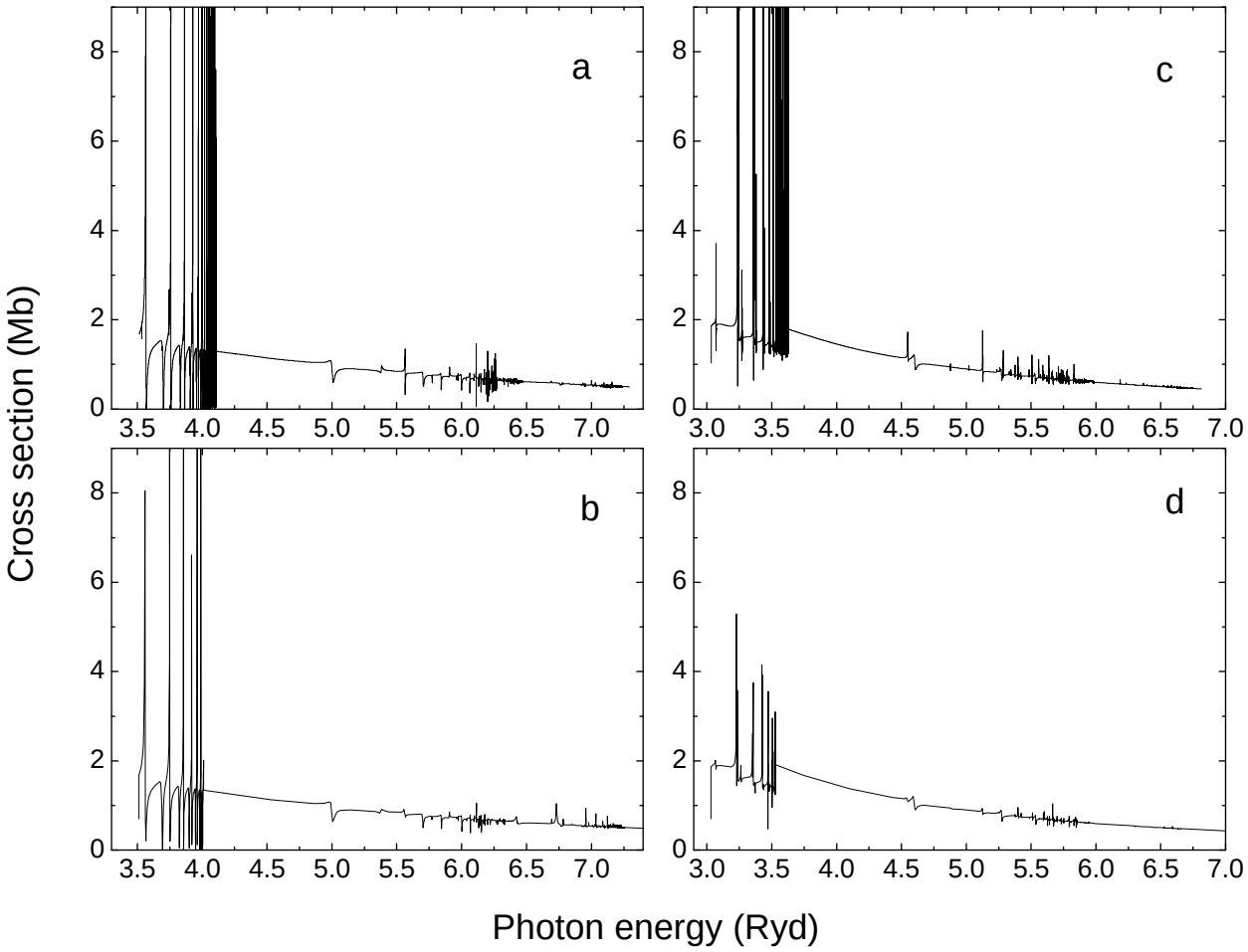

Figure 4.16. Total photoionization cross section of C^{+2}; (a) present BP ground state result, (b) ground state result of Ref. [70], (c) present BP metastable state result, (d) metastable state result of Ref. [70]. The BP metastable state cross section is a statistical average of the three $^3P_j^o$ cross sections.

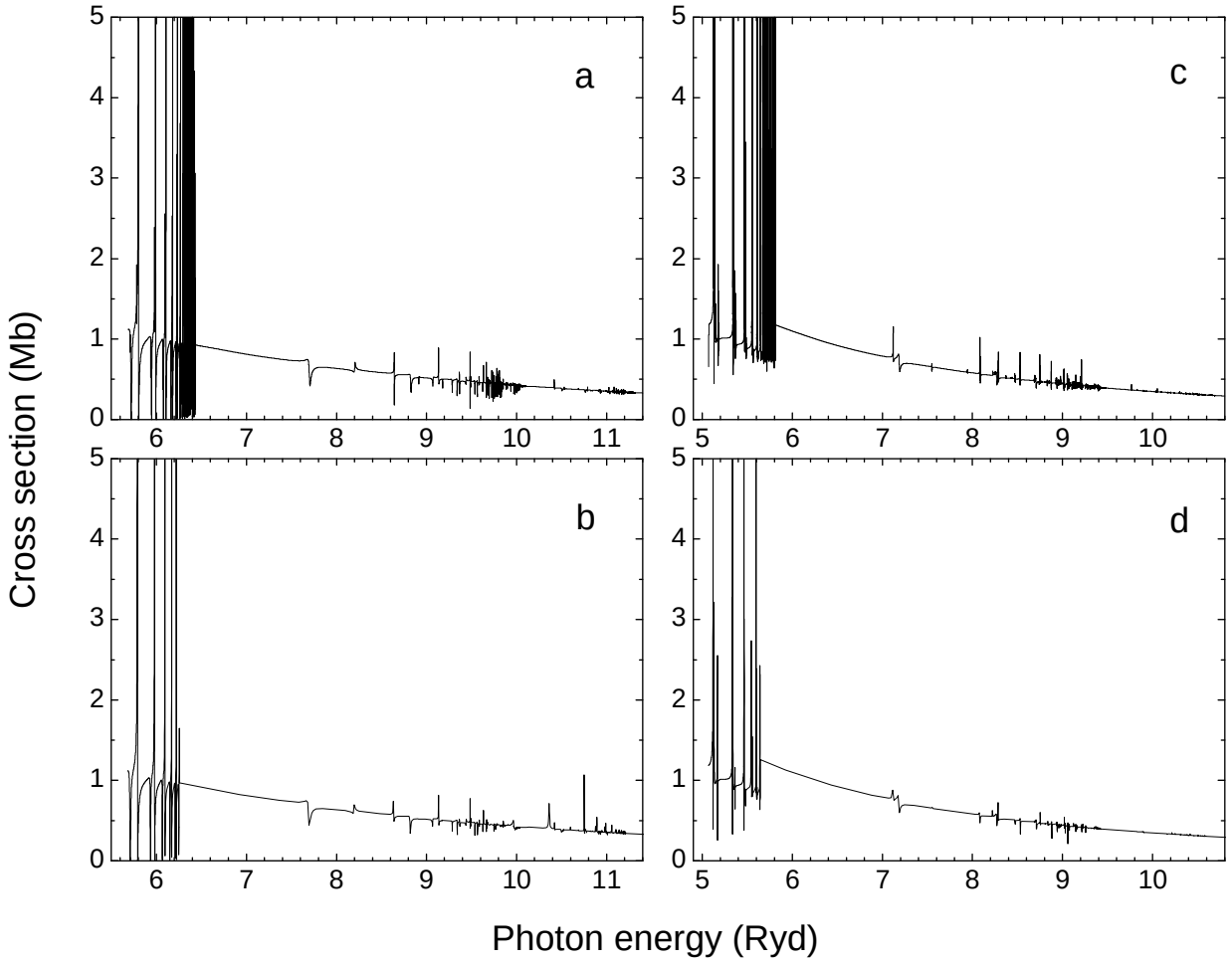

Figure 4.17. As Figure 4.16 for N^{+3}.

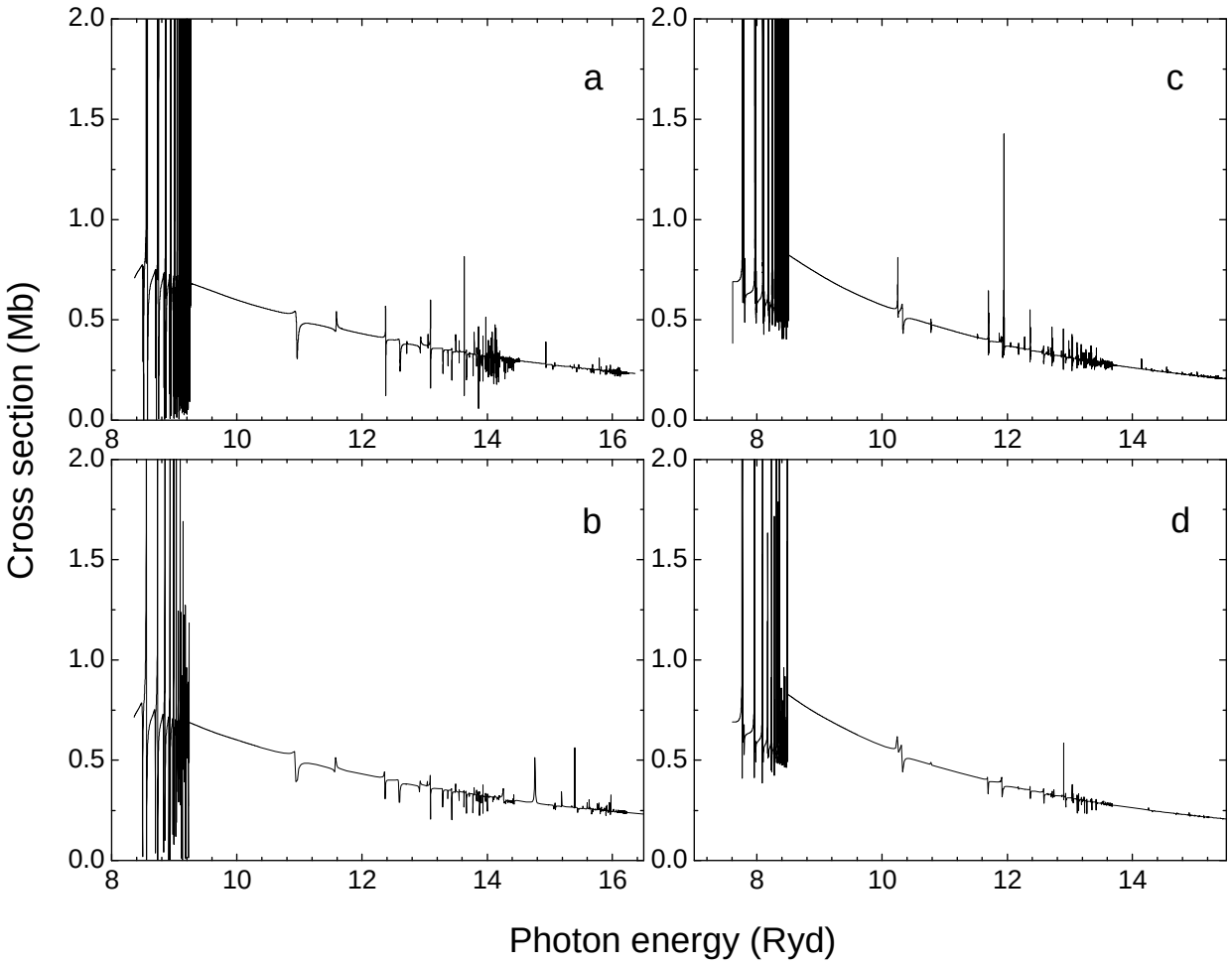

Figure 4.18. As Figure 4.16 for O^{+4}, but compared with results from Ref. [72].

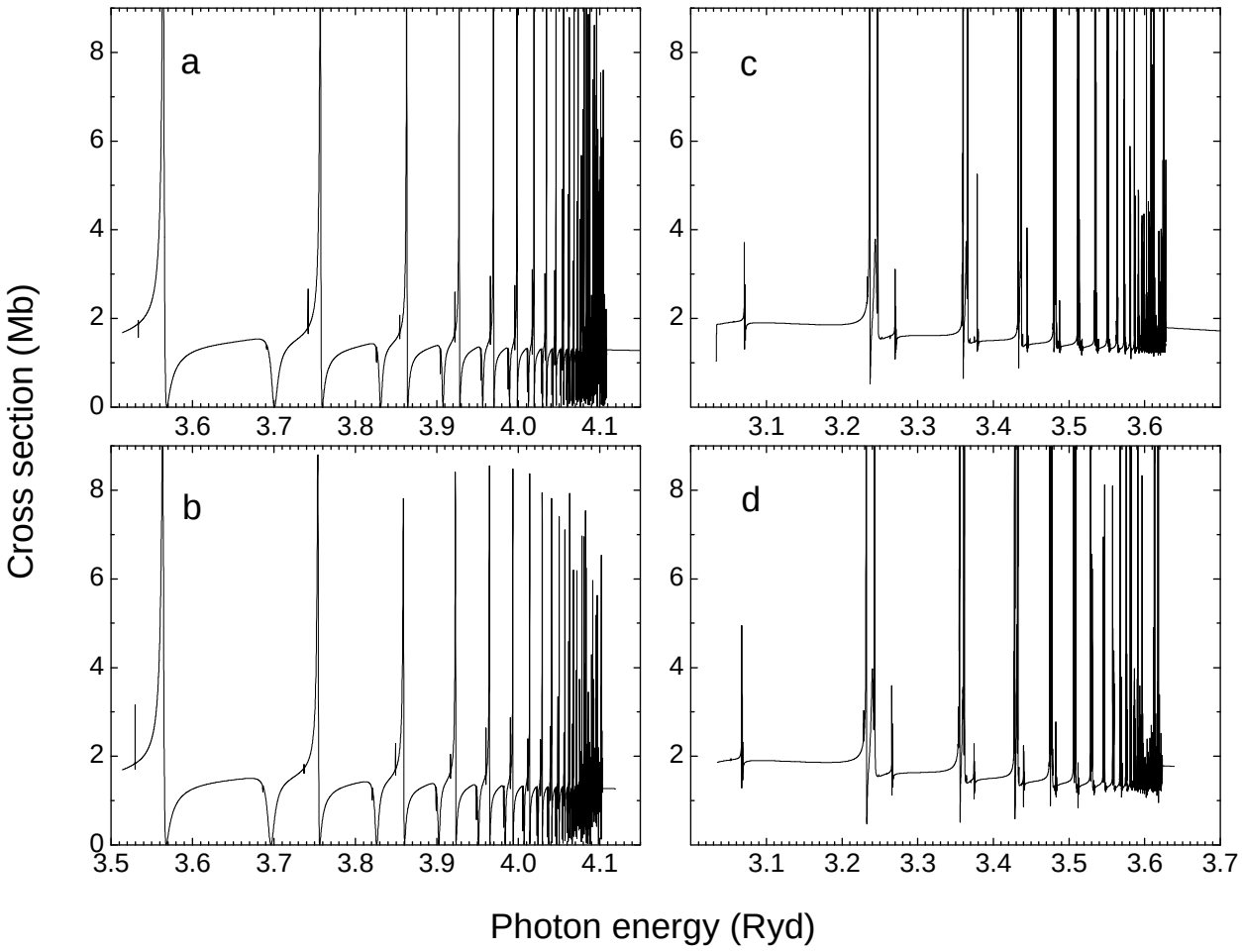

Figure 4.19. As Figure 4.16 for C^{+2}, but compared with the relativistic results of Ref. [71].

5. ANALYSIS

5.1. General Appearance of Cross Sections

In this section we discuss the overall appearance of the cross sections along the whole sequence, as demonstrated by Figure 4.1 and Figure 4.2, for ground state and metastable state, respectively. To make the notations simple and clear, we use T_{nl_j} as the threshold energy of the nl_j target state, and E_{range} for the energy range of study, which is from 2*s* threshold to 4$f_{7/2}$ threshold, i.e. $E_{\text{range}} = T_{4f_{7/2}} - T_{2s}$.

The area under the cross section curves, in Mb-Ryd, divided by 8.07 is the total oscillator strength in over that energy region [77]; owing to the well-known sum rule [77], the total oscillator strength from the outer shell is 2, the number of outer-shell electrons. This sum includes the discrete oscillator strengths for the excitations below the ionization threshold, and these are large, e.g., in neutral Be, the 2*s* → 2*p* transition has an oscillator strength of 1.36 [78]. It is found, from the present results, that the oscillator strength in E_{range} range, is approximately 0.4 and is about the same for all of the *Z* considered and for both initial states. Then, since the energy scale increases roughly as Z^2 (the hydrogenic energy scaling), it is evident that the cross sections must decrease as $1/Z^2$ to preserve the oscillator strength; this is exactly what is seen in Figure 4.1 and Figure 4.2.

The energy separations between *nl* and *nl'*, on the other hand, do not increase as Z^2 along the isoelectric sequence; they increase, but only roughly linearly with increasing *Z*. To better show the change of these splittings along *Z*, we focus on the ratio of each splitting to E_{range}, namely the "scaled" splitting. In Figure 5.1 we show the scaled energy separations

between *nl* and *nl'* for n=2, 3, 4 in each ion, and find that these values change smoothly down with *Z*, but not as quickly as how the background cross sections do. For example, the interval between T_{2s} and $T_{2p_{3/2}}$ is 0.293 Ryd in Be (*Z*=4), which is about 27% of E_{range}. This percentage is down to 8.8% in Ne^{+6} (*Z*=10), 5.5% in S^{+12}, and 4.1% in Fe^{+22}. For a simple double-exponential decay function, we have found the following fitting parameters:

$$\frac{T_{2p_{3/2}} - T_{2s}}{E_{\text{range}}} = 0.0380 + 2.38\exp\left(-\frac{Z}{1.22}\right) + 0.292\exp\left(-\frac{Z}{5.74}\right), \tag{5.1}$$

$$\frac{T_{3d_{5/2}} - T_{3s}}{E_{\text{range}}} = 0.0159 + 8.64\exp\left(-\frac{Z}{0.579}\right) + 0.134\exp\left(-\frac{Z}{4.70}\right), \tag{5.2}$$

$$\frac{T_{4f_{7/2}} - T_{4s}}{E_{\text{range}}} = 0.00680 + 14.9\exp\left(-\frac{Z}{0.468}\right) + 0.0550\exp\left(-\frac{Z}{0.231}\right). \tag{5.3}$$

Of course in the $Z\rightarrow\infty$, hydrogenic, limit levels of the same principal quantum number are degenerate (nonrelativistically) asymptotically, so a different energy dependence is expected. In any case, owing to the differences in the dependences of the thresholds of differing *n* and *l* along the isoelectronic sequence, the overlapping of resonances converging to threshold having the same principal quantum is considerably altered as a function of *Z*. Of course, with increasing *Z*, spin-orbit effects become important since they increase as Z^4, so the situation for the higher-*Z* ions is rather more complicated.

The width of a resonance indicates the strength of the Coulomb matrix element of the quasi-discrete resonance state with the final continuum state. The resonance widths increase slowly with *Z* while the energy range grows as Z^2 as described above; actually, in the hydrogenic limit, the resonance widths are independent of *Z* [79]. As a total effect, the widths of the resonances relative to the energy range decrease with increasing *Z*, making $\sigma(E)$ a smoother function and the resonance structures less important in the sense that less of the energy range is

resonant and more is nonresonant background cross section. Thus, in the heavier ions, the background cross section can be fit more easily by a simple function without too much disturbance by the resonances. At the lower end of the sequence, owing to the extent of the resonance widths, this is more problematic. Furthermore, the widths also decrease relative to the energy separation of the resonances, with increasing *Z*, strongly affecting the resulting cross section in the resonance region.

There is definitely a wealth of information concerning the evolution of the resonances along the isoelectronic sequence. In Section 5.3, we will characterize the resonances, display these features and analyze their evolution with *Z*.

5.2. Relativistic Effects

To pinpoint the influence of relativistic effects, calculations have been performed at both the *LS*-coupling and BP levels, using exactly the same radial basis set and radial wave functions; this procedure insures that any differences in the cross sections resulting from the two levels of calculation are due solely to relativistic effects. For the first five members of the sequence, both the *LS*-coupling and BP calculations are shown in Figure 4.3 to Figure 4.8. In this low-*Z* part of the isoelectronic sequence, it was seen that there were only small differences between *LS* and BP results; of importance, however, is that in every case, the relativistic result is closer to experiment. Owing to the experimental resolution that our theoretical results have been convoluted with, it is difficult from these figures to make any statement about how the importance of relativistic effects changes with increasing *Z*. However, looking at our unconvoluted results, it is clear that relativity becomes more important with increasing *Z*.

To explore this, the comparison for Ne^{+6} is shown in Figure 5.2 with no convolution for both ground and metastable state cross sections; the metastable BP result presented is a statistical

average of the cross sections of the three $^3P_J^o$ metastable states. While the background cross sections are the same, in both cases the resonances are seen to differ in position size and shape, particularly for the excited state. As an example, for the ground state resonance at about 19.15 Ryd, the nonrelativistic position is about 0.04 Ryd (0.54 eV) lower than the BP location, which is caused by the relativistic shift of the ground state energy plus the shift of the threshold energies of the final states of the ion. Further, for the photoionization of the initial excited metastable states, there is a marked difference in the size and shape of the resonances between *LS* and BP results that is not evident for ground state photoionization. This is seen in Figure 5.2 in the 21.2 Ryd photon energy region where a large narrow nonrelativistic resonance is "surrounded" by a number of smaller relativistic resonances. This disagreement occurs primarily because the three relativistic metastable states have differing threshold energies which results in the resonances being located at somewhat different energies. Thus, in a statistical average, instead of a single resonance, as in the *LS* case, there are three resonances "sharing" the oscillator strength which is more or less preserved.

As *Z* increases further, the energy shifts are expected to grow larger, and, looking at the comparison for S^{+12}, shown in Figure 5.3, this is true. Here, shifts in thresholds and resonances of about 0.2 Ryd (2.7 eV) are evident. And, for Fe^{+22}, shown in Figure 5.5 and Figure 5.6, the shifts of thresholds and resonances are as large as 1.6 Ryd, more than 20 eV are noted. And, for both S^{+12} and Fe^{+22} the discrepancies of the resonances for the excited state are evident, just as in the Ne^{+6} case discussed above. Furthermore, while only three of the higher members of the isoelectronic sequence are shown in detail, there is nothing special about those particular ions; the above discussion applies to all of the higher members of the sequence. In any case, it is clear that relativistic shifts become more and more important with increasing *Z*.

The relativistic splitting of the "target part" of the resonances, i.e. the splitting between different j in the resonance $nl_j n'l'_{j'}$, can be largely summarized by the splitting of the nl_j threshold levels for the different j values which the resonances will converge to. Figure 5.7 plots the scaled j splitting of the thresholds along the whole sequence. In Section 5.1, we have seen in Figure 5.1 that the scaled l splittings decay exponentially with Z; here, on the contrary, the scaled j splittings, which reflect the relativistic effects, increase as Z^2 along the sequence. Good fitting parameters were extracted when the second-order polynomial function

$$\frac{T_{nl_{j'}} - T_{nl_j}}{E_{\text{range}}} = c_0 + c_1 Z + c_2 Z^2 \tag{5.4}$$

was applied to these splittings. With the widened j splittings and the narrowed down l splittings (relative to E_{range}), we expect that the nl_j and the nl'_j thresholds, who have the same n and j but different l, will get closer when Z increases. Examples are $3p_{3/2}$ with $3d_{3/2}$, and $4d_{5/2}$ with $4f_{5/2}$. This might not be seen easily in all the cross section pictures, since the thresholds with the same n are already tightly close together, and the cross section is usually very messy with the narrow resonances near the thresholds. However, it is seen clearly in Table 4.1.

Figure 5.5 and Figure 5.6 give an enlarged view of the ground and metastable state cross sections of Fe^{+22} around the first n=3 resonances, where the splitting of resonances is clearly seen in the plots. Along with Figure 4.3 to Figure 4.8 for the light ions, the resonance splitting increases with Z along the sequence, as obviously seen in the figures. The very small splitting of resonances for B^+ and C^{+2}, seen in Figure 4.5 and Figure 4.6 respectively, are of the order of 100 meV. At the other end of the scale, for Fe^{+22}, the splittings of the resonances can be as large as of the order of 10 eV. The overlapping of resonance series is rather different in the *LS* and BP cases at the higher Z's. Thus, relativistic effects play an important role on perturbing the resonance

positions, splitting them into doublets, and changing the overlaps among resonance series converging to different states of the final-state ion. The details of the resonances, and how they change as a function of *Z*, will be reported in a different section.

5.3. Resonances

5.3.1. Identification of resonances

The concept of photoionization resonance is introduced in Subsection 2.1.3. The resonances in a cross section profile offer the important information of the atomic structure. As mentioned in Section 1.2, although the recent experiments have improved greatly the accuracy and the resolution of photon energy in cross section measurements, the experimental data is still insufficient to study the details of resonances, especially at the near-threshold energy range.

To describe a resonance profile, we use the resonance energy (position) E_r, the width Γ, and the effective quantum number ν (coupled with quantum defect μ) with respect to the threshold to which the Rydberg series converges. As described in Section 3.3, using the QB program, we find many resonances, each characterized by E_r and Γ, covering the energy range from the ionization threshold T_{2s} to the highest threshold in the present calculation $T_{4f_{7/2}}$, for all the ions. Note that there are an infinite number of resonances in each Rydberg series, so we have to specify the highest ν in each energy range in the calculation (see Section 3.3 for details). Our goal is to give each resonance a proper label (in the form $nl_jn'l'_{j'}$ in BP case, where we drop $1s^2$ for abbreviation) that corresponds to an excited discrete state. We have developed a systematic way of identification scheme, described below.

The resonances along a Rydberg series are expected to behave similarly, or at least evolve gradually as a function of principle quantum number *n*, unless perturbations from other series are

presented. In the energy range between T_{2s} and $T_{2p_{3/2}}$, perturbation by other series is weak compared to any other energy region, so we take this region as an example to describe how we identify the resonances. The first step is to divide these resonances to groups. For $^1S_0^e$ ground state photoionization, there are five Rydberg series converging to the $2p$ thresholds: $2p_{1/2}ns$, $2p_{3/2}ns$, $2p_{1/2}nd_{3/2}$, $2p_{3/2}nd_{3/2}$, and $2p_{3/2}nd_{5/2}$, so the resonances are divided to five groups, according to the regularity of their widths, energies, and shapes in cross section. Figure 5.8 clearly shows that for Fe^{+22}, in this energy range, there are five "rows" of resonances that are distinguished from one another. Each "row" then forms a group of a resonance series. Once every resonances is put into one of the five groups, the second step is to relate the groups to the thresholds which the resonances converge to. As shown in Figure 5.8, the members of two groups have nearly constant ν with respect to $T_{2p_{1/2}}$, while the members of the other three groups have nearly constant ν with respect to $T_{2p_{3/2}}$. Because $2p_{1/2}ns$ and $2p_{1/2}nd_{3/2}$ converge to $T_{2p_{1/2}}$, and $2p_{3/2}ns$, $2p_{3/2}nd_{3/2}$ and $2p_{3/2}nd_{5/2}$ converge to $T_{2p_{1/2}}$, we can easily separate the groups belonging to $2p_{1/2}nl_j$ and the groups belonging to $2p_{3/2}nl_j$, and the quantum defect μ for each resonance is calculated. Then in the third step, since the $|\mu|$ for $2p_jns$ should be larger than the $|\mu|$ for $2p_jnd_{j'}$ (see next subsection for details of quantum defects), the groups are further assigned, and now the only unlabeled groups are $2p_{3/2}nd_{3/2}$ and $2p_{3/2}nd_{5/2}$. Finally, we employ the fact that $2p_{3/2}nd_{5/2}$'s bound state energy is higher than $2p_{3/2}nd_{3/2}$'s. This fact comes from either a 4-electron bound level calculation or a table of experimental values. All the groups are thus identified and labeled.

The resonances in higher energy regions are identified in the same manner if the perturbation is not too strong. However, in the more strongly perturbed region, the regularities in position and width, which are seen in an unperturbed Rydberg series, are more or less destroyed. The positions are shifted and the widths are widened or narrowed through the interaction between the series converging to different thresholds. If two or more resonances are very close, they may overlap and the shapes are also distorted. In this case, the regularities in quantum defect is still informative, but how the perturbation affects the resonances needs to be understood and taken into account. Series perturbations and overlapping of resonances will be discussed in detail in Subsection 5.3.3.

We have characterized and identified the $2p_jnl_{j'}$ and the $3l_jnl'_{j'}$ resonances for all the 14 ions. Specifically, for the ground state photoionization where the final state is 1^o, there are 18 Rydberg series, which are $2p_{1/2}ns$, $2p_{3/2}ns$, $2p_{1/2}nd_{3/2}$, $2p_{3/2}nd_{3/2}$, $2p_{3/2}nd_{5/2}$, $3snp_{1/2}$, $3snp_{3/2}$, $3p_{1/2}ns$, $3p_{3/2}ns$, $3p_{1/2}nd_{3/2}$, $3p_{3/2}nd_{3/2}$, $3p_{3/2}nd_{5/2}$, $3d_{3/2}np_{1/2}$, $3d_{3/2}np_{3/2}$, $3d_{5/2}np_{3/2}$, $3d_{3/2}nf_{5/2}$, $3d_{5/2}nf_{5/2}$, and $3d_{5/2}nf_{7/2}$; for the metastable state photoionization, where the final state we are considering is 1^e, there are 17 Rydberg series, which are $2p_{1/2}np_{1/2}$, $2p_{1/2}np_{3/2}$, $2p_{3/2}np_{1/2}$, $2p_{3/2}np_{3/2}$, $2p_{3/2}nf_{5/2}$, $3sns$, $3snd_{3/2}$, $3p_{1/2}np_{1/2}$, $3p_{1/2}np_{3/2}$, $3p_{3/2}np_{1/2}$, $3p_{3/2}np_{3/2}$, $3p_{3/2}nf_{5/2}$, $3d_{3/2}ns$, $3d_{3/2}nd_{3/2}$, $3d_{3/2}nd_{5/2}$, $3d_{5/2}nd_{3/2}$, $3d_{5/2}nd_{5/2}$. The first five resonances in each $2p_jnl_{j'}$ series and the first three resonances in each $3l_jnl'_{j'}$ series are listed in Table 5.1 – Table 5.14 for the ground state photoionization and in Table 5.15 – Table 5.28 for the metastable state photoionization. For both states and for all the ions, it is clearly seen that the $2p_jnl_{j'}$ resonances are more “well aligned”, i.e., regular, than the $3l_jnl'_{j'}$

resonances. In the next two subsections, the general descriptions of their quantum defects and the perturbation between channels will be discussed.

5.3.2. Quantum defects of resonances

Some general observations on the quantum defects can be made. First, we notice that in each Rydberg series, μ converges to a constant value when *n* becomes very large. Second, μ for each resonance decreases with *Z*, as shown in Figure 5.9. The μ value when *n* goes to infinity is denoted as asymptotic quantum defect $\mu_{n\to\infty}$. Due to the facts stated above, we can focus our attention on these $\mu_{n\to\infty}$ in different channels and for different ions in the sequence. Figure 5.10 displays the $\mu_{n\to\infty}$ of the five $2p_jnl_{j'}$ series as functions of *Z*. These five $2p_jnl_{j'}$ series have less interaction between channels and less perturbation by higher resonances than the series converging to higher thresholds.

Looking at the top panel of Figure 5.10 for the ground state case, the two $2p_jns$ curves group together and the three $2p_jnd_{j'}$ curves group together since the different *j*'s curvers will merge into one in the nonrelativistic limit, while the curves of different *l* are widely separate. For all the ions, the $2p_jnd_{j'}$ resonances have much lower (absolute value of) quantum defects than what $2p_jns$ resonances have. For neutral Be, $\mu_{n\to\infty}$ for $2p_jns$ are between 0.6 and 0.7, and $|\mu_{n\to\infty}|$ of $2p_jnd_{j'}$ are lower than 0.1; for Fe^{+22}, these two values, correspondingly, are about 0.06 and less than 0.01. Similarly, this big difference between *s*-orbital (*l*=0) and *d*-orbital (*l*=2) of the photoelectron is seen in all the ions in between. The simple explanation is that when the *l* of the photoelectron is higher, its wave function is less penetrating into the wave function of the target (because of the centrifugal term $l(l+1)/r^2$ in Schrödinger equation), making the effective potential more hydrogenic, thus yielding a smaller quantum defect. When this fact is applied to

the metastable photoionization, the bottom panel of Figure 5.10 shows that the four $4p_jnp_{j'}$ series are grouped together, with much larger $|\mu_{n\to\infty}|$ than that of the $4p_jnf_{j'}$ series.

This basic rule also applies to higher resonances such as $3l_jn'l'_{j'}$ and $4l_jn'l'_{j'}$ too. However, the fact that the much compressed energy spacings between the thresholds accommodate more Rydberg series make more chances for the resonances to be strongly perturbed and to overlap. The seemingly randomness makes it difficult to extract $\mu_{n\to\infty}$ for these resonances shown in Figure 5.10.

To describe quantitatively the general appearance of $\mu_{n\to\infty}$ along the sequence, we have tried different fitting functions for $\mu_{n\to\infty}(Z)$ and found that the double exponential decay in the form of

$$\mu_{n\to\infty}(Z) = c_0 + c_1 \exp\left(-\frac{Z}{t_1}\right) + c_2 \exp\left(-\frac{Z}{t_2}\right) \tag{5.5}$$

works extremely well for all the $2p_jnd_{j'}$ series, except at the low Z end of the $2p_{3/2}nd_{3/2}$ and the $2p_{3/2}nd_{5/2}$ series where the curves exhibit a little bumpiness. For the $3l_jn'l'_{j'}$ resonances, although the $\mu_{n\to\infty}$ is already hard to obtain due to the strong perturbations experienced by the $3l_jn'l'_{j'}$ resonances, the form in Eq. (5.5) still works if $\mu_{n\to\infty}$ is replaced by the average μ over some large n, for example, the average of $\mu_{16},\cdots,\mu_{20}$.

5.3.3. Perturbation and overlapping of resonances

On one hand, since the resonance widths relative to the whole energy range decrease with Z, the narrower resonances are less likely to “touch” their neighbors, with more space around each one. On the other hand, as relativistic effects grow, the group of resonances of the same

nln'l', which are so close together at low *Z*, start to spread out because of the relativistic splitting. They now have more chance to "invade" other groups and to cause perturbations. In addition to using the regularities in Γ and ν, any perturbations must be taken into account in almost all the energy regions beyond $T_{2p_{3/2}}$ for all the ions. We now describe how the resonances change under the strong perturbative circumstances.

Consider a simple case with two resonances. Suppose their excited autoionizing states with wave functions φ_1 and φ_2, are nearly degenerate. As demonstrated in Subsection 2.1.3, the widths of these resonances represent the interaction strength between the continuum and corresponding excited states. In the absence of an interaction between φ_1 and φ_2, the widths of these two resonances are given by $\Gamma_1 = \pi\left|V_{1,E}\right|^2 = \pi\left|\left\langle\varphi_1\left|H\right|\psi_E\right\rangle\right|^2$ and $\Gamma_2 = \pi\left|V_{2,E}\right|^2 = \pi\left|\left\langle\varphi_2\left|H\right|\psi_E\right\rangle\right|^2$, and the energy levels are given by $E_1 = \left\langle\varphi_1\left|H\right|\varphi_1\right\rangle$ and $E_2 = \left\langle\varphi_2\left|H\right|\varphi_2\right\rangle$, following the notations given in Subsection 2.1.3, plus that the subscript of *V* includes the discrete state index 1 or 2. However, the actual total bound state is the linear combination of φ_1 and φ_2, which is given by

$$\varphi_\pm = \frac{1}{\sqrt{2}}\left(\varphi_1 \pm \varphi_2\right) \tag{5.6}$$

for exact degeneracy, i.e., $E_1 = E_2$. The total width is thus

$$\begin{aligned}\Gamma_\pm &= \pi\left|\left\langle\varphi_\pm\left|H\right|\psi_E\right\rangle\right|^2 \\ &= \frac{\pi}{2}\left(V_{1,E} \pm V_{2,E}\right)^2\end{aligned}. \tag{5.7}$$

In the case where the two resonances are about the same size ($V_{1,E} \approx V_{2,E}$), Γ is approximately $2\Gamma_1$ or 0, while in the case where one resonance is much bigger than the other one ($V_{1,E} >> V_{2,E}$), Γ is just Γ_1. The resonance position is given by

$$\begin{aligned} E_{\pm} &= \langle \varphi_{\pm} | H | \varphi_{\pm} \rangle \\ &= \frac{1}{2}(E_1 + E_2) \pm \mathrm{Re}(V_{12}) \end{aligned}, \tag{5.8}$$

which implies the interaction between the two channels shifts the position of each by the same amount from their original position. In the identification process for the resonances, the ideas presented above were brought out and practiced constantly.

Other than the perturbation and overlap between the resonances converging to the same principle quantum number, sometimes the resonances in a higher series may be located below a lower threshold and thus affects the lower series strongly. For example, as shown in Figure 5.11, when Z goes higher than five, the 4*s*4*p* (the total angular momentum j is omitted because relativistic effects are weak at such low Z) resonance starts moving into the energy region below $T_{3d_{5/2}}$, and shifts down further in higher Z's. Since 4*s*4*p* is much wider than any of the higher $3l_j nl'_{j'}$ resonances near the n=3 thresholds, its profile is cut apart into many pieces by these narrow resonances; more precisely speaking, the 4*s*4*p* profile becomes an envelope or a background of these resonances, and its own characteristics, such as position and width, are hard to read. However, the 3*s*3*p* resonance is never below $T_{2p_{3/2}}$, which further guarantees the "cleanness" of the $2p_j nl_{j'}$ resonance region.

5.4. Partial Cross Sections

Experiments up to now measure only the total photoionization cross section, but not the partial cross section to each target state. In the present work, the partial cross sections were calculated and analyzed along the sequence, which in turn gave us more of the physics of the atomic structure of our systems. The notation $\sigma_{nl_j}(E)$ is used throughout the whole dissertation as the partial cross section to $1s^2nl_j$ state, where the core orbitals $1s^2$ is omitted in the notation for simplicity. In the present atomic systems, there are 15 $1s^2nl_j$ states from $1s^22s$ to $1s^24f_{7/2}$. We have calculated these partial cross sections in the energy range between the ionization threshold and the $T_{4f_{7/2}}$ threshold for all 14 ions. Figure 5.12 shows the result for ground state Fe^{+22}. As a general feature found in all the ions, $\sigma_{2s}(E)$ is the main contribution to the total cross section, and its fraction increases monotonically with *Z*. This is reasonable because in the asymptotic condition where $Z \to \infty$, the system is hydrogenic and the ground state is simply $1s^22s^2$; the direct ionization will give only $1s^22s$ state as the target state.

To further study the composition of the total cross section in each ion, we have calculated the ratio of each partial cross section to $\sigma_{2s}(E)$. Furthermore, $\sigma_{nl_j}(E)$ for different *j* values are linearly combined into a $\sigma_{nl}(E)$ to effectively simplify the analysis. The notation $r_{nl}(E) \equiv \sigma_{nl}(E)/\sigma_{2s}(E)$ is used here and later. Figure 5.13 displays these ratios for ground state photoionization at the photon energy just above $T_{4f_{7/2}}$, to avoid the waviness due to the resonances, for different ions. The ratios are shown vs. $1/Z$ in order to show that the high-*Z* part of each curve converges to zero, the hydrogenic result. In this figure, one also notes that for each ion, the relative magnitudes of partial cross sections are generally in the same order as the contribution of each target state to the CI of the ground bound state. That is to say, $\sigma_{nl}(E)$ is

bigger, at around $E \approx T_{4f_{7/2}}$, if the contribution of *nl* target state to the ground state CI is bigger. While this is true, it does not suggest that the partial cross section and the target state contribution have a proportional relationship. As observed in Figure 5.13, $r_{2p}(E)$ is about 29% for Be. The fraction of $1s^2 2p^2$ in the ground state is about 10% in a MCHF calculation with 9 configurations. This comparison simply tells that the partial cross section contains more information than only the target states that go into the construction of the initial state.

However, the same ratios, or ratio patterns, in Figure 5.13 do not necessarily appear at other photon energies, especially the ones much higher than $T_{4f_{7/2}}$. To observe how the ratios change with photon energy, we have rescaled the photon energy by a $1/(Z-N)^2$ factor, where *Z* and *N* are the nuclear charge and the number of target electrons (=3 in our work) for each ion, respectively. The result for 4 widely different ions are presented in Figure 5.14. First we note that in general, all these ratio curves are higher at low *Z* and decrease when *Z* increases. For O^{+4}, as the lightest ion in the figure, all the ratios, in the whole range of photon energy, are higher than 3×10^{-4}, and the highest curve, $r_{2p}(E)$, is approximately 0.1 on average; for Fe^{+22} as the heaviest ion in the figure, most of the ratios are in the range between 10^{-5} and 10^{-4}, and $r_{2p}(E)$ is of the order of 0.01. The fact that all $r_{nl}(E)$ decrease with *Z* and $\sigma_{2s}(E)$ dominates at high Z further confirms what we conclude at $E \approx T_{4f_{7/2}}$ that when *Z* is infinity, the system becomes hydrogenic.

Other than the overall behavior of these ratios along *Z*, there are some complexities among the ratios as functions of *E*. First, all the ratios decrease with *E* except $r_{ns}(E)$; $r_{3s}(E)$ is a rising function during the whole energy range; $r_{4s}(E)$ is curvier but inclined in most energy

ranges; $r_{np}(E)$ and $r_{nd}(E)$ are all decreasing functions in almost the whole range, except $r_{4p}(E)$, which becomes an increasing function at some point. This fact suggests that when the photon energy increases, the system also behaves more like a hydrogenic system. However, the change from low to high energy is more complicated than the change from low *Z* to high *Z*, where the photon energy crosses many regions where the complex atomic structure strongly affects how the partial cross sections behave.

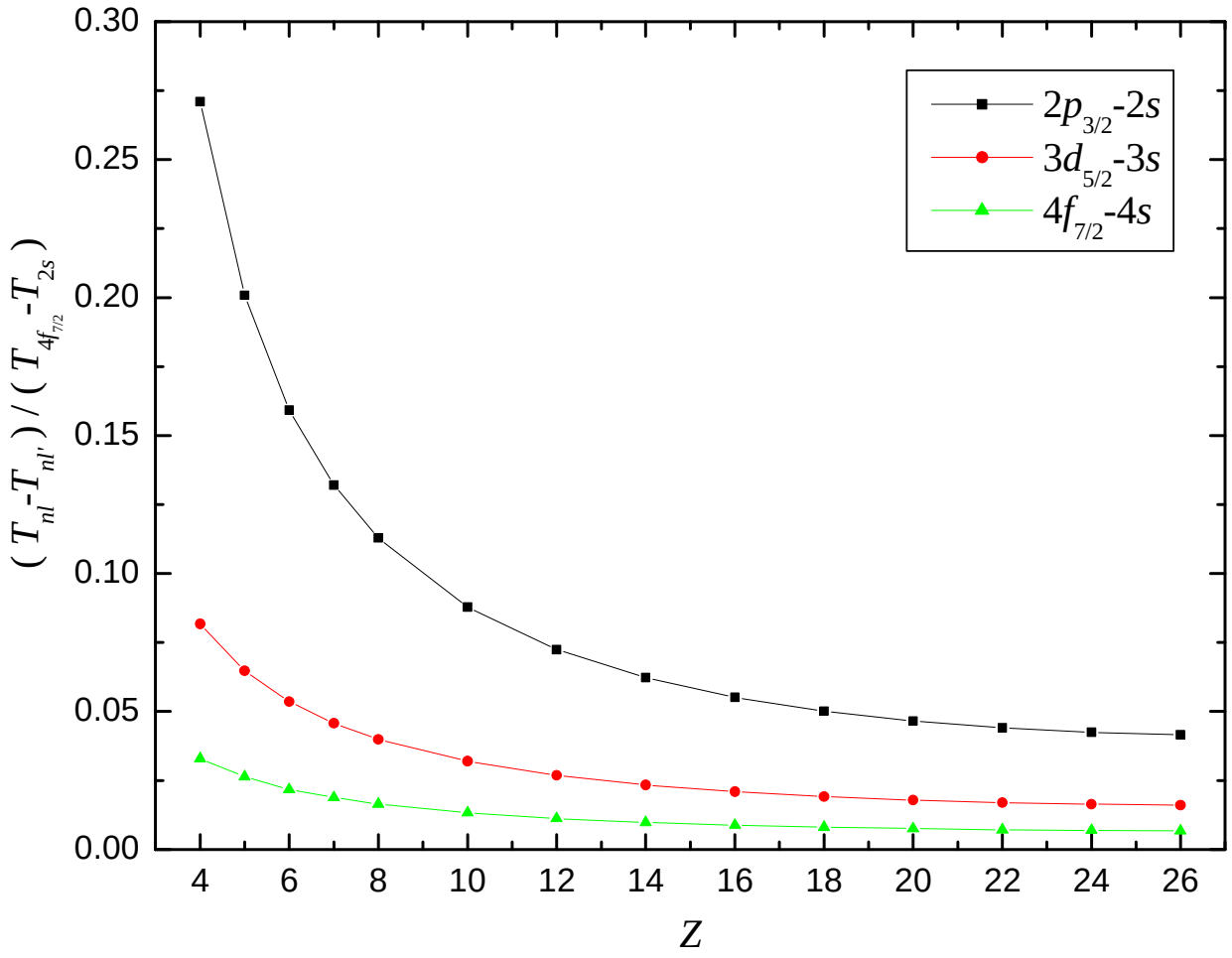

Figure 5.1. The energy difference between the *nl* and the *nl'* thresholds, scaled to the energy range from the 2*s* to the $4f_{7/2}$ threshold of each ion, where *l* is the lowest and *l'* the highest orbital angular momentum. *n*=2, 3, and 4 are shown.

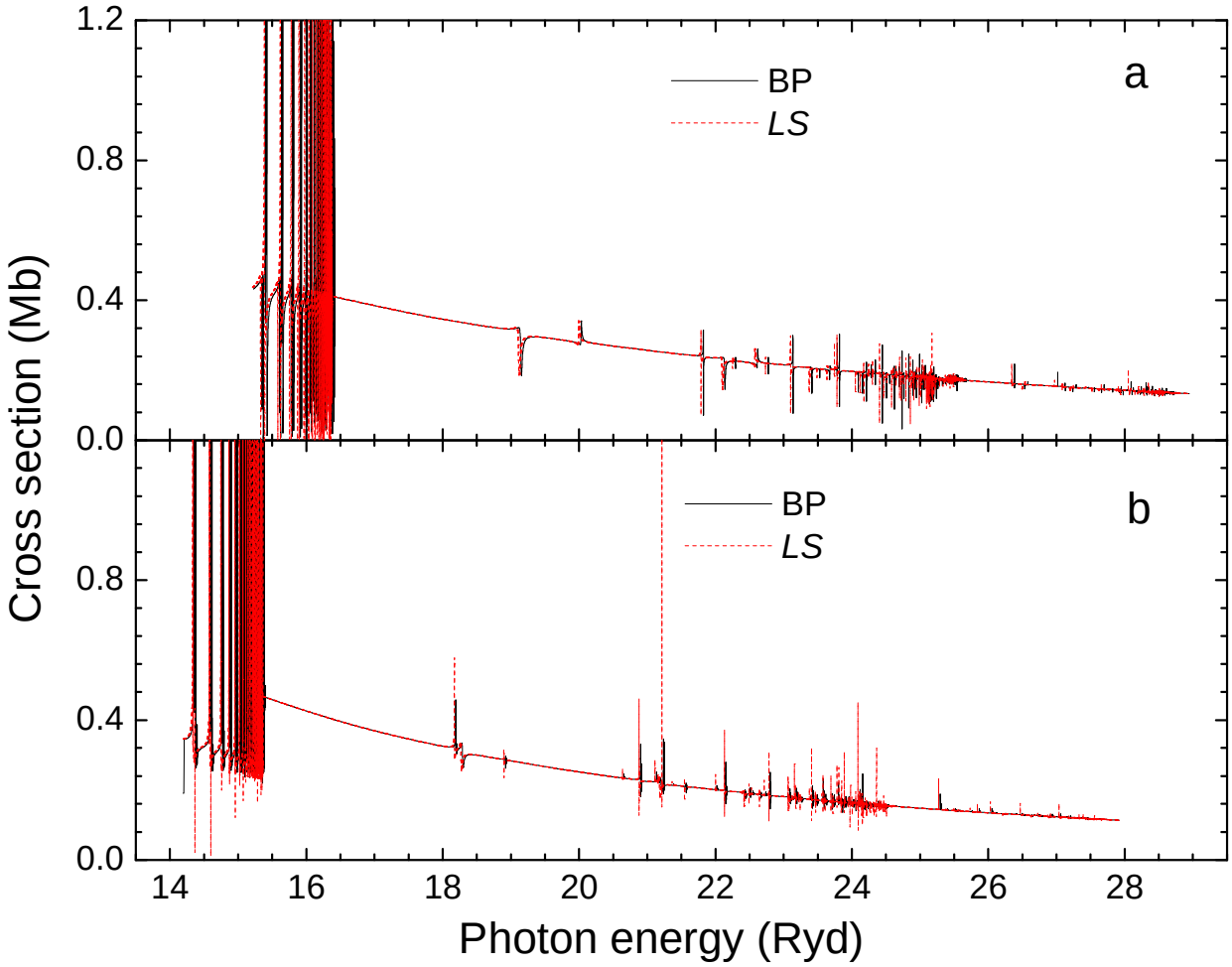

Figure 5.2. Photoionization cross sections of Ne^{+6} for (a) ground state, and (b) metastable state photoionization. The BP calculations are shown by solid lines, and the LS calculations are shown by dashed lines. The BP metastable state cross section is a statistical average of the three $^3P_j^o$ cross sections.

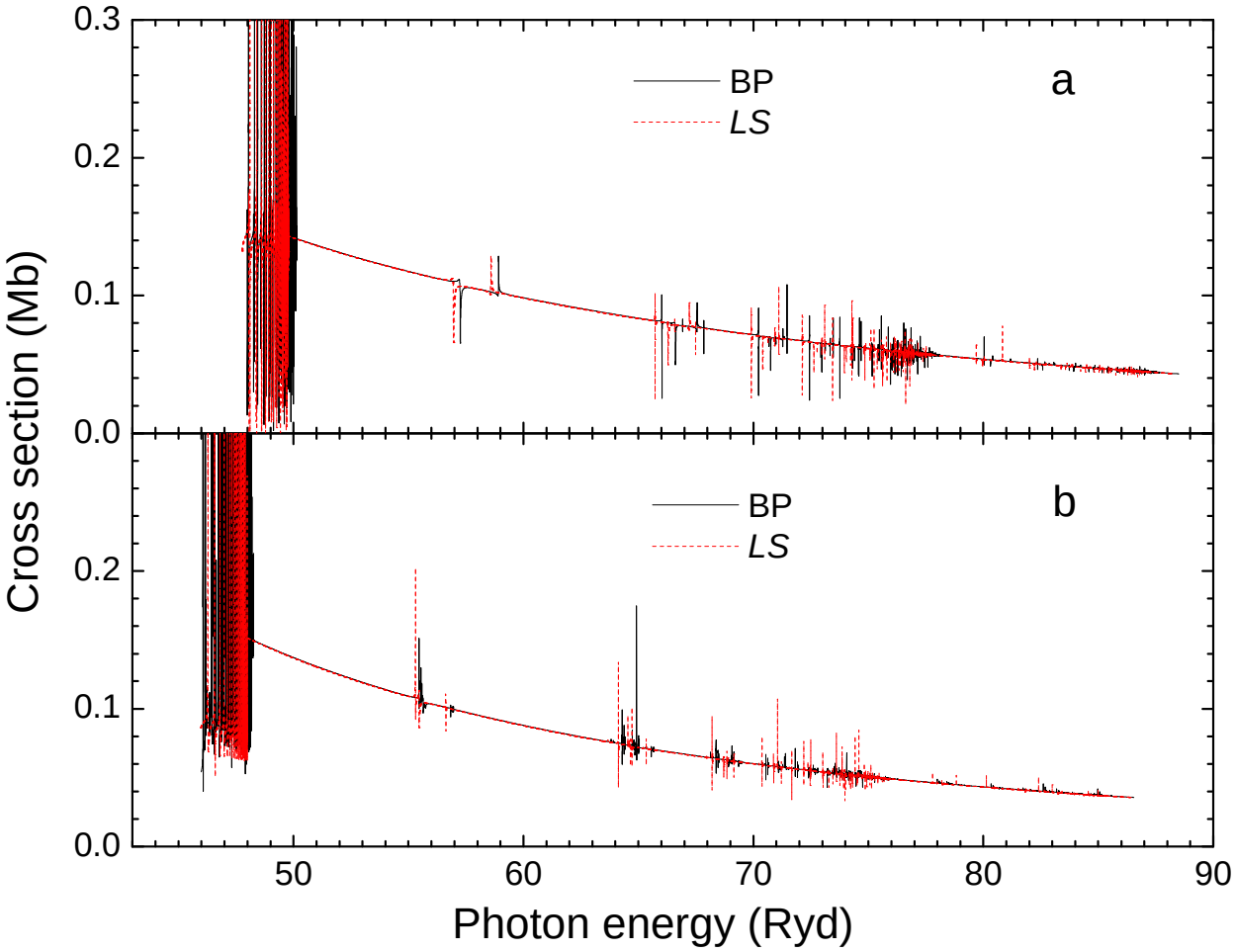

Figure 5.3. As Figure 5.2 for S^{+12}.

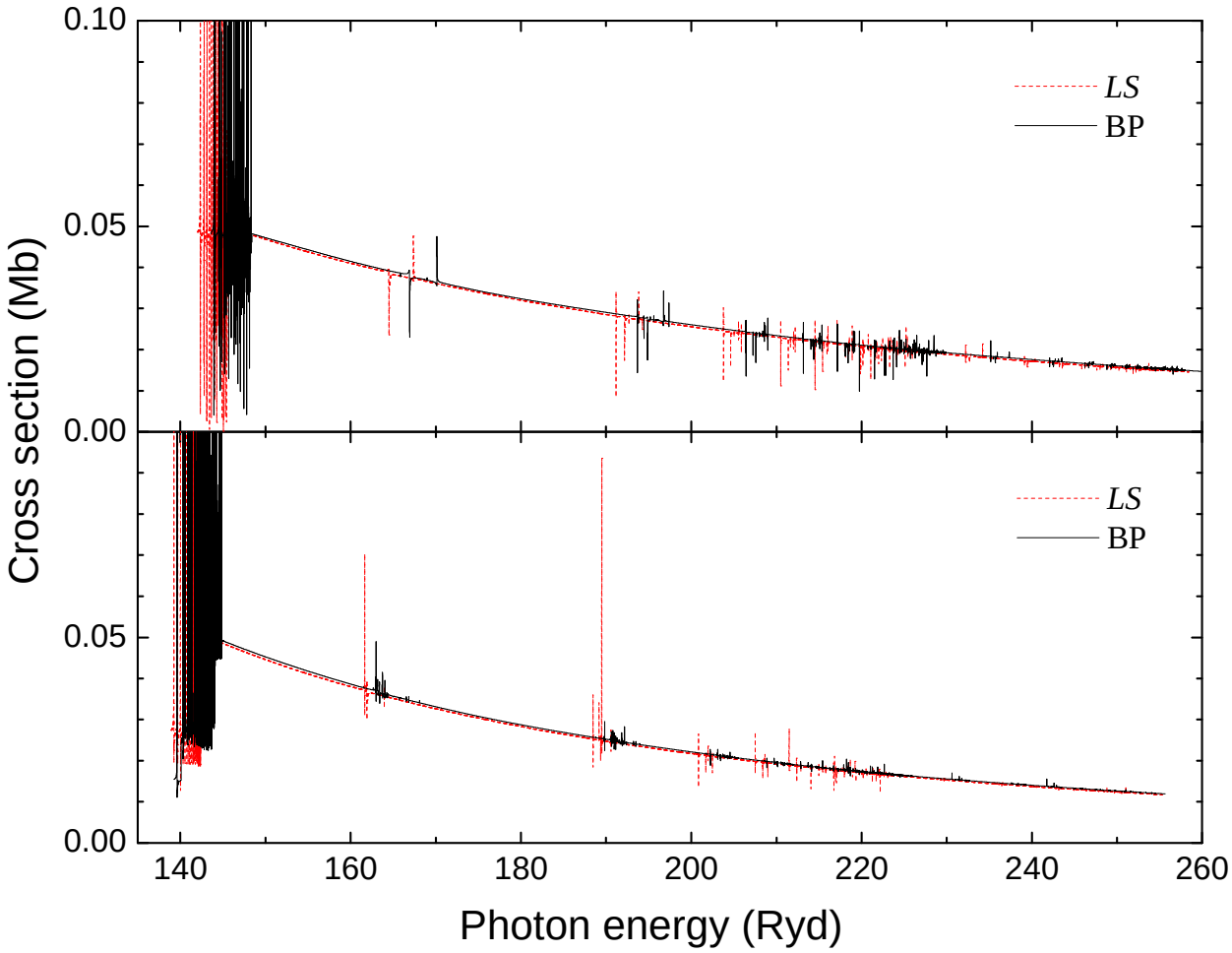

Figure 5.4. As Figure 5.2 for Fe^{+22}.

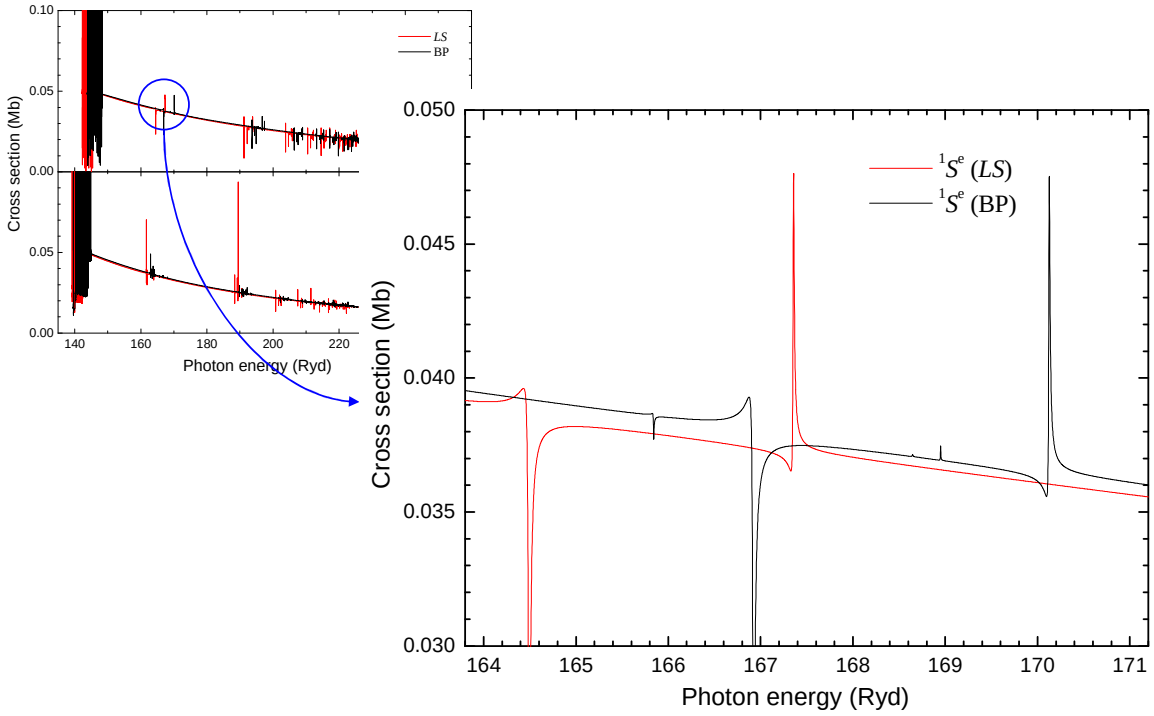

Figure 5.5. Close-up look of the $^1S_0^e$ cross section in Figure 5.4 around the 3*s*3*p* and 3*p*3*d* resonances.

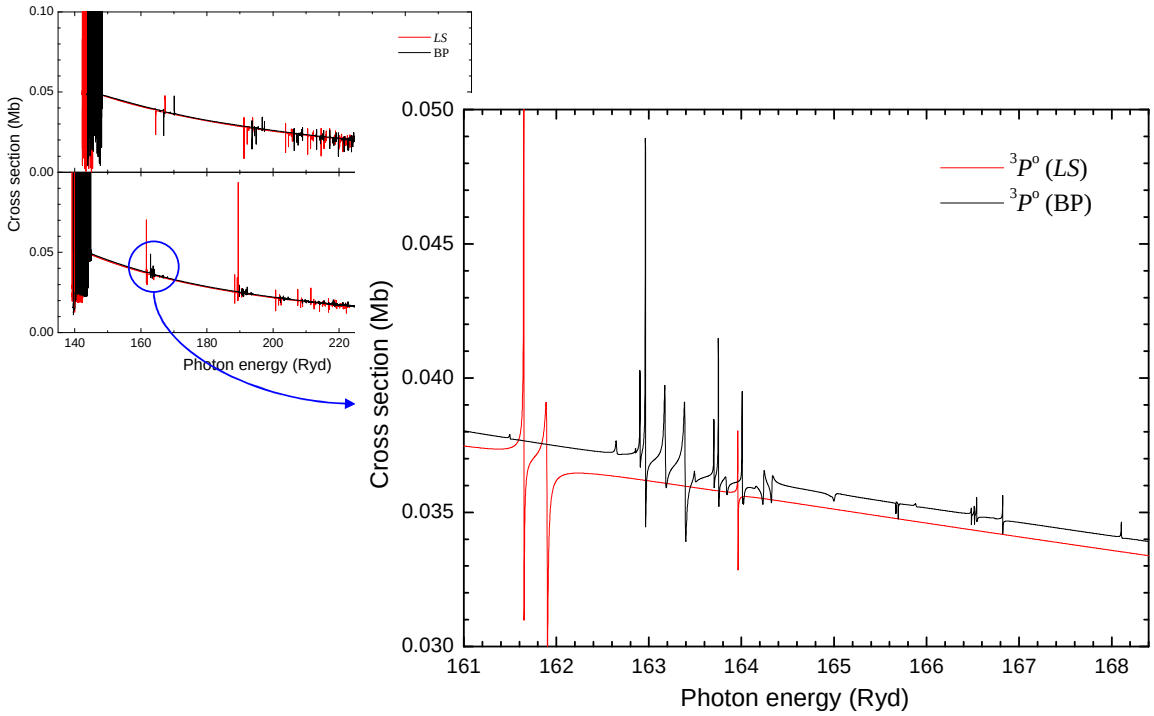

Figure 5.6. Close-up look of the $^3P^o$ cross section in Figure 5.4 around the 3*s*3*s* and 3*s*3*d* resonances.

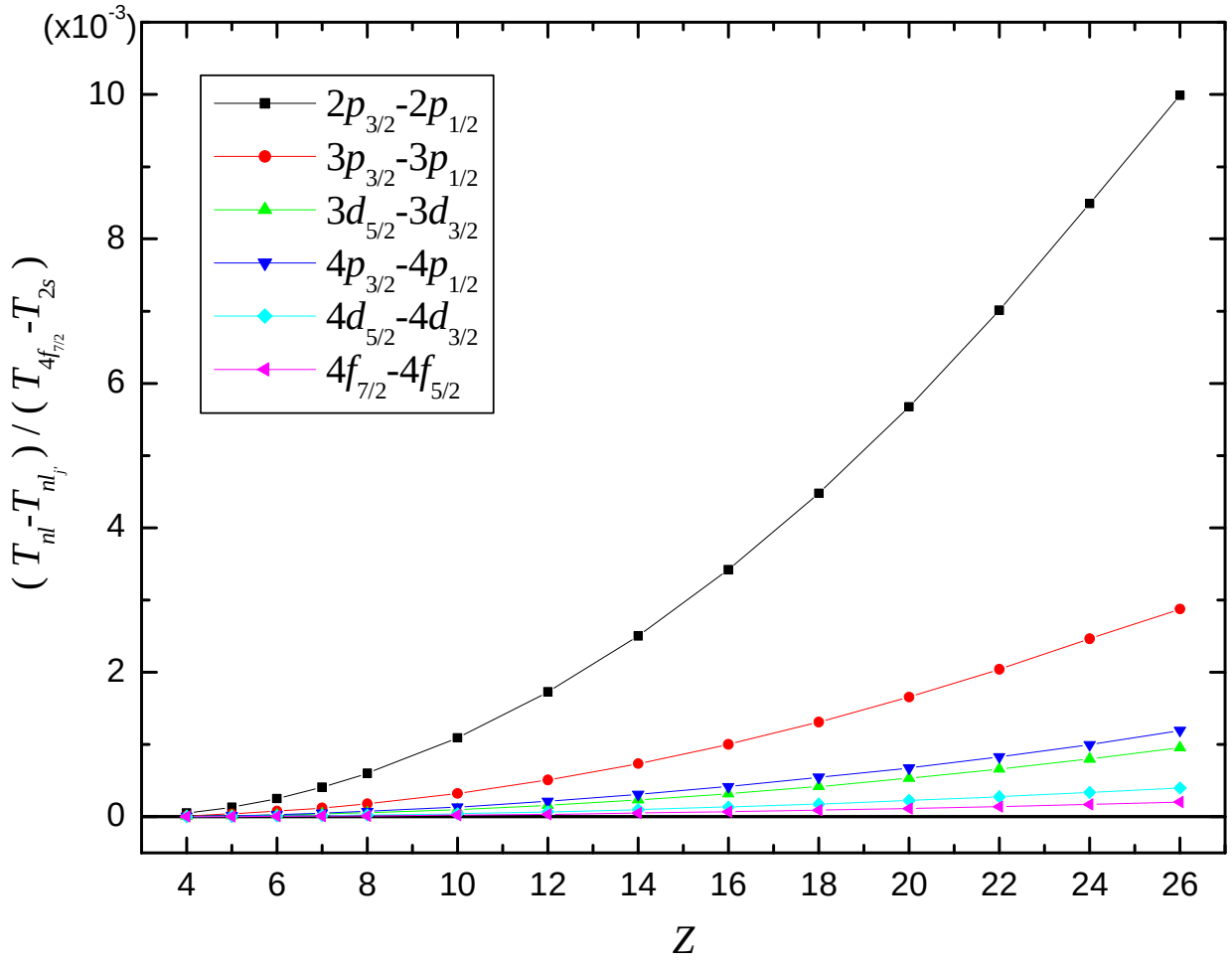

Figure 5.7. The energy difference between the nl_j and the $nl_{j'}$ thresholds, scaled to the energy range from the 2*s* to the $4f_{7/2}$ threshold of each ion.

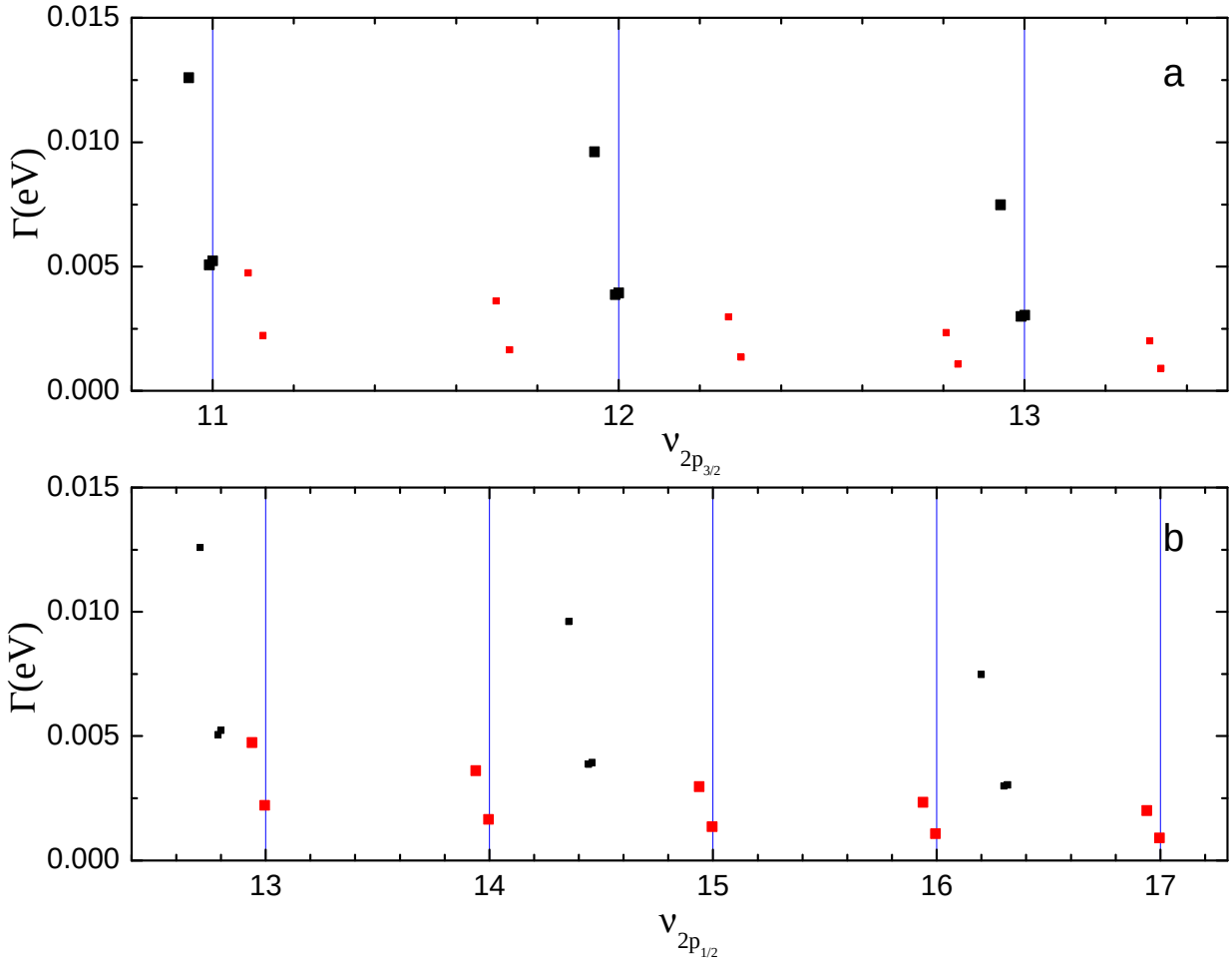

Figure 5.8. The widths and the positions of the first few photoionization resonances for Fe^{+22}. The positions are converted to the effective quantum number ν with respect to (a) $2p_{3/2}$ (b) $2p_{1/2}$ threshold. The larger dots in the lower (upper) panel represent the ones with nearly fixed ν and can be identified as among the series converging to the $2p_{1/2}$ ($2p_{3/2}$) threshold.

Table 5.1. The energy positions E_r (Ryd), the widths Γ (Ryd), and the quantum defects μ of $2l_j$ and $3l_j$ photoionization resonances for ground state Be.

	E_r	Γ	μ	E_r	Γ	μ
		$2p_{1/2}ns$			$2p_{3/2}ns$	
n = 3	0.779	6.26(-6)	7.42(-1)	0.803	3.61(-2)	5.92(-1)
4	0.882	5.63(-5)	7.22(-1)	0.890	1.15(-2)	5.88(-1)
5	0.921	5.26(-5)	7.15(-1)	0.924	5.25(-3)	5.85(-1)
6	0.940	3.24(-5)	7.11(-1)	0.941	2.80(-3)	5.88(-1)
7	0.950	2.18(-5)	7.09(-1)	0.951	1.67(-3)	5.91(-1)
		$2p_{1/2}nd_{3/2}$			$2p_{3/2}nd_{3/2}$	
n = 3				0.867	9.33(-4)	-3.66(-2)
4				0.914	4.62(-4)	-1.60(-2)
5	0.934	1.85(-2)	7.09(-2)	0.936	2.79(-4)	-6.74(-3)
6	0.947	1.95(-2)	6.89(-2)	0.948	1.66(-4)	-2.58(-3)
7	0.955	2.00(-2)	6.68(-2)	0.955	1.07(-4)	4.01(-4)
		$2p_{3/2}nd_{5/2}$				
n = 3	0.871	2.56(-5)	-9.79(-2)			
4	0.916	1.04(-5)	-9.51(-2)			
5	0.937	5.99(-6)	-9.11(-2)			
6	0.949	3.67(-6)	-9.01(-2)			
7	0.956	2.64(-6)	-8.89(-2)			
		$3snp_{1/2}$			$3snp_{3/2}$	
n = 3	1.241	4.77(-3)	9.62(-1)	1.292	1.20(-2)	7.05(-1)
4	1.378	1.31(-3)	8.90(-1)	1.385	1.49(-3)	7.77(-1)
5	1.419	4.85(-4)	1.01(0)	1.426	6.35(-4)	7.77(-1)
		$3p_{1/2}ns$			$3p_{3/2}ns$	
n = 4	1.457	8.01(-4)	8.54(-1)	1.468	2.64(-4)	6.58(-1)
5	1.503	2.82(-4)	7.27(-1)	1.500	1.71(-3)	8.44(-1)
6	1.522	1.48(-4)	6.86(-1)	1.525	5.86(-4)	4.69(-1)
		$3p_{1/2}nd_{3/2}$			$3p_{3/2}nd_{3/2}$	
n = 3	1.434	7.02(-4)	1.58(-1)	1.436	1.30(-3)	1.38(-1)
4	1.490	2.88(-4)	1.64(-1)	1.492	5.71(-4)	1.15(-1)
5	1.511	4.56(-6)	3.56(-1)	1.516	2.65(-4)	1.09(-1)
		$3p_{3/2}nd_{5/2}$				
n = 3	1.449	2.34(-3)	-2.61(-2)			
4	1.495	5.12(-3)	2.51(-2)			
5	1.519	2.21(-4)	-4.79(-2)			
		$3d_{3/2}np_{1/2}$			$3d_{3/2}np_{3/2}$	
n = 4				1.485	1.05(-3)	5.63(-1)
5	1.519	1.43(-4)	5.79(-1)	1.518	2.15(-4)	6.37(-1)
6	1.537	3.43(-5)	5.43(-1)	1.536	6.37(-6)	6.26(-1)
		$3d_{5/2}np_{3/2}$			$3d_{3/2}nf_{5/2}$	
n = 4	1.492	2.34(-3)	4.18(-1)			
5	1.524	3.92(-4)	3.48(-1)			
6	1.539	1.74(-4)	3.39(-1)			
		$3d_{5/2}nf_{5/2}$			$3d_{5/2}nf_{7/2}$	
n = 4				1.510	3.42(-4)	-6.16(-2)
5	1.529	1.46(-4)	4.80(-2)	1.533	1.08(-4)	-1.58(-1)
6	1.542	6.62(-5)	4.72(-2)	1.543	7.15(-5)	-1.05(-1)

Table 5.2. The energy positions E_r (Ryd), the widths Γ (Ryd), and the quantum defects μ of $2l_j$ and $3l_j$ photoionization resonances for ground state B^+.

	E_r	Γ	μ	E_r	Γ	μ
		$2p_{1/2}ns$			$2p_{3/2}ns$	
n = 4	1.97	1.73(-4)	4.73(-1)	1.981	1.79(-2)	3.98(-1)
5	2.09	1.45(-4)	4.68(-1)	2.100	8.18(-3)	4.01(-1)
6	2.16	7.17(-5)	4.65(-1)	2.162	4.17(-3)	4.03(-1)
7	2.20	5.21(-5)	4.63(-1)	2.198	2.47(-3)	4.05(-1)
8	2.22	4.39(-5)	4.60(-1)	2.220	1.58(-3)	4.07(-1)
		$2p_{1/2}nd_{3/2}$			$2p_{3/2}nd_{3/2}$	
n = 3				1.849	4.41(-3)	-1.15(-2)
4				2.039	2.12(-3)	7.17(-3)
5	2.126	9.24(-7)	5.01(-2)	2.129	1.29(-3)	1.59(-2)
6	2.176	2.45(-6)	4.76(-2)	2.178	6.38(-4)	2.12(-2)
7	2.207	4.41(-6)	4.55(-2)	2.207	3.82(-4)	2.43(-2)
		$2p_{3/2}nd_{5/2}$				
n = 3	1.872	2.47(-3)	-9.50(-2)			
4	2.050	1.29(-3)	-8.82(-2)			
5	2.135	8.46(-4)	-8.26(-2)			
6	2.181	4.32(-4)	-7.88(-2)			
7	2.210	2.62(-4)	-7.56(-2)			
		$3snp_{1/2}$			$3snp_{3/2}$	
n = 3	2.777	5.46(-3)	6.16(-1)	2.867	1.68(-2)	4.47(-1)
4	3.150	1.73(-3)	5.22(-1)	3.155	1.54(-3)	4.98(-1)
5	3.269	2.40(-4)	6.57(-1)			
		$3p_{1/2}ns$			$3p_{3/2}ns$	
n = 4	3.223	1.07(-3)	7.34(-1)	3.238	5.25(-3)	6.68(-1)
5	3.387	1.10(-4)	6.50(-1)	3.394	2.34(-3)	5.80(-1)
6	3.458	1.36(-4)	6.53(-1)	3.465	5.25(-4)	5.26(-1)
		$3p_{1/2}nd_{3/2}$			$3p_{3/2}nd_{3/2}$	
n = 3	3.013	5.08(-3)	3.87(-1)	3.023	3.03(-3)	3.63(-1)
4	3.280	8.09(-4)	4.53(-1)	3.293	4.14(-4)	3.83(-1)
5	3.404	4.63(-4)	4.62(-1)	3.421	2.56(-4)	2.47(-1)
		$3p_{3/2}nd_{5/2}$				
n = 3	3.110	4.92(-3)	1.39(-1)			
4	3.326	2.22(-3)	1.66(-1)			
5	3.443	2.15(-4)	-6.71(-2)			
		$3d_{3/2}np_{1/2}$			$3d_{3/2}np_{3/2}$	
n = 4	3.316	6.38(-4)	3.99(-1)	3.350	4.38(-4)	1.82(-1)
5	3.409	1.75(-4)	6.85(-1)	3.429	2.76(-4)	4.70(-1)
6						
		$3d_{5/2}np_{3/2}$			$3d_{3/2}nf_{5/2}$	
n = 4	3.368	1.80(-3)	4.61(-2)			
5	3.438	7.74(-4)	3.71(-1)			
6	3.504	3.90(-4)	2.31(-1)	3.507	4.00(-4)	1.49(-1)
		$3d_{5/2}nf_{5/2}$			$3d_{5/2}nf_{7/2}$	
n = 4				3.394	2.34(-3)	-1.64(-1)
5						
6	3.508	1.54E-3	1.24(-1)	3.513	8.69(-3)	5.75(-3)

Table 5.3. The energy positions E_r (Ryd), the widths Γ (Ryd), and the quantum defects μ of $2l_j$ and $3l_j$ photoionization resonances for ground state C^{+2}.

	E_r	Γ	μ	E_r	Γ	μ
		$2p_{1/2}ns$			$2p_{3/2}ns$	
n = 5	3.691	3.69(0)	3.51(-1)	3.700	9.52(-3)	3.08(-1)
6	3.826	3.83(0)	3.48(-1)	3.831	4.76(-3)	3.09(-1)
7	3.904	3.9(0)	3.45(-1)	3.907	2.84(-3)	3.11(-1)
8	3.954	3.95(0)	3.43(-1)	3.956	1.82(-3)	3.12(-1)
9	3.988	3.99(0)	3.41(-1)	3.989	1.22(-3)	3.14(-1)
		$2p_{1/2}nd_{3/2}$			$2p_{3/2}nd_{3/2}$	
n = 4	3.534	1.28(-6)	4.03(-2)	3.542	3.74(-3)	1.39(-2)
5	3.742	7.86(-6)	3.86(-2)	3.746	1.96(-3)	2.04(-2)
6	3.855	1.73(-5)	3.61(-2)	3.856	8.94(-4)	2.40(-2)
7	3.922	2.63(-5)	3.39(-2)	3.923	5.47(-4)	2.59(-2)
8	3.966	3.28(-5)	3.14(-2)	3.967	3.62(-4)	2.71(-2)
		$2p_{3/2}nd_{5/2}$				
n = 4	3.565	3.05(-3)	-6.82(-2)			
5	3.757	1.69(-3)	-6.16(-2)			
6	3.863	8.00(-4)	-5.72(-2)			
7	3.928	5.02(-4)	-5.39(-2)			
8	3.970	3.45(-4)	-5.08(-2)			
		$3snp_{1/2}$			$3snp_{3/2}$	
n = 3	4.877	5.86(-3)	4.56(-1)	5.005	1.94(-2)	3.31(-1)
4	5.565	8.81(-4)	4.22(-1)	5.578	2.13(-3)	3.88(-1)
5	5.803	1.11(-3)	5.99(-1)	5.829	2.88(-3)	4.70(-1)
		$3p_{1/2}ns$			$3p_{3/2}ns$	
n = 4	5.674	1.15(-3)	5.41(-1)	5.704	8.58(-3)	4.69(-1)
5	5.985	1.65(-4)	4.81(-1)	5.998	3.82(-3)	4.14(-1)
6	6.130	2.24(-4)	4.83(-1)	6.136	6.15(-4)	4.35(-1)
		$3p_{1/2}nd_{3/2}$			$3p_{3/2}nd_{3/2}$	
n = 3	5.230	3.37(-3)	2.57(-1)	5.213	6.05(-3)	2.77(-1)
4	5.840	7.10(-4)	8.08(-2)	5.855	7.39(-4)	3.12(-2)
5	6.067	2.73(-4)	-8.27(-3)	6.075	2.41(-4)	-6.04(-2)
		$3p_{3/2}nd_{5/2}$				
n = 3	5.381	7.60(-3)	6.61(-2)			
4	5.906	2.65(-3)	-1.60(-1)			
5	6.095	1.52(-3)	-2.09(-1)			
		$3d_{3/2}np_{1/2}$			$3d_{3/2}np_{3/2}$	
n = 4				5.744	2.82(-4)	4.74(-1)
5	6.017	4.39(-4)	5.30(-1)	6.036	5.75(-4)	4.34(-1)
6						
		$3d_{5/2}np_{3/2}$			$3d_{3/2}nf_{5/2}$	
n = 4	5.773	8.74(-4)	4.00(-1)	5.913	3.12(-6)	-2.91(-2)
5	6.043	6.14(-4)	3.96(-1)	6.109	3.75(-5)	-8.75(-3)
6						
		$3d_{5/2}nf_{5/2}$			$3d_{5/2}nf_{7/2}$	
n = 4	5.937	3.59(-5)	-1.19(-1)	5.971	3.63(-4)	-2.57(-1)
5	6.111	5.09(-5)	-2.65(-2)	6.114	7.61(-5)	-4.74(-2)
6						

Table 5.4. The energy positions E_r (Ryd), the widths Γ (Ryd), and the quantum defects μ of $2l_j$ and $3l_j$ photoionization resonances for ground state N^{+3}.

	E_r	Γ	μ	E_r	Γ	μ
		$2p_{1/2}ns$			$2p_{3/2}ns$	
n = 5	5.710	4.28(-3)	2.81(-1)	5.721	1.42(-1)	4.75(0)
6	5.939	3.34(-3)	2.78(-1)	5.946	7.12(-2)	5.75(0)
7	6.074	3.55(-3)	2.76(-1)	6.079	4.23(-2)	6.75(0)
8	6.160	3.63(-3)	2.74(-1)	6.164	2.68(-2)	7.75(0)
9	6.218	3.44(-3)	2.72(-1)	6.221	1.77(-2)	8.74(0)
		$2p_{1/2}nd_{3/2}$			$2p_{3/2}nd_{3/2}$	
n = 5	5.780	4.93(-4)	3.07(-2)	5.785	3.29(-2)	4.98(0)
6	5.979	8.26(-4)	2.82(-2)	5.983	1.53(-2)	5.98(0)
7	6.099	1.07(-3)	2.58(-2)	6.102	9.54(-3)	6.98(0)
8	6.177	1.16(-3)	2.33(-2)	6.179	6.37(-3)	7.98(0)
9	6.230	1.11(-3)	2.07(-2)	6.232	4.38(-3)	8.97(0)
		$2p_{3/2}nd_{5/2}$				
n = 5	5.802	3.05(-2)	5.05(0)			
6	5.992	1.50(-2)	6.04(0)			
7	6.107	9.76(-3)	7.04(0)			
8	6.183	6.79(-3)	8.04(0)			
9	6.234	4.83(-3)	9.03(0)			
		$3snp_{1/2}$			$3snp_{3/2}$	
n = 3	7.702	2.12(-2)	2.63(-1)	7.536	6.13(-3)	3.64(-1)
4	8.663	2.35(-3)	3.10(-1)	8.642	9.26(-4)	3.42(-1)
5	9.179	1.63(-4)	7.32(-1)	9.142	2.12(-4)	2.07(-1)
		$3p_{1/2}ns$			$3p_{3/2}ns$	
n = 4	8.782	1.21(-3)	4.29(-1)	8.827	1.03(-2)	3.65(-1)
5	9.276	7.00(-4)	4.15(-1)	9.284	2.54(-3)	3.92(-1)
6	9.529	3.19(-4)	3.90(-1)	9.535	1.28(-3)	3.59(-1)
		$3p_{1/2}nd_{3/2}$			$3p_{3/2}nd_{3/2}$	
n = 3	7.974	6.68(-3)	2.15(-1)	7.997	3.58(-3)	2.00(-1)
4	8.877	3.06(-4)	2.86(-1)	9.006	1.07(-3)	6.29(-2)
5	9.331	4.92(-4)	2.41(-1)	9.366	5.64(-4)	1.18(-1)
		$3p_{3/2}nd_{5/2}$				
n = 3	8.204	9.01(-3)	4.61(-2)			
4	9.072	4.80(-3)	-6.99(-2)			
5	9.396	1.29(-3)	7.20(-3)			
		$3d_{3/2}np_{1/2}$			$3d_{3/2}np_{3/2}$	
n = 4	8.917	7.16(-4)	3.15(-1)	8.961	1.03(-3)	2.43(-1)
5	9.378	5.11(-4)	2.76(-1)	9.410	2.83(-4)	1.67(-1)
6	9.614	4.36(-4)	2.33(-1)	9.620	2.53(-4)	1.97(-1)
		$3d_{5/2}np_{3/2}$			$3d_{3/2}nf_{5/2}$	
n = 4	8.991	3.36(-3)	1.94(-1)	9.105	1.43(-6)	-1.98(-2)
5	9.439	2.13(-3)	6.26(-2)	9.456	2.02(-5)	-5.66(-3)
6	9.624	1.02(-3)	1.73(-1)	9.648	8.98(-5)	1.85(-2)
		$3d_{5/2}nf_{5/2}$			$3d_{5/2}nf_{7/2}$	
n = 4	9.114	7.01(-4)	-3.93(-2)	9.136	1.32(-3)	-3.93(-2)
5	9.465	5.69(-5)	-3.90(-2)	9.482	2.06(-4)	-3.90(-2)
6	9.649	1.33(-4)	1.23(-2)	9.663	8.69(-4)	1.23(-2)

Table 5.5. The energy positions E_r (Ryd), the widths Γ (Ryd), and the quantum defects μ of $2l_j$ and $3l_j$ photoionization resonances for ground state O^{+4}.

	E_r	Γ	μ	E_r	Γ	μ
		$2p_{1/2}ns$			$2p_{3/2}ns$	
n = 6	8.499	6.57(-3)	2.32(-1)	8.509	7.63(-2)	2.13(-1)
7	8.705	6.8(-3)	2.30(-1)	8.712	4.47(-2)	2.15(-1)
8	8.837	6.34(-3)	2.28(-1)	8.843	2.81(-2)	2.16(-1)
9	8.926	5.44(-3)	2.27(-1)	8.931	1.85(-2)	2.16(-1)
10	8.989	4.48(-3)	2.27(-1)	8.994	1.28(-2)	2.17(-1)
		$2p_{1/2}nd_{3/2}$			$2p_{3/2}nd_{3/2}$	
n = 6	8.551	1.98(-3)	2.25(-2)			
7	8.738	2.24(-3)	2.01(-2)			
8	8.858	2.17(-3)	1.78(-2)			
9	8.941	1.92(-3)	1.58(-2)			
10	9.000	1.64(-3)	1.41(-2)			
		$2p_{3/2}nd_{5/2}$				
n = 6	8.556	1.84(-2)	2.07(-2)			
7	8.742	1.16(-2)	2.19(-2)			
8	8.863	7.80(-3)	2.26(-2)			
9	8.945	5.39(-3)	2.30(-2)			
10	9.004	3.84(-3)	2.33(-2)			
		$3snp_{1/2}$			$3snp_{3/2}$	
n = 3	10.755	6.31(-3)	3.03(-1)	10.958	2.24(-2)	2.19(-1)
4	12.378	9.75(-4)	2.87(-1)	12.406	2.49(-3)	2.58(-1)
5	13.091	9.27(-4)	2.32(-1)	13.094	1.00(-3)	2.26(-1)
		$3p_{1/2}ns$			$3p_{3/2}ns$	
n = 4	12.548	1.25(-3)	3.56(-1)	12.606	1.14(-2)	3.00(-1)
5	13.277	6.92(-4)	3.44(-1)	13.292	3.56(-3)	3.17(-1)
6	13.639	5.95(-4)	3.80(-1)	13.670	2.31(-3)	2.70(-1)
		$3p_{1/2}nd_{3/2}$			$3p_{3/2}nd_{3/2}$	
n = 3	11.294	7.11(-3)	1.77(-1)	11.324	3.72(-3)	1.64(-1)
4	12.668	3.35(-4)	2.34(-1)	12.717	6.62(-4)	1.82(-1)
5	13.347	5.36(-4)	1.96(-1)	13.372	1.40(-3)	1.43(-1)
		$3p_{3/2}nd_{5/2}$				
n = 3	11.587	1.01(-2)	3.59(-2)			
4	12.773	1.04(-3)	1.17(-1)			
5	13.380	8.80(-4)	1.26(-1)			
		$3d_{3/2}np_{1/2}$			$3d_{3/2}np_{3/2}$	
n = 4	12.809	3.67(-3)	1.61(-1)	12.828	1.21(-3)	1.39(-1)
5	13.445	4.62(-4)	1.45(-1)	13.453	2.64(-4)	1.26(-1)
6	13.764	4.98(-4)	1.93(-1)	13.782	1.73(-4)	1.24(-1)
		$3d_{5/2}np_{3/2}$			$3d_{3/2}nf_{5/2}$	
n = 4	12.934	5.79(-3)	1.19(-2)			
5	13.496	1.81(-3)	2.58(-2)	13.507	1.46(-5)	-2.97(-3)
6	13.791	5.65(-4)	8.83(-2)	13.808	5.66(-5)	1.35(-2)
		$3d_{5/2}nf_{5/2}$			$3d_{5/2}nf_{7/2}$	
n = 4	12.990	4.51(-5)	-6.14(-2)	13.053	1.68(-4)	-1.48(-1)
5	13.519	5.88(-5)	-3.33(-2)	13.552	3.64(-4)	-1.20(-1)
6	13.811	9.99(-5)	3.96(-3)	13.830	6.19(-4)	-8.04(-2)

Table 5.6. The energy positions E_r (Ryd), the widths Γ (Ryd), and the quantum defects μ of $2l_j$ and $3l_j$ photoionization resonances for ground state Ne^{+6}.

	E_r	Γ	μ	E_r	Γ	μ
		$2p_{1/2}ns$			$2p_{3/2}ns$	
n = 7	15.353	1.44(-2)	1.73(-1)	15.370	4.73(-2)	1.65(-1)
8	15.604	1.13(-2)	1.72(-1)	15.621	3.00(-2)	1.65(-1)
9	15.775	8.63(-3)	1.72(-1)	15.791	2.01(-2)	1.65(-1)
10	15.897	6.57(-3)	1.72(-1)	15.912	1.44(-2)	1.65(-1)
11	15.986	5.06(-3)	1.71(-1)	16.002	1.00(-2)	1.66(-1)
		$2p_{1/2}nd_{3/2}$			$2p_{3/2}nd_{3/2}$	
n = 7	15.400	5.25(-3)	1.30(-2)	15.414	1.51(-2)	1.84(-2)
8	15.636	4.36(-3)	1.15(-2)	15.650	1.02(-2)	1.88(-2)
9	15.798	3.38(-3)	1.04(-2)	15.811	7.07(-3)	1.90(-2)
10	15.913	1.68(-3)	9.74(-3)	15.927	5.03(-3)	1.92(-2)
11	15.999	2.35(-3)	8.89(-3)	16.013	3.70(-3)	1.93(-2)
		$2p_{3/2}nd_{5/2}$				
n = 7	15.423	1.67(-2)	-1.55(-2)			
8	15.656	1.13(-2)	-1.31(-2)			
9	15.816	7.81(-3)	-1.15(-2)			
10	15.930	5.55(-3)	-1.04(-2)			
11	16.015	4.06(-3)	-9.52(-3)			
		$3snp_{1/2}$			$3snp_{3/2}$	
n = 3	18.873	6.55(-3)	2.27(-1)	19.150	2.42(-2)	1.65(-1)
4	21.822	1.05(-3)	2.17(-1)	21.863	2.66(-3)	1.94(-1)
5	23.136	1.08(-3)	1.81(-1)	23.137	9.78(-4)	1.79(-1)
		$3p_{1/2}ns$			$3p_{3/2}ns$	
n = 4	22.051	1.32(-3)	2.66(-1)	22.137	1.29(-3)	2.22(-1)
5	23.389	7.19(-4)	2.56(-1)	23.414	4.41(-3)	2.33(-1)
6	24.086	5.07(-4)	2.47(-1)	24.093	1.16(-3)	2.40(-1)
		$3p_{1/2}nd_{3/2}$			$3p_{3/2}nd_{3/2}$	
n = 3	19.617	7.69(-3)	1.30(-1)	19.660	3.90(-3)	1.21(-1)
4	22.224	3.68(-4)	1.71(-1)	22.293	6.14(-4)	1.33(-1)
5	23.489	6.00(-4)	1.42(-1)	23.530	1.07(-3)	9.93(-2)
		$3p_{3/2}nd_{5/2}$				
n = 3	20.032	1.15(-2)	2.55(-2)			
4	22.421	4.07(-3)	5.52(-2)			
5	23.545	9.08(-4)	8.16(-2)			
		$3d_{3/2}np_{1/2}$			$3d_{3/2}np_{3/2}$	
n = 4	22.372	1.05(-3)	1.50(-1)	22.448	1.39(-3)	1.05(-1)
5	23.607	1.50(-3)	1.35(-1)	23.634	3.90(-4)	1.04(-1)
6	24.249	5.69(-4)	1.44(-1)	24.264	2.73(-4)	1.13(-1)
		$3d_{5/2}np_{3/2}$			$3d_{3/2}nf_{5/2}$	
n = 4	22.617	6.71(-3)	-1.07(-4)			
5	23.676	3.46(-3)	5.43(-2)	23.718	1.03(-5)	-3.77(-4)
6	24.282	1.37(-3)	7.66(-2)	24.312	3.30(-5)	9.10(-3)
		$3d_{5/2}nf_{5/2}$			$3d_{5/2}nf_{7/2}$	
n = 4	22.679	2.96(-5)	-4.16(-2)	22.775	1.37(-4)	-1.08(-1)
5	23.733	6.79(-5)	-1.76(-2)	23.784	3.13(-4)	-8.53(-2)
6	24.318	7.09(-5)	-2.04(-4)	24.345	4.31(-4)	-6.14(-2)

Table 5.7. The energy positions E_r (Ryd), the widths Γ (Ryd), and the quantum defects μ of $2l_j$ and $3l_j$ photoionization resonances for ground state Mg^{+8}.

	E_r	Γ	μ	E_r	Γ	μ
		$2p_{1/2}ns$			$2p_{3/2}ns$	
n = 8	24.263	1.48(-2)	1.39(-1)	24.300	3.27(-2)	1.34(-1)
9	24.542	1.06(-2)	1.38(-1)	24.579	2.04(-2)	1.34(-1)
10	24.741	7.81(-3)	1.38(-1)	24.777	1.46(-2)	1.34(-1)
11	24.887	5.88(-3)	1.38(-1)	24.923	1.07(-2)	1.34(-1)
12	24.998	4.54(-3)	1.38(-1)	25.034	8.09(-3)	1.34(-1)
		$2p_{1/2}nd_{3/2}$			$2p_{3/2}nd_{3/2}$	
n = 8	24.305	4.81(-3)	8.44(-3)	24.339	1.19(-2)	1.60(-2)
9	24.572	5.44(-3)	7.89(-3)	24.606	8.11(-3)	1.61(-2)
10	24.762	3.79(-3)	7.57(-3)	24.797	5.71(-3)	1.62(-2)
11	24.903	2.84(-3)	7.32(-3)	24.938	4.16(-3)	1.63(-2)
12	25.010	2.19(-3)	7.12(-3)	25.045	3.13(-3)	1.64(-2)
		$2p_{3/2}nd_{5/2}$				
n = 8	24.346	1.28(-2)	-7.81(-3)			
9	24.611	8.69(-3)	-6.87(-3)			
10	24.800	6.12(-3)	-6.18(-3)			
11	24.941	4.46(-3)	-5.65(-3)			
12	25.047	3.35(-3)	-5.21(-3)			
		$3snp_{1/2}$			$3snp_{3/2}$	
n = 3	29.235	6.69(-3)	1.82(-1)	29.589	2.54(-2)	1.32(-1)
4	33.904	1.12(-3)	1.74(-1)	33.955	2.77(-3)	1.56(-1)
5	35.998	1.25(-3)	1.47(-1)	36.002	1.10(-3)	1.45(-1)
		$3p_{1/2}ns$			$3p_{3/2}ns$	
n = 4	34.191	1.37(-3)	2.13(-1)	34.306	1.38(-2)	1.78(-1)
5	36.318	7.74(-4)	2.04(-1)	36.354	4.80(-3)	1.86(-1)
6	37.435	5.31(-4)	1.96(-1)	37.452	1.65(-3)	1.88(-1)
		$3p_{1/2}nd_{3/2}$			$3p_{3/2}nd_{3/2}$	
n = 3	30.189	8.05(-3)	1.03(-1)	30.246	4.03(-3)	9.59(-2)
4	34.420	3.89(-4)	1.34(-1)	34.510	5.92(-4)	1.05(-1)
5	36.451	6.53(-4)	1.11(-1)	36.507	1.02(-3)	7.77(-2)
		$3p_{3/2}nd_{5/2}$				
n = 3	30.726	1.25(-2)	2.04(-2)			
4	34.611	1.07(-3)	6.81(-2)			
5	36.526	9.27(-4)	6.34(-2)			
		$3d_{3/2}np_{1/2}$			$3d_{3/2}np_{3/2}$	
n = 4	34.674	4.32(-3)	9.72(-2)	34.709	1.51(-3)	8.41(-2)
5	36.606	1.56(-3)	1.09(-1)	36.641	4.28(-4)	8.30(-2)
6	37.653	6.19(-4)	1.15(-1)	37.672	3.24(-4)	9.04(-2)
		$3d_{5/2}np_{3/2}$			$3d_{3/2}nf_{5/2}$	
n = 4	34.937	7.36(-3)	-1.85(-3)			
5	36.705	3.67(-3)	3.82(-2)	36.751	9.75(-6)	3.40(-4)
6	37.681	1.74(-3)	8.36(-2)	37.737	2.16(-5)	6.18(-3)
		$3d_{5/2}nf_{5/2}$			$3d_{5/2}nf_{7/2}$	
n = 4	35.008	3.03(-5)	-3.03(-2)	35.139	1.21(-4)	-8.42(-2)
5	36.773	5.72(-5)	-1.41(-2)	36.837	2.79(-4)	-6.49(-2)
6	37.750	8.63(-5)	-6.55(-3)	37.780	3.34(-4)	-4.80(-2)

Table 5.8. The energy positions E_r (Ryd), the widths Γ (Ryd), and the quantum defects μ of $2l_j$ and $3l_j$ photoionization resonances for ground state Si^{+10}.

	E_r	Γ	μ	E_r	Γ	μ
		$2p_{1/2}ns$			$2p_{3/2}ns$	
n = 9	35.234	1.20(-2)	1.16(-1)	35.309	2.19(-2)	1.13(-1)
10	35.529	8.74(-3)	1.16(-1)	35.603	1.55(-2)	1.13(-1)
11	35.746	6.53(-3)	1.16(-1)	35.820	1.14(-2)	1.13(-1)
12	35.910	5.01(-3)	1.16(-1)	35.985	8.56(-3)	1.13(-1)
13	36.038	3.95(-3)	1.16(-1)	36.112	6.59(-3)	1.13(-1)
		$2p_{1/2}nd_{3/2}$			$2p_{3/2}nd_{3/2}$	
n = 9	35.271	5.98(-3)	6.64(-3)	35.343	8.91(-3)	1.39(-2)
10	35.556	4.31(-3)	6.47(-3)	35.628	6.26(-3)	1.40(-2)
11	35.766	3.22(-3)	6.35(-3)	35.838	4.56(-3)	1.41(-2)
12	35.926	2.47(-3)	6.22(-3)	35.999	3.41(-3)	1.42(-2)
13	36.051	1.95(-3)	6.04(-3)	36.123	2.59(-3)	1.43(-2)
		$2p_{3/2}nd_{5/2}$				
n = 9	35.349	9.33(-3)	-4.46(-3)			
10	35.632	6.58(-3)	-4.01(-3)			
11	35.842	4.80(-3)	-3.64(-3)			
12	36.001	3.61(-3)	-3.29(-3)			
13	36.125	2.78(-3)	-2.80(-3)			
		$3snp_{1/2}$			$3snp_{3/2}$	
n = 3	41.851	6.79(-3)	1.53(-1)	42.285	2.62(-2)	1.11(-1)
4	48.633	1.18(-3)	1.46(-1)	48.695	2.83(-3)	1.31(-1)
5	51.691	1.32(-3)	1.24(-1)	51.696	1.14(-3)	1.21(-1)
		$3p_{1/2}ns$			$3p_{3/2}ns$	
n = 4	48.980	1.41(-3)	1.78(-1)	49.125	1.44(-2)	1.49(-1)
5	52.079	8.67(-4)	1.69(-1)	52.128	4.97(-3)	1.56(-1)
6	53.712	6.13(-4)	1.62(-1)	53.741	1.79(-3)	1.57(-1)
		$3p_{1/2}nd_{3/2}$			$3p_{3/2}nd_{3/2}$	
n = 3	43.022	8.28(-3)	8.51(-2)	43.095	4.13(-3)	7.98(-2)
4	49.266	4.22(-4)	1.10(-1)	49.379	5.83(-4)	8.77(-2)
5	52.245	6.99(-4)	8.94(-2)	52.317	1.02(-3)	6.45(-2)
		$3p_{3/2}nd_{5/2}$				
n = 3	43.682	1.32(-2)	1.75(-2)			
4	49.500	1.09(-3)	5.74(-2)			
5	52.341	9.41(-4)	5.25(-2)			
		$3d_{3/2}np_{1/2}$			$3d_{3/2}np_{3/2}$	
n = 4	49.578	4.46(-3)	8.23(-2)	49.624	1.59(-3)	7.09(-2)
5	52.439	1.59(-3)	9.15(-2)	52.484	4.56(-4)	6.94(-2)
6	53.990	6.33(-4)	9.60(-2)	54.016	3.36(-4)	7.41(-2)
		$3d_{5/2}np_{3/2}$			$3d_{3/2}nf_{5/2}$	
n = 4	49.909	7.76(-3)	-1.01(-3)	49.916	5.53(-5)	-4.68(-3)
5	52.566	3.80(-3)	3.19(-2)			
6	54.038	1.87(-3)	6.07(-2)	54.095	2.24(-5)	4.57(-3)
		$3d_{5/2}nf_{5/2}$			$3d_{5/2}nf_{7/2}$	
n = 4	49.992	3.34(-5)	-2.32(-2)	50.157	1.15E	-6.82E-2
5	52.649	5.55(-5)	-1.08(-2)	52.726	2.63E	-5.16E-2
6	54.107	5.53(-5)	4.24(-4)	54.149	3.15E	-3.78E-2

Table 5.9. The energy positions E_r (Ryd), the widths Γ (Ryd), and the quantum defects μ of $2l_j$ and $3l_j$ photoionization resonances for ground state S^{+12}.

	E_r	Γ	μ	E_r	Γ	μ
		$2p_{1/2}ns$			$2p_{3/2}ns$	
n = 9				47.999	2.26(-2)	9.74(-2)
10	48.271	9.28(-3)	1.00(-1)	48.408	1.59(-2)	9.74(-2)
11	48.573	6.89(-3)	1.00(-1)	48.709	1.16(-2)	9.75(-2)
12	48.802	5.28(-3)	1.00(-1)	48.938	8.73(-3)	9.75(-2)
13	48.980	4.18(-3)	9.99(-2)	49.116	5.95(-3)	9.79(-2)
		$2p_{1/2}nd_{3/2}$			$2p_{3/2}nd_{3/2}$	
n = 9				48.039	9.26(-3)	1.23(-2)
10	48.303	4.55(-3)	5.73(-3)	48.437	6.43(-3)	1.24(-2)
11	48.597	3.37(-3)	5.67(-3)	48.731	4.65(-3)	1.25(-2)
12	48.821	2.59(-3)	5.55(-3)	48.955	3.44(-3)	1.26(-2)
13	48.994	2.08(-3)	5.21(-3)	49.129	2.34(-3)	1.25(-2)
		$2p_{3/2}nd_{5/2}$				
n = 9	48.046	9.60(-3)	-3.15(-3)			
10	48.442	6.70(-3)	-2.78(-3)			
11	48.735	4.87(-3)	-2.45(-3)			
12	48.958	3.66(-3)	-1.99(-3)			
13	49.133	2.94(-3)	-1.58(-2)			
		$3snp_{1/2}$			$3snp_{3/2}$	
n = 3	56.736	6.86(-3)	1.32(-1)	57.254	2.67(-2)	9.55(-2)
4	66.026	1.24(-3)	1.26(-1)	66.097	2.87(-3)	1.14(-1)
5	70.230	1.38(-3)	1.06(-1)	70.235	1.16(-3)	1.05(-1)
		$3p_{1/2}ns$			$3p_{3/2}ns$	
n = 4	66.433	1.48(-3)	1.53(-1)	66.611	1.48(-2)	1.30(-1)
5	70.686	1.01(-3)	1.44(-1)	70.753	4.99(-3)	1.35(-1)
6	72.933	6.94(-4)	1.39(-1)	72.980	1.85(-3)	1.35(-1)
		$3p_{1/2}nd_{3/2}$			$3p_{3/2}nd_{3/2}$	
n = 3	58.132	8.44(-3)	7.26(-2)	58.225	4.23(-3)	6.87(-2)
4	66.781	4.53(-4)	9.31(-2)	66.920	5.78(-4)	7.54(-2)
5	70.888	7.51(-4)	7.40(-2)	70.980	1.03(-3)	5.55(-2)
		$3p_{3/2}nd_{5/2}$				
n = 3	58.916	1.37(-2)	1.58(-2)			
4	67.062	1.11(-3)	4.99(-2)			
5	71.009	9.53(-4)	4.51(-2)			
		$3d_{3/2}np_{1/2}$			$3d_{3/2}np_{3/2}$	
n = 4	67.152	4.54(-3)	7.20(-2)	67.209	1.67(-3)	6.16(-2)
5	71.126	1.60(-3)	7.91(-2)	71.180	4.96(-4)	5.96(-2)
6	73.278	6.46(-4)	8.26(-2)	73.311	3.52(-4)	6.26(-2)
		$3d_{5/2}np_{3/2}$			$3d_{3/2}nf_{5/2}$	
n = 4	67.552	8.09(-3)	4.48(-4)			
5	71.280	3.89(-3)	2.84(-2)	71.345	1.37(-5)	-2.37(-6)
6	73.343	1.83(-3)	5.03(-2)	73.406	2.42(-5)	2.82(-3)
		$3d_{5/2}nf_{5/2}$			$3d_{5/2}nf_{7/2}$	
n = 4	67.562	1.03(-4)	-1.42(-3)	67.849	1.12(-4)	-5.69(-2)
5	71.380	5.76(-5)	-8.38(-3)	71.470	2.58(-4)	-4.22(-2)
6	73.423	5.05(-5)	-9.58(-5)	73.471	2.86(-4)	-3.10(-2)

Table 5.10. The energy positions E_r (Ryd), the widths Γ (Ryd), and the quantum defects μ of $2l_j$ and $3l_j$ photoionization resonances for ground state Ar^{+14}.

	E_r	Γ	μ	E_r	Γ	μ
		$2p_{1/2}ns$			$2p_{3/2}ns$	
n = 10	62.980	9.75(-3)	8.82(-2)	63.212	1.63(-2)	8.59(-2)
11	63.381	7.22(-3)	8.82(-2)	63.612	1.19(-2)	8.60(-2)
12	63.684	5.56(-3)	8.81(-2)	63.916	7.43(-3)	8.65(-2)
13	63.921	5.95(-3)	8.79(-2)	64.152	7.12(-3)	8.60(-2)
14	64.108	3.24(-3)	8.84(-2)	64.339	5.58(-3)	8.61(-2)
		$2p_{1/2}nd_{3/2}$			$2p_{3/2}nd_{3/2}$	
n = 10	63.018	4.76(-3)	5.19(-3)	63.246	6.61(-3)	1.11(-2)
11	63.409	3.51(-3)	5.13(-3)	63.637	4.73(-3)	1.12(-2)
12	63.706	2.73(-3)	4.89(-3)	63.935	1.64(-3)	1.16(-2)
13	63.936	3.42(-3)	1.36(-2)	64.167	2.86(-3)	1.12(-2)
14	64.121	1.57(-3)	5.78(-3)	64.351	2.22(-3)	1.13(-2)
		$2p_{3/2}nd_{5/2}$				
n = 10	63.252	6.84(-3)	-1.97(-3)			
11	63.642	4.97(-3)	-1.57(-3)			
12	63.941	4.20(-3)	-8.84(-3)			
13	64.170	2.96(-3)	-1.97(-3)			
14	64.353	2.32(-3)	-1.52(-3)			
		$3snp_{1/2}$			$3snp_{3/2}$	
n = 3	73.905	6.92(-3)	1.17(-1)	74.513	2.71(-2)	8.43(-2)
4	86.100	1.31(-3)	1.11(-1)	86.179	2.89(-3)	1.01(-1)
5				91.633	1.42(-3)	9.35(-2)
		$3p_{1/2}ns$			$3p_{3/2}ns$	
n = 4	86.568	1.57(-3)	1.35(-1)	86.783	1.50(-2)	1.16(-1)
5	92.159	1.18(-3)	1.26(-1)	92.251	4.91(-3)	1.19(-1)
6	95.117	7.67(-4)	1.22(-1)	95.190	1.86(-3)	1.19(-1)
		$3p_{1/2}nd_{3/2}$			$3p_{3/2}nd_{3/2}$	
n = 3	75.539	8.53(-3)	6.33(-2)	75.655	4.33(-3)	6.06(-2)
4	86.984	4.90(-4)	8.03(-2)	87.153	5.77(-4)	6.66(-2)
5	92.400	8.07(-4)	6.24(-2)	92.516	1.04(-3)	4.92(-2)
		$3p_{3/2}nd_{5/2}$				
n = 3	76.449	1.42(-2)	1.47(-2)			
4	87.415	4.57(-3)	3.07(-2)			
5	92.551	9.66(-4)	3.97(-2)			
		$3d_{3/2}np_{1/2}$			$3d_{3/2}np_{3/2}$	
n = 4	87.314	1.13(-3)	7.82(-2)	87.488	1.75(-3)	5.48(-2)
5	92.687	1.59(-3)	6.98(-2)	92.752	5.37(-4)	5.24(-2)
6	95.539	6.47(-4)	7.27(-2)	95.578	4.09(-4)	5.48(-2)
		$3d_{5/2}np_{3/2}$			$3d_{3/2}nf_{5/2}$	
n = 4	87.887	8.41(-3)	2.24(-3)			
5	92.869	3.94(-3)	2.64(-2)	92.945	1.97(-5)	-4.70(-4)
6	95.621	1.79(-3)	4.45(-2)	95.690	3.22(-5)	1.58(-3)
		$3d_{5/2}nf_{5/2}$			$3d_{5/2}nf_{7/2}$	
n = 4	88.005	4.03(-5)	-1.46(-2)	88.237	1.13(-4)	-4.84(-2)
5	92.988	5.86(-5)	-6.51(-3)	93.091	2.57(-4)	-3.53(-2)
6	95.714	4.94(-5)	3.07(-4)	95.768	2.77(-4)	-2.55(-2)

Table 5.11. The energy positions E_r (Ryd), the widths Γ (Ryd), and the quantum defects μ of $2l_j$ and $3l_j$ photoionization resonances for ground state Ca^{+16}.

	E_r	Γ	μ	E_r	Γ	μ
		$2p_{1/2}ns$			$2p_{3/2}ns$	
n = 10				80.041	1.67(-2)	7.69(-2)
11	80.185	7.58(-3)	7.88(-2)	80.554	1.16(-2)	7.71(-2)
12	80.575	6.34(-3)	7.92(-2)	80.943	9.40(-3)	7.70(-2)
13	80.877	4.24(-3)	7.91(-2)	81.246	7.22(-3)	7.71(-2)
14	81.117	3.44(-3)	7.91(-2)	81.486	5.77(-3)	7.70(-2)
		$2p_{1/2}nd_{3/2}$			$2p_{3/2}nd_{3/2}$	
n = 10				80.081	6.79(-3)	1.00(-2)
11	80.218	3.68(-3)	4.60(-3)	80.584	5.18(-3)	9.80(-3)
12	80.601	3.70(-3)	2.16(-3)	80.966	3.79(-3)	1.01(-2)
13	80.897	2.03(-3)	5.33(-3)	81.264	2.86(-3)	1.02(-2)
14	81.133	1.63(-3)	5.12(-3)	81.500	2.34(-3)	1.01(-2)
		$2p_{3/2}nd_{5/2}$				
n = 10	80.087	7.02(-3)	-1.39(-3)			
11	80.588	3.90(-3)	6.15(-4)			
12	80.970	3.89(-3)	-1.57(-3)			
13	81.267	2.97(-3)	-1.16(-3)			
14	81.502	2.40(-3)	-1.68(-3)			
		$3snp_{1/2}$			$3snp_{3/2}$	
n = 3	93.377	6.99(-3)	1.06(-1)	94.083	2.72(-2)	7.58(-2)
4	108.877	1.39(-3)	1.00(-1)	108.964	2.89(-3)	9.15(-2)
5				115.925	1.44(-3)	8.36(-2)
		$3p_{1/2}ns$			$3p_{3/2}ns$	
n = 4	109.408	1.71(-3)	1.21(-1)	109.666	1.50(-2)	1.06(-1)
5	116.520	1.36(-3)	1.12(-1)	116.649	4.78(-3)	1.07(-1)
6	120.289	8.21(-4)	1.08(-1)	120.400	1.86(-3)	1.07(-1)
		$3p_{1/2}nd_{3/2}$			$3p_{3/2}nd_{3/2}$	
n = 3	95.265	8.57(-3)	5.62(-2)	95.412	4.45(-3)	5.45(-2)
4	109.899	5.38(-4)	7.03(-2)	110.105	5.79(-4)	5.99(-2)
5	116.803	8.64(-4)	5.33(-2)	116.953	1.04(-3)	4.44(-2)
		$3p_{3/2}nd_{5/2}$				
n = 3	96.305	1.46(-2)	1.42(-2)			
4	110.395	4.55(-3)	2.89(-2)			
5	116.995	9.82(-4)	3.55(-2)			
		$3d_{3/2}np_{1/2}$			$3d_{3/2}np_{3/2}$	
n = 4	110.285	1.16(-3)	7.09(-2)	110.485	1.84(-3)	4.97(-2)
5	117.149	1.58(-3)	6.29(-2)	117.225	5.88(-4)	4.69(-2)
6	120.800	6.46(-4)	6.50(-2)	120.845	4.94(-4)	4.90(-2)
		$3d_{5/2}np_{3/2}$			$3d_{3/2}nf_{5/2}$	
n = 4	110.939	8.71(-3)	4.20(-3)	110.969	9.14(-5)	-2.90(-3)
5	117.362	3.95(-3)	2.53(-2)	117.449	2.92(-5)	-9.60(-4)
6	120.902	1.75(-3)	4.08(-2)	120.975	4.44(-5)	6.97(-4)
		$3d_{5/2}nf_{5/2}$			$3d_{5/2}nf_{7/2}$	
n = 4	111.083	4.45(-5)	-1.18(-2)	111.348	1.17(-4)	-4.18(-2)
5	117.503	5.88(-5)	-5.01(-3)	117.617	2.58(-4)	-2.99(-2)
6	121.009	4.66(-5)	9.53(-4)	121.068	2.75(-4)	-2.10(-2)

Table 5.12. The energy positions E_r (Ryd), the widths Γ (Ryd), and the quantum defects μ of $2l_j$ and $3l_j$ photoionization resonances for ground state Ti^{+18}.

	E_r	Γ	μ	E_r	Γ	μ
		$2p_{1/2}ns$			$2p_{3/2}ns$	
n = 11				99.562	1.25(-2)	7.01(-2)
12	99.487	5.49(-3)	7.20(-2)	100.048	9.36(-3)	7.02(-2)
13	99.865	4.41(-3)	7.19(-2)	100.425	7.22(-3)	7.01(-2)
14	100.164	3.56(-3)	7.19(-2)	100.724	5.76(-3)	7.02(-2)
15	100.405	2.59(-3)	7.21(-2)	100.965	4.68(-3)	7.02(-2)
		$2p_{1/2}nd_{3/2}$			$2p_{3/2}nd_{3/2}$	
n = 11				99.596	5.07(-3)	9.32(-3)
12	99.516	2.65(-3)	5.12(-3)	100.073	3.75(-3)	9.37(-3)
13	99.887	2.08(-3)	4.78(-3)	100.445	3.01(-3)	9.30(-3)
14	100.182	1.69(-3)	4.55(-3)	100.740	2.29(-3)	9.38(-3)
15	100.419	1.52(-3)	5.51(-3)	100.978	1.87(-3)	9.33(-3)
		$2p_{3/2}nd_{5/2}$				
n = 11	99.601	5.17(-3)	-1.33E(-3)			
12	100.078	3.87(-3)	-9.49(-4)			
13	100.448	3.07(-3)	-1.40(-3)			
14	100.742	2.38(-3)	-7.30(-4)			
15	100.980	1.93(-3)	-8.96(-4)			
		$3snp_{1/2}$			$3snp_{3/2}$	
n = 3	115.171	7.06(-3)	9.73(-2)	115.987	2.73(-2)	6.92(-2)
4	134.379	1.50(-3)	9.20(-2)	134.473	2.87(-3)	8.42(-2)
5				143.130	1.44(-3)	7.55(-2)
		$3p_{1/2}ns$			$3p_{3/2}ns$	
n = 4	134.975	1.90(-3)	1.10(-1)	135.285	1.49(-2)	9.81(-2)
5	143.797	1.53(-3)	1.00(-1)	143.976	4.64(-3)	9.76(-2)
6	148.471	8.59(-4)	9.78(-2)	148.632	1.91(-3)	9.83(-2)
		$3p_{1/2}nd_{3/2}$			$3p_{3/2}nd_{3/2}$	
n = 3	117.334	8.57(-3)	5.06(-2)	117.521	4.58(-3)	4.97(-2)
4	135.549	5.97(-4)	6.25(-2)	135.803	5.84(-4)	5.48(-2)
5	144.124	9.22(-4)	4.6(-2)	144.319	1.04(-3)	4.06(-2)
		$3p_{3/2}nd_{5/2}$				
n = 3	118.511	1.50(-2)	1.39(-2)			
4	136.115	4.48(-3)	2.80(-2)			
5	144.369	1.00(-3)	3.21(-2)			
		$3d_{3/2}np_{1/2}$			$3d_{3/2}np_{3/2}$	
n = 4	136.000	1.20(-3)	6.52(-2)	136.228	1.94(-3)	4.58(-2)
5	144.540	1.56(-3)	5.72(-2)	144.629	6.68(-4)	4.23(-2)
6	149.088	6.37(-4)	5.92(-2)	149.139	5.57(-4)	4.43(-2)
		$3d_{5/2}np_{3/2}$			$3d_{3/2}nf_{5/2}$	
n = 4	136.736	8.97(-3)	6.27(-3)	136.784	8.06(-5)	-2.63(-3)
5	144.787	3.93(-3)	2.44(-2)	144.885	4.41(-5)	-1.46(-3)
6	149.216	1.66(-3)	3.72(-2)	149.289	6.59(-5)	-1.57(-4)
		$3d_{5/2}nf_{5/2}$			$3d_{5/2}nf_{7/2}$	
n = 4	136.912	4.91(-5)	-9.37(-3)	137.211	1.24(-4)	-3.64(2)
5	144.951	6.00(-5)	-3.86(-3)	145.076	2.63(-4)	-2.57(-2)
6	149.338	4.98(-5)	1.05(-3)	149.401	2.70(-4)	-1.79(-2)

Table 5.13. The energy positions E_r (Ryd), the widths Γ (Ryd), and the quantum defects μ of $2l_j$ and $3l_j$ photoionization resonances for ground state Cr^{+20}.

	E_r	Γ	μ	E_r	Γ	μ
		$2p_{1/2}ns$			$2p_{3/2}ns$	
n = 11				120.670	1.25(-2)	6.46(-2)
12	120.444	5.78(-3)	6.62(-2)	121.262	8.16(-3)	6.49(-2)
13	120.905	4.58(-3)	6.60(-2)	121.723	7.38(-3)	6.45(-2)
14	121.270	5.06(-3)	6.56(-2)	122.087	5.90(-3)	6.44(-2)
15	121.563	2.91(-3)	6.58(-2)	122.381	4.76(-3)	6.43(-2)
		$2p_{1/2}nd_{3/2}$			$2p_{3/2}nd_{3/2}$	
n = 11				120.708	5.07(-3)	8.70(-3)
12	120.476	2.74(-3)	4.54(-3)	121.291	4.56(-3)	8.44(-3)
13	120.930	2.18(-3)	4.33(-3)	121.745	3.00(-3)	8.61(-3)
14	121.288	5.60(-4)	7.83(-3)	122.105	2.41(-3)	8.56(-3)
15	121.580	1.38(-3)	4.42(-3)	122.396	1.94(-3)	8.53(-3)
		$2p_{3/2}nd_{5/2}$				
n = 11	120.714	5.20(-3)	-8.18(-4)			
12	121.297	4.27(-3)	-2.86(-3)			
13	121.749	3.09(-3)	-6.81(-4)			
14	122.108	2.47(-3)	-7.59(-4)			
15	122.398	2.00(-3)	-7.00(-4)			
		$3snp_{1/2}$			$3snp_{3/2}$	
n = 3	139.315	7.15(-3)	9.07(-2)	140.254	2.72(-2)	6.41(-2)
4	162.634	1.63(-3)	8.57(-2)	162.738	2.81(-3)	7.86(-2)
5	173.280	1.42(-3)	6.89(-2)			
		$3p_{1/2}ns$			$3p_{3/2}ns$	
n = 4	163.297	2.15(-3)	1.02(-1)	163.671	1.46(-2)	9.27(-2)
5	174.020	1.66(-3)	9.09(-2)	174.264	4.50(-3)	8.99(-2)
6	179.695	8.88(-4)	8.96(-2)	179.906	1.57(-3)	9.56(-2)
		$3p_{1/2}nd_{3/2}$			$3p_{3/2}nd_{3/2}$	
n = 3	141.776	8.55(-3)	4.62(-2)	142.015	4.72(-3)	4.61(-2)
4	163.964	6.71(-4)	5.63(-2)	164.281	5.90(-4)	5.07(-2)
5	174.393	9.79(-4)	4.00(-2)	174.650	1.04(-3)	3.74(-2)
		$3p_{3/2}nd_{5/2}$				
n = 3	143.099	1.54(-2)	1.39(-2)			
4	164.609	4.34(-3)	2.76(-2)			
5	174.707	1.03(-3)	2.93(-2)			
		$3d_{3/2}np_{1/2}$			$3d_{3/2}np_{3/2}$	
n = 4	164.493	1.29(-3)	6.08(-2)	164.750	2.05(-3)	4.29(-2)
5	174.897	1.54(-3)	5.26(-2)	174.997	7.64(-4)	3.87(-2)
6	180.437	6.25(-4)	5.47(-2)	180.495	6.47(-4)	4.08(-2)
		$3d_{5/2}np_{3/2}$			$3d_{3/2}nf_{5/2}$	
n = 4	165.312	9.21(-3)	8.42(-3)			
5	175.181	3.86(-3)	2.39(-2)	175.287	6.46(-5)	-1.89(-3)
6	180.597	1.60(-3)	3.48(-2)	180.666	9.76(-5)	-7.21(-4)
		$3d_{5/2}nf_{5/2}$			$3d_{5/2}nf_{7/2}$	
n = 4				165.863	1.34(-4)	-3.19(-2)
5	175.371	5.96(-5)	-2.93(-3)	175.506	2.68(-4)	-2.22(-2)
6	180.735	5.44(-5)	1.28(-3)	180.802	2.72(-4)	-1.52(-2)

Table 5.14. The energy positions E_r (Ryd), the widths Γ (Ryd), and the quantum defects μ of $2l_j$ and $3l_j$ photoionization resonances for ground state Fe^{+22}.

	E_r	Γ	μ	E_r	Γ	μ
		$2p_{1/2}ns$			$2p_{3/2}ns$	
n = 11				143.927	1.26(-2)	5.92(-2)
12				144.636	9.61(-3)	5.93(-2)
13	144.044	4.73(-3)	6.08(-2)	145.187	7.48(-3)	5.94(-2)
14	144.481	3.61(-3)	6.10(-2)	145.624	5.91(-3)	5.95(-2)
15	144.833	2.97(-3)	6.10(-2)	145.976	4.70(-3)	5.96(-2)
		$2p_{1/2}nd_{3/2}$			$2p_{3/2}nd_{3/2}$	
n = 11				143.968	5.06(-3)	8.00(-3)
12				144.668	3.86(-3)	8.04(-3)
13	144.071	2.22(-3)	3.91(-3)	145.212	2.99(-3)	8.07(-3)
14	144.503	1.65(-3)	4.41(-3)	145.644	2.34(-3)	8.10(-3)
15	144.851	1.35(-3)	4.21(-3)	145.993	1.75(-3)	8.25(-3)
		$2p_{3/2}nd_{5/2}$				
n = 11	143.975	5.22(-3)	-4.93(-4)			
12	144.673	3.93(-3)	-6.21(-4)			
13	145.216	3.04(-3)	-6.34(-4)			
14	145.647	2.39(-3)	-5.38(-4)			
15	145.995	2.11(-3)	1.31(-4)			
		$3snp_{1/2}$			$3snp_{3/2}$	
n = 3	165.824	7.23(-3)	8.57(-2)	166.903	2.70(-2)	6.01(-2)
4	193.659	1.85(-3)	8.14(-2)	193.777	2.71(-2)	7.47(-2)
5	206.395	1.38(-3)	6.42(-2)	206.414	1.41(-2)	6.22(-2)
		$3p_{1/2}ns$			$3p_{3/2}ns$	
n = 4	194.411	2.43(-3)	9.59(-2)	194.858	1.42(-2)	8.92(-2)
5	207.225	1.76(-3)	8.42(-2)	207.550	4.33(-3)	8.47(-2)
6	214.015	8.95(-4)	8.14(-2)	214.351	1.41(-3)	8.01(-2)
		$3p_{1/2}nd_{3/2}$			$3p_{3/2}nd_{3/2}$	
n = 3	168.628	8.57(-3)	4.27(-2)	168.932	4.87(-3)	4.33(-2)
4	195.180	7.53(-4)	5.18(-2)	195.578	6.03(-4)	4.78(-2)
5	207.655	1.07(-3)	3.52(-2)	207.987	1.05(-3)	3.49(-2)
		$3p_{3/2}nd_{5/2}$				
n = 3	170.108	1.58(-2)	1.42(-2)			
4	195.913	4.14(-3)	2.81(-2)			
5	208.053	1.07(-3)	2.72(-2)			
		$3d_{3/2}np_{1/2}$			$3d_{3/2}np_{3/2}$	
n = 4	195.802	1.44(-3)	5.75(-2)	196.090	2.17(-3)	4.07(-2)
5	208.252	1.53(-3)	4.93(-2)	208.366	8.79(-4)	3.62(-2)
6	214.892	6.36(-4)	5.02(-2)	214.953	7.23(-4)	3.80(-2)
		$3d_{5/2}np_{3/2}$			$3d_{3/2}nf_{5/2}$	
n = 4	196.705	9.45(-3)	1.07(-2)			
5	208.582	3.78(-3)	2.38(-2)	208.694	8.91(-5)	-2.17(-3)
6	215.086	1.54(-3)	3.33(-2)	215.146	1.34(-4)	-9.41(-4)
		$3d_{5/2}nf_{5/2}$			$3d_{5/2}nf_{7/2}$	
n = 4	196.973	5.72(-5)	-5.52(-3)	197.342	1.43(-4)	-2.81(-2)
5	208.802	5.75(-5)	-2.11(-3)	208.947	2.67(-4)	-1.93(-2)
6	215.241	4.42(-5)	1.87(-3)	215.312	2.62(-4)	-1.27(-2)

Table 5.15. The energy positions E_r (Ryd), the widths Γ (Ryd), and the quantum defects μ of $2l_j$ and $3l_j$ photoionization resonances for metastable state Be.

	E_r	Γ	μ	E_r	Γ	μ
		$2p_{1/2}np_{1/2}$			$2p_{1/2}np_{3/2}$	
n = 3	0.612	6.95(-6)	5.26(-1)	0.620	9.13(-5)	4.62(-1)
4				0.696	5.44(-6)	4.40(-1)
5				0.727	1.97(-6)	4.31(-1)
6	0.743	1.49(-8)	4.66(-1)	0.743	5.84(-7)	4.27(-1)
7	0.752	2.05(-8)	4.61(-1)	0.752	3.42(-7)	4.25(-1)
		$2p_{3/2}np_{1/2}$			$2p_{3/2}np_{3/2}$	
n = 3	0.633	8.37(-4)	3.48(-1)			
4	0.701	3.96(-4)	3.35(-1)			
5	0.729	1.87(-4)	3.33(-1)	0.731	4.02(-8)	2.66(-1)
6	0.744	1.14(-4)	3.31(-1)	0.745	8.50(-8)	2.65(-1)
7	0.753	7.61(-5)	3.31(-1)	0.753	1.54(-7)	2.65(-1)
		$2p_{3/2}nf_{5/2}$				
n = 4	0.714	4.01(-7)	-2.87(-2)			
5	0.736	4.96(-7)	-2.67(-2)			
6	0.748	4.29(-7)	-2.67(-2)			
7	0.755	4.61(-7)	-2.65(-2)			
8	0.760	4.39(-7)	-2.64(-2)			
		$3sns$			$3snd_{3/2}$	
n = 3	1.100	1.76(-3)	6.55(-1)	1.126	1.02(-2)	4.59(-1)
4	1.155	6.35(-5)	1.18(0)	1.194	2.18(-4)	6.23(-1)
5	1.215	3.76(-5)	1.13(0)	1.232	2.28(-4)	5.07(-1)
		$3p_{1/2}np_{1/2}$			$3p_{1/2}np_{3/2}$	
n = 4	1.243	2.29(-4)	1.04(0)	1.245	8.18(-5)	1.02(0)
5	1.298	5.41(-5)	8.99(-1)			
6						
		$3p_{3/2}np_{1/2}$			$3p_{3/2}np_{3/2}$	
n = 4	1.255	6.87(-5)	8.73(-1)	1.260	3.88(-3)	7.99(-1)
5	1.298	3.46(-5)	8.94(-1)	1.308	3.82(-4)	5.25(-1)
6	1.318	2.60(-4)	9.51(-1)	1.320	9.47(-4)	8.09(-1)
		$3p_{3/2}nf_{5/2}$				
n = 4	1.295	7.31(-4)	1.38(-2)			
5	1.315	1.25(-4)	1.56(-1)			
6	1.328	5.74(-5)	1.48(-1)			
		$3d_{3/2}ns$				
n = 4	1.292	2.00(-5)	4.21(-1)			
5						
6						
		$3d_{3/2}nd_{3/2}$			$3d_{3/2}nd_{5/2}$	
n = 4	1.284	3.78(-4)	5.83(-1)	1.301	1.20(-3)	1.95(-1)
5	1.317	2.80(-5)	6.39(-1)	1.325	7.02(-5)	2.95(-1)
6	1.336	1.13(-4)	5.48(-1)	1.340	1.35(-4)	2.50(-1)
		$3d_{5/2}nd_{3/2}$			$3d_{5/2}nd_{5/2}$	
n = 4				1.310	8.21(-4)	-1.02(-1)
5	1.329	8.24(-5)	7.78(-2)	1.330	1.18(-3)	7.71(-3)
6	1.341	3.56(-5)	7.83(-2)	1.342	5.66(-4)	1.26(-2)

Table 5.16. The energy positions E_r (Ryd), the widths Γ (Ryd), and the quantum defects μ of $2l_j$ and $3l_j$ photoionization resonances for metastable state B^+.

	E_r	Γ	μ	E_r	Γ	μ
		$2p_{1/2}np_{1/2}$			$2p_{1/2}np_{3/2}$	
n = 4	1.654	1.51(-7)	3.11(-1)	1.659	5.14(-5)	2.80(-1)
5	1.767	2.90(-7)	3.00(-1)	1.769	2.86(-5)	2.73(-1)
6	1.825	4.47(-7)	2.93(-1)	1.826	2.92(-6)	2.70(-1)
7	1.859	7.37(-7)	2.88(-1)	1.859	1.08(-6)	2.67(-1)
8	1.880	1.10(-6)	2.83(-1)	1.881	7.67(-7)	2.65(-1)
		$2p_{3/2}np_{1/2}$			$2p_{3/2}np_{3/2}$	
n = 4	1.669	2.77(-3)	2.10(-1)	1.674	3.21(-2)	1.80(-1)
5	1.774	1.74(-3)	2.08(-1)	1.776	2.80(-6)	1.78(-1)
6	1.829	8.91(-4)	2.10(-1)	1.830	5.21(-6)	1.79(-1)
7	1.861	5.51(-4)	2.11(-1)	1.862	9.13(-6)	1.80(-1)
8	1.882	3.61(-4)	2.13(-1)	1.882	1.46(-5)	1.82(-1)
		$2p_{3/2}nf_{5/2}$				
n = 4	1.701	2.03(-5)	-2.64(-2)			
5	1.789	3.35(-5)	-2.42(-2)			
6	1.838	7.01(-6)	-2.23(-2)			
7	1.867	4.29(-6)	-2.18(-2)			
8	1.886	3.21(-6)	-2.15(-2)			
		$3sns$			$3snd_{3/2}$	
n = 3	2.541	1.58(-3)	4.15(-1)	2.583	1.18(-2)	3.19(-1)
4	2.756	4.17(-5)	7.70(-1)	2.771	2.24(-4)	7.03(-1)
5	2.944	3.72(-6)	4.77(-1)	2.956	2.62(-4)	3.27(-1)
		$3p_{1/2}np_{1/2}$			$3p_{1/2}np_{3/2}$	
n = 4	2.905	1.18(-4)	6.28(-1)	2.906	5.11(-4)	6.20(-1)
5	3.052	7.83(-5)	5.79(-1)	3.056	2.19(-4)	5.30(-1)
6						
		$3p_{3/2}np_{1/2}$			$3p_{3/2}np_{3/2}$	
n = 4	2.916	8.45(-5)	5.75(-1)	2.934	5.67(-3)	4.78(-1)
5	3.063	3.53(-5)	4.60(-1)	3.067	6.23(-5)	4.07(-1)
6						
		$3p_{3/2}nf_{5/2}$				
n = 4	2.982	2.79(-5)	1.83(-1)			
5	3.090	4.84(-5)	9.79(-2)			
6	3.143	1.85(-3)	7.45(-2)			
		$3d_{3/2}ns$				
n = 4	2.996	1.54(-5)	2.66(-1)			
5	3.104	1.07(-5)	2.66(-1)			
6	3.156	4.39(-5)	3.68(-1)			
		$3d_{3/2}nd_{3/2}$			$3d_{3/2}nd_{5/2}$	
n = 4	2.928	1.13(-4)	6.40(-1)	3.009	1.55(-4)	1.77(-1)
5	3.080	3.17(-5)	5.60(-1)	3.110	4.45(-5)	1.88(-1)
6	3.146	2.72(-4)	5.97(-1)	3.167	5.52(-4)	1.28(-1)
		$3d_{5/2}nd_{3/2}$			$3d_{5/2}nd_{5/2}$	
n = 4	3.023	3.37(-5)	7.30(-2)	3.030	3.60(-4)	1.95(-2)
5	3.115	3.60(-3)	1.09(-1)	3.116	7.53(-4)	9.79(-2)
6	3.172	2.97(-6)	-2.1(-3)	3.173	2.77(-4)	-3.01(-2)

Table 5.17. The energy positions E_r (Ryd), the widths Γ (Ryd), and the quantum defects μ of $2l_j$ and $3l_j$ photoionization resonances for metastable state C^{+2}.

	E_r	Γ	μ	E_r	Γ	μ
		$2p_{1/2}np_{1/2}$			$2p_{1/2}np_{3/2}$	
n = 5	3.234	2.47(-6)	2.21(-1)	3.247	2.98(-5)	1.34(-1)
6	3.359	3.46(-6)	2.15(-1)	3.366	5.54(-5)	1.31(-1)
7	3.432	5.38(-6)	2.10(-1)	3.437	9.65(-5)	1.27(-1)
8	3.479	6.62(-6)	2.07(-1)	3.483	1.33(-4)	1.20(-1)
9	3.511	6.47(-6)	2.04(-1)	3.514	1.47(-4)	1.10(-1)
		$2p_{3/2}np_{1/2}$			$2p_{3/2}np_{3/2}$	
n = 5	3.237	5.32(-5)	2.08(-1)	3.245	3.47(-3)	1.58(-1)
6	3.360	4.94(-6)	2.09(-1)	3.365	1.64(-3)	1.60(-1)
7	3.433	4.44(-6)	2.12(-1)	3.436	9.74(-4)	1.62(-1)
8	3.480	7.57(-6)	2.16(-1)	3.482	5.86(-4)	1.66(-1)
9	3.512	1.46(-5)	2.21(-1)	3.513	3.54(-4)	1.71(-1)
		$2p_{3/2}nf_{5/2}$				
n = 4	3.072	7.02(-5)	-2.13(-2)			
5	3.271	5.76(-5)	-1.88(-2)			
6	3.380	7.75(-6)	-1.70(-2)			
7	3.446	7.88(-6)	-1.64(-2)			
8	3.489	7.04(-6)	-1.60(-2)			
		$3sns$			$3snd_{3/2}$	
n = 3	4.550	1.54(-3)	3.04(-1)	4.605	1.23(-2)	2.42(-1)
4	5.021	4.37(-5)	5.75(-1)	5.127	2.76(-4)	3.09(-1)
5	5.334	3.80(-5)	5.47(-1)	5.377	3.08(-4)	3.18(-1)
		$3p_{1/2}np_{1/2}$			$3p_{1/2}np_{3/2}$	
n = 4	5.229	1.39(-4)	4.57(-1)	5.237	5.92(-4)	4.38(-1)
5	5.516	9.56(-5)	4.23(-1)	5.527	2.60(-4)	3.67(-1)
6	5.641	5.20(-6)	5.72(-1)	5.662	5.68(-5)	3.76(-1)
		$3p_{3/2}np_{1/2}$			$3p_{3/2}np_{3/2}$	
n = 4	5.258	2.20(-4)	3.83(-1)	5.272	6.43(-3)	3.46(-1)
5	5.532	2.84(-3)	3.38(-1)	5.536	1.32(-4)	3.15(-1)
6	5.663	6.56(-5)	3.62(-1)	5.670	1.27(-3)	2.97(-1)
		$3p_{3/2}nf_{5/2}$				
n = 4	5.346	3.65(-5)	1.29(-1)			
5	5.575	1.04(-4)	7.97(-2)			
6	5.696	2.76(-5)	6.23(-3)			
		$3d_{3/2}ns$				
n = 4	5.399	1.37(-4)	9.03(-2)			
5	5.601	6.08(-5)	1.77(-1)			
6	5.721	9.37(-5)	1.88(-1)			
		$3d_{3/2}nd_{3/2}$			$3d_{3/2}nd_{5/2}$	
n = 4	5.287	1.52(-5)	4.17(-1)	5.366	1.19(-5)	1.96(-1)
5	5.560	1.51(-5)	4.14(-1)	5.601	2.17(-5)	1.77(-1)
6	5.711	2.08(-5)	2.99(-1)	5.719	4.11(-5)	2.15(-1)
		$3d_{5/2}nd_{3/2}$			$3d_{5/2}nd_{5/2}$	
n = 4	5.411	3.16(-5)	4.81(-2)	5.422	2.88(-4)	1.07(-2)
5	5.615	4.87(-5)	8.67(-2)	5.622	3.85(-4)	4.06(-2)
6	5.723	1.40(-5)	1.69(-1)	5.728	6.99(-4)	1.09(-1)

Table 5.18. The energy positions E_r (Ryd), the widths Γ (Ryd), and the quantum defects μ of $2l_j$ and $3l_j$ photoionization resonances for metastable state N^{+3}.

	E_r	Γ	μ	E_r	Γ	μ
		$2p_{1/2}np_{1/2}$			$2p_{1/2}np_{3/2}$	
n = 5	5.125	1.20(-5)	1.75(-1)	5.129	8.28(-5)	1.61(-1)
6	5.341	1.54(-5)	1.69(-1)	5.343	1.77(-5)	1.57(-1)
7	5.469	2.02(-5)	1.65(-1)	5.471	2.97(-5)	1.52(-1)
8	5.552	2.00(-5)	1.63(-1)	5.553	5.91(-5)	1.46(-1)
9	5.607	1.72(-5)	1.62(-1)	5.608	9.22(-5)	1.40(-1)
		$2p_{3/2}np_{1/2}$			$2p_{3/2}np_{3/2}$	
n = 5	5.140	4.76(-3)	1.30(-1)	5.143	1.61(-4)	1.17(-1)
6	5.350	2.11(-3)	1.32(-1)	5.352	3.01(-4)	1.19(-1)
7	5.475	1.15(-3)	1.36(-1)	5.476	4.08(-4)	1.20(-1)
8	5.555	6.49(-4)	1.42(-1)	5.557	4.13(-4)	1.21(-1)
9	5.610	3.62(-4)	1.47(-1)	5.611	3.56(-4)	1.21(-1)
		$2p_{3/2}nf_{5/2}$				
n = 5	5.178	7.57(-5)	-1.48(-2)			
6	5.372	1.35(-5)	-1.33(-2)			
7	5.489	1.85(-5)	-1.25(-2)			
8	5.565	1.74(-5)	-1.21(-2)			
9	5.617	1.36(-5)	-1.18(-2)			
		$3sns$			$3snd_{3/2}$	
n = 3	7.121	1.56(-3)	2.40(-1)	7.188	1.25(-2)	1.95(-1)
4	7.945	5.05(-5)	4.61(-1)	8.087	3.27(-4)	2.46(-1)
5	8.471	2.42(-5)	3.85(-1)	8.529	2.23(-4)	1.97(-1)
		$3p_{1/2}np_{1/2}$			$3p_{1/2}np_{3/2}$	
n = 4	8.213	1.51(-4)	3.60(-1)	8.227	6.13(-4)	3.40(-1)
5	8.686	1.09(-4)	3.34(-1)	8.688	1.90(-4)	3.28(-1)
6	8.928	6.79(-5)	3.02(-1)	8.931	9.35(-5)	2.84(-1)
		$3p_{3/2}np_{1/2}$			$3p_{3/2}np_{3/2}$	
n = 4	8.254	2.56(-4)	2.99(-1)	8.270	6.81(-3)	2.72(-1)
5	8.693	7.10(-5)	3.15(-1)	8.707	3.05(-3)	2.69(-1)
6	8.934	3.40(-5)	2.74(-1)	8.938	1.46(-3)	2.47(-1)
		$3p_{3/2}nf_{5/2}$				
n = 4	8.372	3.62(-5)	9.68(-2)			
5	8.771	7.28(-5)	4.08(-2)			
6	8.973	4.49(-5)	3.04(-2)			
		$3d_{3/2}ns$				
n = 4	8.397	1.44(-5)	1.55(-1)			
5	8.802	9.40(-5)	1.38(-1)			
6	9.011	3.60(-5)	1.55(-1)			
		$3d_{3/2}nd_{3/2}$			$3d_{3/2}nd_{5/2}$	
n = 4	8.290	2.00(-5)	3.32(-1)	8.423	2.94(-4)	1.07(-1)
5	8.742	8.46(-5)	3.41(-1)	8.803	1.82(-5)	1.36(-1)
6	8.979	6.22(-5)	3.40(-1)	9.017	8.91(-5)	1.17(-1)
		$3d_{5/2}nd_{3/2}$			$3d_{5/2}nd_{5/2}$	
n = 4	8.441	5.87(-5)	7.32(-2)	8.475	3.03(-4)	8.50(-3)
5	8.824	5.39(-5)	5.74(-2)	8.831	3.13(-4)	3.07(-2)
6	9.017	3.52(-5)	1.14(-1)	9.024	4.82(-4)	7.09(-2)

Table 5.19. The energy positions E_r (Ryd), the widths Γ (Ryd), and the quantum defects μ of $2l_j$ and $3l_j$ photoionization resonances for metastable state O^{+4}.

	E_r	Γ	μ	E_r	Γ	μ
		$2p_{1/2}np_{1/2}$			$2p_{1/2}np_{3/2}$	
n = 6	7.772	4.65(-5)	1.39(-1)	7.775	6.9(-5)	1.28(-1)
7	7.969	4.92(-5)	1.37(-1)	7.971	1.43(-4)	1.22(-1)
8	8.096	4.34(-5)	1.36(-1)	8.098	2.22(-4)	1.17(-1)
9	8.182	3.49(-5)	1.35(-1)	8.183	2.37(-4)	1.13(-1)
10	8.243	2.74(-5)	1.34(-1)	8.244	2.08(-4)	1.11(-1)
		$2p_{3/2}np_{1/2}$			$2p_{3/2}np_{3/2}$	
n = 6	7.783	2.25(-3)	1.15(-1)	7.786	8.89(-4)	1.02(-1)
7	7.976	1.19(-3)	1.21(-1)	7.979	8.66(-4)	1.03(-1)
8	8.101	6.15(-4)	1.25(-1)	8.104	7.22(-4)	1.03(-1)
9	8.187	3.20(-4)	1.28(-1)	8.189	5.63(-4)	1.03(-1)
10	8.248	1.81(-4)	1.30(-1)	8.249	4.33(-4)	1.03(-1)
		$2p_{3/2}nf_{5/2}$				
n = 6	7.813	2.91(-5)	-1.07(-2)			
7	7.996	3.89(-5)	-9.88(-3)			
8	8.115	3.45(-5)	-9.45(-3)			
9	8.196	2.59(-5)	-9.19(-3)			
10	8.255	1.90(-5)	-9.02(-3)			
		$3sns$			$3snd_{3/2}$	
n = 3	10.254	1.59(-3)	1.99(-1)	10.332	1.27(-2)	1.64(-1)
4	11.527	5.71(-5)	3.85(-1)	11.704	3.73(-4)	2.06(-1)
5	12.281	4.13(-5)	3.57(-1)	12.369	2.63(-4)	1.68(-1)
		$3p_{1/2}np_{1/2}$			$3p_{1/2}np_{3/2}$	
n = 4	11.856	1.59(-4)	2.98(-1)	11.875	6.23(-4)	2.78(-1)
5	12.560	1.18(-4)	2.75(-1)	12.564	2.09(-4)	2.66(-1)
6	12.923	7.51(-5)	2.51(-1)	12.932	1.34(-4)	2.17(-1)
		$3p_{3/2}np_{1/2}$			$3p_{3/2}np_{3/2}$	
n = 4	11.907	2.82(-4)	2.46(-1)	11.927	7.05(-3)	2.25(-1)
5				12.584	2.91(-4)	2.26(-1)
6	12.935	1.53(-3)	2.10(-1)	12.944	9.38(-5)	1.74(-1)
		$3p_{3/2}nf_{5/2}$				
n = 4	12.056	3.64(-5)	7.82(-2)			
5	12.659	1.98(-4)	5.53(-2)			
6	12.975	7.60(-5)	4.90(-2)			
		$3d_{3/2}ns$				
n = 4	12.086	1.63(-5)	1.29(-1)			
5	12.709	1.84(-5)	1.11(-1)			
6	13.031	3.23(-5)	1.22(-1)			
		$3d_{3/2}nd_{3/2}$			$3d_{3/2}nd_{5/2}$	
n = 4	11.951	2.69(-5)	2.77(-1)	12.120	3.14(-4)	8.95(-2)
5	12.634	2.09(-6)	2.76(-1)	12.720	8.43(-5)	8.35(-2)
6	12.990	5.85(-5)	2.81(-1)	13.038	4.80(-5)	9.56(-2)
		$3d_{5/2}nd_{3/2}$			$3d_{5/2}nd_{5/2}$	
n = 4	12.160	5.47(-5)	4.08(-2)	12.185	3.22(-4)	9.20(-3)
5	12.739	5.30(-5)	3.86(-2)	12.744	2.96(-4)	2.68(-2)
6	13.041	8.38(-5)	8.30(-2)	13.048	3.92(-4)	5.47(-2)

Table 5.20. The energy positions E_r (Ryd), the widths Γ (Ryd), and the quantum defects μ of $2l_j$ and $3l_j$ photoionization resonances for metastable state Ne^{+6}.

	E_r	Γ	μ	E_r	Γ	μ
		$2p_{1/2}np_{1/2}$			$2p_{1/2}np_{3/2}$	
n = 7	14.355	1.41(-4)	1.03(-1)	14.360	7.28(-4)	8.69(-2)
8	14.600	1.10(-4)	1.02(-1)	14.603	6.23(-4)	8.52(-2)
9	14.767	8.21(-5)	1.01(-1)	14.769	4.77(-4)	8.42(-2)
10	14.885	6.11(-5)	1.01(-1)	14.887	3.60(-4)	8.37(-2)
11	14.973	4.62(-5)	1.01(-1)	14.974	2.75(-4)	8.34(-2)
		$2p_{3/2}np_{1/2}$			$2p_{3/2}np_{3/2}$	
n = 7	14.372	9.44(-4)	9.85(-2)	14.377	1.68(-3)	7.98(-2)
8	14.615	4.85(-4)	9.97(-2)	14.619	1.24(-3)	7.98(-2)
9	14.782	2.81(-4)	1.00(-1)	14.784	9.06(-4)	7.97(-2)
10	14.900	1.79(-4)	1.00(-1)	14.902	6.73(-4)	7.96(-2)
11	14.988	1.22(-4)	1.01(-1)	14.989	5.10(-4)	7.95(-2)
		$2p_{3/2}nf_{5/2}$				
n = 7	14.402	9.37(-5)	-6.64(-3)			
8	14.636	7.49(-5)	-6.31(-3)			
9	14.796	5.28(-5)	-6.12(-3)			
10	14.911	3.72(-5)	-5.97(-3)			
11	14.996	2.70(-5)	-5.84(-3)			
		$3sns$			$3snd_{3/2}$	
n = 3	18.203	1.66(-3)	1.48(-1)	18.302	1.28(-2)	1.24(-1)
4	20.666	6.73(-5)	2.90(-1)	20.914	4.39(-4)	1.54(-1)
5	22.035	5.49(-5)	2.72(-1)	22.162	3.18(-4)	1.28(-1)
		$3p_{1/2}np_{1/2}$			$3p_{1/2}np_{3/2}$	
n = 4	21.116	1.70(-4)	2.21(-1)	21.146	6.36(-4)	2.04(-1)
5	22.418	1.32(-4)	2.03(-1)	22.425	2.17(-4)	1.94(-1)
6	23.097	8.65(-5)	1.87(-1)	23.100	1.06(-4)	1.81(-1)
		$3p_{3/2}np_{1/2}$			$3p_{3/2}np_{3/2}$	
n = 4	21.190	3.19(-4)	1.82(-1)	21.214	7.32(-3)	1.68(-1)
5	22.452	3.12(-3)	1.69(-1)	22.458	3.18(-4)	1.62(-1)
6	23.102	7.09(-5)	1.85(-1)	23.114	1.61(-3)	1.62(-1)
		$3p_{3/2}nf_{5/2}$				
n = 3	18.936	4.61(-4)	4.62(-2)			
4	21.489	3.50(-4)	7.62(-5)			
5	22.564	1.83(-4)	3.48(-2)			
		$3d_{3/2}ns$				
n = 4	21.401	3.81(-5)	1.21(-1)			
5	22.628	1.39(-4)	8.77(-2)			
6	23.254	6.44(-5)	9.37(-2)			
		$3d_{3/2}nd_{3/2}$			$3d_{3/2}nd_{5/2}$	
n = 4	21.249	4.30(-5)	2.09(-1)	21.443	1.98(-5)	9.65(-2)
5	22.525	6.55(-6)	2.07(-1)	22.633	2.33(-5)	8.16(-2)
6	23.197	5.65(-5)	2.11(-1)	23.258	3.02(-5)	8.54(-2)
		$3d_{5/2}nd_{3/2}$			$3d_{5/2}nd_{5/2}$	
n = 4	21.550	6.35(-5)	3.06(-2)	21.584	3.65(-4)	8.88(-3)
5	22.667	1.05(-4)	4.21(-2)	22.683	2.98(-4)	2.23(-2)
6	23.274	9.59(-5)	5.50(-2)	23.281	3.24(-4)	3.91(-2)

Table 5.21. The energy positions E_r (Ryd), the widths Γ (Ryd), and the quantum defects μ of $2l_j$ and $3l_j$ photoionization resonances for metastable state Mg^{+8}.

	E_r	Γ	μ	E_r	Γ	μ
		$2p_{1/2}np_{1/2}$			$2p_{1/2}np_{3/2}$	
n = 8	22.996	1.79(-4)	8.21(-2)	23.001	8.67(-4)	6.83(-2)
9	23.270	1.26(-4)	8.16(-2)	23.273	6.20(-4)	6.79(-2)
10	23.465	9.01(-5)	8.13(-2)	23.467	4.52(-4)	6.77(-2)
11	23.609	6.66(-5)	8.11(-2)	23.610	3.38(-4)	6.75(-2)
12	23.718	5.08(-5)	8.10(-2)	23.719	2.59(-4)	6.74(-2)
		$2p_{3/2}np_{1/2}$			$2p_{3/2}np_{3/2}$	
n = 8	23.032	4.47(-4)	8.15(-2)	23.037	1.61(-3)	6.53(-2)
9	23.306	2.79(-4)	8.14(-2)	23.309	1.14(-3)	6.51(-2)
10	23.501	1.86(-4)	8.14(-2)	23.503	8.32(-4)	6.51(-2)
11	23.645	1.31(-4)	8.14(-2)	23.647	6.22(-4)	6.50(-2)
12	23.754	9.54(-5)	8.14(-2)	23.755	4.77(-4)	6.50(-2)
		$2p_{3/2}nf_{5/2}$				
n = 8	23.060	1.05(-4)	-4.63(-3)			
9	23.325	6.83(-5)	-4.46(-3)			
10	23.515	4.61(-5)	-4.31(-3)			
11	23.655	3.28(-5)	-4.19(-3)			
12	23.762	2.45(-5)	-4.10(-3)			
		$3sns$			$3snd_{3/2}$	
n = 3	28.399	1.71(-3)	1.18(-1)	28.520	1.29(-2)	1.00(-1)
4	32.442	7.45(-5)	2.34(-1)	32.763	4.86(-4)	1.23(-1)
5	34.608	6.29(-5)	2.19(-1)	34.774	3.57(-4)	1.03(-1)
		$3p_{1/2}np_{1/2}$			$3p_{1/2}np_{3/2}$	
n = 4	33.017	1.79(-4)	1.75(-1)	33.056	6.43(-4)	1.62(-1)
5	35.096	1.47(-4)	1.60(-1)	35.106	2.26(-4)	1.53(-1)
6	36.188	9.42(-5)	1.48(-1)	36.195	1.62(-4)	1.40(-1)
		$3p_{3/2}np_{1/2}$			$3p_{3/2}np_{3/2}$	
n = 4	33.114	3.54(-4)	1.45(-1)	33.141	7.45(-3)	1.35(-1)
5	35.139	3.11(-3)	1.37(-1)	35.152	4.10(-4)	1.28(-1)
6	36.209	1.23(-3)	1.35(-1)	36.217	4.63(-4)	1.26(-1)
		$3p_{3/2}nf_{5/2}$				
n = 4	33.499	3.74(-4)	9.82(-4)			
5	35.290	1.91(-4)	2.63(-2)			
6	36.288	1.22(-4)	3.44(-2)			
		$3d_{3/2}ns$				
n = 4	33.444	2.30(-5)	7.66(-2)			
5	35.381	3.04(-5)	6.41(-2)			
6	36.398	8.43(-5)	7.62(-2)			
		$3d_{3/2}nd_{3/2}$			$3d_{3/2}nd_{5/2}$	
n = 4	33.188	5.93(-5)	1.69(-1)	33.390	4.03(-5)	9.65(-2)
5	35.238	1.07(-5)	1.67(-1)	35.374	1.43(-4)	6.94(-2)
6	36.324	5.78(-5)	1.68(-1)	36.394	1.08(-4)	8.06(-2)
		$3d_{5/2}nd_{3/2}$			$3d_{5/2}nd_{5/2}$	
n = 4	33.582	7.37(-5)	2.54(-2)	33.626	4.05(-4)	8.13(-3)
5	35.432	1.11(-4)	2.87(-2)	35.444	3.11(-4)	1.94(-2)
6	36.407	2.43(-5)	6.89(-2)	36.435	2.61(-4)	3.16(-2)

Table 5.22. The energy positions E_r (Ryd), the widths Γ (Ryd), and the quantum defects μ of $2l_j$ and $3l_j$ photoionization resonances for metastable state Si^{+10}.

	E_r	Γ	μ	E_r	Γ	μ
		$2p_{1/2}np_{1/2}$			$2p_{1/2}np_{3/2}$	
n = 9	33.698	1.68(-4)	6.85(-2)	33.702	7.22(-4)	5.71(-2)
10	33.988	1.19(-4)	6.83(-2)	33.991	5.22(-4)	5.70(-2)
11	34.203	8.73(-5)	6.81(-2)	34.205	3.88(-4)	5.69(-2)
12	34.365	6.60(-5)	6.80(-2)	34.367	2.96(-4)	5.68(-2)
13	34.492	5.14(-5)	6.79(-2)	34.493	2.32(-4)	5.68(-2)
		$2p_{3/2}np_{1/2}$			$2p_{3/2}np_{3/2}$	
n = 9	33.772	2.91(-4)	6.86(-2)	33.776	1.32(-3)	5.53(-2)
10	34.062	1.99(-4)	6.85(-2)	34.065	9.56(-4)	5.52(-2)
11	34.276	1.41(-4)	6.85(-2)	34.279	7.13(-4)	5.52(-2)
12	34.439	1.03(-4)	6.85(-2)	34.441	5.46(-4)	5.52(-2)
13	34.565	7.59(-5)	6.85(-2)	34.567	4.28(-4)	5.52(-2)
		$2p_{3/2}nf_{5/2}$				
n = 9	33.796	8.35(-5)	-3.41(-3)			
10	34.080	5.53(-5)	-3.28(-3)			
11	34.289	3.87(-5)	-3.17(-3)			
12	34.449	2.85(-5)	-3.09(-3)			
13	34.573	2.19(-5)	-3.01(-3)			
		$3sns$			$3snd_{3/2}$	
n = 3	40.854	1.76(-3)	9.86(-2)	40.996	1.29(-2)	8.41(-2)
4	46.864	7.97(-5)	1.96(-1)	47.258	5.21(-4)	1.03(-1)
5	50.011	6.81(-5)	1.84(-1)	50.216	3.84(-4)	8.62(-2)
		$3p_{1/2}np_{1/2}$			$3p_{1/2}np_{3/2}$	
n = 4	47.568	1.91(-4)	1.45(-1)	47.615	6.38(-4)	1.34(-1)
5	50.605	1.63(-4)	1.32(-1)	50.620	2.60(-4)	1.25(-1)
6	52.209	1.01(-4)	1.22(-1)	52.219	3.22(-4)	1.13(-1)
		$3p_{3/2}np_{1/2}$			$3p_{3/2}np_{3/2}$	
n = 4	47.689	4.22(-4)	1.22(-1)	47.719	7.49(-3)	1.14(-1)
5	50.658	2.98(-3)	1.17(-1)	50.679	5.31(-4)	1.07(-1)
6	52.238	1.18(-3)	1.16(-1)	52.253	4.05(-4)	1.03(-1)
		$3p_{3/2}nf_{5/2}$				
n = 4	48.163	3.94(-4)	1.95(-3)			
5	50.851	1.99(-4)	2.13(-2)			
6	52.341	1.17(-4)	2.67(-2)			
		$3d_{3/2}ns$				
n = 4	48.098	2.59(-5)	6.42(-2)			
5						
6	52.489	3.13(-5)	5.19(-2)			
		$3d_{3/2}nd_{3/2}$			$3d_{3/2}nd_{5/2}$	
n = 4	47.778	7.52(-5)	1.42(-1)	48.032	3.99(-5)	8.06(-2)
5	50.786	1.50(-5)	1.40(-1)	50.955	1.44(-4)	5.79(-2)
6	52.385	6.20(-5)	1.41(-1)	52.478	8.10(-5)	6.18(-2)
		$3d_{5/2}nd_{3/2}$			$3d_{5/2}nd_{5/2}$	
n = 4	48.266	8.28(-5)	2.30(-2)	48.321	4.37(-4)	8.57(-3)
5	51.029	1.26(-4)	2.42(-2)	51.042	3.11(-4)	1.75(-2)
6	52.509	1.31(-4)	4.02(-2)	52.524	2.77(-4)	2.69(-2)

Table 5.23. The energy positions E_r (Ryd), the widths Γ (Ryd), and the quantum defects μ of $2l_j$ and $3l_j$ photoionization resonances for metastable state S^{+12}.

	E_r	Γ	μ	E_r	Γ	μ
		$2p_{1/2}np_{1/2}$			$2p_{1/2}np_{3/2}$	
n = 9						
10	46.465	1.36(-4)	5.90(-2)	46.469	5.60(-4)	4.93(-2)
11	46.764	9.89(-5)	5.89(-2)	46.766	4.14(-4)	4.93(-2)
12	46.990	7.48(-5)	5.88(-2)	46.992	3.15(-4)	4.92(-2)
13	47.166	5.86(-5)	5.88(-2)	47.168	2.47(-4)	4.91(-2)
		$2p_{3/2}np_{1/2}$			$2p_{3/2}np_{3/2}$	
n = 9	46.197	2.90(-4)	5.93(-2)	46.202	1.43(-3)	4.81(-2)
10	46.601	1.97(-4)	5.92(-2)	46.605	1.03(-3)	4.80(-2)
11	46.899	1.40(-4)	5.92(-2)	46.902	7.63(-4)	4.81(-2)
12	47.126	9.96(-5)	5.92(-2)	47.128	5.84(-4)	4.81(-2)
13	47.302	4.04(-5)	6.00(-2)	47.304	4.74(-4)	4.82(-2)
		$2p_{3/2}nf_{5/2}$				
n = 9	46.226	8.59(-5)	-2.71(-3)			
10	46.622	5.60(-5)	-2.58(-3)			
11	46.915	3.96(-5)	-2.49(-3)			
12	47.138	2.99(-5)	-2.41(-3)			
13	47.312	1.94(-5)	-2.55(-3)			
		$3sns$			$3snd_{3/2}$	
n = 3	55.581	1.79(-3)	8.48(-2)	55.746	1.30(-2)	7.26(-2)
4	63.945	8.36(-5)	1.70(-1)	64.417	5.48(-4)	8.93(-2)
5	68.258	7.22(-5)	1.58(-1)	68.503	4.04(-4)	7.41(-2)
		$3p_{1/2}np_{1/2}$			$3p_{1/2}np_{3/2}$	
n = 4	64.784	2.11(-4)	1.24(-1)	64.839	6.25(-4)	1.15(-1)
5	68.961	1.78(-4)	1.12(-1)	68.982	3.81(-4)	1.04(-1)
6	71.172	1.01(-4)	1.04(-1)	71.186	5.49(-4)	9.54(-2)
		$3p_{3/2}np_{1/2}$			$3p_{3/2}np_{3/2}$	
n = 4	64.932	6.04(-4)	1.05(-1)	64.963	7.36(-3)	9.99(-2)
5	69.026	2.75(-3)	1.03(-1)	69.059	6.57(-4)	9.15(-2)
6	71.215	9.51(-4)	1.02(-1)	71.238	4.19(-4)	8.76(-2)
		$3p_{3/2}nf_{5/2}$				
n = 4	65.497	4.09(-4)	2.60(-3)			
5	69.264	2.06(-4)	1.79(-2)			
6	71.344	1.17(-4)	2.20(-2)			
		$3d_{3/2}ns$				
n = 4	65.426	2.98(-5)	5.51(-2)			
5	69.405	4.46(-5)	4.38(-2)			
6	71.524	3.26(-5)	4.20(-2)			
		$3d_{3/2}nd_{3/2}$			$3d_{3/2}nd_{5/2}$	
n = 4	65.036	9.17(-5)	1.24(-1)	65.346	4.02(-5)	6.94(-2)
5	69.184	1.89(-5)	1.21(-1)	69.388	1.46(-4)	4.99(-2)
6	71.395	6.49(-5)	1.21(-1)	71.508	7.63(-5)	5.21(-2)
		$3d_{5/2}nd_{3/2}$			$3d_{5/2}nd_{5/2}$	
n = 4	65.622	9.22(-5)	2.12(-2)	65.689	4.71(-4)	8.67(-3)
5	69.478	1.57(-4)	2.19(-2)	69.494	3.11(-4)	1.60(-2)
6	71.551	1.30(-4)	3.28(-2)	71.566	2.42(-4)	2.33(-2)

Table 5.24. The energy positions E_r (Ryd), the widths Γ (Ryd), and the quantum defects μ of $2l_j$ and $3l_j$ photoionization resonances for metastable state Ar^{+14}.

	E_r	Γ	μ	E_r	Γ	μ
		$2p_{1/2}np_{1/2}$			$2p_{1/2}np_{3/2}$	
n = 10	60.908	1.53(-4)	5.21(-2)	60.912	5.93(-4)	4.35(-2)
11	61.304	1.11(-4)	5.20(-2)	61.307	4.37(-4)	4.34(-2)
12	61.606	8.42(-5)	5.20(-2)	61.608	3.33(-4)	4.34(-2)
13	61.840	1.76(-4)	5.15(-2)	61.842	2.27(-4)	4.22(-2)
14	62.025	4.95(-5)	5.20(-2)	62.027	2.03(-4)	4.36(-2)
		$2p_{3/2}np_{1/2}$			$2p_{3/2}np_{3/2}$	
n = 10	61.139	1.95(-4)	5.22(-2)	61.143	1.09(-3)	4.27(-2)
11	61.535	1.35(-4)	5.22(-2)	61.538	8.10(-4)	4.27(-2)
12	61.836	3.63(-5)	5.32(-2)	61.839	5.90(-4)	4.30(-2)
13	62.070	8.86(-5)	5.20(-2)	62.072	4.75(-4)	4.27(-2)
14	62.256	6.45(-5)	5.20(-2)	62.257	3.81(-4)	4.28(-2)
		$2p_{3/2}nf_{5/2}$				
n = 10	61.163	5.84(-5)	-2.09(-3)			
11	61.553	4.15(-5)	-2.00(-3)			
12	61.850	2.67(-5)	-2.08(-3)			
13	62.081	2.28(-5)	-1.97(-3)			
14	62.265	1.84(-5)	-1.93(-3)			
		$3sns$			$3snd_{3/2}$	
n = 3	72.598	1.81(-3)	7.47(-2)	72.787	1.30(-2)	6.42(-2)
4	83.703	8.69(-5)	1.51(-1)	84.257	5.68(-4)	7.89(-2)
5	89.368	7.51(-5)	1.39(-1)	89.653	4.18(-4)	6.49(-2)
		$3p_{1/2}np_{1/2}$			$3p_{1/2}np_{3/2}$	
n = 4	84.684	2.48(-4)	1.08(-1)	84.862	1.12(-3)	8.47(-2)
5	90.181	1.84(-4)	9.69(-2)	90.211	6.43(-4)	8.91(-2)
6	93.097	1.00(-4)	9.07(-2)	93.115	7.22(-4)	8.22(-2)
		$3p_{3/2}np_{1/2}$			$3p_{3/2}np_{3/2}$	
n = 4	84.748	6.04(-4)	1.09(-1)	84.893	6.85(-3)	8.96(-2)
5	90.266	2.38(-3)	9.23(-2)	90.311	7.65(-4)	8.04(-2)
6	93.164	7.51(-4)	9.07(-2)	93.194	4.59(-4)	7.68(-2)
		$3p_{3/2}nf_{5/2}$				
n = 4	85.523	4.21(-4)	3.19(-3)			
5	90.551	2.13(-4)	1.56(-2)			
6	93.318	1.17(-4)	1.90(-2)			
		$3d_{3/2}ns$				
n = 4	85.447	3.60(-5)	4.83(-2)			
5	90.720	5.19(-5)	3.72(-2)			
6	93.532	4.29(-5)	3.47(-2)			
		$3d_{3/2}nd_{3/2}$			$3d_{3/2}nd_{5/2}$	
n = 4	84.980	1.10(-4)	1.11(-1)	85.353	4.02(-5)	6.11(-2)
5	90.456	2.32(-5)	1.07(-1)	90.695	1.46(-4)	4.40(-2)
6	93.376	6.83(-5)	1.07(-1)	93.509	7.62(-5)	4.54(-2)
		$3d_{5/2}nd_{3/2}$			$3d_{5/2}nd_{5/2}$	
n = 4	85.671	1.02(-4)	2.02(-2)	85.751	5.06(-4)	8.95(-3)
5	90.801	1.88(-4)	2.08(-2)	90.823	3.02(-4)	1.48(-2)
6	93.563	1.46(-4)	3.00(-2)	93.583	2.27(-4)	2.10(-2)

Table 5.25. The energy positions E_r (Ryd), the widths Γ (Ryd), and the quantum defects μ of $2l_j$ and $3l_j$ photoionization resonances for metastable state Ca^{+16}.

	E_r	Γ	μ	E_r	Γ	μ
		$2p_{1/2}np_{1/2}$			$2p_{1/2}np_{3/2}$	
n = 10						
11	77.840	1.24(-4)	4.65(-2)	77.843	4.59(-4)	3.88(-2)
12	78.226	1.19(-4)	4.69(-2)	78.229	3.29(-4)	3.87(-2)
13	78.526	6.88(-5)	4.66(-2)	78.528	2.67(-4)	3.90(-2)
14	78.764	5.50(-5)	4.66(-2)	78.766	2.13(-4)	3.89(-2)
		$2p_{3/2}np_{1/2}$			$2p_{3/2}np_{3/2}$	
n = 10	77.700	1.96(-4)	4.66(-2)	77.704	1.15(-3)	3.83(-2)
11	78.208	1.06(-4)	4.69(-2)	78.211	8.69(-4)	3.83(-2)
12	78.594	1.17(-4)	4.64(-2)	78.597	6.38(-4)	3.84(-2)
13	78.894	8.23(-5)	4.65(-2)	78.896	5.01(-4)	3.84(-2)
14	79.132	7.60(-5)	4.63(-2)	79.134	3.92(-4)	3.84(-2)
		$2p_{3/2}nf_{5/2}$				
n = 10	77.728	6.16(-5)	-1.74(-3)			
11						
12	78.610	2.93(-5)	-1.64(-3)			
13	78.907	2.26(-5)	-1.60(-3)			
14	79.142	1.69(-5)	-1.62(-3)			
		$3sns$			$3snd_{3/2}$	
n = 3	91.926	1.83(-3)	6.70(-2)	92.139	1.30(-2)	5.77(-2)
4	106.158	8.97(-5)	1.37(-1)	106.800	5.83(-4)	7.11(-2)
5	113.363	7.68(-5)	1.25(-1)	113.689	4.29(-4)	5.79(-2)
		$3p_{1/2}np_{1/2}$			$3p_{1/2}np_{3/2}$	
n = 4	107.286	2.98(-4)	9.66(-2)	107.503	2.36(-3)	7.42(-2)
5	114.287	1.83(-4)	8.58(-2)	114.328	9.89(-4)	7.74(-2)
6	118.008	9.98(-5)	8.01(-2)	118.030	8.11(-4)	7.20(-2)
		$3p_{3/2}np_{1/2}$			$3p_{3/2}np_{3/2}$	
n = 4	107.366	5.92(-4)	9.95(-2)	107.536	5.58(-3)	8.19(-2)
5	114.403	1.95(-3)	8.41(-2)	114.461	8.37(-4)	7.20(-2)
6	118.112	6.25(-4)	8.12(-2)	118.148	5.01(-4)	6.84(-2)
		$3p_{3/2}nf_{5/2}$				
n = 4	108.265	4.27(-4)	3.71(-3)			
5	114.737	2.20(-4)	1.38(-2)			
6	118.289	1.18(-4)	1.68(-2)			
		$3d_{3/2}ns$				
n = 4	108.188	4.73(-5)	4.30(-2)			
5	114.937	5.97(-5)	3.18(-2)			
6	118.539	6.39(-5)	2.92(-2)			
		$3d_{3/2}nd_{3/2}$			$3d_{3/2}nd_{5/2}$	
n = 4	107.635	1.31(-4)	1.01(-1)	108.077	3.99(-5)	5.49(-2)
5	114.625	2.82(-5)	9.66(-2)	114.900	1.45(-4)	3.96(-2)
6	118.354	7.11(-5)	9.60(-2)	118.508	7.83(-5)	4.06(-2)
		$3d_{5/2}nd_{3/2}$			$3d_{5/2}nd_{5/2}$	
n = 4	108.439	1.14(-4)	1.96(-2)	108.532	5.42(-4)	9.38(-3)
5	115.024	2.14(-4)	2.05(-2)	115.055	2.93(-4)	1.39(-2)
6	118.574	1.55(-4)	2.89(-2)	118.600	2.27(-4)	1.94(-2)

Table 5.26. The energy positions E_r (Ryd), the widths Γ (Ryd), and the quantum defects μ of $2l_j$ and $3l_j$ photoionization resonances for metastable state Ti^{+18}.

	E_r	Γ	μ	E_r	Γ	μ
		$2p_{1/2}np_{1/2}$			$2p_{1/2}np_{3/2}$	
n = 11						
12	96.866	9.26(-5)	4.27(-2)	96.870	3.48(-4)	3.55(-2)
13	97.241	7.31(-5)	4.26(-2)	97.244	2.73(-4)	3.54(-2)
14	97.538	5.86(-5)	4.25(-2)	97.540	2.18(-4)	3.53(-2)
15	97.778	4.44(-5)	4.26(-2)	97.779	1.72(-4)	3.56(-2)
		$2p_{3/2}np_{1/2}$			$2p_{3/2}np_{3/2}$	
n = 11	96.944	1.43(-4)	4.22(-2)	96.948	8.62(-4)	3.52(-2)
12	97.426	9.73(-5)	4.23(-2)	97.429	6.62(-4)	3.53(-2)
13	97.801	8.99(-5)	4.21(-2)	97.803	5.10(-4)	3.52(-2)
14	98.098	5.81(-5)	4.22(-2)	98.100	4.13(-4)	3.52(-2)
15	98.337	4.93(-5)	4.21(-2)	98.339	3.33(-4)	3.52(-2)
		$2p_{3/2}nf_{5/2}$				
n = 11	96.968	4.16(-5)	-1.41(-3)			
12	97.444	3.18(-5)	-1.39(-3)			
13	97.815	2.38(-5)	-1.41(-3)			
14	98.109	1.98(-5)	-1.38(-3)			
15	98.347	1.57(-5)	-1.40(-3)			
		$3sns$			$3snd_{3/2}$	
n = 3	113.586	1.84(-3)	6.11(-2)	113.827	1.30(-2)	5.26(-2)
4	131.333	9.17(-5)	1.26(-1)	132.067	5.96(-4)	6.51(-2)
5	140.269	7.76(-5)	1.13(-1)	140.637	4.37(-4)	5.21(-2)
		$3p_{1/2}np_{1/2}$			$3p_{1/2}np_{3/2}$	
n = 4	132.612	3.47(-4)	8.79(-2)	132.876	4.05(-3)	6.58(-2)
5	141.306	1.81(-4)	7.68(-2)	141.357	1.28(-3)	6.84(-2)
6	145.925	9.70(-5)	7.26(-2)	145.953	8.56(-4)	6.47(-2)
		$3p_{3/2}np_{1/2}$			$3p_{3/2}np_{3/2}$	
n = 4	132.718	6.35(-4)	9.26(-2)	132.919	3.80(-3)	7.59(-2)
5	141.468	1.59(-3)	7.69(-2)	141.539	9.00(-4)	6.51(-2)
6	146.082	5.79(-4)	7.42(-2)	146.124	5.03(-4)	6.22(-2)
		$3p_{3/2}nf_{5/2}$				
n = 3	115.738	7.87(-4)	1.90(-2)			
4	133.753	4.24(-4)	4.17(-3)			
5	141.851	2.27(-4)	1.24(-2)			
		$3d_{3/2}ns$				
n = 4	133.952	1.27(-4)	1.49(-2)			
5	142.177	2.40(-4)	1.15(-2)			
6	146.572	9.22(-5)	2.47(-2)			
		$3d_{3/2}nd_{3/2}$			$3d_{3/2}nd_{5/2}$	
n = 4	133.027	1.53(-4)	9.36(-2)	133.545	3.91(-5)	5.01(-2)
5	141.722	3.26(-5)	8.79(-2)	142.033	1.47(-4)	3.60(-2)
6	146.356	7.46(-5)	8.76(-2)	146.532	7.77(-5)	3.67(-2)
		$3d_{5/2}nd_{3/2}$			$3d_{5/2}nd_{5/2}$	
n = 4	133.675	6.81(-5)	4.34(-2)	134.061	5.81(-4)	9.96(-3)
5	142.084	7.37(-5)	3.63(-2)	142.220	2.93(-4)	1.31(-2)
6	146.616	1.49(-4)	2.74(-2)	146.649	2.13(-4)	1.77(-2)

Table 5.27. The energy positions E_r (Ryd), the widths Γ (Ryd), and the quantum defects μ of $2l_j$ and $3l_j$ photoionization resonances for metastable state Cr^{+20}.

	E_r	Γ	μ	E_r	Γ	μ
		$2p_{1/2}np_{1/2}$			$2p_{1/2}np_{3/2}$	
n = 11						
12	117.547	9.99(-5)	3.94(-2)	117.551	3.60(-4)	3.25(-2)
13	118.005	7.87(-5)	3.92(-2)	118.008	2.82(-4)	3.23(-2)
14	118.367	9.59(-5)	3.94(-2)	118.370	1.48(-4)	3.09(-2)
15	118.660	5.02(-5)	3.90(-2)	118.662	1.82(-4)	3.23(-2)
		$2p_{3/2}np_{1/2}$			$2p_{3/2}np_{3/2}$	
n = 11	117.777	1.16(-4)	3.89(-2)	117.781	8.99(-4)	3.27(-2)
12	118.365	1.65(-5)	3.98(-2)	118.368	7.81(-4)	3.23(-2)
13	118.822	6.92(-5)	3.87(-2)	118.825	5.38(-4)	3.25(-2)
14	119.185	5.78(-5)	3.86(-2)	119.187	4.28(-4)	3.24(-2)
15	119.477	4.70(-5)	3.85(-2)	119.479	3.47(-4)	3.23(-2)
		$2p_{3/2}nf_{5/2}$				
n = 11	117.804	4.62(-5)	-1.23(-3)			
12	118.386	3.25(-5)	-1.30(-3)			
13	118.839	2.77(-5)	-1.25(-3)			
14	119.198	2.18(-5)	-1.26(-3)			
15	119.488	1.77(-5)	-1.26(-3)			
		$3sns$			$3snd_{3/2}$	
n = 3	137.608	1.84(-3)	5.65(-2)	137.877	1.30(-2)	4.86(-2)
4	159.253	9.39(-5)	1.17(-1)	160.088	6.04(-4)	6.06(-2)
5	170.116	7.68(-5)	1.03(-1)	170.526	4.42(-4)	4.74(-2)
		$3p_{1/2}np_{1/2}$			$3p_{1/2}np_{3/2}$	
n = 4	160.687	3.82(-4)	8.15(-2)	161.013	5.27(-3)	5.91(-2)
5	171.267	1.75(-4)	6.96(-2)	171.327	1.46(-3)	6.14(-2)
6	176.882	9.56(-5)	6.66(-2)	176.915	8.79(-4)	5.87(-2)
		$3p_{3/2}np_{1/2}$			$3p_{3/2}np_{3/2}$	
n = 4	160.833	7.95(-4)	8.77(-2)	161.076	2.39(-3)	-9.29(-1)
5	171.496	1.35(-3)	7.07(-2)	171.578	9.37(-4)	-9.40(-1)
6	177.111	5.63(-4)	6.84(-2)	177.158	5.04(-4)	-9.43(-1)
		$3p_{3/2}nf_{5/2}$				
n = 3	140.066	8.49(-4)	1.76(-2)			
4	161.942	1.06(-4)	1.02(-2)			
5	171.925	2.33(-4)	1.13(-2)			
		$3d_{3/2}ns$				
n = 4	162.245	1.42(-4)	1.41(-2)			
5	172.293	2.52(-4)	9.81(-2)			
6	177.665	1.36(-4)	2.15(-2)			
		$3d_{3/2}nd_{3/2}$			$3d_{3/2}nd_{5/2}$	
n = 4				161.791	3.83(-5)	4.63(-2)
5	171.778	3.75(-5)	8.09(-2)	172.127	1.48(-4)	3.32(-2)
6	177.416	7.81(-5)	8.09(-2)	177.614	8.31(-5)	3.37(-2)
		$3d_{5/2}nd_{3/2}$			$3d_{5/2}nd_{5/2}$	
n = 4	162.021	4.05(-4)	3.56(-2)	162.370	6.22(-4)	1.07(-2)
5	172.195	9.37(-5)	3.43(-2)	172.351	2.93(-4)	1.25(-2)
6	177.722	1.44(-4)	2.62(-2)	177.762	2.24(-4)	1.65(-2)

Table 5.28. The energy positions E_r (Ryd), the widths Γ (Ryd), and the quantum defects μ of $2l_j$ and $3l_j$ photoionization resonances for metastable state Fe^{+22}.

	E_r	Γ	μ	E_r	Γ	μ
		$2p_{1/2}np_{1/2}$			$2p_{1/2}np_{3/2}$	
n = 11						
12						
13	140.865	8.23(-5)	3.64(-2)	140.869	2.87(-4)	2.98(-2)
14	141.300	6.28(-5)	3.65(-2)	141.303	2.25(-4)	2.99(-2)
15	141.651	5.10(-5)	3.65(-2)	141.653	1.82(-4)	2.99(-2)
		$2p_{3/2}np_{1/2}$			$2p_{3/2}np_{3/2}$	
n = 11	140.756	1.12(-4)	3.57(-2)	140.760	9.29(-4)	3.00(-2)
12	141.461	8.71(-5)	3.57(-2)	141.464	7.05(-4)	3.01(-2)
13	142.009	6.73(-5)	3.57(-2)	142.011	5.49(-4)	3.02(-2)
14	142.443	5.08(-5)	3.57(-2)	142.445	4.36(-4)	3.03(-2)
15	142.794	3.55(-5)	3.58(-2)	142.796	3.54(-4)	3.03(-2)
		$2p_{3/2}nf_{5/2}$				
n = 11	140.785	4.23(-5)	-9.80(-4)			
12	141.483	2.93(-5)	-9.60(-4)			
13	142.026	2.16(-5)	-9.52(-4)			
14	142.458	1.67(-5)	-9.45(-4)			
15	142.805	1.48(-5)	-8.87(-4)			
		$3sns$			$3snd_{3/2}$	
n = 3	164.008	1.84(-3)	5.30(-2)	164.328	1.30(-2)	4.53(-2)
4	189.937	9.59(-5)	1.11(-1)	190.885	6.15(-4)	5.75(-2)
5	202.924	7.73(-5)	9.59(-2)	203.385	4.45(-4)	4.37(-2)
		$3p_{1/2}np_{1/2}$			$3p_{1/2}np_{3/2}$	
n = 4	191.543	4.02(-4)	7.76(-2)	191.954	5.96(-3)	5.39(-2)
5	204.209	1.71(-4)	6.45(-2)	204.283	1.55(-3)	5.61(-2)
6	210.931	9.62(-5)	6.05(-2)	210.968	8.73(-4)	5.32(-2)
		$3p_{3/2}np_{1/2}$			$3p_{3/2}np_{3/2}$	
n = 4	191.746	1.06(-3)	8.47(-2)	192.046	1.45(-3)	6.77(-2)
5	204.526	1.25(-3)	6.60(-2)	204.617	9.31(-4)	5.56(-2)
6	211.251	5.25(-4)	6.23(-2)	211.300	5.32(-4)	5.25(-2)
		$3p_{3/2}nf_{5/2}$				
n = 3	166.822	9.10(-4)	1.66(-2)			
4						
5	205.005	2.39(-4)	1.06(-2)			
		$3d_{3/2}ns$				
n = 4	193.359	1.55(-4)	1.34(-2)			
5	205.417	2.45(-4)	8.08(-2)			
6	211.854	1.65(-4)	1.96(-2)			
		$3d_{3/2}nd_{3/2}$			$3d_{3/2}nd_{5/2}$	
n = 4	192.150	1.84(-4)	8.39(-2)	193.026	1.65(-4)	3.32(-2)
5	204.829	4.58(-4)	7.58(-2)	205.220	1.47(-4)	3.10(-2)
6	211.580	8.10(-5)	7.43(-2)	211.797	8.24(-5)	3.11(-2)
		$3d_{5/2}nd_{3/2}$			$3d_{5/2}nd_{5/2}$	
n = 4	193.110	3.68(-4)	3.47(-2)			
5	205.309	1.22(-4)	3.34(-2)			
6	211.935	1.22(-4)	2.53(-2)			

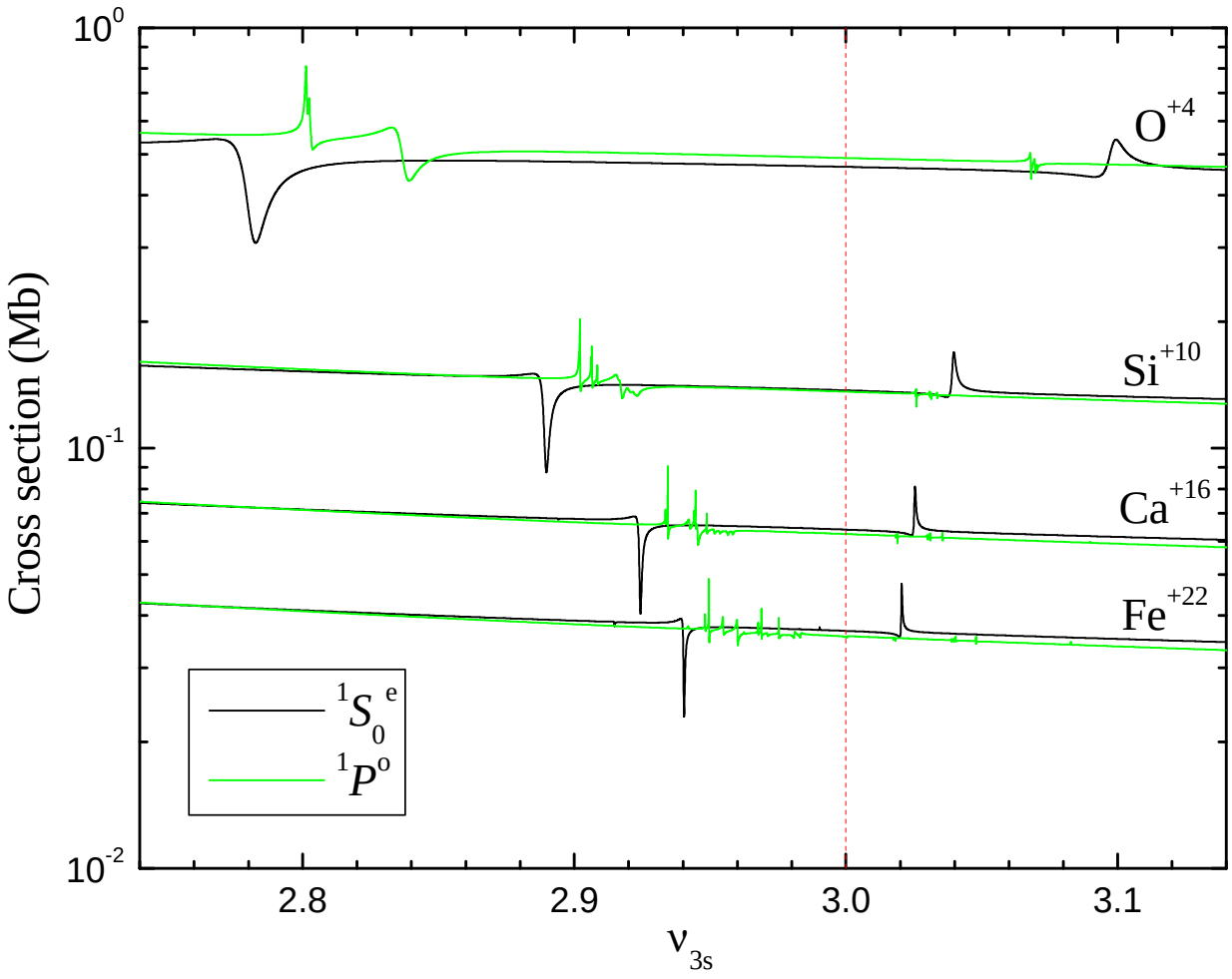

Figure 5.9. Photoionization cross sections for ${}^1S_0^e$ state and ${}^3P^o$ state (with the statistical weights of the three ${}^1P_J^o$ states) of O^{+4}, Si^{+10}, Ca^{+16}, and Fe^{+22} vs. the effective quantum number ν (with respect to 3*s* threshold in each ion). The vertical dashed line indicates quantum defect $\mu = 0$ for the resonances. The smooth change (in position, width and shape) of the resonances with *Z* helps the identification process.

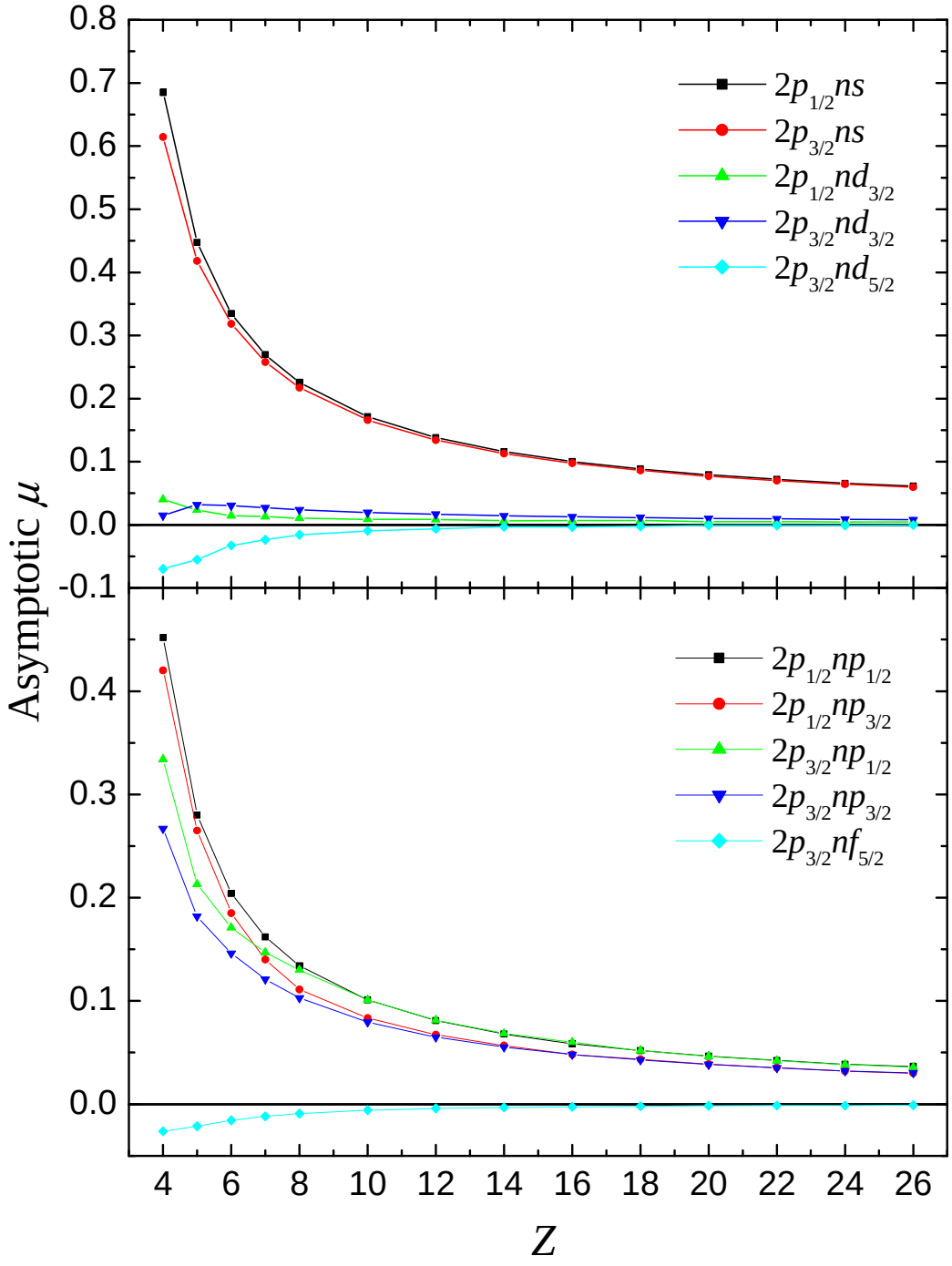

Figure 5.10. The asymptotic quantum defects ($\mu_{n\to\infty}$) of the $2p_j nl_{j'}$ resonances along the isoelectronic sequence, for ground state photoionization in the top panel and for metastable photoionization in the bottom panel.

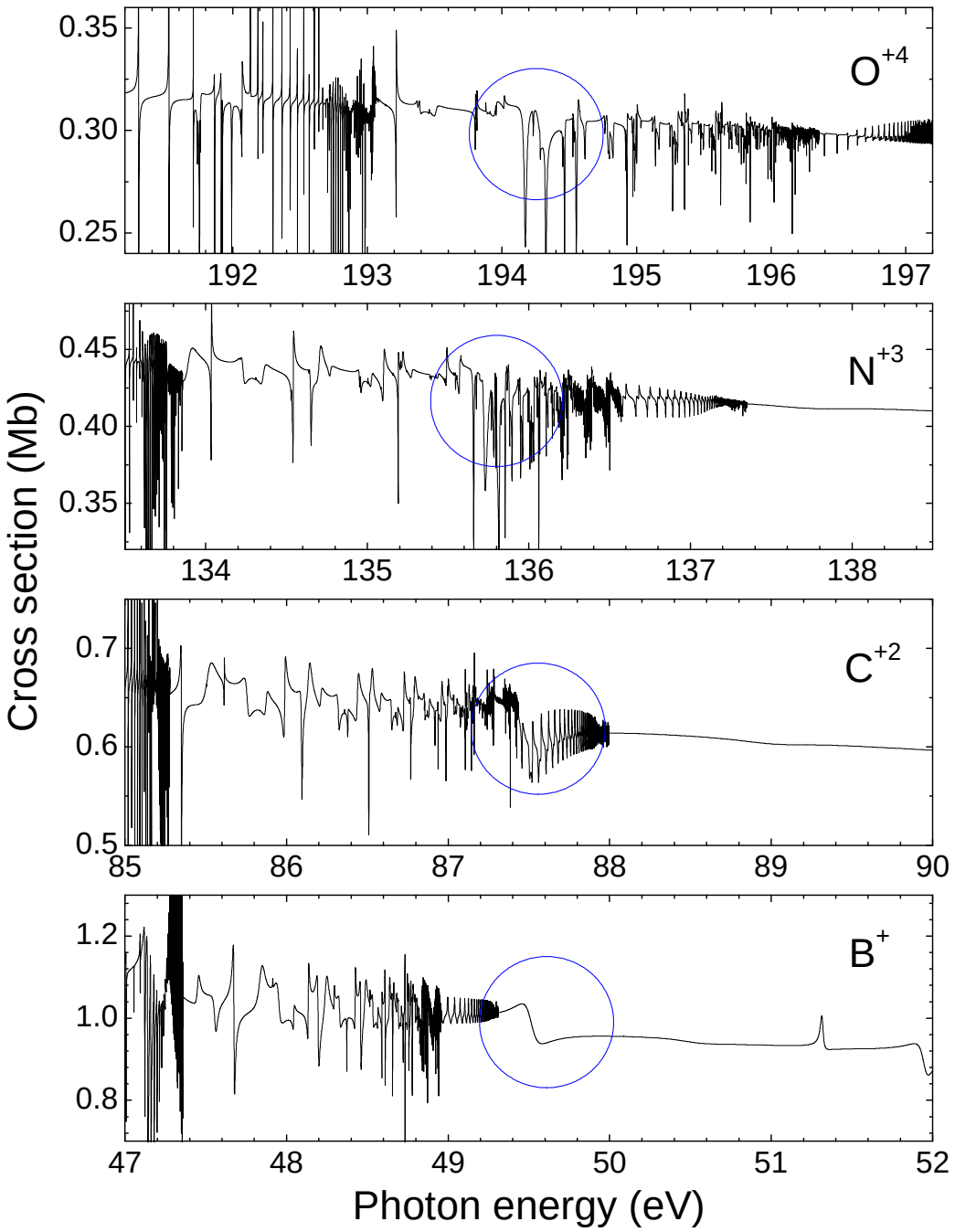

Figure 5.11. The photoionization cross sections near the 4*s*4*p* resonance (encircled) of B^{+}, C^{+2}, N^{+3}, and O^{+4}, in the same energy scale. The 4*s*4*p* resonance is beyond $3d_{5/2}$ threshold and recognizable in B^{+}, but is strongly perturbed by the lower resonances and spreads out in heavier ions.

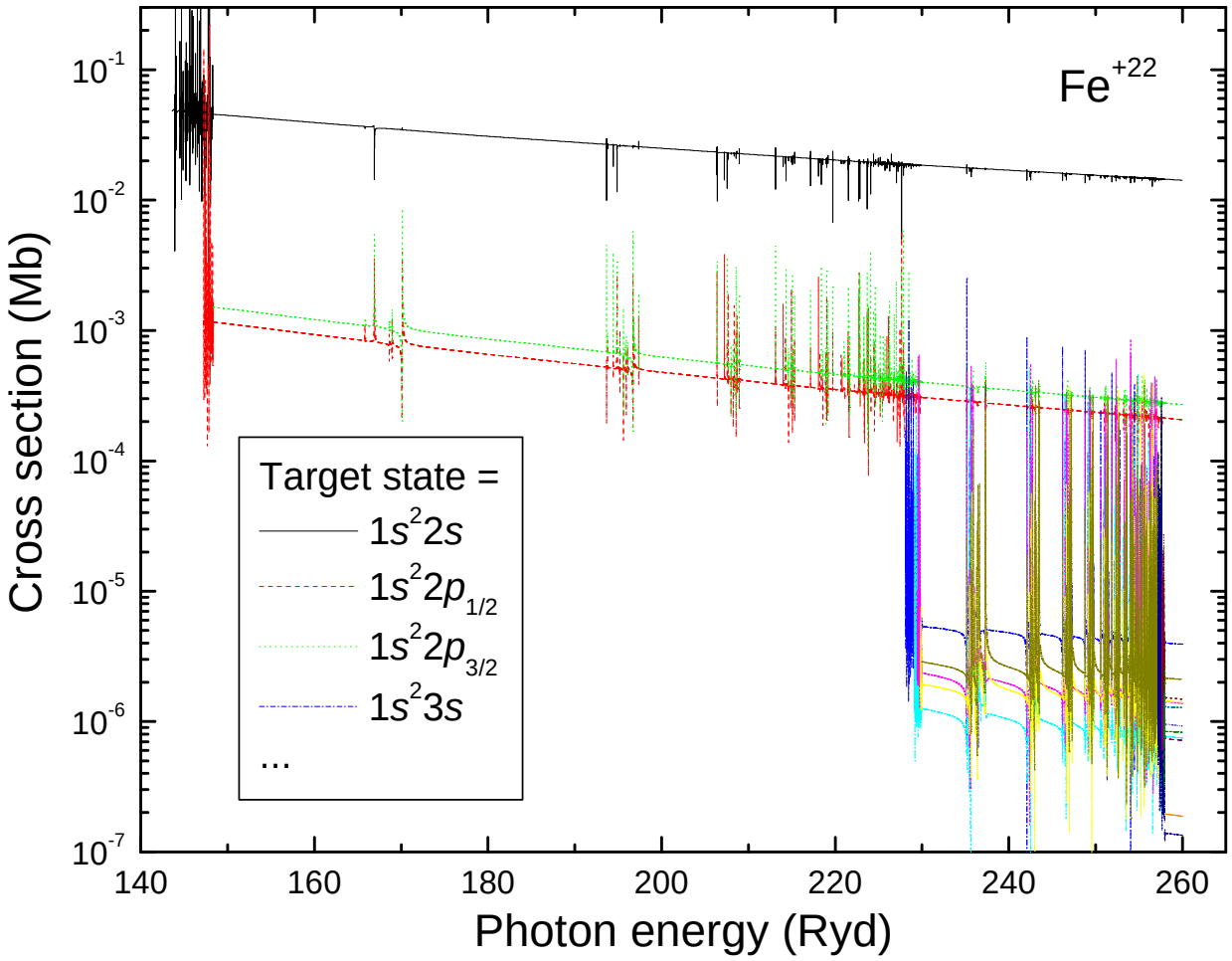

Figure 5.12. Partial photoionization cross sections for Fe^{+22} to different target states, in the energy range from the ionization threshold to right above $T_{4f_{7/2}}$.

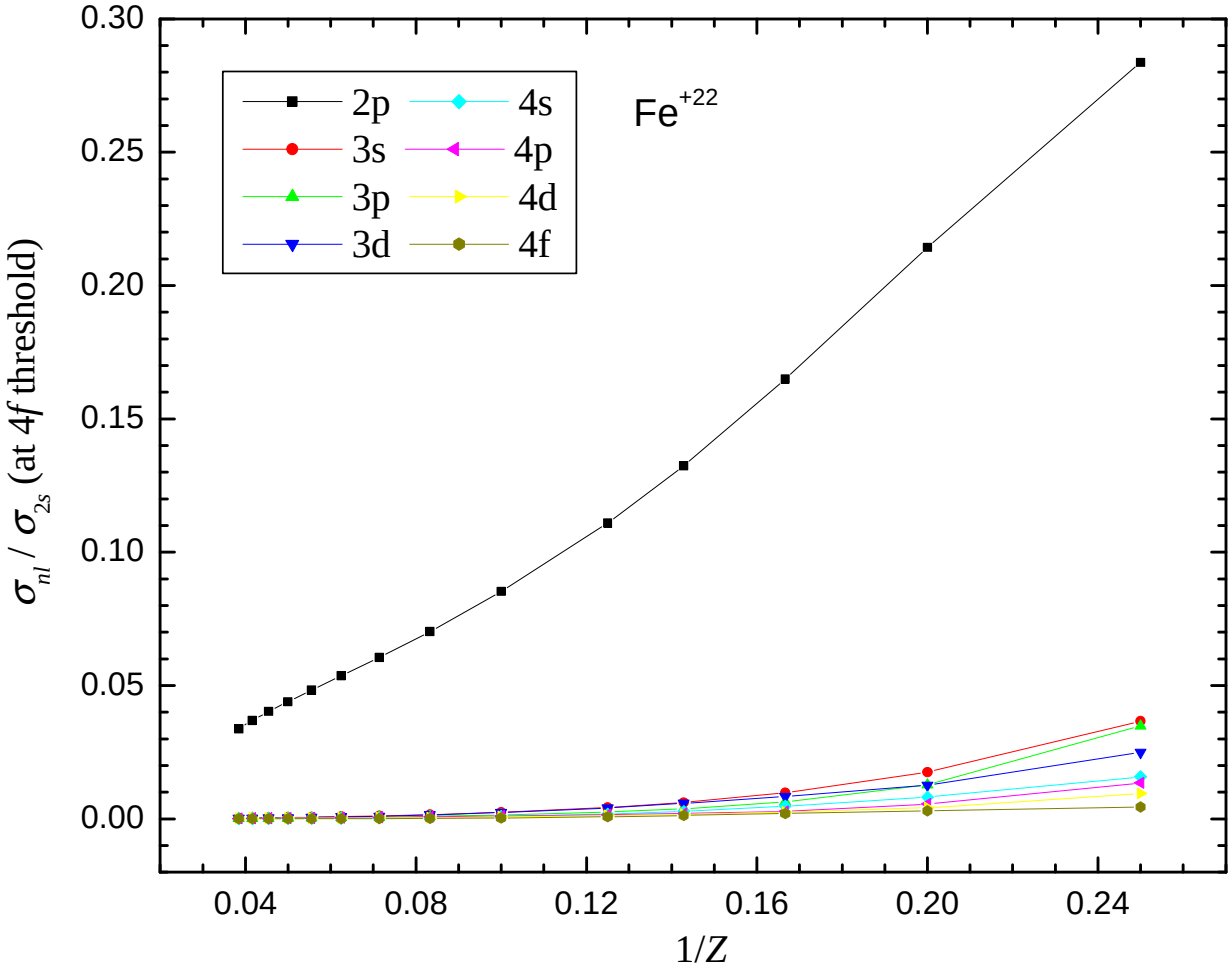

Figure 5.13. The ratio of $\sigma_{nl}(E)$ to $\sigma_{2s}(E)$ just above $T_{4f_{7/2}}$ threshold.

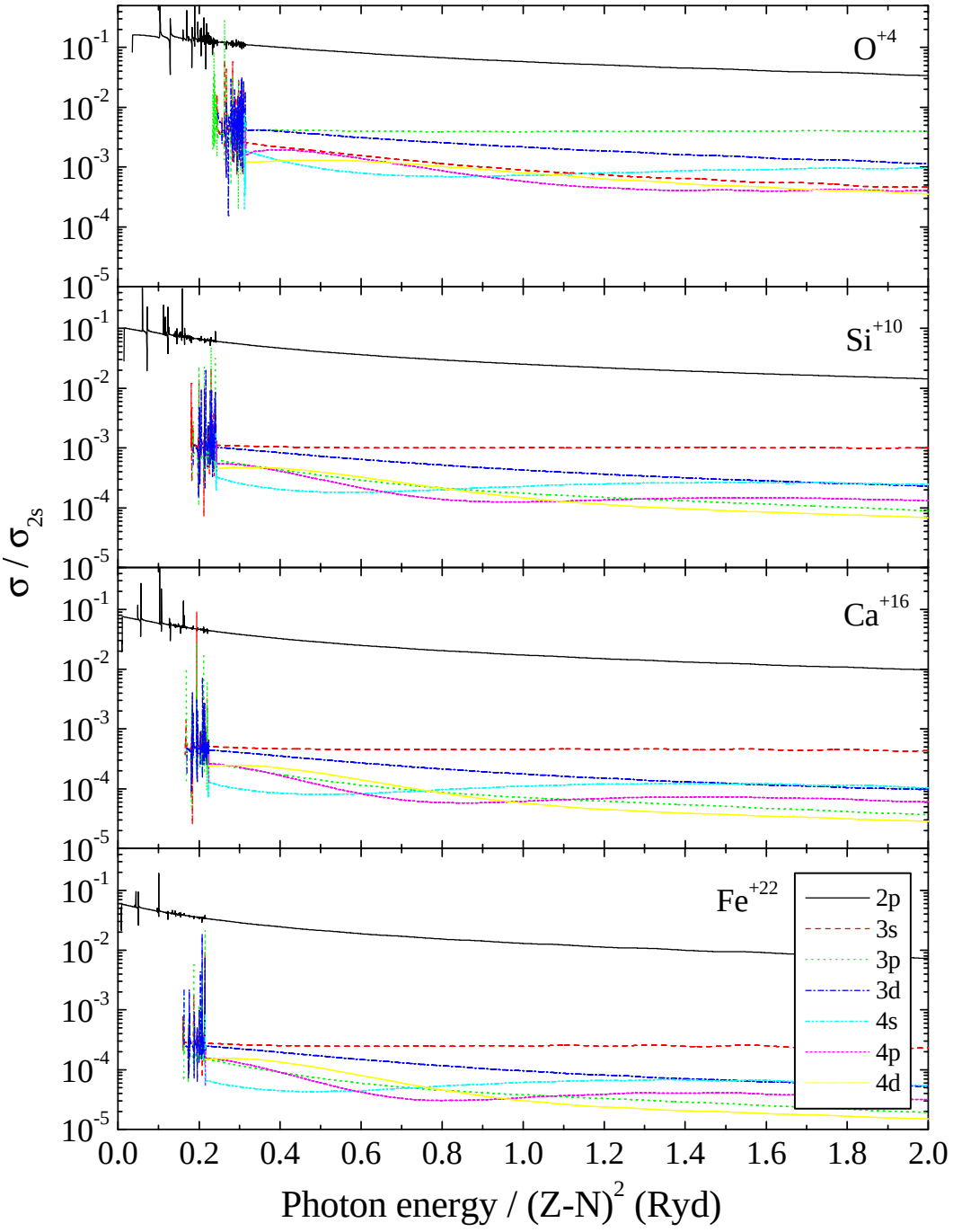

Figure 5.14. The ratios σ_{nl}/σ_{2s} up to photon energy $E = 2(Z-N)^2$ Ryd for O^{+4}, Si^{+10}, Ca^{+16}, and Fe^{+22}.

6. CONCLUSIONS

We have done a thorough investigation of the photoionization of the Be-like ions from neutral beryllium to the iron ion. Our calculation provides high resolution cross section data for astrophysics and plasma studies. From the comparison of our calculated cross sections for the ground and metastable states of a number of members of the Be isoelectronic sequence with experiment (where available) and previous calculations, we find that the relativistic Breit-Pauli *R*-matrix methodology, along with an extensive high-quality set of discrete orbitals to represent the final ionic (target) states and the initial states, provides an extremely accurate description of the photoionization process in the four-electron system. This is further confirmed by the excellent agreement between length and velocity gauges (within a few percent), and by the excellent agreement of the initial state binding energies and target state excitation energies with the NIST data compilation, presented in Table 4.1 - Table 4.3.

In our study, it has been found that the overall magnitudes of the cross sections decrease with *Z*, which is necessary to satisfy the oscillator strength sum rule [77]. Inclusion of relativistic effects is found to be of importance to achieve high accuracy even at the lowest values of *Z*, owing to the splittings and shifts of the resonances engendered by these relativistic effects. And, since relativistic effects in energies increase as Z^4, while electrostatic energies increase as Z^2, these effects become much more important at the higher *Z*'s; for Fe^{+22}, for example, relativistic resonance energy shifts of close to 100 eV were found. And for the excited states, relativistic effects were even more important because the single nonrelativistic $^3P^o$ state is split into three states, $^3P_0^o$, $^3P_1^o$ and $^3P_2^o$, each with a different threshold energy. Further, it is important to note that these conclusions should be quite general and not restricted just to the four-electron Be-like systems studied in detail here.

Many of the cross sections were seen to exhibit large numbers of very narrow resonances. Thus, to calculate cross sections which include all of the oscillator strength, the calculational energy mesh must be dense enough to include the maxima of these resonances. Furthermore, to show the physics concerning the structure of the resonances, the energy mesh should be even denser in the range of each resonance, so that the cross section and the eigenphase can be well characterized in the vicinity of each resonance. As seen in some of the comparisons of theoretical cross sections, some of the reported results contain the proper physics but are still inaccurate owing to the failure to include enough points in the energy mesh.

In the analysis, we have characterized the resonances using the QB program and developed successfully a systematic way to identify the resonances. A large volume of resonance data has been acquired. The comparison with other theoretical results is difficult because relativistic effects split our resonances to many more components than *LS* results, and there is no exact correspondence between ours and the *LS* results. However, the features of the resonances, with a complete characterization with E_r (coupled with ν and μ in each channel) and Γ, have been shown and described as they evolve along n in a Rydberg series and along the isoelectronic sequence. The general behaviors of $2p_jnl_{j'}$ resonances are fairly simple, since channel interactions have not played important roles in these resonance features. For higher energy regions, the Rydberg series converging to nearby thresholds are strongly mixed, and the perturbations between the resonances are more obvious since there are more series compressed into smaller energy regions.

How the quantum defects evolve along the isoelectronic sequence have been demonstrated by the asymptotic quantum defects $\mu_{n\to\infty}$ of the $2p_jnl_{j'}$ resonances, and we found an analytical form to well describe the evolution along Z, as well as other general features. For

detailed discussions on the perturbations, we have developed from basic theory how the resonances are influenced by the perturbations, and applied it in the identification for the resonances. As a special and interesting case, 4*s*4*p* has shown how a wide resonance overlaps the narrow ones converging to the lower thresholds.

The partial cross sections to different target states, which are so far unavailable in experiments, have been studied using BPRM. Their background values are displayed and analyzed along the sequence. The ratios of the partial cross sections suggest that at the very high *Z* end of the sequence, the system will converge to the hydrogenic result, which has already been suggested by the analysis on the quantum defects. We further note that high photon energy also makes the system more hydrogenic, but the related details are not understood yet.

REFERENCES

[1] D. H. Bilderback, P. Elleaume, and E. Weckert, J. Phys. B: At. Mol. Opt. Phys. **38**, S773 (2005).

[2] H. Kjeldsen, J. Phys. B: At. Mol. Opt. Phys. **39**, R325 (2006).

[3] J. B. Peart, G. Stevenson, and K. T. Dolder, J. Phys. B: Atom. Molec. Phys. **6**, 146 (1973).

[4] C. Lyon, B. Peart, J. B. West, and K. Dolder, J. Phys. B: At. Mol. Phys. **19**, 4137 (1986).

[5] J. B. West, J. Phys. B: At. Mol. Opt. Phys. **34**, R45 (2001).

[6] C. Lyon, B. Peart, K. Dolder, and J. B. West, J. Phys. B: At. Mol. Phys. **20**, 1471 (1987).

[7] C. Lyon, B. Peart, and K. Dolder, J. Phys. B: At. Mol. Phys. **20**, 1925 (1987).

[8] T. Koizumi, Y. Itoh, M. Kimura, T. M. Kojima, S. Kravis, M. Oura, M. Sano, T. Sekioka and Y. Awaya, At. Collis. Res. Jpn. Prog. Rep. **19,** 98 (1993).

[9] C. F. Fischer, Comp. Phys. Comm. **43**, 355 (1987).

[10] C. F. Fischer, G. Tachiev, G. Gaigalas, and M. R. Godefroid, Comp. Phys. Comm. **176**, 559 (2007).

[11] P. L. Altick and A. E. Glassgold, Phys. Rev. **133**, A632 (1964).

[12] M. Y. Amusia and N. A. Cherepkov, Case Stud. At. Phys. **5**, 47 (1975).

[13] W. R. Johnson and C. D. Lin, Phys. Rev. A **20**, 964 (1979).

[14] K. N. Huang, W. R. Johnson, and K. T. Cheng, At. Data Nucl. Data Tables **26**, 33 (1981).

[15] K. N. Huang and W. R. Johnson, Phys. Rev. A **25**, 634 (1982).

[16] J. Goldstone, Proc. Roy. Soc. **A239**, 267 (1957).

[17] H. P. Kelly, Phys. Rev. **131**, 684 (1963).

[18] H. P. Kelly, Phys. Rev. **136**, B896 (1964).

[19] H. P. Kelly, Phys. Rev. **144**, 39 (1966).

[20] H. P. Kelly, Phys. Scr. **T17**, 109 (1987).

[21] T. N. Chang, T. Ishihara, and R. T. Poe, Phys. Rev. Lett. **27**, 838 (1971).

[22] E. P. Wigner and L. Eisenbud, Phys. Rev. **72**, 29 (1947).

[23] A. M. Lane and D. Robson, Phys. Rev. **151**, 774 (1966).

[24] K. A. Berrington, P. G. Burke, J. J. Chang, A. T. Chivers, W. D. Robb, and K. T. Taylor, Comp. Phys. Comm. **8**, 149 (1974).

[25] P. G. Burke and M. J. Seaton, Methods Comput. Phys. **10**, 1 (1971).

[26] N. S. Scott and K. T. Taylor, Comp. Phys. Comm. **25**, 347 (1982).

[27] http://amdpp.phys.strath.ac.uk/tamoc/code.html

[28] M. J. Seaton, J. Phys. B: At. Mol. Phys. **20**, 6363 (1987).

[29] D. G. Hummer, K. A. Berrington, W. Eissner, A. K. Pradhan, H. E. Saraph, and J. A. Tully, Astron. Astrophys. **279**, 298 (1993).

[30] P. G. Burke, A. Hibbert, and W. D. Robb, J. Phys. B: Atom. Molec. Phys. **4**, 153 (1971).

[31] K. A. Berrington, W. B. Eissner, and P. H. Norrington, Comp. Phys. Comm. **92**, 290 (1995).

[32] K. A. Berrington, P. G. Burke, M. L. Dourneuf, W. D. Robb, K. T. Taylor, and V. K. Lan, Comp. Phys. Comm. **14**, 367 (1978).

[33] A. Hibbert, Comp. Phys. Comm. **9**, 141 (1975).

[34] L. Quigley and K. A. Berrington, J. Phys. B: At. Mol. Opt. Phys. **29**, 4529 (1996).

[35] L. Quigley, K. A. Berrington, and J. Pelan, Comp. Phys. Comm. **114**, 225 (1998).

[36] P. G. Burke and B. L. Moiseiwitsch, *Atomic processes and applications: in honour of David R. Bates' 60th birthday* (North-Holland Pub. Co., New York, 1976).

[37] M. Ya. Amusia, *Atomic Photoeffect* (Plenum Press, New York, 1990).

[38] E. Merzbacher, *Quantum Mechanics*, 3rd Ed. (John Wiley & Sons Inc., New York, 1998).

[39] J. J. Sakurai, *Modern Quantum Mechanics*, Rev. Ed. (Addison-Wesley Pub. Co., Reading, Mass., 1994).

[40] H. A. Bethe and E. E. Saltpeter, *Quantum Mechanics of One- and Two- Electron Atoms* (Academic Press, New York, 1957).

[41] U. Fano, Phys. Rev. **124**, 1866 (1961).

[42] P. G. Burke, A. Hibbert, and W. D. Robb, J. Phys. B: Atom. Molec. Phys. **4**, 153 (1971).

[43] P. G. Burke and K. Taylor, J. Phys. B: At. Mol. Opt. Phys. **8**, 2620 (1975).

[44] N. S. Scott and P. G. Burke, J. Phys. B: At. Mol. Opt. Phys. **13**, 4299 (1980).

[45] K. A. Berrington, W. B. Eissner, and P. H. Norrington, Comp. Phys. Comm. **92**, 290 (1995).

[46] J. P. A. Buttle, Phys. Rev. **160**,719 (1967).

[47] M. J. Seaton, J. Phys. B: At. Mol. Opt. Phys. **20**, L69 (1987).

[48] U. Fano and G. Racah, *Irreducible Tensorial Sets* (Academic Press Inc., New York, 1959).

[49] M. J. Seaton, J. Phys. B: At. Mol. Phys. **19**, 2601 (1986).

[50] E. Clementi and C. Roetti, At. Data Nucl. Data Tables **14**, 177 (1974).

[51] A. W. Weiss, Astronphys. J. **138**, 1262 (1963).

[52] G. Breit and E. P. Wigner, Phys. Rev. **49**, 519 (1936).

[53] http://physics.nist.gov/PhysRefData/ASD/index.html

[54] R. Wehlitz, D. Lukié, and J. B. Bluett, Phys. Rev. A **68**, 052708 (2003).

[55] P. Olalde-Velasco, E. Méndez-Martínez, and J. Jiménez-Mier, Phys. Rev. A **76**, 032701 (2007).

[56] S. Schippers, A. Müller, B. M. McLaughlin, A. Aguilar, C. Cisneros, E. D. Emmons, M. F. Gharaibeh, and R. A. Phaneuf, J. Phys. B: At. Mol. Opt. Phys. **36**, 3371 (2003).

[57] A. Müller, R. A. Phaneuf, A. Aguilar, M. F. Gharaibeh, A. S. Schlachter, I. Alvarez, C. Cisneros, G. Hinojosa, and B. M. McLaughlin, J. Phys. B: At. Mol. Opt. Phys. Lett. **35**, L137 (2002).

[58] J.-M. Bizau, J.-P. Champeauz, D. Cubaynes, F. J. Wuilleumier, F. Folkmann, T. S. Jacobsen, F. Penent, C. Blancard, and H. Kjeldsen, Astron. Astrophys. **439**, 387 (2005).

[59] A. Müller, S. Schippers, R. A. Phaneuf, A. L. D . Kilcoyne, H. Bräuning, A. S. Schlachter, M. Lu and B. M. McLaughlin, J. Phys. Conf. Ser. **58**, 383 (2007).

[60] J.-P. Champeaux, J.-M. Bizau, D. Cubaynes, C. Blancard, S. Nahar, D. Hitz, J. Bruneau, and F. J. Wuilleumier, Astrophys. J. Suppl. S. **148**, 583 (2003).

[61] J. A. Tully, M. J. Seaton, and K. A. Berrington, J. Phys. B: At. Mol. Opt. Phys. **23,** 3811 (1990).

[62] R. F. Reilman and S. T. Manson, Astrophys. J. Supp. **40**, 815 (1979).

[63] D. S. Kim, S. S. Tayal, H.-L. Zhou, and S. T. Manson, Phys. Rev. A **61**, 062701 (2000).

[64] D. S. Kim, H.-L. Zhou, S. T. Manson, and S. S. Tayal, Phys. Rev. A **64**, 042713 (2001).

[65] D. S. Kim and S. T. Manson, J. Phys. B: At. Mol. Opt. Phys. **37**, 4013 (2004).

[66] D. S. Kim and S. T. Manson, Phys. Rev. A **71**, 032701 (2005).

[67] D. S. Kim and S. T. Manson, J. Phys. B: At. Mol. Opt. Phys. **37**, 4707 (2004).

[68] D. S. Kim and Y. S. Kim, J. Phys. B: At. Mol. Opt. Phys. **40**, 3807 (2007).

[69] F. Robicheaux, Phys. Rev. A **43**, 5946 (1991).

[70] S. N. Nahar and A. K. Pradhan, Astrophys. J. Suppl. S. **111**, 339 (1997).

[71] A. K. Pradhan, G. X. Chen, and S. N. Nahar, Phys. Rev. Lett. **87**, 183201 (2001).

[72] S. N. Nahar, Phys. Rev. A **58**, 3766 (1998).

[73] W. Eissner, M. Jones, and H. Nussbaumer, Comp. Phys. Comm. **8**, 270 (1974).

[74] http://www.astronomy.ohio-state.edu/~nahar/nahar_radiativeatomicdata/c3/c3.px.fs.txt

[75] S. N. Nahar, Phys. Rev. A **69**, 042714 (2004).

[76] B. M. McLaughlin, private communication.

[77] H. A. Bethe and E. E. Saltpeter, *Quantum Mechanics of One- and Two- Electron Atoms* (Academic Press, New York, 1957), p. 255ff.

[78] W. L Wiese, M. W. Smith and B. M. Glennon, *Atomic Transition Probabilities* (U. S. GPO, Washington, D.C., 1966), Vol. 1, p. 22.

[79] R. D. Cowan, *The Theory of Atomic Structure and Spectra* (University of California Press, Berkeley, 1981).

APPENDIX A ATOMIC SYSTEM IN AN ELECTROMAGNETIC FIELD

Suppose there is an atomic system with a nucleus of charge *Ze* and infinite weight and with *N* electrons of charge $-e$ and mass *m*. The Hamiltonian consists of three summations: the sum of kinetic and potential energies of the electrons under the central field of the nucleus, and the sum of Coulomb interactions between each pair of electrons. In Gaussian (cgs) units, the Hamiltonian is written as

$$H_0 = \sum_{n=1}^{N}\left[\left(\frac{\vec{p}_n^{\,2}}{2m} - \frac{Ze^2}{r_n}\right) + \sum_{m=n+1}^{N}\frac{e^2}{|\vec{r}_m - \vec{r}_n|}\right] \tag{A.1}$$

where $\vec{r}_n$ are the electron positions from the nucleus and $\vec{p}_n$ are the electron momentums. The state of this atom is described by the *N*-electron wave function $\Psi_E(x_1 \ldots x_N)$ which is the solution to the time-independent Schrödinger equation

$$H_0\Psi_E(x_1 \ldots x_N) = E\Psi_E(x_1 \ldots x_N) \tag{A.2}$$

corresponding to the total energy *E* of the system, and $x_n \equiv \vec{r}_n, \sigma_n$ are the spatial coordinates and the spin projections of the electrons. When an external electromagnetic field is added to the system, we modify the Hamiltonian by including the vector potential $\vec{A}(\vec{r},t)$ to the momentum term:

$$\begin{aligned} H_A &= H_0 + V(t) \\ &= \sum_{n=1}^{N}\left\{\left[\frac{1}{2m}\left(\vec{p}_n + \frac{e}{c}\vec{A}(\vec{r}_n,t)\right)^2 - \frac{Ze^2}{r_n}\right] + \sum_{m=n+1}^{N}\frac{e^2}{|\vec{r}_m - \vec{r}_n|}\right\} \end{aligned} \tag{A.3}$$

where $V(t)$ represents the interaction term. The time-dependent Schrödinger equation

$$i\hbar\frac{\partial\Psi(x_1 \ldots x_N, t)}{\partial t} = H_A\Psi(x_1 \ldots x_N, t) \tag{A.4}$$

is to be solved for the wave function.

In the weak field assumption, the $\vec{A}^2$ term in Eq. (A.3) is neglected. If we choose the potential gauge satisfying $\vec{\nabla}\cdot\vec{A}=0$, the interaction between the atom and the electromagnetic field in the Hamiltonian is

$$V(t)=\frac{e}{mc}\sum_{n=1}^{N}A(\vec{r}_n,t)\cdot\vec{p}_n\,. \tag{A.5}$$

Considering the electromagnetic field as a plane wave of single frequency ω and wave number $k=\omega/c$, traveling in the direction $\hat{k}$ which is perpendicular to the polarization direction $\hat{\varepsilon}$, $\vec{A}(\vec{r},t)$ is represented by

$$\vec{A}(\vec{r},t)=A_0\hat{\varepsilon}\left(e^{i\vec{k}\cdot\vec{r}-i\omega t}+e^{-i\vec{k}\cdot\vec{r}+i\omega t}\right), \tag{A.6}$$

where the $e^{-i\omega t}$ term is responsible for absorption and $e^{+i\omega t}$ term is responsible for stimulated emission. $V(t)$ is then reduced to

$$V(t)=\frac{eA_0}{mc}\sum_{n=1}^{N}\left(e^{i\vec{k}\cdot\vec{r}_n-i\omega t}+e^{-i\vec{k}\cdot\vec{r}_n+i\omega t}\right)\hat{\varepsilon}\cdot\vec{p}_n\,. \tag{A.7}$$

It is well known in the perturbation theory that the (first order) probability amplitude $c_\beta(t)$ of state $|\beta\rangle$ evolves with time, in a system initially at $|\alpha\rangle$, as

$$i\hbar\frac{\partial c_\beta(t)}{\partial t}=e^{i\omega_{\beta\alpha}t}\langle\beta|V(t)|\alpha\rangle \tag{A.8}$$

where $\omega_{\beta\alpha}=(E_\beta-E_\alpha)/\hbar$. The total transition probability is $\lim_{t\to\infty}|c_\beta(t)|^2$, and the transition probability rate is defined by

$$W_{\alpha\to\beta}=\lim_{t\to\infty}\frac{\partial|c_\beta(t)|^2}{\partial t}\,. \tag{A.9}$$

Suppose $|\alpha\rangle$ and $|\beta\rangle$ are discrete states with the normalization $\langle\alpha|\alpha\rangle = \langle\beta|\beta\rangle = 1$ and their eigenvalues $E_\alpha < E_\beta$. If we look at the details of only the absorption case ($e^{-i\omega t}$ term), applying the Fermi's golden rule, the transition probability rate is given by

$$W_{\alpha\to\beta} = \frac{2\pi}{\hbar}\left|\langle\beta|v^+|\alpha\rangle\right|^2 \delta\left(E_\beta - E_\alpha - \hbar\omega\right) \tag{A.10}$$

where

$$v^+ = \frac{eA_0}{mc}\sum_{n=1}^{N} e^{i\vec{k}\cdot\vec{r}_n}\hat{\varepsilon}\cdot\vec{p}_n\,, \tag{A.11}$$

and the delta function ensures the conservation of energy. If the final state $|\beta\rangle$ is continuum state, the form of Eq. (A.10) is integrated with $\int\rho(E_\beta)dE_\beta$ where $\rho(E)$ is the number of states per unit energy around *E*.

The exponential term in Eq. (A.11) has the expansion

$$e^{i\vec{k}\cdot\vec{r}} = 1 + i\vec{k}\cdot\vec{r} - \frac{1}{2}\left(\vec{k}\cdot\vec{r}\right)^2 + \cdots \tag{A.12}$$

Under the weak field condition that the wavelength is long relative to the size of the atomic system, i.e. $\vec{k}\cdot\vec{r} << 1$ in our working region, the electric dipole (E1) approximation $e^{i\vec{k}\cdot\vec{r}} = 1$ is fairly accurate, and $\langle\beta|v^+|\alpha\rangle$ is given by

$$\begin{aligned}\langle\beta|v^+|\alpha\rangle &= \frac{eA_0}{mc}\sum_{n=1}^{N}\hat{\varepsilon}\cdot\langle\beta|\vec{p}_n|\alpha\rangle \\ &= -\frac{i\hbar eA_0}{mc}\sum_{n=1}^{N}\hat{\varepsilon}\cdot\langle\beta|\vec{\nabla}_n|\alpha\rangle\end{aligned}\,, \tag{A.13}$$

and Eq. (A.10) becomes

$$W_{\alpha\to\beta} = \frac{2\pi\hbar e^2|A_0|^2}{m^2c^2}\left|\langle\beta|\hat{\varepsilon}\cdot\vec{D}_V|\alpha\rangle\right|^2 \delta\left(E_\beta - E_\alpha - \hbar\omega\right) \tag{A.14}$$

where we have defined the dipole velocity operator as

$$\vec{D}_V = \sum_{n=1}^{N} \vec{\nabla}_n \,. \tag{A.15}$$

Applying the relation

$$[\vec{r}_n, H_0] = \frac{i\hbar}{m} \vec{p}_n \,, \tag{A.16}$$

$W_{\alpha\to\beta}$ is also given by

$$W_{\alpha\to\beta} = \frac{2\pi e^2 |A_0|^2 \omega_{\beta\alpha}^2}{\hbar c^2} \left| \left\langle \beta \left| \hat{\varepsilon} \cdot \vec{D}_L \right| \alpha \right\rangle \right|^2 \delta\left(E_\beta - E_\alpha - \hbar\omega\right) \tag{A.17}$$

where the dipole length operator is

$$\vec{D}_L = \sum_{n=1}^{N} \vec{r}_n \,. \tag{A.18}$$

Eq. (A.14) and Eq. (A.18), namely velocity gauge and length gauge, are in principle equivalent.

APPENDIX B ORBITALS BY THE CIV3 CALCULATION

The coefficients in Eq. (3.6) optimized by CIV3 are listed here. To be consistent with the published Hartree-Fock data, the Clementi-type coefficients C'_{jnl} are used through out all tables here instead of the Slater-type coefficients C_{jnl}. C'_{jnl} are defined in terms of the normalized Slater-type orbitals $\{\chi_{jnl}\}$ as

$$P_{nl} = \sum_{j=1}^{k} C'_{jnl}\chi_{jnl} , \tag{B.1}$$

and C'_{jnl} and C_{jnl} are related by

$$C_{jnl} = C'_{jnl} \frac{\left(2\zeta_{jnl}\right)^{I_{jnl}+1/2}}{\left[\left(2I_{jnl}\right)!\right]^{1/2}} . \tag{B.2}$$

Table B.1. The coefficients of the Be^{+}, B^{+2}, and C^{+3} orbitals optimized by CIV3 program.

	Be^{+}			B^{+2}			C^{+3}		
	I	*C'*	*ζ*	*I*	*C'*	*ζ*	*I*	*C'*	*ζ*
1*s*	1	4.0000000	0.9171100	1	5.0000000	0.9329900	1	6.0000000	0.9437300
	3	10.8100000	-0.0012900	3	12.0000000	-0.0015100	3	13.2300000	-0.0017200
	3	4.6800000	0.0796000	3	5.9700000	0.0639000	3	7.2700000	0.0535100
	3	3.4000000	0.0431400	3	4.2800000	0.0366100	3	5.1600000	0.0319500
	3	1.9700000	-0.0033100	3	2.7000000	-0.0040900	3	3.4300000	-0.0043900
	3	1.3100000	0.0017800	3	1.8630000	0.0019200	3	2.4160000	0.0018600
2*s*	1	4.0000000	-0.1992200	1	5.0000000	-0.2327000	1	6.0000000	-0.2541900
	3	10.8100000	0.0004500	3	12.0000000	0.0005000	3	13.2300000	0.0006100
	3	4.6800000	-0.0108100	3	5.9700000	-0.0078700	3	7.2700000	-0.0064900
	3	3.4000000	0.0072800	3	4.2800000	0.0045100	3	5.1600000	0.0047400
	3	1.9700000	0.4294300	3	2.7000000	0.4234400	3	3.4300000	0.4106400
	3	1.3100000	0.6159900	3	1.8630000	0.6235000	3	2.4160000	0.6376600
3*s*	1	3.3304542	0.1321823	1	3.9660659	0.1693043	1	4.5629781	0.1991709
	2	0.8986102	-1.1940417	2	1.1640852	-1.6244024	2	1.2998607	-2.4936938
	3	0.7387247	1.7013591	3	1.0868761	2.1222834	3	1.4101801	3.0351461
	3	3.3346249	0.0484321	3	4.1298510	0.0573848	3	4.8946047	0.0625941
4*s*	1	3.0977618	0.0888357	1	3.8400517	0.1092443	1	4.4881866	0.1269501
	2	0.4074257	-4.4828747	2	1.6108771	-0.3640869	2	0.7793965	-4.5990206
	3	0.6955830	2.8095534	3	0.6682133	-2.6725457	3	1.8127226	0.9084591
	4	0.7710069	1.5592736	4	1.1440490	2.5841563	4	1.4856833	3.6971358
2*p*	2	1.0285432	0.9648286	2	1.5392912	0.9622371	2	2.0462592	0.9631823
	2	1.9795848	0.0396062	2	2.7334581	0.0395819	2	3.4644980	0.0370940
	2	4.2236186	0.0130096	2	5.5359502	0.0128475	2	6.8204101	0.0120670
3*p*	2	0.8011493	1.0642058	2	1.1774909	1.1029278	2	1.6009661	1.1665611
	2	2.4589010	0.0416875	2	5.1545334	0.0133588	2	6.6969447	0.0077833
	3	0.6693055	-1.6440256	3	1.0056206	-1.6893808	3	1.3375835	-1.6763067
	3	3.4158230	-0.0156516	3	3.4533955	0.0166913	3	2.4743213	-0.0605406
4*p*	2	1.3830550	0.2385109	2	1.2765885	0.6840949	2	2.6362754	0.2502244
	3	0.4320269	2.8553060	3	0.7243708	-3.6612029	3	0.8541568	2.7499294
	4	0.7150823	-2.6711706	4	0.7381173	3.7734627	4	1.4317722	-2.5727978
3*d*	3	0.6670936	0.9999322	3	1.0008012	0.9998792	3	1.3344598	0.9998457
	3	3.4858469	0.0005869	3	4.5462539	0.0007576	3	5.6188048	0.0008187
4*d*	3	0.5568674	1.5091079	3	1.2035699	0.4153945	3	1.6049899	0.4155527
	4	0.4938150	-1.9788648	4	0.7328835	-1.7298294	4	0.9772786	-1.7305176
	4	1.1581891	-0.0124900	4	1.0121284	0.9077065	4	1.3492634	0.9082497
4*f*	4	0.4999978	1.0000000	4	0.7500021	1.0000000	4	1.0000000	1.0000000

Table B.2. The coefficients of the N^{+4}, O^{+5}, and Ne^{+7} orbitals optimized by CIV3 program.

	N^{+4}			O^{+5}			Ne^{+7}		
	I	*C'*	*ζ*	*I*	*C'*	*ζ*	*I*	*C'*	*ζ*
1*s*	1	7.0000000	0.9514900	1	8.0000000	0.9573800	1	10.0000000	0.9656800
	3	14.4400000	-0.0018900	3	15.6500000	-0.0020900	3	18.0700000	-0.0024600
	3	8.5600000	0.0465600	3	9.8600000	0.0413200	3	12.4500000	0.0342900
	3	6.0400000	0.0277900	3	6.9200000	0.0246700	3	8.6800000	0.0197300
	3	4.1500000	-0.0041900	3	4.8800000	-0.0039700	3	6.3500000	-0.0033200
	3	2.9700000	0.0016800	3	3.5230000	0.0015000	3	4.6300000	0.0011600
2*s*	1	7.0000000	-0.2691700	1	8.0000000	-0.2802200	1	10.0000000	-0.2954200
	3	14.4400000	0.0008700	3	15.6500000	0.0010900	3	18.0700000	0.0016400
	3	8.5600000	-0.0067800	3	9.8600000	-0.0067200	3	12.4500000	-0.0072400
	3	6.0400000	0.0095000	3	6.9200000	0.0119700	3	8.6800000	0.0168100
	3	4.1500000	0.3953400	3	4.8800000	0.3823500	3	6.3500000	0.3592200
	3	2.9700000	0.6512100	3	3.5230000	0.6641300	3	4.6300000	0.6866400
3*s*	1	5.1420949	0.2237521	1	5.7079659	0.2446209	1	6.6878661	0.2860111
	2	1.5770703	-2.6768872	2	1.8627397	-2.7877471	2	2.7493987	-2.2447647
	3	1.7316852	3.2051477	3	2.0545073	3.3016419	3	2.7511866	2.6506986
	3	5.6627806	0.0646773	3	6.4306027	0.0649758	3	7.6794501	0.0715804
4*s*	1	5.0622118	0.1433053	1	5.5757311	0.1591569	1	6.4314209	0.1918745
	2	0.9713345	-4.8280742	2	1.1662884	-5.0795314	2	1.5638841	-5.6092072
	3	2.3203887	0.9044489	3	2.8020756	0.9666983	3	3.7072470	1.1696812
	4	1.8354091	3.9534682	4	2.1787225	4.1643689	4	2.8523061	4.5300029
2*p*	2	2.5510248	0.9651222	2	3.0544040	0.9671858	2	4.0589654	0.9711854
	2	4.1822137	0.0342568	2	4.8873934	0.0316461	2	6.2927820	0.0271621
	2	8.0907587	0.0111979	2	9.3497647	0.0103934	2	11.8641422	0.0089750
3*p*	2	2.7770379	0.5010025	2	2.2733151	1.1877552	2	2.6389721	1.7721534
	2	7.8574595	0.0076410	2	5.6653357	0.0330389	2	11.3038661	0.0067014
	3	1.6651547	-1.6303989	3	2.0084277	-1.7769553	3	2.6977590	-2.3335337
	3	2.2995966	0.6226624	3	7.7349580	-0.0108319	3	4.0061634	-0.0652322
4*p*	2	3.2405181	0.2538757	2	3.8373884	0.2568007	2	5.0218450	0.2608394
	3	1.0641483	2.7323478	3	1.2735821	2.7200350	3	1.6920758	2.7077597
	4	1.7881261	-2.5585024	4	2.1438432	-2.5488810	4	2.8538142	-2.5406051
3*d*	3	1.6680617	0.9998277	3	2.0016157	0.9998196	3	2.6686176	0.9998186
	3	6.6963496	0.0008260	3	7.7764180	0.0008082	3	9.9403492	0.0007460
4*d*	3	1.0034115	-1.6388030	3	1.4880384	2.1899201	3	2.2111326	1.5428587
	4	2.0632843	1.2593528	4	1.5013922	-2.7189374	4	1.9787629	-2.0155077
	4	4.7128846	0.1035452				4	4.4579198	-0.0118113
4*f*	4	1.2500200	1.0000000	4	1.5000236	1.0000000	4	2.0000329	1.0000000

Table B.3. The coefficients of the Mg^{+9}, Si^{+11}, and S^{+13} orbitals optimized by CIV3 program.

	Mg^{+9}			Si^{+11}			S^{+13}		
	I	*C'*	*ζ*	*I*	*C'*	*ζ*	*I*	*C'*	*ζ*
1*s*	1	11.5737000	0.9759300	1	13.5692000	0.9774100	1	15.5562000	0.9787700
	1	21.8524000	0.0193500	1	24.9593000	0.0181200	1	27.9444000	0.0174900
	2	5.4927400	-0.0073600	2	6.5046300	-0.0086500	2	7.5063500	-0.0082300
	2	8.6105600	0.0120200	2	10.1935000	0.0113100	2	11.7901000	0.0097100
	2	4.9354800	0.0053700	2	5.8752600	0.0064300	2	6.8144100	0.0062800
2*s*	1	11.5737000	-0.3190000	1	13.5692000	-0.3255000	1	15.5562000	-0.3303400
	1	21.8524000	-0.0013400	1	24.9593000	-0.0007900	1	27.9444000	-0.0004500
	2	5.4927400	0.6370600	2	6.5046300	0.6683400	2	7.5063500	0.6954900
	2	8.6105600	-0.3458100	2	10.1935000	-0.3547700	2	11.7901000	-0.3593300
	2	4.9354800	0.6945400	2	5.8752600	0.6731800	2	6.8144100	0.6514700
3*s*	1	7.8904342	0.3053758	1	8.9470758	0.3271048	1	9.9887022	0.3453276
	2	3.0295706	-3.0111154	2	3.6194631	-3.0701628	2	4.2120730	-3.1140270
	3	3.3511972	3.4782091	3	4.0013965	3.5200975	3	4.6525242	3.5493910
	3	9.4983495	0.0594372	3	11.0272823	0.0557105	3	12.5544642	0.0521331
4*s*	1	7.4263522	0.2101621	1	8.4645517	0.2243175	1	9.4847229	0.2362469
	2	1.7068381	-7.8362825	2	2.0543374	-7.9094446	2	2.4046674	-7.9609595
	3	2.0709063	19.2855776	3	2.4847254	19.3417552	3	2.9007821	19.3617698
	4	2.3809746	-12.2472754	4	2.8508146	-12.2383968	4	3.3220916	-12.2138352
2*p*	2	5.0617509	0.9744178	2	6.0636530	0.9770750	2	7.0650144	0.9792563
	2	7.6781465	0.0237658	2	9.0590249	0.0210932	2	10.4352956	0.0189553
	2	14.3641346	0.0078763	2	16.8616664	0.0069967	2	19.3562704	0.0062872
3*p*	2	3.3075467	1.7425292	2	4.0915263	1.6037013	2	4.5625806	1.7856743
	2	13.7522280	0.0057843	2	16.1987887	0.0050762	2	18.6139339	0.0045506
	3	3.3661608	-2.3101158	3	4.0341938	-2.1647008	3	4.6974640	-2.3678800
	3	4.9559514	-0.0549060	3	5.9078479	-0.0472072	3	6.8162583	-0.0425696
4*p*	2	6.1987604	0.2636121	2	7.3768738	0.2653024	2	8.5422989	0.2671262
	3	2.1102083	2.7017643	3	2.5288044	2.7016836	3	2.9459749	2.6963852
	4	3.5627628	-2.5375377	4	4.2704820	-2.5395102	4	4.9791699	-2.5359993
3*d*	3	3.3355240	0.9998262	3	4.0023697	0.9998363	3	4.6691744	0.9998468
	3	12.1063538	0.0006786	3	14.2734005	0.0006172	3	16.4413314	0.0005636
4*d*	3	2.0076536	1.6415446	3	4.5590394	0.4983061	3	5.2610336	0.5168522
	4	4.1233318	-1.2617533	4	2.9442409	-1.7959447	4	3.4376456	-1.8096464
	4	9.3999850	-0.1041397	4	3.9331287	0.8852632	4	4.5617707	0.8791405
4*f*	4	2.5000421	1.0000000	4	3.0000418	1.0000000	4	3.5000527	1.0000000

Table B.4. The coefficients of the Ar^{+15}, Ca^{+17}, and Ti^{+19} orbitals optimized by CIV3 program.

	Ar^{+15}			Ca^{+17}			Ti^{+19}		
	I	*C'*	*ζ*	*I*	*C'*	*ζ*	*I*	*C'*	*ζ*
1*s*	1	17.5357000	0.9800700	1	19.5095000	0.9813400	1	21.4790000	0.9826200
	1	30.8607000	0.0171900	1	33.7538000	0.0170600	1	36.6670000	0.0169500
	2	8.5000000	-0.0067100	2	9.4870300	-0.0045800	2	10.4693000	-0.0020700
	2	13.3961000	0.0076100	2	15.0073000	0.0053200	2	16.6193000	0.0030000
	2	7.7555000	0.0053100	2	8.7002400	0.0038500	2	9.6508100	0.0020400
2*s*	1	17.5357000	-0.3341100	1	19.5095000	-0.3371700	1	21.4790000	-0.3397600
	1	30.8607000	-0.0002400	1	33.7538000	-0.0000900	1	36.6670000	0.0000300
	2	8.5000000	0.7181800	2	9.4870300	0.7371900	2	10.4693000	0.7521500
	2	13.3961000	-0.3614100	2	15.0073000	-0.3621700	2	16.6193000	-0.3623400
	2	7.7555000	0.6316800	2	8.7002400	0.6142000	2	9.6508100	0.6001600
3*s*	1	11.0178241	0.3609422	1	12.0362309	0.3745398	1	13.0454059	0.3865384
	2	4.8069922	-3.1480387	2	5.4038048	-3.1753582	2	6.0022173	-3.1978894
	3	5.3044776	3.5707402	3	5.9571219	3.5868889	3	6.6103551	3.5994461
	3	14.0793365	0.0488479	3	15.6023109	0.0458732	3	17.1234670	0.0431965
4*s*	1	10.4882318	0.2465847	1	11.4779913	0.2556792	1	11.8440259	0.2836014
	2	2.7584370	-7.9922026	2	3.1148463	-8.0122043	2	3.0636417	-11.5978083
	3	3.3194829	19.3448722	3	3.7402103	19.3110990	3	5.4380726	8.6460587
	4	3.7950066	-12.1718091	4	4.2691673	-12.1235118	4	3.6578826	3.4395774
2*p*	2	8.0660295	0.9810654	2	9.0668160	0.9825922	2	10.0674392	0.9838937
	2	11.8073223	0.0172126	2	13.1779103	0.0157621	2	14.5469103	0.0145380
	2	21.8482627	0.0057061	2	24.3400204	0.0052204	2	26.8306929	0.0048098
3*p*	2	5.1691162	1.8174426	2	5.2726804	2.2971288	2	6.8114529	1.5261249
	2	21.0239488	0.0041243	2	22.1762705	0.0047312	2	24.0138986	0.0066247
	3	5.3605420	-2.4055016	3	5.8148556	-2.4132523	3	6.6985132	-2.1376925
	3	7.7126756	-0.0390904	3	6.5692872	-0.5572907	3	16.2690571	0.0097865
4*p*	2	9.7142448	0.2681660	2	6.7282579	0.8549167	2	7.4001603	0.8733676
	3	3.3642034	2.6967112	3	3.8816715	-5.9643527	3	4.3288462	-5.9739325
	4	5.6865908	-2.5376100	4	4.2955864	6.0290201	4	4.7814730	6.0177012
3*d*	3	5.3359506	0.9998567	3	6.0027067	0.9998659	3	6.6694472	0.9998741
	3	18.6094715	0.0005174	3	20.7783359	0.0004775	3	22.9476129	0.0004429
4*d*	3	5.9548345	0.5338553	3	6.6418442	0.5495091	3	5.4078813	1.6403478
	4	3.9314251	-1.8219774	4	4.4255158	-1.8331524	4	4.9650913	-2.1251412
	4	5.1862185	0.8732958	4	5.8071099	0.8677370	4	10.9561941	-0.0064000
4*f*	4	4.0000566	1.0000000	4	4.5000556	1.0000000	4	5.0000614	1.0000000

Table B.5. The coefficients of the Cr^{+21}, and Fe^{+23} orbitals optimized by CIV3 program.

	Cr^{+21}			Fe^{+23}		
	I	*C'*	*ζ*	*I*	*C'*	*ζ*
1*s*	1	23.4464000	0.9839300	1	25.4141000	0.9852700
	1	39.6364000	0.0167800	1	42.6930000	0.0164700
	2	11.4482000	0.0007100	2	12.4248000	0.0036300
	2	18.2279000	0.0007800	2	19.8289000	-0.0012200
	2	10.6086000	-0.0000500	2	11.5747000	-0.0023300
2*s*	1	23.4464000	-0.3420400	1	25.4141000	-0.3441200
	1	39.6364000	0.0001800	1	42.6930000	0.0003900
	2	11.4482000	0.7631800	2	12.4248000	0.7706800
	2	18.2279000	-0.3623700	2	19.8289000	-0.3626000
	2	10.6086000	0.5898800	2	11.5747000	0.5833000
3*s*	1	13.5474919	0.4191871	1	24.3834953	0.1981281
	2	7.3923897	-2.5359723	2	5.6766725	-1.0584557
	3	7.3965898	2.8256307	3	13.7309493	-0.7740042
	3	17.5771984	0.0512380	3	7.2314671	2.3110819
4*s*	1	12.7325112	0.2927465	1	5.1953560	1.2648206
	2	3.3802657	-11.6459630	2	8.8057530	-2.2525467
	3	5.9780469	8.7163549	3	5.0547813	6.9947757
	4	4.0296366	3.4094387	4	5.6453173	-7.0629575
2*p*	2	11.0678834	0.9849874	2	12.3678517	0.9340900
	2	15.9089098	0.0135205	2	9.4260799	0.0393047
	2	29.3246217	0.0044572	2	9.5203407	0.0293982
3*p*	2	7.5779710	1.4864859	2	8.1657554	1.5983298
	2	16.5767794	0.0191742	2	7.0264595	0.0042760
	3	7.3620603	-2.0922845	3	7.2009279	-0.3554371
	3	23.4188698	-0.0058268	3	8.2617170	-1.8498345
4*p*	2	8.0675001	0.8901509	2	12.7730041	0.3567527
	3	4.7774091	-5.9821387	3	14.0098516	0.0101985
	4	5.2680328	6.0068555	4	5.7342152	2.1047149
				4	8.2258920	-1.8794994
3*d*	3	7.3361762	0.9998816	3	8.0183045	0.9891707
	3	25.1165664	0.0004127	3	6.7934533	0.0110896
4*d*	3	5.9352032	1.6512490	3	6.5021446	1.6243685
	4	5.4634900	-2.1372653	4	5.9513282	-2.1086966
	4	12.0358861	-0.0059310	4	12.0003765	-0.0058041
4*f*	4	5.5000650	1.0000000	4	6.0000370	1.0000000